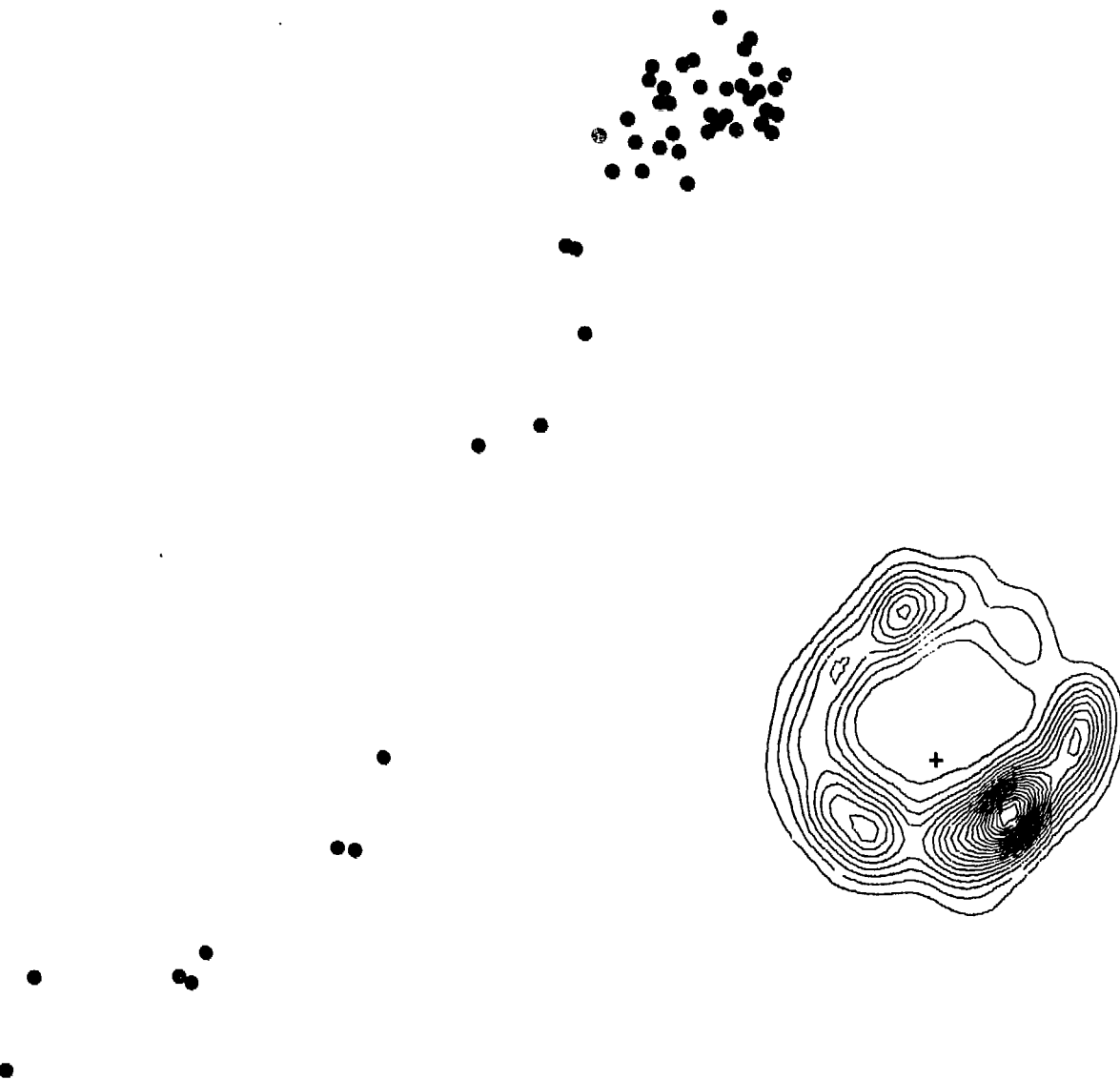


NL 84 C 00 3 0

INIS-mf--9020

# THE NATURE OF OH/IR STARS

Properties and characteristics of an evolved stellar population



Jaap Herman

# THE NATURE OF OH/IR STARS

properties and characteristics of an evolved stellar population

**THE NATURE OF OH/IR STARS**  
properties and characteristics of an evolved stellar population

proefschrift

ter verkrijging van de graad van Doctor  
in de Wiskunde en Natuurwetenschappen  
aan de Rijksuniversiteit te Leiden,  
op gezag van de Rector Magnificus Dr. A.A.H. Kassenaar,  
hoogleraar in de faculteit der Geneeskunde,  
volgens besluit van het college van dekanen  
te verdedigen op donderdag 8 september 1983  
te klokke 14.15 uur

door

**Jacobus Herman**  
geboren te Haarlem in 1954

Sterrewacht Leiden

1983  
Beugelsdijk Leiden B.V.

De beoordelingscommissie bestond uit de volgende leden:

Professor dr. H.J. Habing, promotor

Dr. J. Lub, referent

Dr. L.L.E. Braes, referent

Professor dr. W.B. Burton

Professor dr. H.C. van de Hulst

Professor dr. T. de Jong

Professor dr. J.H. van der Waals, q.q.

This research was supported by a grant from ASTRON, the Netherlands Foundation for Astronomical Research. ASTRON receives its funds from ZWO, the Netherlands Organization for the Advancement of Pure Research.

**aan mijn ouders**

The nature of OH/IR stars  
Properties and characteristics of an evolved stellar population

Contents

Contents	7	
Summary	11	
Chapter I	General Introduction	
I.1	History	15
I.2	Present state of knowledge	19
I.3	Means	21
Chapter II	Dwingeloo Monitor	
II.1	Introduction	27
II.2	Observations	27
II.3	Calibration	27
II.4	Reduction	28
II.5	Confusion	30
II.6	Data analysis	
a.	First approach	32
b.	Internal calibration	35
c.	Results	37
d.	Remarks on individual stars	40
e.	Asymmetry of the radio light curves	44
f.	Phase lag	45
g.	Results	51
h.	Radii	57
II.7	Conclusion	63
Chapter III	VLA Line Observations	
III.1	Introduction	69
III.2	Observations and reduction	69
III.3	Data analysis	
a.	Positions and synthesized beamsizes	71
b.	Shell sizes	79

	c. Asymmetry and thickness of the OH shells	83
	d. Distances	88
	e. Distance to the galactic centre	89
	III.4 Conclusion	90
Chapter IV	IR Observations	
	IV.1 Introduction	93
	IV.2 Observations and reduction	93
	IV.3 Results	94
	IV.4 Mean luminosities	
	a. Variability	98
	b. Interstellar extinction	99
	IV.5 The 9.7 $\mu\text{m}$ feature	102
	IV.6 The colour temperatures	104
	IV.7 Maser pump	105
	IV.8 Conclusion	107
Chapter V	Properties of OH/IR stars	
	V.1 Introduction	111
	V.2 Shell geometry	111
	V.3 Saturation and radiative pumping	113
	V.4 Distance determinations	114
	a. OH luminosity as function of the radius of the OH shell	115
	b. Influence of the interstellar UV field on the size of the OH shells	116
	c. Resulting distances	118
	V.5 Masers in the solar neighbourhood	121
	a1. Distances	122
	a2. Probability of maser emission in classical Mira's	122
	b1. Z-distribution for OH masers	124
	b2. Space density of 1612 MHz OH masers	125
	c1. Luminosity function of OH masers (1612 MHz)	128
	c2. Other masers	130

V.6 OH/IR stars as a galactic population	
a. Z-distribution for 1612 MHz OH masers	130
b. Space density of OH masers as function of galacto centric distance	133
c. Synthesis	134
V.7 Properties of OH/IR stars	135
a. Effective temperatures	136
b. Pulsation masses	137
c. Main-sequence masses	
c1. Iben and Truran	137
c2. Olmon	138
c3. Baud and Habing	138
d. Mass of the stellar cores	
d1. Present core mass	140
d2. Initial core mass	140
e. Mass loss rates	
e1. $\dot{M}$ based on infrared observations	141
e2. $\dot{M}$ based on radio observations	141
e3. Reimers formula	142
f. Envelope mass and time scales	143
g. Results and discussion	146
h. Individual cases	150
V.8 Conclusion and suggestions for future work	152
Appendix A Simplified model for maser emission from a circumstellar shell	158
Appendix B Light curves	
a. Radio light curves of OH masers	165
b. IR light curves of OH Mira variables	170
Appendix C Phase lag as function of velocity	172
a. Mira variables and M-type supergiants	173
b. OH/IR stars with large amplitudes ( $\Delta m_r > 0^m.60$ )	174
c. OH/IR stars with intermediate amplitudes ( $0^m.30 < \Delta m_r < 0^m.60$ )	175
d. OH/IR stars with small amplitudes ( $\Delta m_r < 0^m.30$ )	176

<b>Appendix D</b>	<b>VLA continuum observations at 6 cm</b>	
	<b>a. Introduction</b>	177
	<b>b. Observations</b>	177
	<b>c. Results</b>	178
	<b>d. Conclusion</b>	179
<b>Appendix E</b>	<b>Results of the infrared observations at UKIRT</b>	180
	<b>Nederlandse samenvatting</b>	182
	<b>Curriculum vitae</b>	187
	<b>Dankbetuiging</b>	188

## Summary

At the end of the sixties and in the beginning of the seventies anomalous emission was discovered from such molecules as OH, H<sub>2</sub>O, and SiO. Further investigations revealed that one was dealing with masers, a natural equivalent to the well known terrestrial lasers. Masers are operating at much longer wavelengths (in the radio regime) in very large, coherent complexes of gas and dust, that act as the cavity of a laser, where one gets large pathlengths, and hence large amplification of radiation, by multiple reflections between two mirrors. The necessary population inversion in the levels where the maser transitions occur, is sustained by radiation from a luminous central star. These conditions, a huge amount of circumstellar dust and gas, and the presence of a luminous star, imply that we observe masers in two categories of objects mainly: (i) extremely young stars, still embedded in the cloud from which they were formed, and (ii) very old, evolved stars, that return a considerable fraction of their mass to the interstellar medium at the end of their lives. The study of masers may thus give valuable insight in these two important phases in stellar evolution.

In this work masers in *evolved* stars are studied, in particular the emission from the OH radical. This is mainly because OH masers can be seen throughout our Galaxy, whereas the SiO and H<sub>2</sub>O masers are observable only within relatively small distances from the Sun, and furthermore, because the OH emission from evolved stars has several, easily recognized, characteristics which distinguish it from that of other types of objects. In large survey programs several hundred of these evolved, so-called 'OH/IR stars' have been found, from which we have chosen a small sample for more detailed study. Our aims were knowledge of the underlying stars, and a determination of the properties of the circumstellar envelopes, that veil the stars from view totally. Three different kinds of observations form the basis of this thesis.

In the first place, the time variability of the OH masers was measured over a period of five years with the Dwingeloo Radio Telescope. These single-dish observations proved that most of the underlying stars are very long period variables (VLPV), apparently a kind of extension of the well known long period Mira variables. Shapes and amplitudes of the radio light curves for the OH/IR stars appeared to be completely compatible with those

measured for the Mira's, but the periods are much longer. Further, we obtained with the Dwingeloo program the mean OH fluxes, epochs, a confirmation of the radiative coupling between the maser and the star (by comparison with infrared data provided by other observers), the degree of saturation, and, most important of all, a determination of the linear dimensions of the circumstellar shells. This determination was possible, because in the variations of different parts in the shell small time differences show up.

In the second place, multi element interferometer observations were made in order to study the spatial structure of OH masers. They contained information primarily on the shape and the density of the circumstellar shells, and its three dimensional structure. By combining the phase lag measurements and the spatial extent distances to individual stars could be determined with a high, unprecedented accuracy.

In the third place infrared broad band photometry was done in the wavelength region from 3  $\mu\text{m}$  to 20  $\mu\text{m}$ , where most of the energy of these objects is radiated. This provided us with the bolometric luminosities of the stars, and with an estimate of the amount of material in the circumstellar envelopes.

The theoretical part of this thesis (chapter V) is concerned with the picture emerging from a synthesis of all observations, from ourselves but also from others. The space density and galactic distribution of OH/IR stars are discussed and compared with the appearance of OH masers in the solar neighbourhood. Briefly, the occurrence of other type masers in evolved stars is contemplated. Intrinsic properties of the stars, such as age, luminosity, temperature, radius, mass, and mass loss rate are derived, as well as the masses, the extents, the dynamics, and the time scales of the outflowing circumstellar shells.

OH/IR stars appear to be very luminous ( $\sim 10^4 L_{\odot}$ ), intermediate mass (initially  $\sim 4 M_{\odot}$ ) stars with very high mass loss rates ( $\sim 10^{-5} M_{\odot} \text{ yr}^{-1}$ ). They are cool ( $\sim 2700 \text{ K}$ ) giants on the asymptotic giant branch, seen at a moment that they have lost already a considerable fraction ( $\gtrsim 50\%$ ) of their original main-sequence mass. They are in the last phase of evolution and very close ( $\lesssim 10^4 \text{ yr}$ ) to the end of their stellar lives. A large fraction of them will eventually show up as a planetary nebula, some will evolve directly towards the white dwarf stage, and a small percentage of them will

explode as a supernova. The total number of OH/IR stars in our Galaxy and their death rate are completely consistent with the birth rate and the observed numbers of their end products. Also, their galactic distribution is in agreement with that of their progenitors and with that of their final remnants.

## I. General Introduction

### I.1 History

Although some variable stars were known in classical times already (e.g. Algol in the star catalogue Almagest, Ptolemaeus, 138), the eternal constancy of the heavens was unchallenged. The only recognized changes were the ununderstood movements of the planets, or the occasional appearance of a comet or a supernova.

The history of variable stars begins on August 13, 1596 when the clergyman David Fabricius discovered a red star in the constellation Cetus (Fabricius, 1605). It remained visible for about three months and after its disappearance it was several years (1609) before it was seen again. But from the middle of the 17th century (1638) every maximum of this star (now known as  $\alpha$  Ceti) has been observed. Fabricius was rather puzzled by this object and he called it a 'stella mira'. In later years many similar stars were discovered and by now 'Mira' stands for the whole class of long period variables (LPV) with variations in the optical part of the spectrum typically more than  $2^m$  and periods from 200 to 500 days. The stars are red giants of spectral type M, characterized by the presence of emission lines in their spectra. Therefore one also calls them Me-variables. Many observations of these LPV have been made, and are still made, by amateur astronomers; but the professionals have never shown much interest for these stars, that vary so boringly slowly and uncouthly irregularly at the eve of their death.

Death was the leading thought in the middle years of the present century, providing mankind with one positive acquisition only: technical skill, which enabled astronomers to look at completely new topics, and at long buried ones, with new eyes. After the second world war they could for the first time make accurate observations at wavelengths shortward

( $\lambda < 3000 \text{ \AA}$ ) and longward of the optical part of the spectrum (infrared:  $1 \mu\text{m} < \lambda < 1 \text{ mm}$ , and radio:  $\lambda > 1 \text{ mm}$ ). And the LPV proved to be among the more interesting objects, having many molecular absorption bands in the (near) infrared and more IR radiation than expected, caused by reradiation from an extended envelope of dust and gas around the star. At the long radio wavelengths they showed anomalous emission lines from such molecules as SiO, H<sub>2</sub>O, and OH.

True, already in the early twenties Abbot had done 'IR' astronomy ( $\lambda < 2.2 \mu\text{m}$ ), determining the energy distribution of some (20) stars (Abbot, 1924 and 1929), but spectrograms of resolution sufficient to show absorption lines were not published until 1947 (Sanford, 1947; Kuiper *et al.*, 1947). In the following years more sensitive detectors and high altitude and airborne observatories extended our knowledge to ever longer wavelengths. Milestones along this road include the 2 micron sky survey (IRC; Neugebauer and Leighton, 1969), the AFGL four colour sky survey ( $\lambda < 27.4 \mu\text{m}$ ; Price and Walker, 1976) and IRAS, the InfraRed Astronomical Satellite (1983), observing as far as  $100 \mu\text{m}$ .

Just so, the first radiotelescope was built by Karl G. Jansky in 1931, but it remained until March 25, 1951 before the first major discovery in radio astronomy, emission from the 21-cm line of HI (predicted in 1945 by van de Hulst), was made by Ewen and Purcell. Within a few weeks it was also detected by Muller and Oort (1951). Three years later (Hagen and McClain, 1954) HI was detected in absorption. In the beginning of the 1960's a very similar transition was observed at  $\lambda = 18 \text{ cm}$ , from the OH radical.

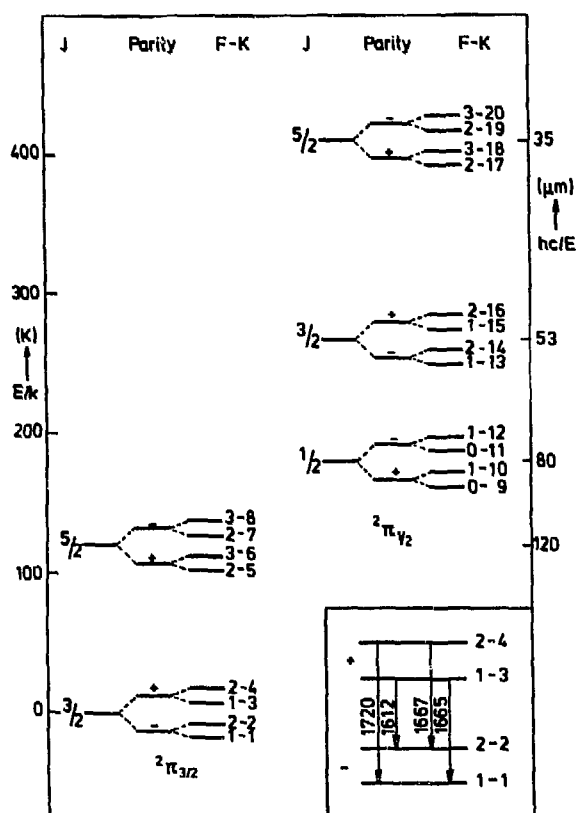


Figure 1 Rotation levels of OH in the ground vibrational state (not to scale). The ground state, where the strong maser transitions occur, is enlarged. The numbers are the frequencies in MHz. The satellite lines ( $F' \neq F$ ) are at 1612 and 1720 MHz, the main lines ( $F' = F$ ) at 1665 and 1667 MHz ( $\lambda = 18 \text{ cm}$ ).

Similar because the hyperfine splitting is caused by spin-orbit coupling; the nuclear spin of the H atom with the (only) unpaired electron, also from the H atom. At first OH was seen only in absorption (Weinreb *et al.*, 1963; See for a review: Burke, 1965), and it seemed to behave similarly to HI, but soon after it was found also in emission (Gundermann, 1965; Weaver *et al.*, 1965) in the direction of the star forming regions W3, W49, and Ori A. The four lines from the ground state (see figure 1) appeared never to be in thermodynamic equilibrium; the main lines being far stronger than the satellite lines and the 1667 MHz line being weaker than the 1665 MHz line. The lines were strongly polarized. Raimond and Eliasson (1967, 1969) determined positions with the Caltech interferometer and found a.o. that the main line OH source in Orion coincides with the Becklin-Neugebauer object, a well known point source at 2  $\mu\text{m}$ . As a consequence searches were started for main line emission from IRC sources (i.e. sources from the 2  $\mu\text{m}$  sky survey), without much success. In hindsight, this is no surprise, because the bulk of IRC sources consists of evolved stars, while the BN-object is extremely young.

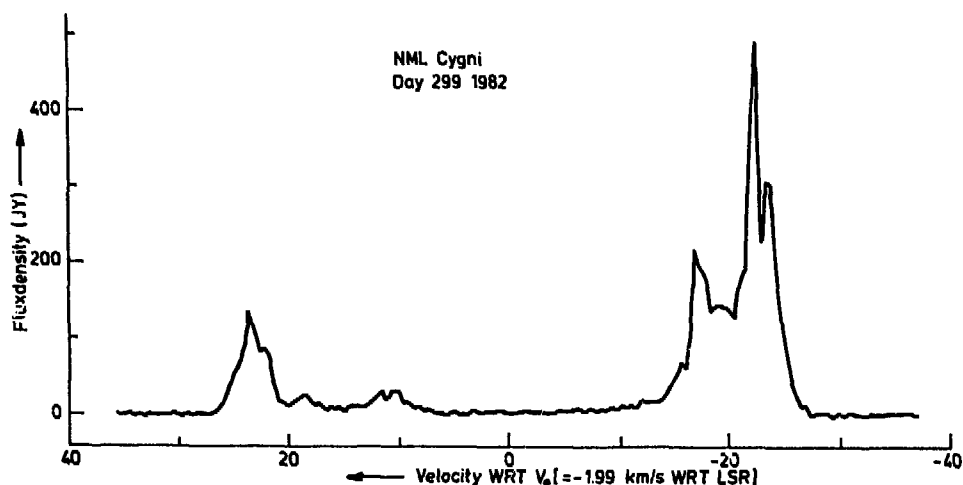


Figure 2. Single-dish profile of NML Cygni (one of the first known type IIb masers) on Julian Day 2445269. The frequency is 1612 MHz, the resolution  $0.54 \text{ km s}^{-1}$ . Velocities on the horizontal axis are given with respect to the central velocity of the profile, which is assumed to be the stellar velocity.

FREQUENCY OBJECTS (MHz)	1612	1665	1667	1720	TYPE	POLARI- SATION	TURNER CLASS	OTHER MASERS	ASSOCIATED OBJECTS
EVOLVED STARS	++	±	+	(ABS)	MASER	NONE	II b	(H <sub>2</sub> O)	OH/IR STARS, IRC STARS
	±	+	++	-	MASER	NONE	I	H <sub>2</sub> O, SiO	MIRA'S, M SUPERGIANTS
YOUNG STARS	±	++	±	±	MASER	CIRC.	I	H <sub>2</sub> O	PROTOSTARS COMPACT H II REGIONS
CLOUDS	(ABS)	(ABS)	(ABS)	+	WEAK MASER/ QUASI THERMAL	NONE	II a		MOLECULAR CLOUDS
	(ABS)	(ABS)	(ABS)	(ABS)		NONE	III		

Figure 3 Classification scheme for OH sources (partly as Turner's, 1970)  
 ++ → - stands for strong to no emission; (abs) for absorption.

But in 1968, Wilson and Barrett discovered satellite MHz line-emission at 1612 from four very red objects (NML Cyg, NML Tau, CIT3 and CIT7), with characteristics totally different from the (young) sources known until then. These stars were strongest in the 1612 MHz satellite line and showed no polarization. Where the young ones had unordered spectra, with many narrow components in a small velocity range, the Wilson and Barrett objects had two broad emission features, well separated in velocity with steep outer edges and a more shallow decline on the inside (see figure 2). In common between the young and old objects was only the absence of thermodynamic equilibrium. VLBI experiments revealed brightness temperatures of up to  $10^{12}$  K (Moran *et al.*, 1968), while the line widths indicated an excitation temperature of  $\sim 100$  K. This all pointed to a maser\*<sup>\*</sup>-type of action, first postulated by Perkins *et al.* (1963). Wilson and Barrett searched in more than 400 IR stars for 1612 MHz maser emission and in 1972 published the first catalogue, containing 27 so-called type IIB OH masers (see figure 3). After identification the optical counterparts of all appeared to be Mira variables or occasionally M-type supergiants, both oxygen rich, evolved stars. In later years many more of these LPV were searched for OH maser emission, and about a hundred were found; some with

\* microwave amplification by stimulated emission of radiation

the strongest emission at 1612 MHz, most at 1667 MHz (see figure 3). Other molecules were also found to show maser emission. H<sub>2</sub>O, like OH, was detected in the direction of star forming regions and in the evolved LPV (Cheung *et al.*, 1969), but SiO masers in late-type stars only, except for the Orion nebula (Snyder and Buhl, 1974). The H<sub>2</sub>O (at 22.2 GHz) and SiO (at 43.1 and 86.2 GHz) masers associated with LPV are relatively weak and can only be seen at small distances ( $D < 1$  kpc), also because receivers at these high frequencies are still comparatively insensitive. The type IIB OH masers (see figure 3) can be seen at large distances, because of their high brightness temperatures, and recognized, because of their characteristic, double peaked spectra, even in other galaxies (Rieu *et al.*, 1976). Casswell and Haynes (1975) and Johansson *et al.* (1977) carried out unbiased surveys along the galactic plane, later followed by others (Bowers, 1978; Baud *et al.*, 1981 and Olton *et al.*, 1982), picking up several hundred of these type IIB stars (Engels, 1980). None of them had optical, nor even IR, counterparts, though tentatively they were named OH/IR stars. In recent years much effort was given to the identification (Schultz *et al.*, 1976; Evans and Beckwith, 1977; Glass, 1978; Epchtein and Rieu, 1982, and Jones *et al.*, 1982) and by now more than half of the OH sources are identified with IR point sources (though many detections are still unpublished), confirming the name OH/IR stars. The IR observations show that they are stars on the asymptotic giant branch with much thicker circumstellar envelopes than the optically known Mira's and that they loose mass at extremely high rates (up to  $10^{-4}$  M<sub>⊙</sub>/yr). Consequently they must be in a dramatic, and rather short lived, phase near the end of their evolution, probably on the verge of becoming a planetary nebula or supernova.

And as Fabricius was almost 400 years ago, we are puzzled by these OH/IR stars; or should we call them 'stellae mirae' and consider that name an omen?

## I.2 Present state of knowledge

Maser emission, originating from various molecules, is associated with the first and the last stages of stellar life. In both cases the very luminous central object is surrounded by a thick envelope of dust and gas. The study of these sources, that often can be seen to large distances from

the sun, can give us answers to many, divergent astronomical problems. In this work we shall concentrate on the masers in late type stars only, but most of the leading questions are more general (for a review of masers in young objects see Habing and Israel, 1979). Below, a number of subjects are listed in various fields of research for which the study of masers is of importance. Between brackets a reference is given to literature where the mentioned topic has been, directly or indirectly, discussed.

- |              |  |              |
|--------------|--|--------------|
| A. Molecular | i. How are the molecules formed and sustained?   | (20)         |
|              | ii. What are their abundances?   | (31)         |
|              | iii. Which molecules 'maser' and how is the population in the relevant levels inverted?  | (12)<br>(42) |
| B. Dust      | i. Where and how is the dust formed?   | (11)         |
|              | ii. What is its size and composition?  | (28)         |
| C. Stellar   | i. What kind of stars are we dealing with?   | (30)         |
|              | What are their intrinsic properties (mass, luminosity, radius, effective temperature, spectral type, magnetic field and internal structure)? | (14)         |
|              | ii. Are they variable?   | (24)         |
|              | iii. In what stage of stellar evolution are they and what will become of them?   | (27)         |
|              | iv. What is their mass loss and what are the dynamics and time scales of the outflowing material?  | ( 3)         |
|              | v. What fraction are the maser-stars of the total population with the same stellar properties?   |              |
|              | vi. What is the maser luminosity function?   |              |
| D. Galactic  | i. What are the distances to OH/IR stars, what are their galactic distribution and kinematics?   | ( 6)         |
|              | ii. What is the relation with the gas component and the contents of the interstellar medium?   |              |
|              | iii. What is, or was, the starformation rate in  |              |

different parts of the galaxy?  
iv. What are the density and velocity distributions  
at the centre of our galaxy? (37)

E. Extragalactic 1. What different evolutionary processes have  
different galaxies experienced?

Some of these questions have been answered satisfactorily, for some answers good guesses exist and a number of problems have not been contemplated yet. The main concern of this work will be the properties of the OH/IR stars and their envelopes (C), and the closely related problem of their distances (D.1).

### I.3 Means

The weaker, nearby OH emitters are all identified with Mira variables, or M-type supergiants. Because the unidentified OH/IR stars, that are much stronger masers, have very similarly shaped radio spectra and have kinematic properties resembling those of the longer period Mira's and supergiants, they too seem to be a kind of long period variables. Because they are extremely reddened, they are thought to have thick circumstellar dust shells. The obvious way to find out if they are LPV is to follow them in time. Harvey *et al.* (1974) determined light curves, simultaneously in the IR and the radio, for a number of (identified) OH Mira's. They found that the variations were in phase and that the flux ratio between IR and radio was constant over the period. And so, *mutatis mutandi*, observations in one wavelength regime alone should be sufficient. That this is indeed correct, was proven by an independent IR program that has a number of stars in common with our study (Engels, 1982).

In 1976, Baud during his survey program (Baud *et al.*, 1979), observed some (unidentified) OH/IR stars a few times and found indeed small, but meaningful variations. So in 1978 a modest monitor program was started using the Dwingeloo Radio Telescope. It included a number of OH Mira's and OH/IR stars. Later, in 1980 this source watch was extended to a total of 60 objects, including a homogeneous sample of OH/IR stars. The results of this program can be found in chapter II.

For a small set of stars VLA\* maps were made, enabling us to study the

structure of the circumstellar shell. These observations and their direct consequences will be discussed in chapter III.

Finally, a single run of IR observations was made with UKIRT<sup>\*\*</sup>, giving spectra from 2-20 $\mu$ m, primarily to determine bolometric magnitudes. They will be presented in chapter IV.

In chapter V we shall discuss the observational results and see what we can say about the nature of the OH/IR stars and the properties of their circumstellar envelopes.

\*Very Large Array (New Mexico)

\*\*United Kingdom InfraRed Telescope (Hawaii)

Literature cited in chapter I

1. Abbot, C.G.: 1924, *Astroph. J.* 60, 87
2. \_\_\_\_\_ : 1929, *Astroph. J.* 69, 293
3. Baud, B., Habing H.J.: 1983, *Astron. Astroph.* submitted
4. Baud, B., Habing, H.J., Winnberg, A., Matthews, H.E.: 1979, *Astron. Astroph. Suppl.* 35, 179
5. \_\_\_\_\_ : 1939, *Astron. Astroph. Suppl.* 36, 193
6. \_\_\_\_\_ : 1983, *Astron. Astroph.*
7. Bowers, P.F.: 1978, *Astron. Astroph. Suppl.* 31, 127
8. Burke, B.F.: 1965, *Radio Radiation from the Galactic Nuclear Regions*, *Ann. Review Astron. Astroph.*, vol 3 pp 275-296
9. Caswell, J.L., Haynes, R.: 1975, *M.N.R.A.S.* 173, 649
10. Cheung, A.C., Rank, D.M., Townes, C.H., Thornton, D.D., Welch, W.J.: 1969, *Nature* 221, 626
11. Draine, B.T.: 1981, *Dust formation Processes around Red Giants and Supergiants*, in *Physical Processes in Red Giants*, Eds. Iben, I. and Renzini, A., Reidel, pp 317-344.
12. Elitzur, M.: 1981, *Red Giant Masers*, as 11. pp 363-382
13. Engels, D.: 1979, *Astron. Astroph. Suppl.* 36, 337
14. \_\_\_\_\_ : 1982, *Zur Natur von OH/IR-Objekten*. Ph.D. thesis. *Veröffentlichungen der Astronomischen Institute Bonn* 95
15. Epchtein, N., Nguyen-Q-Rien: 1982, *Astron. Astroph.* 197, 229
16. Evans, N.J., Beckwith, S.: 1977, *Astroph. J.* 217, 726
17. Ewen, H.I., Purcell, E.M.: 1951, *Radiation from Galactic Hydrogen at 1420 Mc/s*, *Nature* 168, 356
18. Fabricius, D.: 1605, *Kurtzer und gründlicher Bericht*. Hamburg (auf der Herzogl. Bibl. Gotha Math. 4, p 124). See 1918, *Geschichte und Literatur der veränderlichen Sterne* Vol. 1
19. Glass, I.: 1978, *M.N.R.A.S.* 182, 93
20. Goldreich, P., Scoville, N.: 1976, *Astroph. J.* 205, 144
21. Gundermann, E.: 1965, Ph. D. thesis, Harvard University
22. Habing, H.J., Israël, F.P.: 1979, *Compact HII Regions and OB Star Formation*, *Ann. Review Astron. Astroph.*, vol 17, pp 345-386
23. Hagen, J.P., McClain, E.F.: 1954, *Astroph. J.* 120, 368
24. Harvey, P.M., Bechis, K.P., Wilson, W.J., Ball, J.A.: 1974, *Astroph. J. Suppl.* 27, 331

25. Hulst, H.C. van de: 1945, Radio Waves from Space, Ned. Tijdschrift Natuurk., vol 11, pp 201-221
26. Johansson, L.E.B., Andersson, C., Goss, W.M., Winnberg, A.: 1977, Astron. Astroph. Suppl. 28, 199
27. Jones, T.W., Merrill, K.M.: 1976, Astroph. J. 209, 509
28. Jones, T.J., Hyland, A.R., Caswell, J.L., Gatley, I.: 1982, Astroph. J. 253, 208
29. Jones, T.J., Hyland, A.R., Wood, P.R., Gatley, I.: 1983, Paper IV (in press)
30. Jong, T. de: 1983, Astroph. J., submitted
31. Kaler, J.B.: 1983, in Planetary Nebulae, Ed. D.R. Flower, Reidel, pp 245-257
32. Kuiper, G.P., Wilson, W., Cashman, R.J.: 1947, Astroph. J. 106, 243
33. Moran, J.M. Burke, B.F., Barrett, A.H., Rogers, A.E.E., Carter, J.C., Ball, J.A., Cudaback, D.D.: 1968, Astroph. J. Lett. 152, L98
34. Muller, C.A., Oort, J.H.: 1951, Nature 168, 357
35. Neugebauer, G., Leighton, R.B.: 1969, Two micron sky survey. Nasa SP-3047
36. Nguyen-Q-Rieu, Mebold, U., Winnberg, A., Guibert, J., Booth, R.: 1976, Astron. Astroph. Lett. 52, 467
37. Olton, F.M. Walterbos, R.A.M., Habing, H.J., Matthews, H.E., Winnberg, A., Brzezinska, H., Baud, B.: 1981, Astroph. J. Lett. 245, L130
38. Perkins, F., Gold, T., Salpeter, E.E.: 1966, Astroph. J. 145, 361
39. Price, S.D., Walker, R.G.: 1976, The AFGL Four Colour Infrared Sky Survey. AFGL TR-76-0208
40. Ptolemaeus, C.: 138, Almagestum Cl. Ptolemaei pheludiensis alexandrini astronomorum principes, opus ingens et nobile omnes coelorum motus continens, felicibus astris eat in lucem. Venetiis, 1515 (1<sup>st</sup> Latin edition). See 1795, Claudius Ptolemäus, Beobachtung und Beschreibung der Gestirne und der Bewegung der himmlischen Sphäre, ed. J.E. Bode, Berlin und Stettin; or 1915, Revised edition of the Almagest, ed. C.H.F. Peters and E.B. Knobel, Carnegie Institution
41. Raimond, E., Eliasson, B.: 1967, Astroph. J. Lett. 150, L171
42. \_\_\_\_\_ : 1969, Astroph. J. 155, 817
43. Reid, M.J., Moran, J.M.: 1981, Masers in Ann. Rev. Astron. Astroph. 19, pp 231-276
44. Sanford, R.F.: 1947, P.A.S.P. 59, 136

45. Schultz, G.V., Kreysa, E., Sherwood, W.A.: 1976, *Astron. Astroph.* 50, 171
46. Snijder, L.E., Suhl, D.: 1974, *Astroph. J. Lett.* 189, L31
47. Turner, B.E.: 1970, *P.A.S.P.* 82 996
48. Weaver, H.F., Williams, D.R.W., Dieter, N.H., Lum, W.T.: 1965, *Nature* 208, 29
49. Weinreb, S., Barrett, A.H., Meeks, M.L., Henrey, J.C.: 1963, *Nature* 200, 829
50. Wilson, W.J., Barrett, A.H.: 1970, *Astron. Astroph.* 17, 385

## II. Dwingeloo Monitor

### II.1 Introduction

In 1978 we started a monitor program with the 25-m Dwingeloo Radio Telescope (DRT). The intent was to compare the variability of well known Mira's with that of unidentified OH/IR stars. In 1980 we extended the program and included all OH/IR stars ( $10^\circ < \lambda < 180^\circ$ ) with a harmonic mean flux,  $\{S_L \cdot S_H\}^{\frac{1}{2}} > 4$  Jy from Baud's catalogue (Baud *et al.*, 1981). Also added were three supergiants (VY CMa, PZ Cas, and NML Cyg) and three sources at the galactic centre with large (negative) radial velocities. Thus a total of 60 stars was followed regularly during 3-5 years. Because the telescope was also used for other programs, our coverage has gaps of months to fortnights, but one stretch of over 200 days was covered continuously. About 4000 usable spectra were measured, reduced, calibrated, and plotted with standard programs. For each star we measured the integrated flux and the various peak flux densities. This resulted in 5-20 radio light curves per star.

### II.2 Observations

The observations were made with the DRT at a wavelength  $\lambda = 18$  cm ( $\nu_0 = 1612.231$  MHz). The half power beam width is  $31'$  at this frequency, the aperture efficiency is 64%, and  $S/T_A = 8.772$  (Jy/K) (Slottje, 1982). The DRT used a closed-cycle helium cooled parametric amplifier and a single linearly polarized feed, replaced in 1982 by a FET amplifier and two linearly polarized feeds. A 256-channel autocorrelation spectrometer was used in the total power mode over a bandwidth of 625 kHz ( $116 \text{ km s}^{-1}$ ), yielding a resolution (uniform weighting) of 2.93 kHz, or  $0.54 \text{ km s}^{-1}$ . The signal was clipped in the one-bit mode. The system temperature typically was 35 K at the beginning of a run, slowly increasing to  $\sim 40$  K after several weeks of observing.

### II.3 Calibration

The system was calibrated continuously against a noise tube of known

constant temperature. This calibration was checked daily (in principle) by measuring a continuum point source with a known flux. We used Virgo A (189.45 Jy at 1612 MHz) or occasionally Cygnus A (1369.3 Jy; Baars *et al.* , 1977). The calibration factor varied less than 1% over one day in general (see figure 1), although some larger deviations occurred, especially during times when the continuum measurements were of poor quality (Murphy's law; see Bloch, 1979). Because a good calibration is important for the determination of the relative phase for the different light curves of one star, we also used an internal calibration, as described in section II.6b.

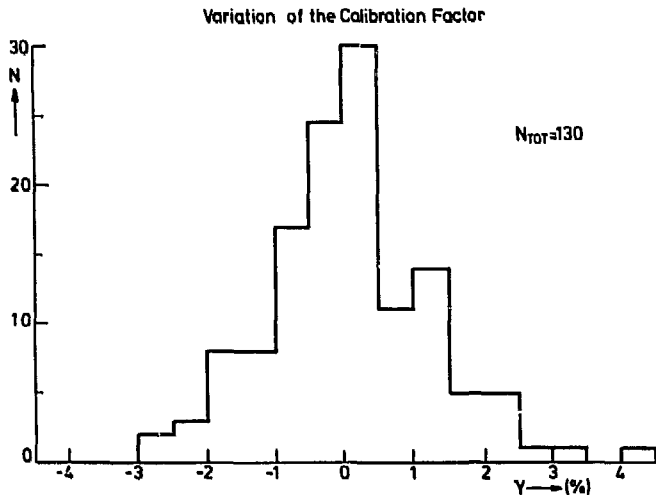


Figure 1.

Variation of the noisestep, NS, on subsequent days  $i$  and  $(i+1)$

$$\gamma \equiv \frac{NS(i+1) - NS(i)}{NS(i)}$$

#### II.4 Reduction

All spectra were split up into 2-8 subscans, allowing part of the integration to be deleted if interference occurred. Once a day we measured a reference spectrum in the direction of the galactic north pole in order to allow correction for gain variations across the band. A third order polynomial was fitted to the emission-free parts at both ends of the band. Usually the spectra were not smoothed, but sometimes interference or malfunctioning of the correlator led us to use Hanning smoothing. In such cases the measured peak flux densities were multiplied by a factor 1.235, and the velocity range of emission was decreased by  $0.685 \text{ (km s}^{-1}\text{)}$ , in order to match the fluxes and velocities of the unsmoothed measurements (see figure 2).

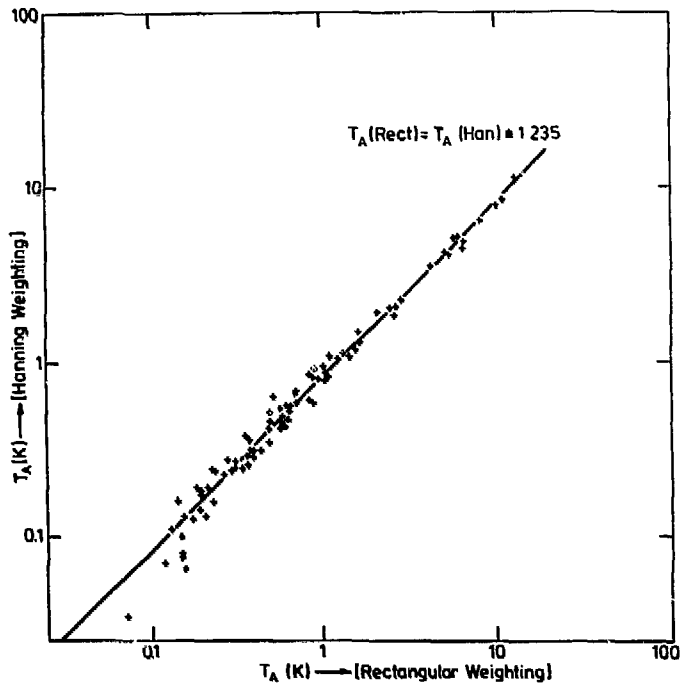
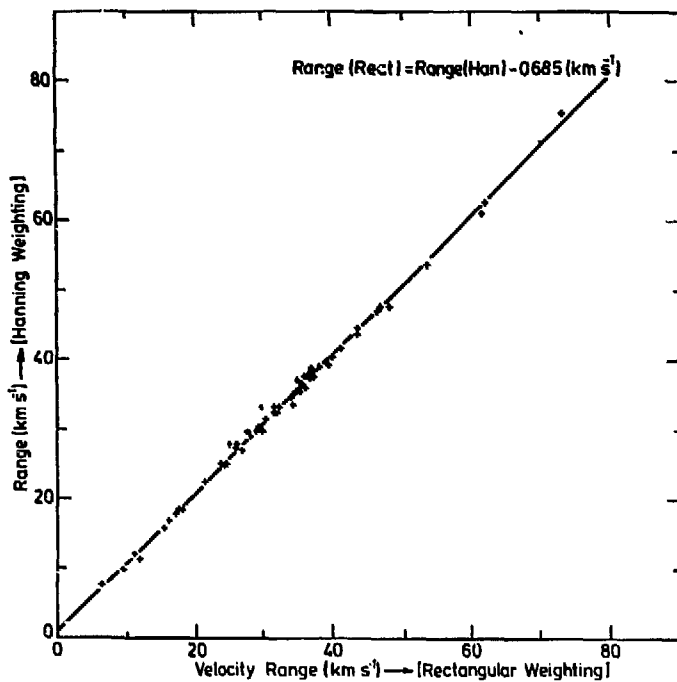


Figure 2a,b.

Comparison of the peak flux density and the velocity range of emission for spectra reduced with Hanning smoothing, and with uniform weighting.



The coverage and integration time for each star depended on the (suspected) period, on its flux density, and on the amount of time available. During the 5 years of the program the time coverage and the integration time were adjusted repeatedly. Because the DRT is a rather

small telescope, some of the weakest sources should have been observed for days in order to get sufficient sensitivity. But in general, even for the weaker features in the spectrum, the signal-to-noise ratio is better than 10. In addition the weaker sources appear to have the shorter periods, so that in these cases we can combine 3-5 cycles.

The off-line reduction was performed with available standard programs, yielding spectra calibrated in antenna temperature. The theoretical noise in the spectra is given by (see Ball, 1976)

$$\Delta T_{\text{RMS}} = \frac{\alpha \gamma T_{\text{sys}}}{\sqrt{1.2 \beta t}} \quad (\text{K}) \quad (1)$$

where  $1 \lesssim \alpha < 2$  for optimum total power,  $\gamma$  is 1.47 for the 1-bit mode,  $\beta$  is the channel spacing in Hz, and  $t$  is the integration time in seconds. We used integration times ranging from 120 to 7200 s, leading to  $\Delta T_{\text{RMS}} = 0.15\text{-}0.019$  K. This is in reasonable agreement with the noise measured in the emission-free parts of the band, except at smaller galactic longitudes where confusion and background radiation can enhance the noise by a factor 2 (see figure 3). In our analysis we always used the measured values.

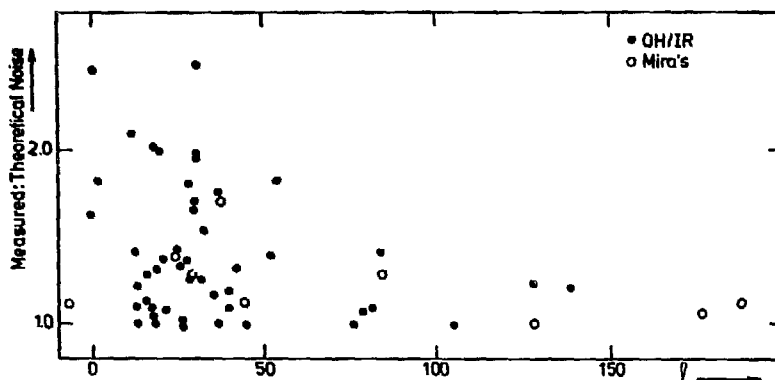


Figure 3. Ratio of the noise measured in the spectra to the noise expected from equation (1) as function of galactic longitude.

## II.5 Confusion

Because of the large beam (31') of the DRT, and the crowding of OH/IR stars around  $\lambda = 10^{\circ}\text{-}35^{\circ}$  (Baud *et al.*, 1981), we were troubled by confusion in several cases. Table 1 lists these program stars and describes the influence of the confusion.

Table 1

Programstar	Confusion by OH	Distance ( $^{\circ}$ )	Position in spectrum	Influence	References (see table 2)
11.5+0.1	11.3+0.0	0.27	In high velocity peak	Weak	30
12.3-0.1	12.3+0.1	0.30	In middle of spectrum	Peaks can be removed	23
17.4-0.3	17.0-0.1	0.45	In high velocity part	HV peak has large scatter	58
18.3+0.4	18.3+0.1	0.30	All spectrum	Very strong	18
20.2-0.1	20.4-0.3	0.28	In middle of spectrum	Peaks can be removed	19,40
20.7+0.1	20.6+0.3	0.22	Just outside spectrum (LV)	Baseline poor	35
21.5+0.5	21.9+0.4	0.41	In low velocity part	Weak	35
25.1-0.3	24.7-0.1	0.45	In low velocity part	Large scatter	8,19,40
27.3+0.2	27.2+0.2	0.10	Same source?	None?	1,41
	27.2+0.2	0.10	Just outside spectrum (HV)	Baseline mildly afflicted	23,35
30.1-0.7	30.1-0.2	0.50	Weak	Baseline uncertain	8,13,20,28,47
30.1-0.2	30.1-0.7	0.50	Outside spectrum (LV)	Baseline bad	8,12,13,20,28
30.7+0.4	30.9+0.2	0.28	In middle of spectrum	Peaks can be removed	24
	31.0+0.0	0.50	Outside spectrum (LV)	Baseline very bad	1,46
31.0-0.2	30.9+0.2	0.51	Outside spectrum	Baseline very bad	24
	31.0+0.0	0.20	Outside spectrum		1,46
	31.2-0.2	0.20	?		
	31.5-0.1	0.51	Outside spectrum		19,40
31.0+0.0	30.7+0.4	0.50	Outside spectrum (HV)	Baseline very bad	18,19,24,40
	30.9+0.2	0.37	Outside spectrum (LV)		24
	31.0-0.2	0.20	Outside spectrum (HV)		8,19,24,40
	31.5-0.1	0.50	Outside spectrum (LV)		19,40
32.0-0.5	31.7-0.8	0.42	In middle of spectrum	Peak can be removed	18,19,40
35.6-0.3	35.3-0.7	0.50	Weak	None	

Confusion mostly affected the integrated flux densities, due to the uncertainties in the baselines. The peak fluxes are only mildly afflicted, except for the worst cases (see figure 4). The time behaviour enabled us to select the features belonging to the program stars.

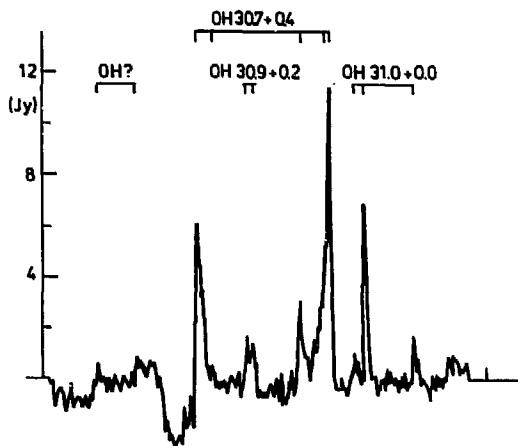


Figure 4. Single-dish profile of the star OH 30.7+0.4. In the middle of the spectrum two peaks of OH 30.9+0.2 can be seen, at the right (LV) side another star OH 31.0+0.0. At the high velocity side strong and broad absorption is always present and sometimes also two peaks of an unknown, variable OH-source. This is one of the worst examples of confusion.

## II.6 Data analysis

The analysis of the measured spectra and the resulting radio light curves is done in a number of steps. In a first approach (section 6.a) such quantities as the mean velocity of the stars, the total velocity range of OH emission, and the width of individual features in the spectra are determined. Also, adopting a simple sinewave function to describe the light curves, the periods, mean fluxes, and amplitudes are derived. In the second step (section 6.b) the calibration is checked by looking for systematic deviations from the sinewave fit for groups of stars that have been observed within one calibration interval. The recalibrated data are used to find slightly adjusted values for the quantities mentioned (step 3, section 6.c). Whereas periods, mean fluxes, and amplitudes are rather insensitive to the precise form of the light curves, the times of maximum, and the phase differences between various features in the spectrum of one star, are. Therefore, in the fourth step of the analysis asymmetries of the curves are taken into account (section 6.e). The new fits are then used to determine phase differences between the light curves for various features of one star (step 5, section 6.f). After constructing normal points, an autocorrelation method is applied to find these (often small) phase lags, making an optimal use of all available data points. In the last step (section 6.h) the phase lags are interpreted in terms of the linear dimensions of the circumstellar shells.

### a. First approach

OH/IR stars characteristically have spectra dominated by two peaks with a separation of  $20\text{--}40 \text{ km s}^{-1}$ , steep outer edges, and a more gradual decline between these peaks (figure 5). This shape of the spectrum can be explained if the maser emission comes from a rather thin, uniformly expanding shell (Reid *et al.*, 1977). In this picture the strongest maser emission originates from the front and from the back sides of the shell, where the gain pathlength along the line of sight is longest (see figure 13 for a graphical display). The separation between the outer peaks is twice the expansion velocity of the shell; the stellar velocity lies halfway between the peaks. There is a lot of evidence in support of this model which will be summarized in chapter V (section V.2).

On a number of Julian Days,  $JD(i)$  (where  $30 < i_{\text{Total}} < 150$ ), we measured for each star the total range of emission,  $\delta v(i)$ ; the stellar velocity,  $v_*(i)$ ; and the velocity, peak flux density and full width at half maximum for a total of  $k_T$  recognized peaks (each indicated by the subscript  $k$ ),  $v_k(i)$ ,  $S_k(i)$  and  $fw_k(i)$  (where  $2 \leq k_T < 20$ ). We integrated the flux density over two equal halves of the spectrum yielding the low- and high-velocity integrated flux density,  $S_{LV}(i)$  and  $S_{HV}(i)$ . Finally the noise was determined from an emission-free part in the band,  $\Delta T_{\text{RMS}}(i)$ .

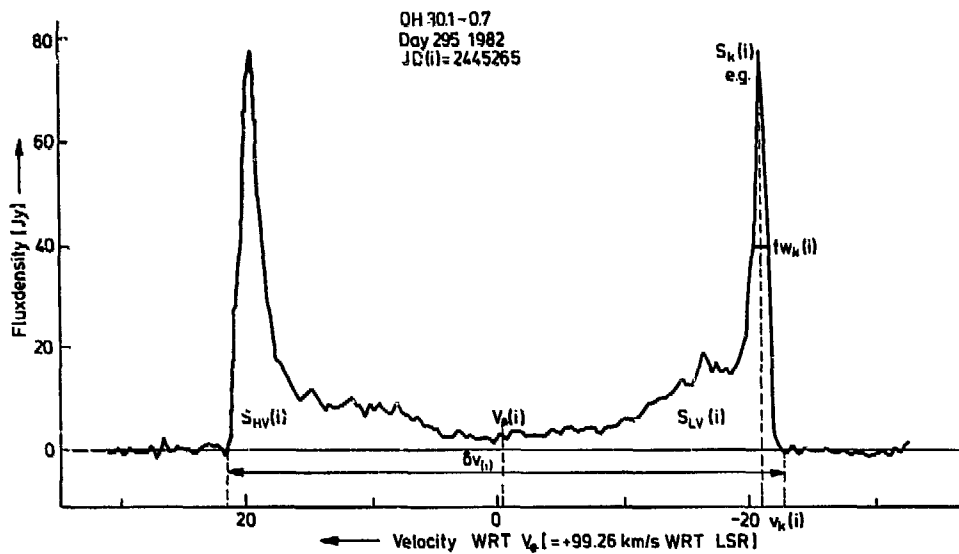


Figure 5. Single-dish profile of OH 30.1-0.7. The quantities that are measured in the monitor program are indicated.

We fit a sinewave function by least squares to the observed flux densities, weighted with the measured RMS noise. For each star this resulted in  $k_T + 2$  light curves, each having four degrees of freedom (the mean flux density  $a_k$ , the amplitude  $b_k$ , the time of maximum  $JD_{k0}$ , and the period  $P_k$ )

$$S_k(i) = a_k + b_k \cos [2\pi\{JD(i) - JD_{k0}\}/P_k] \quad (2)$$

It is known (Harvey *et al.*, 1974) that (optically identified) OH masers vary nearly in phase with their optical or infrared counterparts

with a fixed amplitude ratio between the wavelength regimes. This indicates that the masers are radiatively pumped by the central star and saturated. If this situation is also true for the unidentified OH/IR stars, we would expect the period ( $P_k$ ) and the relative amplitude ( $B_k \equiv b_k/a_k$ ) to be the same for all peaks in the spectrum of one star. Our results show that this is indeed the case (figure 6a and 6b). Furthermore, for some OH/IR stars Engels (1982) determined light curves in the IR, yielding the same periods and phases as the radio light curves. Measurements by Feast (private communication) also confirm the coupling between IR and radio (see Appendix B). This result supports a further step: we demand the period and relative amplitude to be constant for a given source.

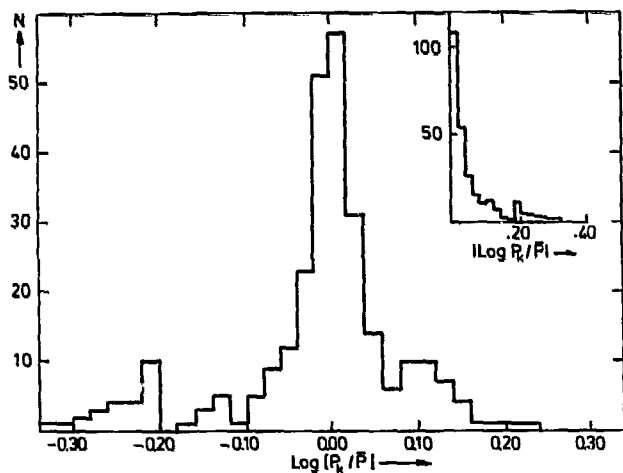


Figure 6a. Distribution of the periods for various peaks ( $k$ ), normalized to the mean value  $\bar{P}$  of a given source, for all variable OH/IR stars. Note the second maximum at  $-0.20$ , caused by some weak peaks with less phase coverage than the others, through which the sine wave fits with half the main period.

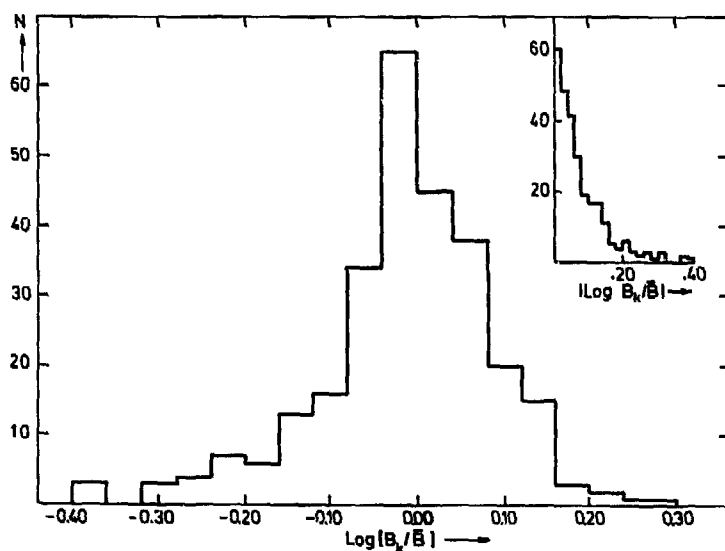


Figure 6b. Distribution of the amplitudes for various peaks, normalized as in figure 6a.  $B_k \equiv b_k/a_k$ , and  $B$  is the mean (relative) amplitude for a given star.

These parameters were calculated by taking the mean over all curves, weighted by the quality of the sinewave fit and the strength of the feature. Thus

$$P = \frac{\sum_k P_k w_k}{\sum_k w_k}, \text{ and } B = \frac{\sum_k \frac{b_k}{a_k} w_k}{\sum_k w_k} \quad (3)$$

where the summation is over  $k_T$  peaks and over the low- and high-velocity integrated flux. Again we fit a sinewave to the flux densities, but this time one with only two degrees of freedom (the mean flux  $a_k$  and the time of maximum  $JD_{k0}$ )

$$S_k(i) = a_k \{1 + B \cos [2\pi\{JD(i) - JD_{k0}\}/P]\} \quad (4)$$

#### b. Internal calibration

We have seen (II.3) that in general the calibration is good to within 1-2%. On some days, however, no calibration measurement was made at all, or the measurement was ruined by interference or by other causes. In those cases we scaled the spectra with the calibration factor from another day. Clearly this enhances the uncertainties, but with an 'internal' calibration procedure we can check our interpolations, and possibly correct for them. It can also help us to find out whether the calibration factor, being nearly constant from day to day, has larger deviations on shorter timescales. In each calibration interval some 10-20 sources were observed. For all these we can determine the (relative) residuals with respect to the sinewave as calculated in section II.6a (equation 4). So for each star measured at  $JD(i)$ , within a certain calibration interval, we have  $\{k+2\}$  residuals

$$Res_k(i) = \{S_k(i) - Comp_k(i)\}/S_k(i) \quad (5)$$

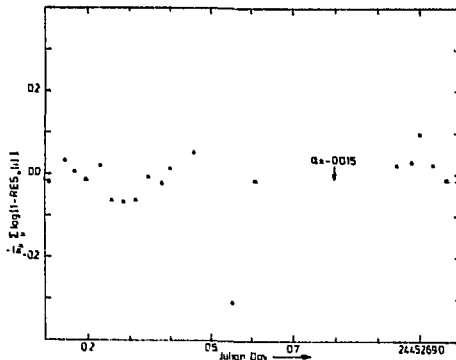


Figure 7. Mean residuals with respect to the sinewave fit for 19 sources observed around a calibration measurement at  $JD = 2445269.8$ .

where  $\text{Comp}_k(i)$  is the calculated value (figure 7). And although an individual star may show systematic deviations from a sinewave, for a sample it is a perfect representation and the sum of the residuals should be zero in each calibration interval. Now let  $N$  be the number of sources in a particular interval. Then the weighted sum of the residuals,  $\alpha$ , is

$$\alpha = \frac{\sum_{i=1}^N [w(i) \sum_k \{w_k \log(1 - \text{Res}_k(i))\}] }{\sum_{i=1}^N w(i) \sum_k w_k} \quad (6)$$

where  $\sum_k \{...\} / \sum w_k$  is a weighted mean of the residuals for the individual peaks and  $\sum_N [...]/\sum w(i)$  over the sources in the calibration interval. The statistical weights include the number of peaks per star and the S/N per peak. Clearly  $\alpha=0$  only if the calibration was correct. The distribution of  $\alpha$ -values is shown in figure 8. The total number of  $\alpha$ -values in this histogram is lower than the total number of observing days, because in most cases where the calibration measurement was disturbed, several monitor sources were also observed poorly. And when  $N < 10$  we could not derive a reliable correction factor. Figure 8 shows that the overall calibration is good, but some larger deviations occur, mostly (as expected) when no calibration measurement was made at all. The few days with a deviation  $>15\%$  include the three runs (on 11 stars only) in 1976 and 1977 during Baud's survey. This may be explained by a number of (minor) changes in the receiver system and in the noise tube temperature that were introduced after the survey.

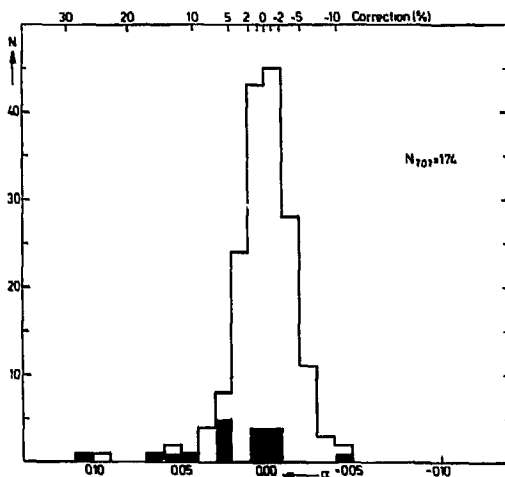


Figure 8. Histogram of  $\alpha$ -values for calibration intervals with  $N > 10$ . Days where no calibration measurement was done are shaded.

All flux densities were adjusted with the correction factor  $10^\alpha$  in the appropriate interval. There is no systematic variation with time within any calibration interval.

### c. Results

Tables 2a and 2b give the results for all program stars. For the identified stars (see table 2a) the variable star name, the IRC number and the AFGL number are given. The period ( $P_R$ ) and the amplitude ( $\Delta m_R \equiv 2.5 \log \{S_{\max}/S_{\min}\}$ ) as determined from the radio light curves, compared with the optical period ( $P_O$ ) and amplitude ( $\Delta m_V$ ), the stellar velocity ( $v_*$  with respect to the Local Standard of Rest) and the total range of emission

( $\delta v$ ) are tabulated with their uncertainties. Columns 12 and 11 give the number of observations and the time interval in which they were made. Most observations were made from April, 1980 till October 1982; 20 sources have been followed regularly from 1978 onward, and for 11 stars three runs, carried out in 1976 and in 1977, were also added. In the last two columns references can be found, containing information about the star and an indication if IR and/or VLA measurements are known to us.

Table 2a

No.	Name	IRC	$P_R$	$\pm \Delta P$	$\Delta m_R$	$v_*$ (LSR) $\pm$	Range $\pm$	Julian Days	#	IR	References
		AFGL	$P_O$		$\Delta m_V$	( $\text{km s}^{-1}$ )	( $\text{km s}^{-1}$ )	(+244 0000)		VLA	
			(days)		(mag)						
1	R Aql	+10406	279.6	2.3	0.87	+ 47.17 0.03	16.18 0.06	3029-5265	84	A,C	1,3,10,11,17,23
		2324	285.6		6.3					a	33,36,43,53,58
2	RR Aql	+00458	403.8	2.2	0.71	+ 27.77 0.04	15.02 0.11	3689-5271	77	A	1,3,5,17,22,27
		2479	394.33		6.7					a	33,34,36,54,58
3	SY Aql	+10450	349.3	7.9	0.62	- 47.96 0.04	11.30 0.12	3702-5266	110		2,4,27,36,46,58
			355.74		7.1						
4	VY CMa	-30087	988.8	34.3	0.18	+ 23.67 0.04	74.35 0.04	4317-5267	146	A	3,14,17,22,38,39
		1111			0.9					a,b,c	48,49,52,55
5	PZ Cas	+60417	707.3	52.3	0.29	- 37.42 0.05	60.33 0.19	4317-5267	62		2,7,14,29,54,58
			900i		2.9						
+ 6	NHL Cyg	+40448	1109.6	35.7	0.31	- 1.97 0.01	53.70 0.04	4074-5268	177	A	3,11,14,17,22,26
	-OH80.8-1.9	2650	1280i							a	34,37,49,51,53
7	Z Cyg	+50314	270.3	2.1	0.70	-148.25 0.04	6.79 0.08	3690-5268	117		2,4,27,36,46,58
			263.85		7.1						
8	U Ori	+20127	406.3	10.1	(0.94)	- 44.22 0.04	8.65 0.11	3694-5269	91	A	6,10,14,15,27,36
			372.45		7.3					a	43,44,45,54,58
9	WX Pac	+10011	632.0	17.6	1.16	+ 8.96 0.03	38.37 0.05	3029-5268	71	A	1,2,13,16,17,22
		157	660(IR)							a,b,c	33,49,51,53,55
10	WX Ser	+20281	443.0	7.9	0.58	+ 5.95 0.04	17.72 0.09	3688-5266	110	G	1,2,3,14,17,26,27
			425.1		4.					a	43,45,48,51,53,58
11	IK Tau	+10050	455.6	5.7	1.33	+ 33.66 0.04	36.01 0.05	3694-5268	85		1,3,5,13,16,17,42
	-NHL Tau	529	460		4.6						49,51,53,58
12	RS Vir	+00243	363.8	9.2	0.48	- 14.91 0.03	11.12 0.05	3688-5266	132	G	4,9,27,36,44,46,58
			352.80		7.4						

For the OH/IR stars (see table 2b) the same quantities are listed, if they are known; if a second period is quoted it is an IR period from Hügels (1982). The OH/IR stars marked by a + sign form a homogeneous sample from Baud's catalogue (Baud *et al.*, 1981), with a harmonic mean flux  $> 4$  Jy.

Table 2b

No	Name	$P_R$ $P_{IR}$	$\pm \Delta P$	$\Delta m_R$	$v_{\infty}$ (LSR) $\pm$	Range $\pm$	Julian Days (+244 0000)	#	IR VLA	References	Remarks
	OH	(days)		(mag)	(km s <sup>-1</sup> )	(km s <sup>-1</sup> )					
13	359.4-1.3	(930)	115	0.13	-219.58 0.07	35.76 0.12	4318-5269	35		30	Not variable
14	0.3-0.2	(243)	15	0.16	-340.88 0.07	33.63 0.10	3029-5270	48		31	Not variable
15	1.5-0.0	(141)	8	0.21	-127.63 0.08	28.72 0.11	4318-5270	32	c	30	Not variable
+ 16	11.5+0.1	691:	40	0.23	+ 41.79 0.11	61.33 0.13	4318-5271	34	c	30	Variable?
+ 17	12.3-0.2	544	15	0.56	+ 36.60 0.12	30.21 0.16	4318-5269	29	F?	23	
+ 18	12.8-1.9	812	56	0.56	+ 10.44 0.06	47.78 0.14	4318-5270	27	E,G	35	
+ 19	12.8+0.9	1488	81	0.34	+ 26.91 0.07	24.71 0.13	4318-5269	32		23	
+ 20	13.1+5.0	707	40	0.53	- 67.73 0.07	33.89 0.19	4318-5269	27		35	
+ 21	15.7+0.8	(453)	42	0.13	- 0.62 0.04	31.96 0.06	4318-5269	30		23	Not variable
+ 22	16.1-0.3	1012	50	0.55	+ 21.13 0.05	46.70 0.06	4318-5271	33		23	
+ 23	17.4-0.3	1219	40	0.59	+ 29.13 0.08	36.21 0.13	4318-5269	31		23	
+ 24	17.7-2.0	890:	61	0.16	+ 61.19 0.04	28.33 0.03	3688-5266	47	G	23	Variable?
+ 25	18.3+0.4	845:	56	0.27	+ 47.93 0.05	32.66 0.08	4318-5269	31	B,F	8,25	Variable?
+ 26	18.5+1.4	1125:	86	0.19	+176.17 0.06	24.25 0.14	3688-5268	102	d	23,35	Variable?
+ 27	18.8+0.3	923	20	0.26	+ 12.75 0.05	31.87 0.08	4318-5269	34		1,40	
+ 28	20.2-0.1	857 680	44 40	0.67	+ 26.60 0.07	35.44 0.13	4318-5271	35	B,C,G	18,19,40	
+ 29	20.7+0.1	1130	40	0.99	+136.55 0.04	38.97 0.05	3029-5271	60	B,G d	13,18,19,23,40	
+ 30	21.5+0.5	1975:	60	1.09	+115.77 0.04	40.07 0.06	4318-5271	59	D,G d	8,20,28	
+ 31	25.1-0.3	226:	11	0.21	+142.88 0.08	26.83 0.08	4318-5269	35	F? a,d	19,40	Variable?
+ 32	26.2-0.6	1181 1330	13 50	1.05	+ 71.04 0.07	46.78 0.05	3689-5276	53	B,C,G	18,19,23,40	
+ 33	26.4-1.9	652 540	26 20	0.44	+ 27.65 0.05	26.72 0.10	4318-5270	33	B,C,E,G	18,19,23,40	
+ 34	26.5+0.6	1566 AFGL 2205	16 100	1.13	+ 26.86 0.03	30.69 0.02	3029-5266	70	C,D,E a,b,c,d	13,18,20,21,28 32,40,50,57	
+ 35	27.3+0.2	939	35	0.59	+ 50.42 0.05	28.21 0.10	4318-5269	23		1,41	
+ 36	28.5-0.0	559	16	0.77	+107.65 0.06	28.79 0.07	4318-5270	26	B,G d	19,40	
+ 37	28.7-0.6	627 640	17 10	0.83	+ 46.45 0.04	37.31 0.09	4318-5270	35	B,C,G	18,19,23,40	
+ 38	30.1-0.7	2060: 1730	130 200	0.40	+ 99.26 0.04	43.57 0.05	3689-5265	55	C,G d	8,12,13,20,28	
+ 39	30.1-0.2	853 970	21 40	0.81	+ 50.53 0.05	37.75 0.08	4318-5270	31	C,D,G	8,13,20,28,47	
+ 40	30.7+0.4	1039 1140	27 30	0.57	+ 66.59 0.06	37.03 0.08	3029-5265	52	B,C,G	18,19,24,40	
+ 41	31.0-0.2	(1126)	100	0.13	+125.98 0.06	31.09 0.09	4318-5266	33	B,F,G d	8,19,40,46	Not variable
+ 42	31.0+0.0	400: W43A	8	0.21	+ 35.10 0.03	17.83 0.05	3689-5269	112		1,46	Variable?
+ 43	32.0-0.5	1540	83	0.88	+ 76.04 0.06	43.70 0.08	4318-5270	36	G d	8,19	

No	Name	$P_R$ $P_{IR}$ (days)	$\pm \Delta P$	$\Delta m_R$ (mag)	$v_{\perp}$ (LSR) $\pm$ (km s <sup>-1</sup> )	Range $\pm$ (km s <sup>-1</sup> )	Julian Day (+244 0000)	#	IR VLA	References	Remarks
+ 44	32.8-0.3	1536 1750	10 130	1.24	+ 60.75 0.04	35.32 0.06	3029-5265	77	B,C,D,G a,d	13,18,20,28,40,47	
+ 45	35.6-0.3	840	40	0.78	+ 78.00 0.05	29.59 0.07	3029-5269	36		1,41	
46	36.9+1.3	409	5	0.56	- 12.22 0.03	17.20 0.05	3688-5271	86		35	
+ 47	37.1-0.8	(737)	61	0.13	+ 88.48 0.05	29.72 0.07	3029-5269	37		19,23,35,40	Not variable
+ 48	39.7+1.5	1424 AFGL 2290	16	0.82	+ 20.00 0.03	35.71 0.05	3689-5265	52	G a	23,32,35,57	
+ 49	39.9-0.0	823 770	45 20	0.80	+148.84 0.04	31.97 0.08	4318-5270	39	C,G a	19,35,40	
+ 50	42.3-0.1	1945 1650	83 150	0.36	+ 59.19 0.04	35.29 0.06	3689-5266	54	B,C,G	19,23,35,40	
+ 51	44.8-2.3	552 AFGL 2374	5	0.77	- 71.56 0.03	34.26 0.07	4325-5269	28		23,35	
+ 52	45.5+0.1	750 AFGL 2345	31 20	0.92	+ 34.97 0.08	36.80 0.14	4325-5269	31	C,D	8,13,18,20,28,41	
+ 53	51.8-0.2	(1162)	71	0.16	+ 2.01 0.05	41.22 0.09	4318-5271	31		23,35	Not variable
+ 54	53.6-0.2	(838)	110	0.12	+ 10.47 0.04	29.23 0.08	4324-5270	28		23,35	Not variable
+ 55	75.3-1.8	1603:	54	1.08	- 3.48 0.05	26.60 0.09	4323-5272	36		23,35	
+ 56	77.9+0.2	(1339)	113	0.19	- 39.08 0.05	24.64 0.07	4317-5269	35		1,39	Not variable
+ 57	83.4-0.9	1153	40	1.28	- 38.54 0.02	38.77 0.04	4318-5267	128		23,35	
+ 58	104.9+2.4	1215: AFGL 2885	54	0.66	- 25.62 0.02	32.38 0.03	4318-5268	82		23,35,46	
+ 59	127.9-0.0	1994: AFGL 230	130	1.47	- 54.97 0.02	24.50 0.02	3030-5268	86	a a	23,24,35,57	
+ 60	138.0+7.2	1352:	136	0.81	- 37.72 0.03	21.28 0.05	4318-5268	79	a	23,35	

V.L.A. Observations

- a. Bowers *et al.* (1981)
- b. Reid *et al.* (1981)
- c. Baud
- d. This work

I.R. observations

- A. Harvey *et al.* (1974)
- B. Jones *et al.* (1982)
- C. Engels (1982)
- D. Werner *et al.* (1980)
- E. Willems, de Jong (1982)
- F. Epchtein, Rieu (1982)
- G. This work

References to Tables 1, 2 and 3

1. Wilson and Barrett (1972)	16. Dyck and Lockwood (1974)	31. Baud <i>et al.</i> (1975)	46. Dickinson <i>et al.</i> (1978a)
2. Dickinson (1976)	17. Hyland <i>et al.</i> (1972)	32. Allen <i>et al.</i> (1977)	47. Dickinson <i>et al.</i> (1978b)
3. Snyder and Buhl (1975)	18. Schultz <i>et al.</i> (1976)	33. Blair and Dickinson (1977)	48. Merrill and Stein (1977a)
4. Dickinson <i>et al.</i> (1975)	19. Johansson <i>et al.</i> (1977)	34. Dickinson and Kleinman (1977)	49. Merrill and Stein (1977b)
5. Dickinson <i>et al.</i> (1973)	20. Evans <i>et al.</i> (1976)	35. Baud <i>et al.</i> (1979b)	50. Merrill and Stein (1977c)
6. Wilson <i>et al.</i> (1972)	21. Andersson <i>et al.</i> (1974)	36. Lockwood (1972)	51. Strecker and Ney (1974)
7. Dickinson and Chaisson (1973)	22. Harvey <i>et al.</i> (1974): A	37. Wilson <i>et al.</i> (1970)	52. Hyland <i>et al.</i> (1969)
8. Rieu <i>et al.</i> (1971)	23. Bowers (1978)	38. Robinson <i>et al.</i> (1970)	53. Morrison and Simon (1973)
9. Johnston <i>et al.</i> (1972)	24. Bowers and Kerr (1974)	39. Sullivan III (1973)	54. Simon (1974)
10. Lépine <i>et al.</i> (1976)	25. Caswell and Haynes (1975)	40. Winnberg <i>et al.</i> (1975)	55. Lépine <i>et al.</i> (1978)
11. Schwartz and Barrett (1970)	26. Caswell (1973)	41. Turner (1971)	56. Le Squeren <i>et al.</i> (1979)
12. Cato <i>et al.</i> (1976)	27. Rieu <i>et al.</i> (1979)	42. Mendozo (1967)	57. Lebofaky <i>et al.</i> (1976)
13. Dickinson and Blair (1977)	28. Evans and Beckwith (1977)	43. Lockwood and Wing (1971)	58. Kukarkin <i>et al.</i> (1969)
14. Kaifu <i>et al.</i> (1975)	29. Bowers and Kerr (1978)	44. Gillet <i>et al.</i> (1971)	
15. Spencer <i>et al.</i> (1977)	30. Baud <i>et al.</i> (1979a)	45. Gehrz and Woolf (1971)	

d. Remarks on individual stars

1) Table 2a.

All the Mira variables (numbers 1-3 and 7-12) seem to have periods more or less variable in length. A systematic behaviour of the period with time is known only for R Aql. We can write, partly after Schneller (1963), for the times of maximum,  $t_n$ , and the period,  $P_n$ , as function of the cycle,  $n$

$$t_n(\text{max}) = 242\,2301.8 + 312.35 n - 0.2330 n^2 + 0.00045 n^3 \quad (7a)$$

(Julian Days)

$$P_n = \frac{dt_n}{dn} = 312.35 - 0.4660 n + 0.00136 n^2 \text{ (days)} \quad (7b)$$

based on observations of the visual maxima during 126 years. The tabulated optical period is for cycle  $n=73$ , which corresponds to the middle of our radio observations. Omission of the uncertain second order term in equation (7b) brings the period down to 278.3 days, in good agreement with the radio period and the recently determined IR period of 280 days (Rudnitskij, private communication; see also Engels, 1982). For all Mira variables the amplitudes also can change from cycle to cycle, but for most of them these changes are small. In general, observations from different cycles could be combined easily, except for R Aql and U Ori. The latter one flared in 1974 in the 1612 MHz line and its flux has since declined more or less exponentially (figure 9).

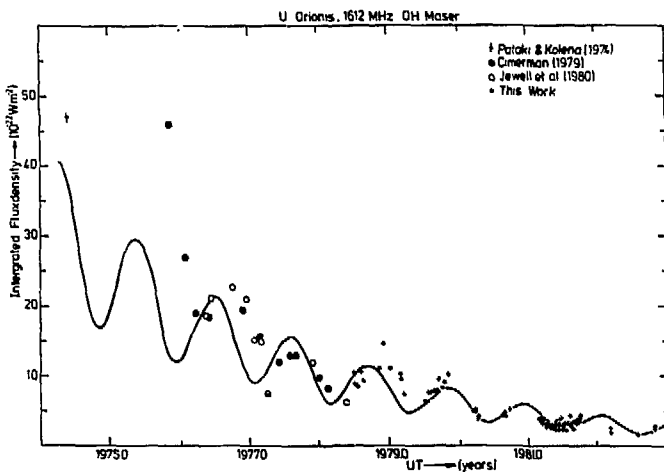


Figure 9. Total flux of U Ori at 1612 MHz. Before 1974 it could only be seen in the main lines.

We can write for the total integrated flux density of U Ori,  $S_{TOT} = (S_{LV} + S_{HV})$

$$S_{TOT} = 0.749 + 0.251 \cos\left[\frac{\{JD(t) - JD_0\}}{P}\right] \exp\left[3.700 - 0.318 \frac{\{JD(t) - JD_0\}}{P}\right] \quad (8)$$

where  $S_{TOT}$  is in  $10^{-22} \text{ Wm}^{-2}$ , the period  $P = 406.3$  days and  $JD_0 = 244\,2152$  corresponding to the year 1974.288. Note that the period changed also. From 1981 on only the two strongest peaks (at  $v = -2.92$  and  $2.63 \text{ km}^{-1}$ ; table 3) could still be seen the two weaker peaks outside have disappeared completely (see also Jewell *et al.*, 1980). R Aql has two weak features, at  $-6.16$  and  $-3.72 \text{ km s}^{-1}$ , the first is usually the stronger of the two. In cycle 75-76 (J.D.244 4700-5100) the relative strength situation was reversed.

M-type supergiants can show drastic changes in behaviour; years of quiescence are followed by periods of (semi) regular variation. VY CMa hardly shows any long term variation in the OH emission, but PZ Cas and NML Cyg do, although the amplitudes are small (see also Harvey *et al.*, 1974). However, all three supergiants have large changes in OH flux (PZ Cas  $>3\sigma$ ;

VY CMa and NML Cyg  $> 5\sigma$ ) on timescales of days (see figure 10). This is probably caused by the fact that for some spectral features a large

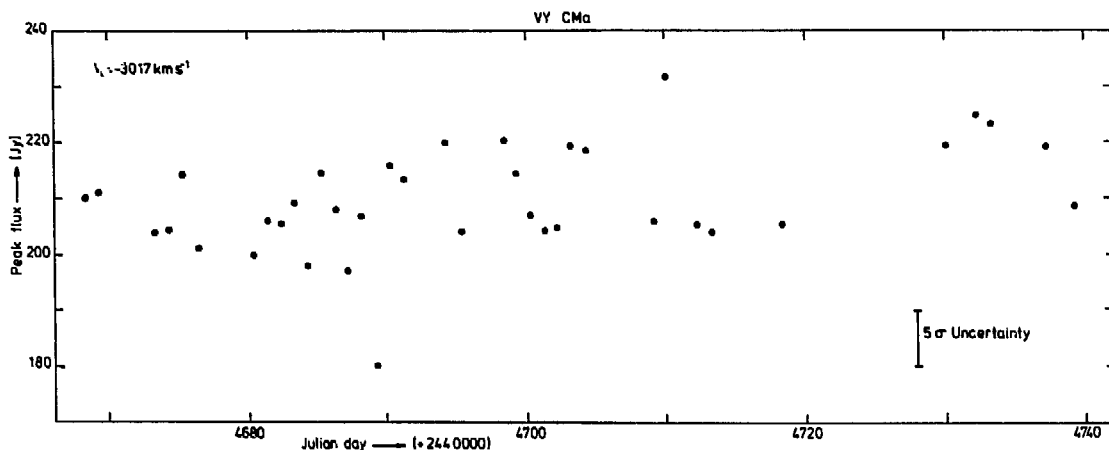


Figure 10. Short term variation of the strongest feature in the spectrum of VY CMa. This star was observed almost daily over a stretch of 200 days. A Fourier analysis reveals a main period of  $\sim 1000$  days, an intermediate time scale of  $\sim 180$  days, and short term variations of  $\lesssim 2$  days.

fraction ( $> 50\%$ ) of the power comes from extremely small ( $< 0.18''$ ) maser hotspots (Benson and Mutel, 1979), that are not completely saturated. In Mira variables this fraction usually is  $\ll 10\%$  (Reid *et al.*, 1977), as it is for OH/IR stars (Bowers *et al.*, 1980). If individual spectral features can be identified with these hotspots then observations of the supergiants with high time-resolution can give good estimates of the distances for these objects, when combined with VLBI experiments. A rough estimate for VY CMa gives a light travel time across the hotspot associated with the strongest peak in the spectrum ( $v_k = -30.17 \text{ km s}^{-1}$ ; table 3) of  $\lesssim 2$  days. When combined with the angular size of  $\lesssim 0.18''$ , a distance of  $\sim 1.9$  kpc is found, reasonably close to the literature value of 1.5 kpc (Herbig, 1969). The dimension of the hotspot (2 days corresponds to  $5 \cdot 10^{15}$  cm) indicates that the maser is only partially saturated (*cf.* Goldreich and Keeley, 1972). Note that NML Cyg belongs to the homogenous sample of OH stars, as it was found in Baud's survey.

ii) Table 2b.

The first thing to note in table 2b (see also figure 11) is that the entries can be separated into two groups: variable and non-variable stars.

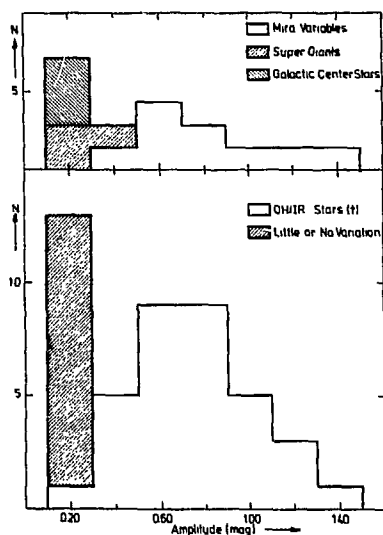


Figure 11. Amplitude distribution of all 60 stars included in the monitor program. The supergiants have extreme  $\Delta v$ 's, the non-variable OH/IR stars normal ones.

From our homogeneous sample six objects show virtually no variations larger than the  $3\sigma$  level: OH 15.7+0.8 ( $\Delta m_r = 0.13^m$ ), OH 31.0-0.2 ( $\Delta m_r = 0.13^m$ ), OH 37.1-0.8 ( $\Delta m_r = 0.13^m$ ), OH 51.8-0.2 ( $\Delta m_r = 0.16^m$ ), OH 53.6-0.2 ( $\Delta m_r = 0.12^m$ ), and OH 77.9+0.2 ( $\Delta m_r = 0.19^m$ ). Except for OH 31.0-0.2, none of these sources

is disturbed by confusion. Six others have small amplitude variation, that might be periodic. But in these cases our sensitivity is too low, mostly due to confusion, to give a definite answer. These six are: OH 11.5+0.1 ( $\Delta m_r = 0^m.23$ ), for which we see no variation in the (very weak) low velocity part of the spectrum, but clear variations in the (much stronger) high velocity peaks. We are unable to decide whether this behaviour is intrinsic to OH 11.5+0.1, or whether it comes from the underlying spectrum of OH 11.3+0.0; OH 17.7-2.0 ( $\Delta m_r = 0^m.16$ ), a strong OH-emitter with some long term variation; OH 18.3+0.4 ( $\Delta m_r = 0^m.27$ ), whose spectrum is completely confused with that of OH 18.3+0.1; OH 18.5+1.4 ( $\Delta m_r = 0^m.19$ ), that has one or two weak peaks outside the mean velocity range present in about 50% of the spectra; OH 25.1-0.3 ( $\Delta m_r = 0^m.21$ ), which is seriously disturbed by confusion of OH 24.7-0.1 in the weaker features and the integrated flux density, but which shows reasonable variation in the two strongest peaks; and OH 31.0+0.0 ( $\Delta m_r = 0^m.13$ ), that is associated with W43 in position, but not in velocity and so may be a pre-mainsequence object, showing irregular and (relatively) short term variations. OH 31.0+0.0 also has the smallest  $\Delta v$  ( $19.3 \text{ km s}^{-1}$ , cf.  $\langle \Delta v \rangle = 30 \text{ km s}^{-1}$ ) of all OH/IR stars in our sample and has all of its flux confined to the VLBI hotspots (Reid *et al.*, 1977). We can conclude for our sample of 44 OH/IR stars (OH 31.0+0.0 omitted) that 14% do not vary at all, 11% have such a small amplitude variation that it is hardly recognized with our beam and sensitivity, and that the remaining 75% vary with amplitudes comparable to those of the nearby, and weak, OH Mira stars. The periods of the OH/IR stars are, however, much longer than the periods of the Mira variables (figure 12).

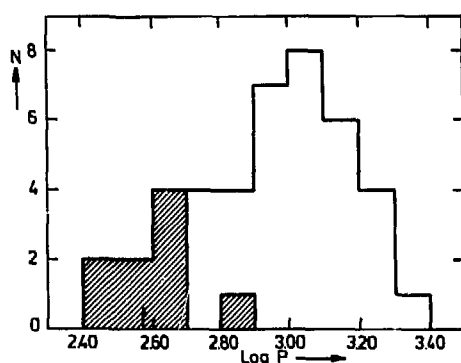


Figure 12. Period distribution for the variable OH/IR stars and for the OH-Mira's (shaded). The arrow marks the mean period for Mira variables (Wood and Cahn, 1977).

Note that for the optically identified masers small amplitudes correspond

to large  $\Delta v$ , i.e. to the supergiants, but that for the OH/IR stars the 'non'-variables are distributed over all  $\Delta v$ ! Finally we note that the three galactic centre sources are constant within their  $2\sigma$  uncertainties.

For a number of stars our time base is too short, or our phase coverage incomplete. For OH 21.5+0.5, OH 30.1-0.7, OH 127.9+0.0, and OH 138.0+7.2 we might not have observed the maximum yet; for OH 75.3-1.8 and OH 104.9+2.4, we might not have observed the minimum light. In these cases the true periods may deviate substantially from the tabulated values.

#### e. Asymmetry of the radio light curves

In general the visual light curves of Mira variables are asymmetric (see e.g. Campbell, 1955), but the asymmetry (usually expressed as  $f \equiv (m-M)/P$ , the fraction of the period between minimum and Maximum) becomes less pronounced at longer wavelengths (Lockwood and Wing, 1971). It is known that the Mira variables with the smaller  $f$ -values, i.e. a steep rise to maximum and a more gradual decline to minimum, are more likely to show maser emission (Bowers and Kerr, 1977). Although the radio light curves reflect the variation at long IR wavelengths (35  $\mu\text{m}$ ; Elitzur, 1981), inspection of our curves for the OH/IR stars revealed clearly systematic deviations from a sinewave function. We may describe the asymmetry quantitatively as follows. Let

$$m_k(i) \equiv \log S_k^*(i) \quad (9)$$

where  $S_k^*$  is the flux density, recalibrated as described in section II.6b, of the low- and high-velocity part of the spectrum and for all the peaks (so that  $k=1,2,\dots,(k_T+2)$  for a star with  $k_T$  peaks). Also let

$$\phi_k(i) = \{JD(i) - JD_{k0}\} / P \quad (10)$$

where we use the period ( $P$ ) and the time of maximum for curve  $k$  ( $JD_{k0}$ ) as found from the sinewave fitting in section II.6c. We may then fit an asymmetric lightcurve to the datapoints using

$$m_k(i) = m_{0k} + m_{1k} \cos\{2\pi \phi_k(i) / 2 f_k\}$$

for  $\phi_k(i) > 1 - f_k$  (ascending branch), (11a)

and

$$m_k(i) = m_{0k} + m_{1k} \cos\{2\pi \frac{\phi_k(i)}{2(1 - f_k)}\}$$

$$\text{for } \phi_k(i) < 1 - f_k \quad (\text{descending branch}) \quad (11b)$$

Again we take two steps: in the first we solve for four unknowns ( $m_{0k}$ ,  $m_{1k}$ ,  $\phi_k$ , and  $f_k$ ), although the mean flux  $m_{0k} \approx \log a_k$  and the amplitude  $m_{1k} \approx \log \{(1+B)/(1-B)\}$  can differ only slightly from the values found in section II.6c. In the second step we demand  $m_1$  and  $f$  to be the same for all  $(k_T+2)$  light curves of a given star. As before we use the mean value over the  $(k_T+2)$  curves, weighted with the strength of the feature and the quality of the fit. The numerical results can be found in table 3; the radio light curves in appendix B (figures 1-59).

#### f. Phase lag

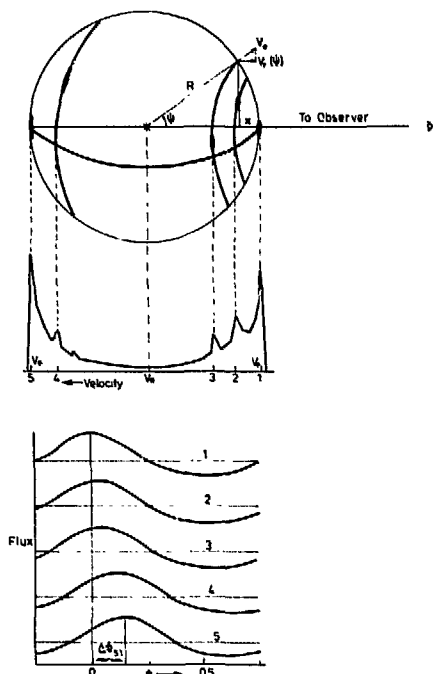


Figure 13. Schematic representation of the uniformly expanding OH shell, the resulting single-dish spectrum, and the variation of different parts in the spectrum.

Because the masers are saturated and pumped by (re)radiation from the central star (see section II.6a), one expects a phase lag (the light travel time) between the times of maximum for the different parts of the spectrum (figure 13: see also Schultz *et al.*, 1978). The phase lags are related

directly to the radius of the circumstellar shell (Appendix A). We may write

$$v_r = -v_e \cos \psi \quad (12)$$

where  $v_e$  is the expansion velocity of the shell,  $v_r$  the radial velocity in the rest frame of the star, and  $\psi$  the angle between the direction of expansion and the line of sight. Note that  $v_r(\psi)$  is negative with respect to the velocity of the star for  $-\frac{\pi}{2} < \psi < \frac{\pi}{2}$ . We may also write

$$R-x = R \cos \psi; \quad x = R[1 - \cos \psi] = R\left[1 + \frac{v_r}{v_e}\right] \quad (13)$$

The quantity  $\frac{x}{c}$  is the time difference between the variation of the 'front' peak (in phase with the star) and the peak k at  $v_{rk}$

$$\Delta t_k = \frac{R}{c} \left\{ 1 + \frac{v_{rk}}{v_e} \right\} \quad (14)$$

Clearly the time difference is greatest between the front ( $v_{rf} = -v_e$ ) and the back ( $v_{rb} = +v_e$ ) with the value  $\frac{2R}{c}$ . If we do not use the 'front' peak as the phase reference, but the peak j instead, we find

$$\Delta t_{kj} = \frac{R}{c v_e} \{v_{rk} - v_{rj}\} \quad (15)$$

or

$$\Delta \phi_{kj} = \frac{R}{c v_e P} \{v_{rk} - v_{rj}\} \quad (16)$$

Because we can measure  $\Delta \phi_{kj}$ ,  $v_e$ ,  $P$ , and  $v_{rk}$ , we can determine  $R$ , the radius of the OH shell. We can also use the phase lag between the curves for the integrated flux densities

$$\Delta \phi(\text{HV-LV}) = \frac{2R}{c v_e P} \left\{ v_e - \delta + v_e \ln\left(\frac{v_e}{2\delta}\right) \right\} \left\{ 1 + \ln\left(\frac{2v_e}{\delta} - 1\right) \right\}^{-1} \quad (17a)$$

where  $\delta = v_e - v_r$  is the difference in velocity between the strongest peak and the expansion velocity: it tells us to what velocity the model spectrum,  $S_\nu \propto \left\{ 1 - \left(\frac{v}{v_e}\right)^2 \right\}^{-1}$ , applies (see appendix A). Because for the OH-masers  $\delta = 0.01-0.1 \text{ km s}^{-1}$  (see figure 14) we can write

$$\Delta \phi(\text{HV-LV}) \approx 0.8 \frac{2R}{cP} \quad (17b)$$

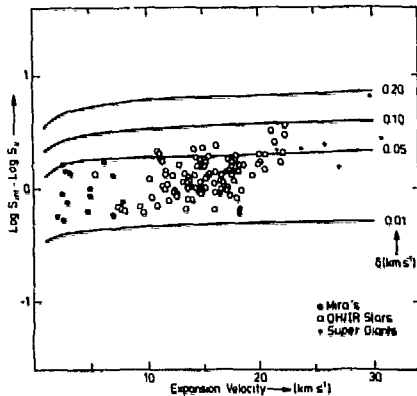


Figure 14. Ratio of the integrated flux density ( $10^{-22} \text{ Wm}^{-2}$ ) and the peak flux density (Jy) as function of the expansion velocity. This ratio is nearly constant with an equivalent width of  $10^4 \text{ Hz}$  ( $1.86 \text{ km s}^{-1}$ ). Here

$$\delta \equiv v_e - v_p.$$

Thus, the determination of the phase lags yields the linear dimensions of the envelopes. But the determination of  $\Delta\phi$ , and hence of  $R$ , is less straightforward than that of the other parameters describing the light curves. We found already (see sections II.6c and 6d) the times of maximum for each star with an accuracy of typically 5% of the period (see also table 3). But the phase lags between the different curves of a given star appear to be of the same order of magnitude ( $< 0.1 P$ ). In other words, phase lags determined in this way are only a zero order approximation. Therefore, a better procedure is to take one curve (say number  $j$ ) of a given star as reference and to look at the flux difference for each individual measurement on curve  $j$  with that on curve  $k$  ( $k \neq j$ ) of the same star. If there is a phase difference between the two curves this flux difference is not constant, but varies over a period (equations 21a and 21b). The amplitude of this variation is related directly to the phase lag,  $\Delta\phi$ , provided one has a good knowledge of the light curve (see for an application of this procedure Jewell *et al.*, 1980). When one adopts a simple sinewave to describe the light curves, this method is accurate to the second order in  $\Delta\phi$ . It still has two severe drawbacks: in the first place our coverage of the curves is not uniform and thus we have different phase coverage for different curves (e.g. in figure 13 there is for curve 1 a dense series of points just at and for curve 5 just before the maximum) and in the second place this method does not use extra features in the light curves (e.g. plateaus, humps, or secondary maxima) that deviate systematically from the adopted sinewave function, affect the sinewave fit, and yet offer a good opportunity to improve on the phase shift determination. This leads us to use a kind of autocorrelation method.

Equation (21) is rewritten, but now the variation is described by an arbitrary 'perfect' fit. Again the flux differences between individual measurements on curve  $k$  and a chosen reference curve  $j$  are analysed. The differences vary over a period, and the amplitude is an infinitely accurate function of  $\Delta\phi$  (equation 23). By shifting the two curves with respect to each other in phase,  $\Delta\phi$  can be found, because the amplitude of this variation in flux differences becomes zero, when the curves are shifted exactly over an amount  $\Delta\phi$ , the phase lag. This method is independent of the exact shape of the curves; it only assumes that all curves for a given star are the same (apart from a scale factor). The only remaining problem is that interpolation is required in order to calculate flux values at slightly shifted moments. For the interpolation we use stretches of the sine wave (equation 11), and so construct normal points on each curve at regularly spaced phases.

We choose the time of maximum for curve  $j$  as the phase reference and define for each measurement  $i$  the phase

$$\phi_j(i) \equiv \{JD(i) - JD_{j0}\}/P \quad (18)$$

and the phase of points on curve  $k$  with respect to the phase reference

$$\Phi_{kj}(i) = \pi \{\phi_j(i) - \Delta\phi_{kj}\}/f \quad \text{if } \Phi_{kj}(i) > 1 - f \quad (19a)$$

$$\Phi_{kj}(i) = \pi \{\phi_j(i) - \Delta\phi_{kj}\}/(1 - f) \quad \text{if } \Phi_{kj}(i) < 1 - f \quad (19b)$$

where  $\Delta\phi_{kj} = \phi_{ok} - \phi_{oj}$ , is the phase difference between  $k$  and  $j$  (as in equation 16), and  $\phi_{ok}$  and  $\phi_{oj}$  denote the phase zero points. Then, (using equations 18, 19, and 11)

$$m_k(i) = m_{ok} + m_1 \cos \Phi_{kj}(i). \quad (20)$$

or

$$m_k(i) - m_{ok} = m_1 \cos \Phi_{kj}(i)$$

We may write in first order approximation

$$\{m_k(i) - m_{ok}\} - \{m_j(i) - m_{oj}\} = m_1 \{ \cos \Phi_{kj}(i) - \cos \Phi_{jj}(i) \}$$

$$= m_1 \Delta \phi_{kj} \sin[\pi \phi_k(i)/f] + O(\Delta^2 \phi) \quad (21a)$$

$$= m_1 \Delta \phi_{kj} \sin[\pi \phi_k(i)/(1-f)] + O(\Delta^2 \phi) \quad (21b)$$

where the uncertainty is of the order  $\Delta^2 \phi$ ;  $O(\Delta^2 \phi)$ . As we know  $m_1$ ,  $f$ , and  $\phi_k$  we might solve equations 21a and 21b for  $\Delta \phi_{kj}$ . But this procedure still is susceptible to the two objections made before. Because the phase lag is not always small ( $\Delta \phi \lesssim 0.1$ ) the errors may in addition be large. A solution to this problem involves writing

$$m_k(i) = m_{ok} + m_1^* g[\Phi_{kj}(i)] \quad (22)$$

where  $m_{ok}$  is the mean flux from the sinewave fit,  $m_1^* \approx m_1$ , but is further unimportant as long as  $m_1^* < \infty$ , and  $g$  is an arbitrary periodic function that describes the light curve to the  $n^{\text{th}}$  degree. Both  $m_1^*$  and  $g$  are the same for all curves (all  $k$ ) of one star and  $g$  is continuous, as are its derivatives. Then, as before

$$\{m_k(i) - m_{ok}\} - \{m_j(i) - m_{oj}\} = m_1^* \{ \Delta \phi_{kj} g'[\Phi_{kj}(i)] + \frac{1}{2} \Delta^2 \phi_{kj} g''[\Phi_{kj}(i)] + \dots \} \quad (23)$$

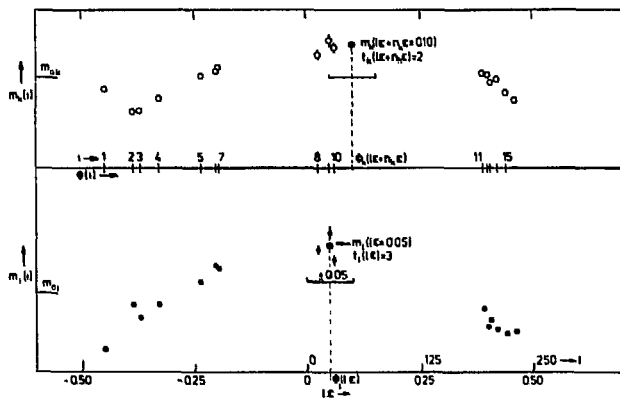


Figure 15. Example of the determination of a normal point  $m_k(1.\epsilon + n_k.\epsilon)$  and the determination of the corresponding point  $m_j(1.\epsilon)$  on the reference curve.

We now calculate the fluxes at normal points  $\lambda.\epsilon$ , where we choose  $\epsilon = 0.002$  and  $\lambda = 0, 1, 2, \dots, 500$ , for all curves,  $m_k(\lambda.\epsilon)$ , of one star. To find the flux  $m_k(\lambda.\epsilon)$  at phase  $\lambda.\epsilon$  we take the mean of a number of observed points (e.g.  $m_k(i' = i-3, \dots, i+4)$ ), weighted by the measured signal-to-noise ratio  $\frac{S}{N}(i')$  and by the phase distance  $|\lambda.\epsilon - \phi_k(i')|$ , after displacing them to the normal point  $\lambda.\epsilon$  along the sinewave as found in II.6e (equation 11a and 11b; see figure 15). Only measurements for which  $|\phi_k(i') - \lambda.\epsilon| < 0.05$  were used to determine  $m_k(\lambda.\epsilon)$ . Clearly not all the normal points are 'filled', because our light curves have phase gaps of 0.1 - 0.3. So let  $t_k(\lambda.\epsilon)$  be the number of observations used to calculate  $m_k(\lambda.\epsilon)$  and define

$$R_{kj}(\lambda, n_k) \equiv \{m_k(\lambda.\epsilon + n_k.\epsilon) - m_{ok}\} - \{m_j(\lambda.\epsilon) - m_{oj}\} \quad (24)$$

where  $n_k \in N$ . Summing over all normal points we find

$$\sum_{\lambda=1, t_k \neq 0, t_j \neq 0}^{500} R_{kj}(\lambda, n_k) = m_1^* \{ \Delta\phi_{kj} n_k.\epsilon \} \sum_{\lambda=1}^{500} \{ g'[\Phi_{kj}(i)] + \frac{1}{2}(\Delta\phi_{kj} - n_k.\epsilon) g''[\Phi_{kj}(i)] + \dots \} \quad (25)$$

Clearly  $\sum_{\lambda} R_{kj}(\lambda, n_k) \rightarrow 0$  if  $n_k.\epsilon \rightarrow \Delta\phi_{kj}$ . Consequently by varying  $n_k$  we may find  $\Delta\phi_{kj}$  as that value of  $n_k.\epsilon$  for which  $\sum_{\lambda} R_{kj}(\lambda, n_k)$  reaches its minimum. In practice we varied  $n_k.\epsilon$  from  $-80.\epsilon$  to  $+80.\epsilon$  around the phase lag  $\Delta\phi_{kj}$  as found from the sinewave fit. We minimized the quantity

$$\sigma_{kj}(n_k.\epsilon) \equiv \frac{\sum_{\lambda=1, t_k \neq 0, t_j \neq 0}^{500} [R_{kj}^2(\lambda, n_k) \{t_k(\lambda.\epsilon) + t_j(\lambda.\epsilon)\}]}{\sum_{\lambda=1}^{500} [t_k(\lambda.\epsilon) + t_j(\lambda.\epsilon)]} \quad (26)$$

to find  $\Delta\phi_{kj}$  (figure 16). We followed this procedure for all sources, shifting the curves (by choosing  $n_k$ ) with respect to a chosen reference curve. Each curve (including those for the integrated fluxes) served in

turn as the reference. This method is redundant, because in theory

$\Delta\phi_{kj} = -\Delta\phi_{jk}$  and  $\Delta\phi_{kj} - \Delta\phi_{k-1,j} = \Delta\phi_{k,j+1} - \Delta\phi_{k-1,j+1}$ , etc. Due to the different phase coverage of the various curves of a given star the equal sign does not hold in practice. Consequently, the redundancy gives us an impression of the accuracy of the procedure.

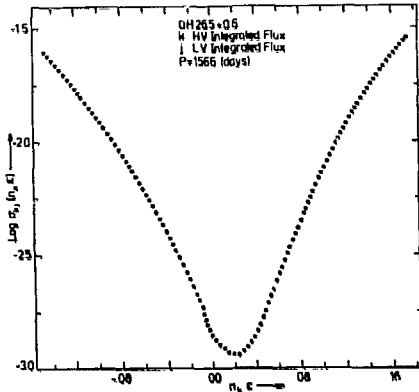


Figure 16.  $\sigma_{kj}(n_k, \epsilon)$  as function of the phase shift  $n_k, \epsilon$  for two curves of OH 26.5+0.6. The minimum lies at  $n_k, \epsilon = 0.022$ , or a  $\Delta t_{kj} = 34.5$  days.

#### g. Results

We list the following quantities in table 3 the name of the star; its period, with below the period the time of maximum for the low velocity integrated flux density ( $JD_0 - 244\ 0000$ ); the f-value ( $\equiv$  risetime/period); the amplitude of the sinewave function ( $m_1 = 0.2 \Delta m_r$ , from equation 11a and 11b); the logarithm of the mean low- and high-velocity integrated flux density ( $\log \bar{S}_{LV}$  and  $\log \bar{S}_{HV}$ ); the mean error ( $1\sigma$ ) for an individual measurement (me); the phase lag  $\Delta\phi$  (HV - LV) and its uncertainty; the velocities of all peaks ( $v_k$  measured with respect to the stellar velocity  $v_*$ ); the full width at half maximum ( $fw_k$ ), if measurable; the logarithm of the mean flux density ( $\log \bar{S}_k$ ); the mean error for an individual measurement ( $me_k$ ); the phase lags ( $\Delta\phi_k$  measured with respect to the given phase zeropoint  $JD_0$ ) and their errors. The uncertainties in the velocities are not tabulated, but they are usually small ( $\sim 0.03 \text{ km s}^{-1}$ ; see table 2a and 2b). Sources for which  $m_1 \lesssim (2-3) me_k$  (depending on the number of observations) are classified as non-variable. Their 'periods' are given between brackets and no phase lags are tabulated. The periods and the phase zeropoints are given to 0.1 day accuracy, although the actual errors are larger, because the phaselags have accuracies of  $\sim 10^{-3} P$ . The radio light curves can be found in appendix B (figures 1-59).

Table 3

Name	$P_R$ JD <sub>0</sub> (Days)	$f_R$	$m_1$	Log $\bar{S}_{LV}$ m.e. Log $\bar{S}_{HV}$ (10) (Log $10^{-22} \text{ Wm}^{-2}$ )	$\Delta\phi$ (HV-LV) $\pm$ ( $10^{-4}$ )	$v_k - v_x$ ( $\text{km s}^{-1}$ )	$f_{v_k}$ ( $\text{km s}^{-1}$ )	Log $\bar{S}_k$ (Log Jy)	$m.e._k$ (10)	$\Delta\phi_k$ ( $10^{-4}$ )	$\pm$	
1 R Aql	279.6 5177.8	0.53	0.174	0.828 .035	123	69	- 6.16	1.88	0.601	.052	130	68
				1.652 .005			- 3.72	0.96	0.605	.052	- 383	43
							+ 6.88	0.95	1.883	.003	404	74
2 RR Aql	403.8 4986.0	0.42	0.142	0.695 .041	47	28	- 6.59	0.71	0.047	.175	- 262	60
				0.818 .031			- 4.92	1.35	0.696	.037	19	20
							+ 4.93	1.13	0.881	.025	41	26
							+ 6.37	1.05	0.427	.070	41	28
3 SY Aql	349.3 5181.9	0.45	0.123	0.187 .065	- 269	200	- 4.87	0.85	-0.127	.147	- 409	224
				0.233 .058			- 3.78	0.80	-0.054	.123	58	139
							- 2.54	0.98	0.139	.078	- 278	181
							+ 1.85	0.74	-0.168	.163	2373	129
							+ 3.20	1.60	0.092	.087	- 326	236
							+ 4.09	1.40	0.032	.100	- 79	165
							+ 5.06	0.61	-0.179	.167	372	354
4 VY Cma	998.9: 5078.9	0.42	0.036	2.880 .003	- 185	55	-36.00	0.87	1.713	.015	907	83
				2.862 .003			-34.28	1.57	2.336	.004	964	107
							-31.58		2.264	.005	317	66
							-30.17		2.364	.004	488	83
							-28.16		2.111	.006	485	81
							-26.97		2.000	.008	8	56
							-25.25		1.567	.022	32	62
							-13.75	0.75	1.161	.035	909	113
							+11.84	1.61	1.474	.027	298	86
							+13.58	0.91	1.659	.017	- 28	75
							+14.78		1.707	.016	-1363	74
							+17.14		1.744	.014	- 85	71
							+18.75		1.788	.013	-1391	109
							+20.61		1.787	.013	4980	165
							+22.16		1.871	.011	- 582	85
							+23.75		1.974	.009	- 157	52
							+26.07		1.956	.009	210	66
	+28.48		2.041	.007	354	49						
	+29.68		1.997	.008	385	53						
	+31.03		1.813	.012	315	69						
5 PZ Cas	707.3 5019.0	0.34	0.059	0.836 .051	275	168	-28.94		-0.005	.168	3051	423
				0.864 .048			-27.09		0.651	.036	- 94	106
							-25.85		0.392	.065	395	216
							-24.62		0.172	.109	482	195
							+ 9.56		-0.096	.213	161	212
							+24.72		0.480	.053	- 68	106
							+25.93		0.464	.055	439	105
							+28.32		0.073	.138	177	134
6 NML Cyg	1109.6 4904.2	0.38	0.062	3.030 .002	- 243	49	-23.05		2.542	.003	75	38
				2.494 .006			-21.70	1.22	2.695	.002	82	39
							-19.16		2.166	.006	75	39
							-18.38		2.155	.006	48	28
							-16.50		2.335	.004	63	37
							-15.13		1.809	.014	- 216	54
							+10.62	1.59	1.488	.029	34	29
							+12.17	1.35	1.473	.030	- 14	11
	+18.74	1.59	1.432	.033	- 170	46						
	+22.33		1.959	.010	62	38						
	+23.80		2.139	.007	77	39						
7 Z Cyg	270.3 5194.1	0.43	0.140	0.365 .044	47	90	- 2.11	0.90	0.609	.034	- 91	34
				-0.127 .077			+ 1.78	0.96	-0.002	.145	- 91	54
							+ 2.91	0.65	-0.287	.314	864	152
8 U Ori	406.3 4959.8	0.39	0.188	0.130 .090	506	114	- 4.37		-0.172	.237	-3309	82
				0.401 .048			- 2.92	1.11	0.306	.073	131	43
							+ 2.63	0.84	0.669	.031	553	110
							+ 3.78		-0.151	.724	1398	244
9 WX Psc	632.0 4955.7	0.31	0.232	1.353 .017	311	5	-18.28	0.96	1.556	.006	20	5
				1.292 .019			+18.21	0.96	1.486	.007	351	7
10 WX Ser	443.0 5212.3	0.42	0.116	0.441 .050	- 217	76	- 8.19		-0.230	.212	1234	112
				0.275 .073			- 6.93	1.85	0.338	.054	11	57

Name	$F_R$ JD <sub>0</sub> (Days)	$f_R$	$m_1$	Log $\bar{S}_{LV}$ m.e. Log $\bar{S}_{HV}$ (1σ) (Log 10 <sup>-22</sup> km <sup>-2</sup> )	$\Delta\phi$ (HV-LV) ± (10 <sup>-6</sup> )	$v_k - v_{*k}$ (km s <sup>-1</sup> )	$f_{v_k}$ (km s <sup>-1</sup> )	Log $\bar{S}_k$ (Log Jy)	m.e. <sub>k</sub> (1σ)	$\Delta\phi_k$ (10 <sup>-6</sup> )	±
						- 6.38	1.64	0.319	.056	246	93
						- 5.51		0.219	.071	- 81	42
						+ 5.04	0.96	-0.235	.215	4217	87
						+ 6.54	0.70	0.087	.096	- 135	40
						+ 7.71	0.88	0.396	.047	- 342	98
11 IK Tau	455.6 5078.5	0.48	0.267	0.595 .063 0.658 .054	54 24	-17.57 -16.25 -14.57 -13.42 +13.33 +14.53 +15.29 +17.03	0.57 0.99 0.96 0.83 0.96 1.41 0.94 0.97	-0.004 0.627 -0.134 -0.187 0.323 0.074 0.075 0.513	.153 .035 .214 .248 .070 .122 .121 .045	321 136 - 31 10 92 89 - 90 174	24 16 27 67 26 17 54 24
12 RR Vir	363.8 5088.7	0.42	0.095	0.489 .034 0.616 .026	155 78	+ 4.80 - 3.52 - 2.62 - 1.57 - 0.38 + 4.66	0.74   0.87 0.64 0.98	-0.289 0.240 0.276 0.216 -0.172 0.817	.239 .065 .060 .069 .175 .017	719 - 144 366 - 232 - 77 70	142 51 56 47 123 50
13 359.4+1.3	(933) (4907.6)	(0.37)	0.027	1.018 .034 0.918 .043		-16.88 -15.16 -13.73 +16.62	 1.66 0.86 1.16	0.319 0.775 0.575 0.915	.103 .036 .057 .026		
14 0.3-0.2	(243) (3116.0)	(0.41)	0.033	0.911 .069 0.966 .061		-15.24 -13.36 -12.49 +13.40 +14.23 +15.41 +16.33	1.17 1.38 1.03 1.65 1.31 1.17	0.713 0.484 0.380 0.382 0.619 0.593 0.426	.067 .115 .148 .091 .083 .029 .132		
15 1.5-0.0	(141) (5107.9)	(0.36)	0.042	0.573 .082 0.720 .058		-13.63 -11.63 +13.44	0.95 0.81 0.84	0.677 0.050 0.898	.043 .191 .026		
16 11.5+0.1	691.4 5016.0	0.34	0.046	1.285 .031 2.059 .005	1522 318	-28.33 -25.88 -22.78 -21.24	1.16   1.50	0.342 0.473 0.575 0.761	.125 .092 .072 .047	-1920 - 9 100 40	289 211 75 40
						+14.64 +17.86 +22.38 +25.70 +28.01	  3.78   	0.906 0.986 1.495 1.121 1.252	.034 .028 .009 .021 .015	- 127 - 81 24 104 56	70 58 295 278 49
17 12.3-0.2	543.8 5133.4	0.50	0.113	0.881 .040 0.876 .040	- 331 88	-13.28 -11.48 +13.68	1.48 1.04 1.03	0.734 0.232 0.861	.036 .118 .027	- 570 -1082 - 821	44 167 121
18 12.8-1.9	812.3 4912.8	0.43	0.112	1.413 .012 1.240 .018	136 38	-23.13 -22.19 -20.31 -18.45 -17.25 +15.58 +16.58 +18.16 +20.39 +21.49	0.68 1.30   1.52   3.07	0.431 0.809 0.468 0.955 1.152 0.377 0.396 0.502 0.789 0.830	.060 .025 .055 .018 .012 .069 .066 .051 .027 .024	57 - 125 869 592 - 133 822 511 738 995 167	39 33 29 35 32 39 64 54 57 35
19 12.8+0.9	1487.8 4247.3	0.35	0.067	0.942 .025 0.985 .052	- 602 250	-11.27 - 9.29 - 7.54 - 6.61 - 5.50 + 6.39 + 8.04 + 9.46 +10.94	0.84 1.77   0.99   1.44	0.689 0.614 0.240 0.232 0.069 0.049 0.530 0.486 0.657	.032 .038 .089 .091 .135 .142 .046 .050 .034	2756 1767 273 -1640 156 305 390 127 - 40	214 364 317 428 220 410 223 202 256
20 13.1+5.0	707.5 4872.6	0.45	0.106	1.134 .017 0.757 .040	926 55	-14.65 +13.61 +15.20	1.74  1.05	1.135 0.391 0.746	.010 .057 .025	145 864 971	47 64 42
21 15.7+0.8	(453) (4896.8)	(0.38)	0.027	1.626 .010 1.464 .014		-14.56 -13.39 - 8.68 - 7.51 +11.28 +14.20	0.99  2.10 2.06 1.24 1.62	1.646 1.228 0.485 0.491 0.707 1.341	.009 .015 .085 .083 .050 .012		

Name	$P_K$ JD <sub>0</sub> (Days)	$f_R$	$m_1$	$\log \bar{S}_{LV}$ m.e. $\log \bar{S}_{HV}$ (1 $\sigma$ ) (Log 10 <sup>-22</sup> Ma <sup>-2</sup> )	$\Delta\phi(NV-LV) \pm$ (10 <sup>-4</sup> )	$v_k - v_x$ (km s <sup>-1</sup> )	$f_{v_k}$ (km s <sup>-1</sup> )	$\log \bar{S}_k$ (Log Jy)	m.e. <sub>k</sub> (1 $\sigma$ )	$\Delta\phi_k$ (10 <sup>-4</sup> )	$\pm$																																																																																																
22	16.1-0.3 1011.7 5055.2	0.46	0.111	1.579 .013 1.579 .013	156 53	-22.37 -20.39 -18.31 -16.26 -11.52 + 9.41 +11.25 +13.92 +17.09 +20.31 +22.02	1.03	1.102 0.988 0.997 0.703 0.465 0.409 0.479 0.617 0.810 0.964 1.337	.020 .026 .050 .087 .100 .085 .061 .039 .028 .012	14 11 47 35 102 33 181 39 30 38 803 45 515 64 476 64 403 64 67 31 68 21																																																																																																	
												23	17.4-0.3 1219.2 4449.8	0.48	0.118	0.944 .031 0.677 .058	350 239	-16.63 -15.05 +14.56 +17.36	1.18	0.873 0.350 0.012 0.741	.022 .072 .163 .029	69 229 989 340 1105 246 55 229																																																																																					
																								24	17.7-2.0 890.1: 5093.1	0.48	0.032	2.031 .005 2.140 .004	- 300 133	-12.19 -10.75 - 8.54 + 7.20 + 8.16 + 9.83 +11.57 +13.20	1.82	1.915 1.606 0.705 0.665 0.848 1.040 2.007 1.873	.004 .008 .062 .069 .045 .029 .003 .004	287 74 601 190 1189 141 3635 101 382 158 233 180 2 136 101 88																																																																									
																																				25	18.3+0.4 845.1: 5010.2	0.44	0.053	0.980 .037 1.066 .030	2900 315	-15.23 - 9.34 + 9.99 +12.22 +14.03 +15.55	1.35	0.893 1.51 -0.000 0.434 0.508 0.927	.028 .163 .239 .081 .068 .026	2180 350 4587 445 -1872 520 3048 208 5432 205 2670 367																																																													
																																																26	18.5+1.4 1124.9: 5124.6	0.47	0.039	1.017 .021 1.047 .020	95 161	-10.10 - 7.40 - 6.38 + 6.42 + 7.59 + 8.88 + 9.90 +11.02	1.74	0.935 1.02 0.071 0.261 0.352 0.620 0.741 0.740	.018 .091 .138 .087 .072 .038 .029 .029	445 249 209 78 95 209 305 179 -1716 414 387 125 552 180 204 172																																																	
																																																												27	18.8+0.4 923.3 5041.3	0.36	0.052	1.536 .011 1.331 .018	- 66 38	-14.65 -12.01 + 9.37 +14.74	1.65	1.541 0.538 0.349 1.375	.007 .074 .109 .010	362 156 496 87 619 300 223 33																																					
																																																																								28	20.2-0.1 856.6 5182.2	0.44	0.133	0.901 .037 0.920 .035	- 132 59	-15.99 -14.32 -12.63 +13.48 +14.87 +16.58	1.15	0.851 0.313 -0.034 0.113 0.350 0.793	.025 .086 .200 .138 .078 .028	632 102 195 70 2956 239 1709 55 920 141 755 98																									
																																																																																				29	20.7+0.1 1129.5 5028.3	0.42	0.199	1.140 .022 1.023 .029	212 24	-18.40 -16.19 -15.37 +14.19 +14.76 +16.17 +18.02 +19.13	0.97	1.147 0.400 0.371 0.357 0.151 0.587 0.729 0.376	.012 .069 .074 .077 .078 .045 .032 .073	626 80 197 18 124 23 566 32 292 23 93 100 221 26 438 32													
																																																																																																30	21.5+0.5 1975.2 3950.5	0.43	0.218	1.500 .013 1.399 .017	76 17	-18.88 -17.86 -16.32 -12.40 +15.37 +16.34 +18.65	1.224	1.243 0.816 0.514 0.441 0.516 1.393	.014 .013 .035 .071 .085 .071 .010	105 43 18 16 205 34 289 78 857 56 1021 75 559 42	
32	26.2-0.6 1180.6 4556.5	0.31	0.210	1.389 .035 1.210 .053	10 7	-22.04 -20.80 -19.71 +21.00 +22.16	0.94	1.246 1.116 0.823 0.957 0.885	.025 .034 .068 .050 .058	48 40 43 42 150 64 45 40 49 41																																																																																																	
												33	26.4-1.9 652.2 4659.2	0.42	0.088	0.937 .027 1.170 .016	- 64 147	-11.82 -10.09 + 9.46 +10.48 +12.55	1.07	1.049 0.231 0.128 0.314 1.232	.014 .094 .120 .077 .009	100 141 2851 136 2721 189 87 247 17 156																																																																																					

Name	$P_R$ JD <sub>0</sub> (Days)	$f_R$	$m_1$	Log $\bar{S}_{LV}$ m.e. Log $\bar{S}_{HV}$ (1 $\sigma$ ) (Log $10^{-22}$ km <sup>-2</sup> )	$\Delta\phi$ (HV-LV) $\pm$ (10 <sup>-4</sup> )	$v_k - v_g$ (km s <sup>-1</sup> )	$\epsilon w_k$ (km s <sup>-1</sup> )	Log $\bar{S}_k$ m.e. <sub>k</sub> (1 $\sigma$ ) (Log Jy)	$\Delta\phi_k$ $\pm$ (10 <sup>-4</sup> )	$\pm$																																																																																																														
34	26.5+0.6 1566.0 4824.8	0.40	0.227	2.365 .004 2.611 .002	188	24	-14.70 -13.70 -12.41 -10.87 -9.13 +7.25 +8.41 +9.79 +10.86 +11.80 +12.83 +14.44	1.18	1.914 .006 2.266 .003 1.814 .008 1.403 .020 1.349 .022 1.048 .045 1.336 .023 1.526 .015 1.664 .011 1.758 .009 1.893 .007 2.613 .001	36 11 65 14 93 19 38 21 107 16 625 31 86 26 100 17 140 27 113 24 266 41 99 31																																																																																																														
											35	27.3+0.2 939.3 4837.8	0.42	0.118	1.456 .012 1.198 .022	-27	84	-12.32 -9.31 +8.48 +11.58 +12.79	1.36	1.484 .008 0.455 .083 0.363 .103 0.761 .041 0.987 .024	540 159 1097 168 923 163 98 187 570 141																																																																																																			
																						36	28.5-0.0 559.2 4968.9	0.46	0.153	1.094 .034 1.141 .030	120	51	-13.34 -11.61 -8.82 +9.56 +11.41 +13.40	1.07	1.038 .026 0.765 .048 0.204 .183 0.222 .175 0.619 .067 1.017 .027	-144 54 -167 57 25 104 -686 116 -138 24 -141 17																																																																																								
																																	37	28.7-0.6 627.2 4871.3	0.44	0.166	1.111 .019 0.974 .026	-13	42	-17.16 -12.07 +16.69 +17.79	1.36 1.82	1.092 .012 -0.039 .164 0.690 .029 0.906 .038	-122 12 357 74 92 45 46 41																																																																													
																																												38	30.1-0.7 2064.4 5330.5	0.34	0.081	1.962 .014 2.028 .012	122	27	-20.61 -17.28 -15.96 -14.14 +6.37 +8.28 +9.78 +11.86 +15.18 +17.20 +20.03	1.26	1.791 .011 1.076 .057 1.160 .047 0.996 .068 0.576 .189 0.813 .105 0.806 .107 0.832 .100 0.962 .074 1.059 .059 1.805 .011	-334 30 -301 34 -386 33 -104 29 -375 34 -129 46 -95 35 -324 29 13 35 -397 45 -202 30																																																																		
																																																							39	30.1-0.2 852.5 5334.6	0.38	0.163	1.257 .028 1.306 .025	-21	26	-17.42 -16.18 -14.47 -13.06 +15.08 +17.55	1.89	1.090 .024 0.843 .042 0.382 .124 0.389 .122 0.663 .064 1.064 .025	-46 19 56 29 326 46 -187 44 -26 21 84 26																																																							
																																																																		40	30.7+0.4 1038.6 4987.4	0.41	0.115	1.105 .055 1.013 .068	2088	135	-17.55 -16.34 -15.08 -13.61 -12.81 -11.95 -11.05 -9.78 +13.42 +16.33 +17.52	0.88	0.973 .022 0.593 .053 0.389 .085 0.200 .134 0.084 .179 0.118 .164 0.230 .125 0.551 .058 0.072 .185 0.496 .066 0.724 .039	125 33 321 101 143 65 -101 155 -2058 140 -1398 77 5035 112 -1786 118 328 98 812 104 897 89																																												
																																																																													41	31.0-0.2 (1126.) (4855.2)	(0.41)	0.026	0.996 .043 1.096 .034			-14.35 -13.22 -11.32 -10.23 +11.96 +13.04 +14.52	1.35	0.727 .050 0.590 .069 0.420 .104 0.455 .095 0.662 .059 0.733 .050 0.895 .034																																		
																																																																																								42	31.0+0.0 399.8: 4988.9	0.50	0.041	1.004 .028 1.574 .008	1280	62	-8.23 -7.40 +3.51 +5.40 +7.51	1.33	0.923 .028 1.162 .016 0.639 .054 1.707 .005 0.702 .047	589 452 1246 67 301 355 1806 327 1044 75																						
																																																																																																			43	32.0-0.5 1540.2 5027.2	0.45	0.175	1.314 .018 1.079 .030	302	34	-20.56 -19.33 -18.23 -16.87 -13.23 +8.54 +15.97 +18.15 +20.07	1.02	1.014 .019 0.845 .028 0.762 .034 0.588 .051 0.279 .105 0.216 .122 0.184 .132 0.404 .078 0.775 .033	-82 27 -380 44 -344 63 -14 50 -88 61 -1847 53 895 72 146 26 295 23											
																																																																																																														44	32.8-0.3 1536.3 4542.3	0.37	0.248	1.841 .006 1.509 .012	665	8	-16.43 -15.04	1.319 1.469	.011 .008	-71 6 -62 6

Name	$P_R$ JD <sub>0</sub> (Days)	$F_R$	$m_1$	Log $\bar{S}_{LV}$ m.e. Log $\bar{S}_{RV}$ (1σ) (Log 10 <sup>-22</sup> km <sup>-2</sup> )	$\Delta\phi$ (RV-LV) ± (10 <sup>-4</sup> )	$v_k - v_{\infty}$ (km m <sup>-1</sup> )	$f w_k$ (km s <sup>-1</sup> )	Log $\bar{S}_k$ (Log Jy)	m.e. <sub>k</sub> (1σ)	$\Delta\phi_k$ (10 <sup>-4</sup> )	±
						-13.13		1.166	.015	- 110	5
						-10.95		0.811	.034	- 19	8
						-10.01		0.802	.035	- 324	18
						- 9.08		0.855	.031	- 198	4
						- 7.54		0.651	.049	- 348	13
						+10.29		0.556	.061	786	16
						+11.43		0.689	.045	432	7
						+13.54		1.024	.021	459	6
						+15.51		1.220	.013	408	5
45	35.6-0.3	839.8 5178.9	0.44	0.156	1.391 .016 1.217 .024	282 245					
						-13.66	1.42	1.317	.013	- 44	156
						-12.49		0.963	.028	1131	282
						- 9.78	1.76	0.564	.071	199	88
						+ 9.68		0.409	.103	274	331
						+11.21		0.558	.072	422	76
						+13.60	1.07	1.211	.016	503	173
46	36.9+1.3	409.0 5050.6	0.38	0.113	0.462 .066 0.453 .068	47 30					
						- 7.62	0.94	0.642	.038	- 20	21
						- 6.39		-0.008	.175	- 117	83
						+ 6.67		0.125	.126	-1371	106
						+ 7.90	0.82	0.643	.037	- 40	25
47	37.1-0.8 (737) (4988.9)		(0.45)	0.027	1.266 .017 1.291 .016						
						-13.30		0.955	.022		
						-11.62	1.12	1.095	.016		
						- 8.89	1.68	0.362	.088		
						- 7.67	0.91	0.235	.119		
						+ 9.70	1.66	0.388	.083		
						+10.39		0.389	.083		
						+13.49	1.23	1.243	.012		
48	39.7+1.5	1423.9 4860.8	0.48	0.164	1.805 .011 2.015 .007	73 29					
						-16.56	1.35	1.723	.008	- 60	32
						-14.97		1.246	.023	- 259	52
						-13.88		0.926	.047	116	27
						-12.70		0.830	.059	- 216	62
						-11.09		0.659	.088	73	27
						+10.99		0.481	.135	7	21
						+14.58		1.637	.009	- 66	30
						+16.07		1.871	.006	28	16
49	39.9-0.0	823.1 5159.1	0.37	0.159	0.946 .025 1.023 .021	139 33					
						-14.66	2.60	0.687	.028	130	38
						-13.66		0.557	.038	1547	71
						-11.83		0.359	.060	83	74
						+10.34	1.28	0.107	.109	728	86
						+12.03		0.226	.082	1122	139
						+13.20		0.438	.050	9	96
						+14.69	1.17	0.965	.015	141	49
50	42.3-0.1	1944.6 5080.2	0.48	0.072	1.234 .020 1.511 .012	- 630 149					
						-16.15	1.02	0.840	.030	- 466	185
						-15.03		0.592	.053	- 710	195
						-14.21		0.525	.062	- 652	165
						-11.65		0.376	.088	- 557	184
						-10.63		0.389	.086	-1250	313
						- 9.31	2.76	0.534	.061	- 572	194
						+11.45	1.81	0.582	.055	-2834	190
						+13.21		0.597	.053	- 564	196
						+16.67	1.38	1.448	.008	- 539	186
51	44.8-2.3	551.7 5064.1	0.34	0.155	0.945 .027 1.172 .016	129 48					
						-16.17	1.36	0.984	.015	- 598	29
						-13.44	1.04	0.194	.095	- 394	75
						+16.00	1.02	1.353	.007	164	53
52	45.5+0.1	760.5 4946.6	0.31	0.185	0.875 .037 0.834 .040	198 17					
						-17.12	1.52	0.884	.021	1	7
						+17.61	0.88	0.975	.017	277	15
53	51.8-0.2 (1162) (4998.2)		(0.41)	0.033	0.970 .023 0.851 .030						
						-19.39	1.61	0.855	.017		
						-17.44		0.456	.041		
						-15.96		0.194	.076		
						-13.62	1.27	-0.069	.142		
						+16.65		0.160	.082		
						+18.34	2.02	0.644	.027		
						+19.59		0.370	.050		
54	53.6-0.2 (838) (4816.4)		(0.44)	0.023	0.980 .030 1.346 .013						
						-13.16	2.04	0.917	.023		
						+ 9.98		0.351	.084		
						+11.85		0.730	.035		
						+13.85	0.89	1.442	.007		
55	75.3-1.8	1602.7; 4481.2	0.39	0.215	0.939 .020 0.892 .022	546 53					
						-12.54		0.861	.017	- 222	29
						-11.69	1.71	0.903	.015	- 390	42
						-10.50		0.297	.061	- 153	45
						- 9.55	0.79	0.183	.080	-1517	80
						+ 9.39		0.286	.063	622	79
						+10.41		0.524	.036	526	61
						+11.43	0.95	0.866	.017	393	39
56	77.9+0.2 (1339) (4939.4)		(0.41)	0.039	0.944 .022 0.867 .026						
						-11.41	0.81	0.828	.021		
						-10.31	0.92	1.024	.013		
						+ 8.65	0.86	-0.007	.145		

Name	$P_R$ JD <sub>0</sub> (Days)	$f_R$	$m_1$	LOG $\bar{S}_{LV}$ m.e. LOG $\bar{S}_{RV}$ (1 $\sigma$ ) (Log 10 <sup>-22</sup> Wm <sup>-2</sup> )	$\Delta\phi$ (HV-LV) $\pm$ (10 <sup>-4</sup> )	$v_k - v_R$ (km s <sup>-1</sup> )	$fv_k$ (km s <sup>-1</sup> )	Log $\bar{S}_k$ (Log Jy)	m.e. <sub>k</sub> (1 $\sigma$ )	$\Delta\phi_k$ (10 <sup>-4</sup> )	$\pm$	
						+ 9.57 +11.51		0.310 0.871	.068 .019			
57	83.4-0.9 4996.8	0.50	0.255	0.994 .022 0.508 .066	- 185	9	-17.99 -13.81 +16.46 +17.44 +18.15	1.21 2.40	1.071 -0.003 0.145 0.245 0.344	.010 .125 - .81 - .390 .055	233 14 7 24 16	
58	104.9+2.4 4880.9	0.50	0.133	1.854 .004 1.741 .005	216	26	-14.81 -13.79 -12.78 -11.23 - 8.09 - 6.44 + 7.14 + 9.72 +10.88 +13.48 +15.27	1.91	1.646 1.494 1.248 1.157 0.488 0.415 0.235 0.525 0.690 1.206 1.622	.004 .005 .009 .011 - .259 - .99 886 187 - 26 237 .004	- 191 - 17 53 30 17 45 29 41 29 23 28 151	23 27 24 17 17 29 29 29 23 28 31
59	127.9-0.0 5765.4	0.49	0.294	1.904 .003 1.640 .005	379	18	-10.78 - 9.65 - 8.63 +10.19 +11.21	0.86 0.83	2.050 1.279 1.002 1.284 1.383	.002 .008 .016 .008 .007	- 123 116 668 452 582	15 40 24 27 25
60	138.0+7.2 5376.3	0.35	0.161	1.108 .014 0.938 .021	188	57	- 9.26 - 7.37 + 8.33 + 9.63		1.267 0.512 0.448 1.150	.008 .043 .050 .010	177 - 232 465 258	76 47 66 57

#### h. Radii

In section II.6f we saw (equations 16 and 17b) that we can determine the radius of the OH shell if it obeys a simple geometric model (see appendix A) and provided that we know the phase lag and the velocity of each peak as well as the expansion velocity of the shell. Usually the expansion velocity ( $v_e$ ) has been taken as half the separation between the two strongest peaks in the lineprofile ( $\frac{1}{2} \Delta v$ ), but we adopt a somewhat different method. We measured in each of the spectra the total range ( $\delta v$ ; see table 2a,b) of emission and compared that with the velocity separation of the two outermost (not necessarily the strongest) peaks in the spectrum ( $\Delta v'$ ) (see figures 17a and 17b). We find, defining  $v_e \equiv \frac{1}{2} \Delta v'$ , with our velocity resolution of 0.54 km s<sup>-1</sup>

$$v_e = \frac{1}{2} \{ \delta v - 2.55 \} \quad (\text{km s}^{-1}) \quad (27)$$

This expression is valid for all 1612 MHz OH emitters.

That equation (27) holds from the smallest  $\Delta v$ 's (the OH-Mira's) to the largest (the supergiants) tells us that the physical conditions in the

masing regions are for all sources more or less the same. Because we see outside  $\pm v_e$  only emission due to thermal motions of the molecules, we can derive from equation (27) the gas temperature in the masing region.

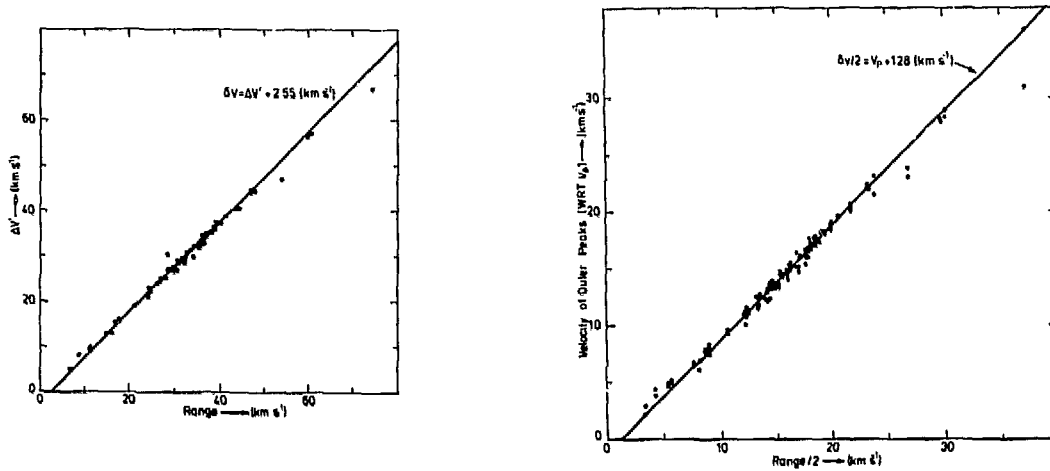


Figure 17a. Comparison between the total range of OH emission ( $\delta v$ ) and the velocity separation of the outermost peaks ( $\Delta v'$ ).

Figure 17b. Comparison of  $\delta v/2$  and  $v_p$ , the velocity of the outermost peak.

Assuming that the masers are saturated, so that no line narrowing occurs, and assuming further that the line profile is Gaussian outside  $\pm v_e$ , we find a Doppler width (deconvolved for our velocity resolution of  $0.54 \text{ km s}^{-1}$ ) of  $v_d = 0.58 \pm 0.05 \text{ (km s}^{-1}\text{)}$  and using (Elitzur, 1982)

$$T = 25 v_d^2 \frac{m_{\text{OH}}}{m_{\text{H}}} \quad (\text{K}) \quad (28)$$

we find a temperature  $T = 140 \pm 25 \text{ (K)}$  for the masing gas in all our OH masers. This is in good agreement with the theoretical values for the gas kinetic temperature of  $\sim 100 \text{ K}$  at  $R = 10^{16} \text{ cm}$  (Goldreich and Scoville, 1976).

We now determine the radii of the OH shells, using the found expansion velocities ( $v_e$ ), the peak velocities ( $v_k$ ), and the phase lags  $\Delta\phi_k$  (see table 3) by fitting a least squares solution to equation (16)

$$R_p = c P \Delta\phi_k \left\{ 1 + \frac{v_k}{v_e} \right\}^{-1} \quad (16')$$

The resulting radii ( $R_p$ ) and their formal errors ( $\Delta R_p$ ) can be found in tables 4 and the least squares fits in appendix C (figures 1-51). We also used the phase lag between the curves for the high- and low-velocity integrated flux density,  $\Delta\phi(HV-LV)$ , in order to find a radius, but only if there was no confusion in the spectrum

$$R_i' = c P \Delta\phi(HV-LV) f_c \quad (17a')$$

where

$$f_c \equiv \left\{ 1 - \frac{\delta}{v_e} + \ln\left(\frac{v_e}{2\delta}\right) \right\} \left\{ 1 + \ln\left(\frac{2v_e}{\delta} - 1\right) \right\}^{-1} \quad (29)$$

(see appendix A). Here  $\delta$  was taken to be the mean of the 'theoretical' value from the ratio of  $S_p$  and  $S_{int}$  (see figure 14) and the value measured in the spectra ( $v_e - v_p$ ).

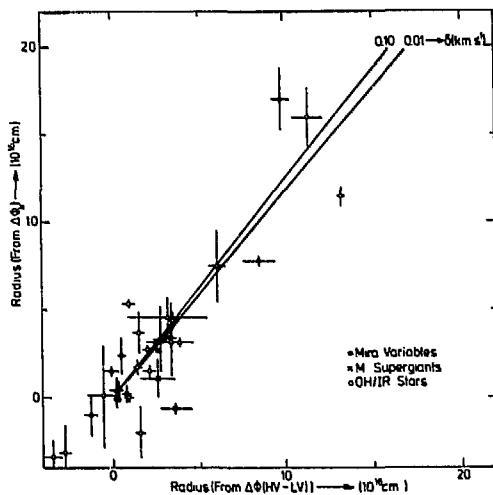
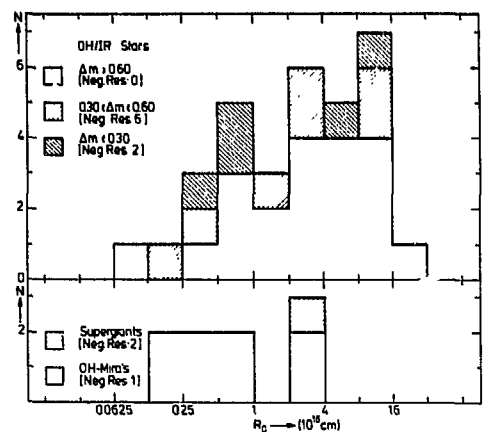


Figure 19. Distribution of the radii ( $R_O$ ) for all variable stars in the program. The number of negative results for each group is given in brackets.

Figure 18. Comparison of the radii determined from the phase lags between the curves of the integrated flux densities and of the peak flux densities. The drawn lines are the expected relation for the model case.



Finally, denoting the uncertainties in the found radii as  $\Delta R_p$  and  $\Delta R'_i$  resp., we calculate  $R_o$  and  $\Delta R_o$ , the best values for each star, as follows

$$R_o = \left\{ \frac{R_p}{\Delta R_p^2} + \frac{R'_i}{\Delta R'_i{}^2} \right\} \left\{ \frac{1}{\Delta R_p^2} + \frac{1}{\Delta R'_i{}^2} \right\}^{-1} \quad (30a)$$

and

$$\Delta R_o = R_o \left[ \left\{ \frac{1}{R_p^2} + \frac{1}{R'_i{}^2} \right\} \left\{ \frac{1}{\Delta R_p^2} + \frac{1}{\Delta R'_i{}^2} \right\}^{-1} \right]^{\frac{1}{2}} \quad (30b)$$

$R_p$ ,  $R'_i$ , and  $R_o$  are tabulated with their uncertainties in tables 4a-4d together with the name of the star, the radio amplitude ( $\Delta m_r$ ), the expansion velocity ( $v_e$ ), the mean phase distance between the measured flux points ( $\delta\phi$ ), and the correction factor ( $f_c$ ), that matches the 'integrated' and 'peak' radii.

Table 4a  
Mira variables and M-type supergiants

Name	$\Delta m_r$ (mag)	$v_e$ (km s <sup>-1</sup> )	$\delta\phi$	$f_c$	$R_p$ (10 <sup>16</sup> cm.)	$\Delta R_p$	$R'_i$ (10 <sup>16</sup> cm.)	$\Delta R'_i$	$R_o$ (10 <sup>16</sup> cm.)	$\Delta R_o$	Remarks
1 R Aql	0.87	6.815	.012	.777	2.37	0.99	0.57	0.32	0.74	0.41	
2 RR Aql	0.71	6.235	.013	.837	0.28	0.23	0.29	0.18	0.29	0.20	
3 SY Aql	0.62	4.375	.009	.694	2.88	1.84	-1.75	1.84	0.57	2.32	Poor baselines
7 Z Cyg	0.70	2.120	.009	.708	0.42	0.76	0.23	0.49	0.29	0.58	
8 U Cri	0.94:	3.050	.011	.753	3.33:	1.86	3.54:	0.80	3.51:	1.06	Flux decreasing
9 WX Pac	1.16	17.910	.014	.810	2.55	0.08	3.14	0.05	2.97	0.06	IRC+10011
10 WX Ser	0.58	7.585	.009	.784	-1.02	1.19	-1.59	0.56	<0.17		
11 IK Tau	1.33	16.730	.012	.788	-0.14	0.13	0.40	0.18	0.13	0.17	
12 RS Vir	0.48	4.285	.008	.722	0.47	0.73	1.01	0.51	0.46	0.86	
4 VY CMa	0.18	35.900	.007	.755	-8.83	1.16	-3.17	0.94	-5.41	1.33	
5 PZ Cas	0.29	28.890	.016	.772	1.04	1.06	3.27	1.99	1.53	1.45	
6 NML Cyg	0.31	25.575	.006	.765	-0.63	0.24	-4.57	0.92	-0.88	0.33	

Except for WX Ser, all Mira variables show positive correlation between  $v_k$  and  $\Delta\phi_k$ , implying that the simple shell model gives a good description of the geometry, although the uncertainties and the deviations for the individual features are large. We find for the OH-Mira's a mean value  $\langle R_o \rangle \pm \langle \Delta R_o \rangle = 0.78 \pm 0.66$  (10<sup>16</sup> cm), corresponding to a typical phase lag of 6 days. In other words, a sampling rate of at least once per 0.014 (phase) is needed ( $P \approx 400$  days), preferably over one cycle. Comparing this with the tabulated  $\delta\phi$ 's, and remembering that our coverage was not uniform and that we combined several cycles, we see that we are unable to decide

whether the deviations from the expanding shell model are intrinsic, or are caused by the uncertainties.

The supergiants VY CMa and NML Cyg have small amplitude long term variations, but show large, random variations on time scales of days. There is some correlation between  $v_k$  and  $\Delta\phi_k$ , but just reversed with respect to the Mira variables and OH/IR stars. This means either that the geometry of the supergiants is different, or that they have large random velocities. We should bear in mind, however, that our method of determining the phase lags is based on the assumption that the variation of the different features are correlated (i.e. complete saturation and radiative pumping). This assumption might be in error for these stars.

Table 4b  
OH/IR stars with large amplitudes ( $\Delta m > 0.60$ )

Name	$\Delta m_r$ (mag)	$v_e$ (km s <sup>-1</sup> )	$\phi$	$f_c$	$R_p$ (10 <sup>16</sup> cm)	$\Delta R_p$	$R_i^1$ (10 <sup>16</sup> cm)	$\Delta R_i^1$	$R_o$ (10 <sup>16</sup> cm)	$\Delta R_o$	Remarks
28 20.2-0.1	0.67	16.445	.029	.801	2.27	2.98		2.27	2.98	Confusion	
29 20.7+0.1	0.99	18.210	.017	.806	10.26	0.92		10.26	0.92	Confusion	
30 21.5+0.5	1.09	18.760	.017	.800	16:33	0.87		16.33	0.87	Confusion	
32 26.2-0.6	1.05	22.115	.019	.803	- 0.11	0.24	0.19	0.13	0.12	0.14	
34 26.5+0.6	1.13	14.070	.014	.792	3.10	0.22	4.82	0.62	3.29	0.26	
36 28.5-0.0	0.77	13.120	.038	.793	0.02	0.19	1.10	0.47	0.17	1.51	
37 28.7-0.6	0.83	17.380	.029	.801	1.48	0.29	- 0.13	0.43	0.98	1.81	
39 30.1-0.2	0.81	17.600	.032	.812	0.90	0.33			0.90	0.33	Confusion
43 32.0-0.5	0.88	20.575	.028	.814	7.47	2.08	7.41	0.83	7.42	1.09	
44 32.8-0.3	1.24	16.385	.013	.764	11.52	0.50	17.33	0.21	16.46	0.33	
45 35.6-0.3	0.78	13.520	.028	.808	4.56	1.16	3.80	3.30	4.48	1.68	
48 39.7+1.5	0.82	16.580	.019	.813	1.73	0.38	1.66	0.66	1.71	0.47	
49 39.9-0.0	0.80	14.710	.026	.822	- 2.05	1.57	1.80	0.43	1.53	0.53	
51 44.8-2.3	0.77	15.855	.036	.809	5.34	0.18	1.14	0.42	4.69	0.70	
52 45.5+0.1	0.92	17.125	.032	.828	2.68	0.11	2.36	0.20	2.61	0.14	
55 75.3-1.8	1.08	12.025	.028	.891	16.00	1.63	12.73	1.24	13.93	1.38	
57 83.4-0.9	1.28	18.110	.008	.822	0.97	0.22			0.97	0.22	Poor baselines
58 104.9+2.4	0.66	14.915	.012	.799	4.42	0.36	4.26	0.51	4.37	0.42	
59 127.9-0.0	1.47	10.975	.012	.791	17.06	1.75	12.38	0.59	12.06	0.72	
60 138.0+7.2	0.81	9.365	.013	.795	3.13	1.98	4.14	1.26	3.85	1.64	

All OH/IR stars with large amplitudes ( $\Delta m_r > 0.60$ ) obey the expanding shell model with rather small deviations ( $\sim 20\%$ ). We find a mean value  $\langle R_o \rangle \pm \langle \Delta R_o \rangle = 5.46 \pm 0.91$  (10<sup>16</sup> cm) considerably larger than for the OH-Mira's. This gives an intrinsic OH-luminosity (see appendix A)  $\sim 300$  times larger than the Mira's, if the conditions are the same. That is in good agreement with the observations (see Baud and Habing, 1983).

Table 4c

OH/IR stars with intermediate amplitudes ( $0.30 < \Delta m < 0.60$ )

Name	$\Delta m_r$ (mag)	$v_e$ (km s <sup>-1</sup> )	$\delta\phi$	$f_c$	$R_p$ (10 <sup>16</sup> cm)	$\Delta R_p$	$R'_i$ (10 <sup>16</sup> cm)	$\Delta R'_i$	$R_o$ (10 <sup>16</sup> cm)	$\Delta R_o$	Remarks
6	80.8-1.9	0.31	25.575	.006	.765	-0.63 0.24	-4.57 0.92	-0.88 0.33		NML Cyg	
17	12.3-0.2	0.56	13.830	.034	.793	-1.63 1.12		-1.63 1.12		Confusion	
18	12.8-1.9	0.56	22.615	.037	.761	3.72 1.17	1.88 0.53	2.19 0.63			
19	12.8+0.9	0.34	11.080	.031	.785					Absorption in spectrum	
20	13.1+5.0	0.53	15.670	.037	.787	7.82 0.23	10.79 0.64	8.16 0.28			
22	16.1-0.3	0.55	22.075	.030	.809	1.50 0.34	2.53 0.86	1.64 0.40			
23	17.4-0.3	0.59	16.830	.032	.801	0.31 3.65		0.31 3.65		Confusion	
33	26.4-1.9	0.44	12.085	.030	.792	0.12 2.88	<0.89 1.57	<0.71			
35	27.3+0.2	0.59	12.830	.043	.801	-1.25 1.40		<0.15		Confusion	
38	30.1-0.7	0.40	20.510	.018	.805	3.40 0.52	4.05 0.90	3.56 0.62			
40	30.7+0.4	0.57	17.240	.019	.795	9.18 3.39		9.18 3.39		Confusion; Peaks 5-8 dubious	
46	36.9+1.3	0.56	7.325	.012	.777	-0.33 0.74	0.32 0.20	0.28 0.23		Weak; S <sub>HARM</sub> < 4 Jy	
50	42.3-0.1	0.36	16.370	.019	.795	-2.37 4.50		<2.13		Confusion? Bad baselines	

Table 4d

OH/IR stars with small amplitudes ( $\Delta m < 0.30$ )

Name	$\Delta m_r$ (mag)	$v_e$ (km s <sup>-1</sup> )	$\delta\phi$	$f_c$	$R_p$ (10 <sup>16</sup> cm)	$\Delta R_p$	$R'_i$ (10 <sup>16</sup> cm)	$\Delta R'_i$	$R_o$ (10 <sup>16</sup> cm)	$\Delta R_o$	Remarks
16	11.5+0.1	0.23	29.390	.029	.755	0.60 0.60		0.60 0.60		Confusion	
24	17.7-2.0	0.16	12.890	.021	.767	-3.38 0.95	-4.51 2.00	-3.59 1.14			
25	18.3+0.4	0.27	15.055	.032	.794	12.72 6.25		12.72 6.25		Confusion	
26	19.5+1.4	0.19	10.850	.010	.757	< 0.49 2.24	1.83 3.10	< 0.95			
27	18.8+0.3	0.26	14.660	.029	.828	< 0.39 1.34	-0.95 0.55	< 0.39			
31	25.1-0.3	0.21	12.140	.029	.796	0.95 0.26	0.36 0.68	0.87 0.63		Confusion	
42	31.0+0.0	0.21	7.640	.009	.764	1.70 1.11		1.70 1.11		W43A; Confusion	

For the OH/IR stars with smaller amplitudes we find an increasing number of sources with a negative correlation between  $v_k$  and  $\Delta\phi_k$ . For

$0.30 < \Delta m_r < 0.60$  these are 5 out of 12, and for  $\Delta m_r < 0.30$  3 out of 6 objects. In all cases a positive value for  $R_o$  is within the uncertainties. The mean value for the small amplitude stars ( $\Delta m_r < 0.60$ ) is  $\langle R_o \rangle \pm \langle \Delta R_o \rangle = 3.75 \pm 1.62$  (10<sup>16</sup> cm). For all OH/IR stars that are variable we find  $\langle R_o \rangle \pm \langle \Delta R_o \rangle = 4.85 \pm 1.16$  (10<sup>16</sup> cm) (see figures 17 and 18). With a mean period of ~1000 (days) this demands a coverage of at least once per 0.036 (phase), a condition that is satisfied by almost all sources (see  $\delta\phi$ , table 4). Furthermore, we did not have to combine more cycles for the OH/IR stars, so avoiding larger uncertainties due to irregular variation.

We conclude that we obtained reasonable and consistent results for

Table 4e  
OH/IR stars without recognizable variation

Name	$\Delta m_r$ (mag)	$v_e$ (km s <sup>-1</sup> )	$\delta\phi$	Remarks
13 359.4-1.3	0.13	16.605	.033	Low S/N
14 0.3-0.2	0.16	15.540	.032	Low S/N
15 1.5-0.0	0.21	13.085	.033	
21 15.7+0.8	0.13	14.705	.033	
41 31.0-0.2	0.13	14.270	.030	Confusion
47 37.1-0.8	0.13	13.585	.027	
53 51.8-0.2	0.16	19.335	.032	
54 53.6-0.2	0.12	13.340	.036	
56 77.9+0.2	0.19	11.045	.029	

the OH-Mira's, determining radii for 8 of them (out of 9) to ~ 50% accuracy. For our homogeneous sample of 44 OH/IR stars we found radii for 29 to ~ 15% accuracy. For 9 stars (including NML Cyg), all with small amplitude variations, our accuracy was too low to allow the determination of a phase lag. 6 OH/IR stars did not vary at all (see table 4e).

## II.7 Conclusion

It is possible to study the time behaviour of strong 1612 MHz OH-masers ( $S_H > 4$  Jy) with a relatively small telescope, although confusion is a serious problem in those regions where the OH/IR stars are close to one another in space and in velocity. To obtain reliable periods it is necessary to follow these sources for several years. The length of our program (3-5 years) proved to be too short for the longest periods ( $P \sim 2000$  days). Furthermore, for most OH/IR stars we covered only one cycle, so that we are unable to say whether or not *l'histoire se repète*, although comparison with older observations (e.g. Wilson and Barrett, 1972; or Harvey *et al.*, 1974) indicates that on the longest timescales now available (over 10 years) the radio light variations do repeat, with the same enigmatic changes in the length of the period and in the strength of the maxima as displayed by the normal Mira variables. We found amplitudes that are comparable with those of the OH-Mira's, but we also found a number of OH/IR stars with small amplitude and irregular variation characteristic of supergiants. Their expansion velocities, however, are much smaller than expected for supergiants.

The phase differences between the various curves of one star gave us a good determination of the shell radius for the OH/IR stars, provided that we had good coverage of either the maximum or the minimum in the light curve. The OH-Mira's, having much smaller sizes, require a sampling rate of

at least once per 6 days. Because they are weak OH-emitters and because the Dwingeloo telescope is rather small, in practice this means even more frequent observing. The combination of several cycles does not seem to increase the accuracy of the phase lags by the expected amount, due to the poor reproducibility of the phase and the amplitude of the variation.

Literature cited in chapter II

- Allen, D.A., Hyland, A.R., Longmore, A.J., Caswell, J.L., Goss, W.N., Haynes, R.F.: 1977, *Astroph. J.* *217*, 108
- Andersson, C., Johansson, L.E.B., Goss, W.N., Winnberg, A., Rieu, Nguyen-O.: 1974, *Astron. Astroph.* *30*, 475
- Baars, J.W.M., Genzel, R., Pauliny-Toth, I.I., Witzel, A.: 1977, *Astron. Astroph.* *61*, 99
- Ball, J.A.: 1976, *Measurements with Radio-Frequency Spectrometers*, Chapter 4.3, p. 46 in *Methods of Experimental Physics* *12 C*; ed. Meeks, M.L.; AP.
- Baud, B., Habing, H.J.: 1983, *Astron. Astroph.* submitted
- Baud, B., Habing, H.J., Matthews, H.E.: 1975, *Nature* *258*, 406
- Baud, B., Habing, H.J., Winnberg, A., Matthews, H.E.: 1979, *Astron. Astroph. Suppl.* *35*, 179
- \_\_\_\_\_ : 1979, *Astron. Astroph. Suppl.* *36*, 193
- \_\_\_\_\_ : 1981, *Astron. Astroph.* *95*, 156
- Benson, J.M., Mutel, R.L.: 1979, *Astroph. J.* *233*, 119
- Blair, G.N., Dickinson, D.F.: 1977, *Astroph. J.* *215*, 552
- Bloch, A.: 1979, *Murphy's Law and other reasons why things go wrong*, Price/Stern/Sloan Publishers, Inc., Los Angeles
- Bowers, P.F.: 1978, *Astron. Astroph.* *64*, 307, 1978
- Bowers, P.F., Johnston, K.J., Spencer, J.H.: 1981, *Nature* *291*, 382
- Bowers, P.F., Kerr, F.J.: 1974, *Astron. Astroph.* *36*, 225
- \_\_\_\_\_ : 1977, *Astron. Astroph.* *57*, 115
- \_\_\_\_\_ : 1978, *Astron. J.* *83*, 487
- Bowers, P.F., Reid, M.J., Johnston, K.J., Spencer, J.H., Moran, J.M.: 1980, *Astroph. J.* *242*, 1088
- Campbell, L.: 1955, *Studies of Long Period Variables*
- Caswell, J.L.: 1973, *Galactic Radio Astronomy*, IAU symp. *60*, 423
- Caswell, J.L., Haynes, R.F.: 1975, *M.N.R.A.S.* *173*, 649
- Cato, B.T., Roennaeng, B.O., Rydbeck, O.E.J., Lewin, P.T., Yngvessen, K.S., Cardiashenos, R.G., Shantey, J.F.: 1976, *Astroph. J.* *208*, 87
- Cimerman, M.: 1979, *Astroph. J. Lett.* *228*, L79
- Dickinson, D.F.: 1976, *Astroph. J. Suppl.* *30*, 259
- Dickinson, D.F., Bechis, K.P., Barrett, A.H.: 1973, *Astroph. J.* *180*, 831

- Dickinson, D.F., Blair, G.N.: *Bull. Am. Astron. Soc.* 8, 348
- Dickinson, D.F., Blair, G.N., Davis, J.H., Cohen, N.L.: 1978, *Astron. J.* 83, 32
- Dickinson, D.F., Chaisson, E.J.: 1973, *Astroph. J. Lett.* 231, L135
- Dickinson, D.F., Kleinmann, S.G.: 1977, *Astroph. J. Lett.* 214, L135
- Dickinson, D.F., Kollberg, E., Yngvesson, S.: 1975, *Astroph. J.* 199, 131
- Dickinson, D.F., Snyder, L.E., Brown, L.W., Buhl, D.: 1978, *Astron. J.* 83, 36
- Dyck, H.M., Lockwood, G.W., Capps, R.W.: 1974, *Astroph. J.* 189, 89
- Elitzur, M.: 1982, *Reviews of modern physics*
- Engels, D.: 1982, *Zur Natur von OH/IR-Objekten. Ph.D. thesis Veröff. Astron. Inst. Bonn* 95
- Epchtein, N., Rieu, Nguyen-Q.: 1982, *Astron. Astroph.* 197, 229
- Evans, N.J., Beckwith, S.: 1977, *Astroph. J.* 217, 729
- Evans, N.J., Crutcher, R.N., Wilson, W.J.: 1976, *Astroph. J.* 206, 440
- Gehrz, R.D., Woolf, N.J.: 1971, *Astroph. J.* 165, 285
- Gillett, F.C., Merrill, K.M., Stein, W.A.: 1971, *Astroph. J.* 164, 83
- Goldreich, P., Keeley, D.A.: 1972, *Astrophys. J.* 174, 517
- Goldreich, P., Scoville, N.: 1976, *Astroph. J.* 205, 144
- Harvey, P.M., Bechis, K.B., Wilson, W.J., Ball, J.A.: 1974, *Astroph. J. Suppl.* 27, 331
- Herbig, G.H.: 1969, *Mém. Soc. Roy. Sci. Liège* 19, 13
- Hyland, A.R., Becklin, E.E., Frogel, J.A., Neugebauer, G.: 1972, *Astron. Astroph.* 16, 204
- Hyland, A.R., Becklin, E.E., Neugebauer, G., Wallerstein, G.: 1969, *Astroph. J.* 158, 619
- Jewell, P.R., Elitzur, M., Webber, J.C., Snyder, L.E.: 1979, *Astroph. J. Suppl.* 41, 191
- Jewell, P.R., Elitzur, M., Snijder, L.E.: 1980, *Astroph. J. Lett.* 242, L29
- Johansson, L.E.B., Andersson, C., Goss, W.N., Winnberg, A.: 1977, *Astron. Astroph. Suppl.* 28, 199
- Johnston, K.J., Robinson, B.J., Caswell, J.L., Batchelor, R.A.: 1972, *Astroph. Lett.* 10, 93
- Jones, T.J., Hyland, A.R., Caswell, J.L., Gatley, I.: 1982, *Astroph. J.* 253, 208
- Kaifu, N., Buhl, D., Snyder, L.E.: 1975, *Astroph. J.* 195, 359

- Kolena, J., Pataki, L.: 1977, *Astron. J.* **82**, 150
- Kukarkin, B.V., Kholopov, P.N., Efremov, Yu.N., Kukarkina, N.P., Kurochkin, N.E., Medvedeva, G.I., Perova, N.B., Fedorovich, V.P., Frolov, M.S.: 1969, *General catalogue of variable stars, Moscow (+ Suppl.)*
- Lebofsky, M.J., Kleinmann, S.G., Rieke, G.H., Low, F.J.: 1976, *Astroph. J. Lett.* **206**, L157
- Lépine, J.R.D., Paes de Barros, M.H., Gammon, R.H.: 1976, *Astron. Astroph.* **48**, 269
- Lépine, J.R.D., Le Squeren, A.M., Scalise Jr., E.: 1978, *Astroph. J.* **225**, 869
- Le Squeren, A.M., Raudry, A., Brillet, J., Darchy, B. 1979, *Astron. Astroph.* **72**, 39
- Lockwood, G.W.: 1972, *Astroph. J. Suppl.* **24**, 375
- Lockwood, G.W., Wing, R.F.: 1971, *Astroph. J.* **169**, 63
- Mendoza, E.E.: 1965, *Boletín de los Observatorios Tonanzintla y Tacubaya* **4**, 51
- Merrill, K.M., Stein, W.A.: 1977, *PASP* **88**, 285  
 \_\_\_\_\_: 1977, *PASP*, **88**, 294  
 \_\_\_\_\_: 1977, *PASP*, **88**, 874
- Morrison, D., Simon, T.: 1973, *Astroph. J.* **186**, 193
- Reid, M.J., Muhleman, D.O., Moran, J.M., Johnston, K.J., Schwartz, P.R.: 1977, *Astroph. J.* **214**, 60
- Reid, M.J., Moran, J.M., Johnston, K.J.: 1981, *Astron. J.* **86**, 897
- Rieu, Nguyen-Q., Fillit, R., Gheudin, M.: 1971, *Astron. Astroph.* **14**, 154
- Rieu, Nguyen-Q., Laury-Micoulaut, C., Winnberg, A., Schultz, G.V.: 1979, *Astron. Astrophys.* **75**, 351
- Robinson, B.J., Caswell, J.L., Goss, W.N.: 1970, *Astroph. Lett.* **7**, 79
- Schneller, H.: 1965, *Sonneberg M.V.S. Bd3, Heft 2*, 86
- Schultz, G.V., Kreysa, E., Sherwood, W.A.: 1976, *Astron. Astroph.* **50**, 171 + correction in **52**, 475
- Schultz, G.V., Sherwood, W.A., Winnberg, A.: 1978, *Astron. Astroph. Lett.* **63**, L5
- Schwartz, P.R., Barrett, A.H. 1970, *Astroph. J. Lett.* **159**, L123
- Simon, T.: 1974, *Astron. J.* **79**, 1054
- Slottje, C.: 1982, *User Note* **43**, Dwingeloo, 810508
- Snyder, L.E., Buhl, D.: 1975, *Astroph. J.* **197**, 329

- Spencer, J.H., Schwartz, P.R., Waak, J.A., Bologna, J.M.: 1977, *Astron. J.* 82, 706
- Strecker, D.W., Ney, E.P.: 1974, *Astron. J.* 79, 794
- \_\_\_\_\_: 1974, *Astron. J.* 79, 1410
- Sullivan, W.J. III: 1973, *Astroph. J. Suppl.* 25, 393
- Turner, B.E.: 1971, *Astroph. Lett.* 8, 73
- Werner, M.W., Beckwith, S., Gatley, I., Sellgren, K., Berriman, G.: 1980, *Astroph. J.* 239, 540
- Willems, F., de Jong, T.: 1983, *Astron. Astrophys. Lett.* submitted
- Wilson, W.J., Barrett, A.H.: 1972, *Astron. Astroph.* 17, 385
- Wilson, W.J., Barrett, A.H., Moran, J.N.: 1970, *Astroph. J.* 160, 545
- Wilson, W.J., Schwartz, P.R., Neugebauer, G., Harvey, P.M., Becklin, E.E.: 1972, *Astroph. J.* 177, 523
- Winnberg, A., Rieu, Nguyen-Q., Johansson, L.E.B., Goss, W.N.: 1975, *Astron. Astroph.* 38, 145
- Wood, P.R., Cahn, J.H.: 1977, *Astrophys. J.* 211, 499

### III.1) VLA<sup>a)</sup> Line Observations

#### III.1 Introduction

In the past decade one has tried to study the spatial structure of OH shells around late-type stars by using VLBI<sup>b)</sup> techniques (e.g. Reid *et al.*, 1977; Benson and Mutel, 1979; Bowers *et al.*, 1980). Extremely small emission spots were found with very high brightness temperatures ( $T_B > 10^{10}$  K), that confirmed the presence of natural masers. But in the VLBI measurements only a small fraction of the total flux could be detected and the results neither contradicted, nor confirmed the suggested expanding shell geometry. Not until observations with intermediate baselines became available (Booth *et al.*, 1981; using MERLIN<sup>c)</sup>), such a geometry was found indeed. By making maps at different velocities, i.e. at different depths along the line of sight (see Baud, 1981, using the VLA), one may study the 3-dimensional structure of the envelope. We can verify the expanding shell geometry, find the radii of the OH shells, and, by combining these with the 'phase lag' radii as found in the Dwingeloo monitor program, determine distances to the individual objects with high accuracy.

#### III.2 Observations and reduction

We used the VLA in the A-configuration (see for a general description of the VLA: Thompson *et al.*, 1980) on February 28 and March 1, 1982 to observe 11 OH/IR stars. Ten of these sources have large radial velocities, selected because (a) they were thought to be at their tangential points, thus not having the kinematic distance ambiguity; (b) we had good positions for them; and (c) they were in the Dwingeloo monitor program. As a check on our procedures we included OH 26.5+0.6, which had been observed before (Baud, 1981). Six of our objects have small expansion velocities ( $v_e < 15 \text{ km s}^{-1}$ ) and five have large ones ( $v_e > 15 \text{ km s}^{-1}$ ). All sources were observed in 4 short cuts of 10-15 minutes each, separated over 1½ hours, except for OH 26.5+0.6, which was observed only once ( $t_{\text{int}} = 5$  minutes). Calibrations were done every

- 1) Proposed and obtained in collaboration with B. Baud, H.J. Habing, and A. Winnberg
- a) Very Large Array
- b) Very Long Baseline Interferometry
- c) Multi Element Radio Linked Interferometer Network

20 minutes on the continuum source 1741-038 ( $1.972 \pm 0.012$  Jy on 28-2-82, based on 13.830 Jy for 3C286 at 1612 MHz).

On the first day we observed the small  $\Delta V$  sources. We could use 13 telescopes, a bandwidth of 197 kHz, and 64 frequency (= velocity) channels, after Hanning smoothing yielding a resolution of 6.2 kHz ( $1.2 \text{ km s}^{-1}$ ) and a noise  $N = 0.03$  Jy per channel ( $t_{\text{int}} = 50$  minutes). The largest spacing was 36.6 km, giving a resolution of  $1''0$  at 18 cm; the shortest, 2.4 km, corresponding to a largest structure of  $15''5$  still visible. On the second day, when observing the sources with large  $\Delta V$ , only 9 telescopes could be used, the shortest baseline being 3.8 km ( $\sim 9''8$ ). Our bandwidth on that day was 396 kHz, split into 128 channels, giving the same resolution, but  $N = 0.04$  Jy per Hanning smoothed channel.

We used standard reduction programs to produce small maps ( $32'' \times 32''$ ; cleaned  $16'' \times 16''$ ) for each channel. For the weak emission part in the middle of the spectrum we usually had to add a number of channel maps to get a sufficient signal-to-noise ratio. This procedure provided us with 20-60 maps for each star. A selection of representative channel maps can be seen in figures 1-11.

Shortly after the VLA run all sources were observed with the Dwingeloo Radio Telescope. In table 1 the phases of the VLA and of the Dwingeloo single-dish observations can be found (columns 2 and 5), together with the integrated flux densities for the low- and the high-velocity parts of the spectrum. Columns 3 and 4 are the VLA values, columns 6 and 7 the Dwingeloo measurements. Column 8 gives the percentage of the total flux detected at the VLA.

Table 1

Name	$\phi$	$S_{\text{LV}}$	$S_{\text{HV}}$	$\phi$	$S_{\text{LV}}$	$S_{\text{HV}}$	$\%$
OH	VLA	( $10^{-22}$ )	( $\text{Wm}^{-2}$ )	Dwing.	( $10^{-22}$ )	( $\text{Wm}^{-2}$ )	
(1)	(2)	(3)	(4)	(5)	(6)	(7)	(8)
18.5+1.4	0.915:	11.49	12.52	0.920:	11.91	12.47	98
20.7+0.1	0.001	16.39	10.89	0.007	16.26	15.74	85
21.5+0.5	0.546	15.06	11.77	0.550	24.89	17.70	63
25.1-0.3	0.795:	5.55	4.33	0.823:	6.22	6.29	79
26.5+0.6	0.130	272.0	466.3	0.138	362.2	616.6	75
28.5-0.0	0.107	15.53	14.67	0.112	13.40	13.27	113
30.1-0.7	0.854	96.02	96.26	0.860	111.4	122.2	82
31.0-0.2	(0.154)	6.26	8.88	(0.160)	9.89	12.97	66
32.0-0.5	0.001	26.39	11.84	0.006	31.91	16.48	79
32.8-0.3	0.317	58.84	28.73	0.320	73.79	38.81	78
37.1-0.8	(0.054)	13.21	13.47	(0.062)	18.88	19.91	69

Generally,  $\geq 80\%$  of the total flux was seen in the VLA maps. Fluctuations on timescales of days to weeks may account for 5-10% differences (see e.g. OH 28.5-0.0), as may the different methods of calibrating. In fact, no

special attention was paid to the flux calibration in the VLA measurements. We applied no bandpass correction, and assumed that the flux of 1741-038 was constant. We therefore conclude that (with a possible exception for OH 21.5+0.5, OH 31.0-0.2, and OH 37.1-0.8) no significant part of the flux was missed, or in other words all flux is confined to structures  $\lesssim 8''$ .

### III.3 Data analysis

#### a. Positions and synthesized beamsizes

For an uniformly expanding shell the strongest maser emission peaks come from the front and from the back sides (see appendix A). We thus expect the peaks to coincide spatially and to be unresolved. In table 2 the positions of the low velocity (front) and high velocity (back) peak are listed. They all coincide within one cell (our cellsize is  $0''.25$ ) except for OH 26.5+0.6, which has an offset of  $0''.25$  in  $\alpha$  and  $\delta$ , and for OH 32.8-0.3 where the high velocity peak shows two components, both displaced by  $\sim 0''.8$  with respect to the position of the low velocity peak.

Table 2

Name	$\alpha(1950.0)$	$\Delta\alpha$	$\delta(1950.0)$	$\Delta\delta$	Remarks
OH	h m s	s	o ' "	"	"
18.5+1.4	18 16 47.370	.01	-12 09 27.30	.13	
20.7+0.1	18 25 44.320	.01	-10 52 50.85	.13	
21.5+0.5	18 25 45.490	.01	-10 00 12.40	.13	
25.1-0.3	18 35 33.360	.01	-07 12 34.65	.13	
26.5+0.6	18 34 52.470	.01	-05 26 37.15	.13	front
	.486	.01	36.90	.13	back
28.5-0.0	18 40 47.450	.01	-03 58 57.60	.13	
30.1-0.7	18 46 34.877	.01	-02 53 54.60	.13	
31.0-0.2	18 46 07.150	.01	-01 51 56.50	.13	
32.0-0.5	18 48 51.210	.01	-01 07 29.30	.13	
32.8-0.3	18 49 48.167	.02	-00 17 52.8	.75	front
	.150	.01	53.2	.13	back; shows structure
37.1-0.8	18 59 36.220	.01	+03 15 53.3	.13	

The tabulated positions are in excellent agreement with previously determined values (cf. Bowers *et al.*, 1981; Baud, 1981). We shall use the listed coordinates for the stellar positions, taking the mean of 'front' and 'back' for OH 26.5+0.6 and the 'front' position for OH 32.8-0.3 (indicated by a cross in figures 1-11).

The two strongest peaks of every star have a Gaussian brightness distribution (the high velocity peak of OH 32.8-0.3 excluded) that is exactly

Contour values in figures 1-11 are 5, 10, ..., 95% of the strongest peak in each map.

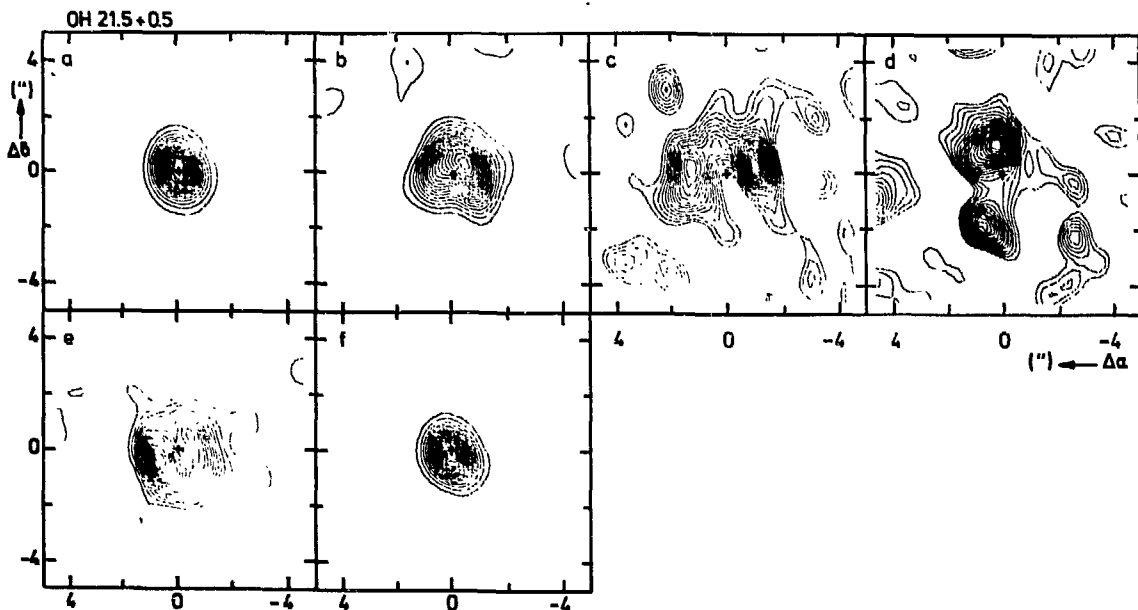
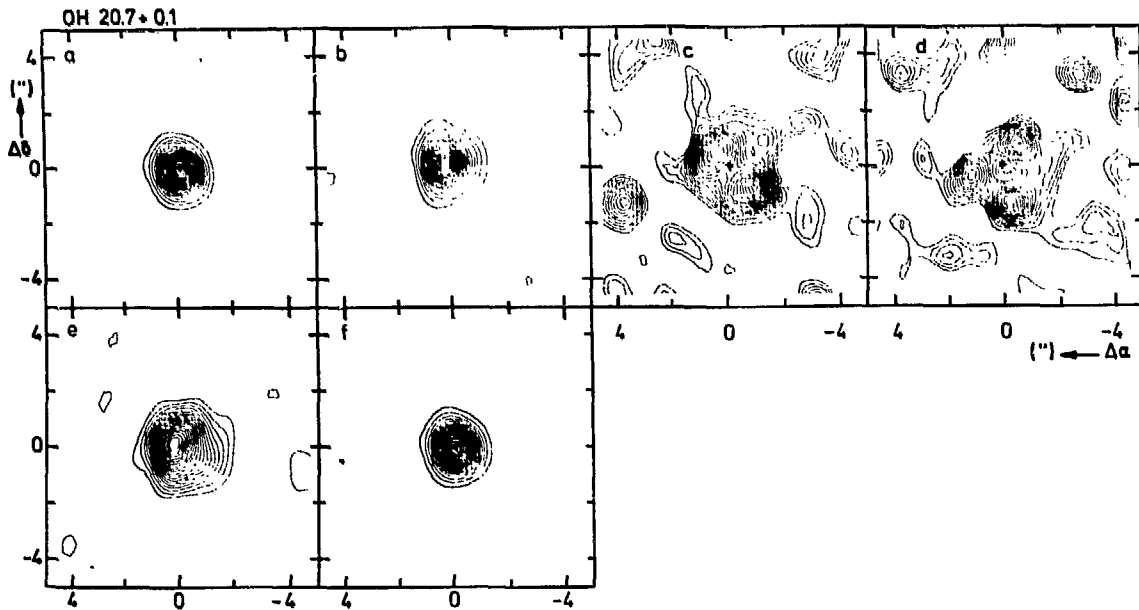
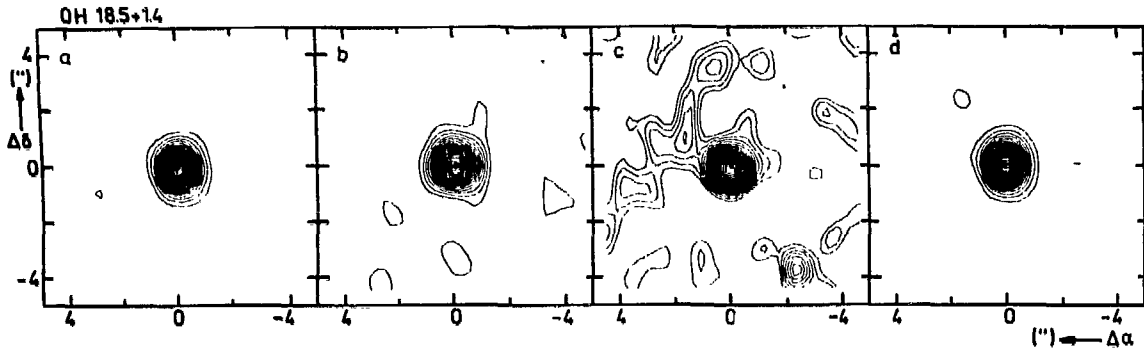


Figure 1. OH 18.5+1.4  $v_{\text{LSR}}=+176.17 \text{ km s}^{-1}$   $v_e=10.85 \text{ km s}^{-1}$  Total 30 maps

map	velocity ( $\text{km s}^{-1}$ )	strongest peak (Jy)
a	10.73	4.1
b	6.72	1.2
c	-4.19	0.3
d	-9.93	6.0

Figure 2. OH 20.7+0.1  $v_{\text{LSR}}=+136.55 \text{ km s}^{-1}$   $v_e=18.21 \text{ km s}^{-1}$  Total 20 maps

map	velocity ( $\text{km s}^{-1}$ )	strongest peak (Jy)
a	18.31	4.2
b	16.02	2.4
c*	5.40	0.06
d*	-6.08	0.5
e	-14.98	0.9
f	-18.43	9.2

\*c and d are the mean over  $10.9 \text{ km s}^{-1}$

Figure 3. OH 21.5+0.5  $v_{\text{LSR}}=+115.77 \text{ km s}^{-1}$   $v_e=18.76 \text{ km s}^{-1}$  Total 21 maps

map	velocity ( $\text{km s}^{-1}$ )	strongest peak (Jy)
a	18.60	8.2
b	16.88	0.9
c*	7.69	0.07
d*	-4.94	0.06
e*	-13.55	0.47
f	-18.71	7.1

\*c is the mean over  $14.9 \text{ km s}^{-1}$

d is the mean over  $9.2 \text{ km s}^{-1}$

e is the mean over  $2.3 \text{ km s}^{-1}$

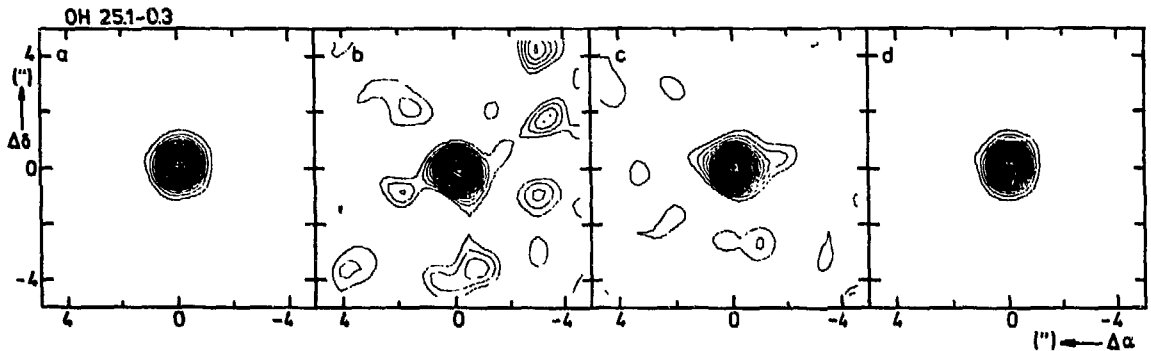


Figure 4. OH 25.1-0.3  $v_{\text{LSR}}=+142.88 \text{ km s}^{-1}$   $v_e=12.14 \text{ km s}^{-1}$  Total 16 maps

map	velocity ( $\text{km s}^{-1}$ )	strongest peak (Jy)
a	12.23	4.4
b*	7.63	0.21
c*	-9.30	0.40
d	-12.45	5.2

\*b is the mean over  $2.3 \text{ km s}^{-1}$

c is the mean over  $1.7 \text{ km s}^{-1}$

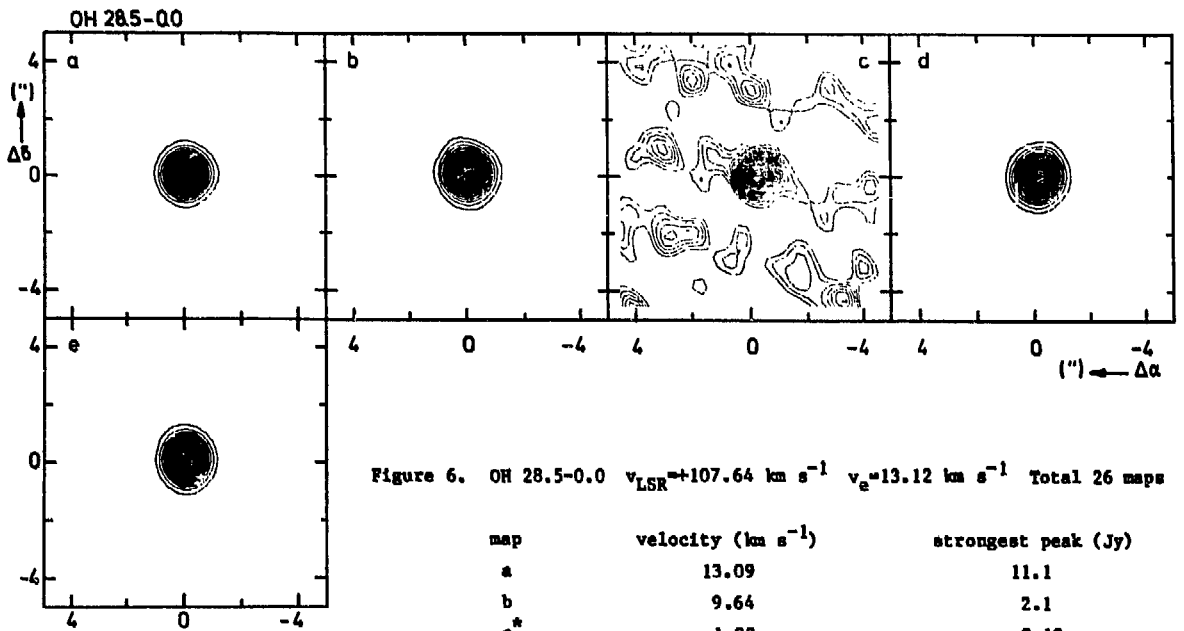
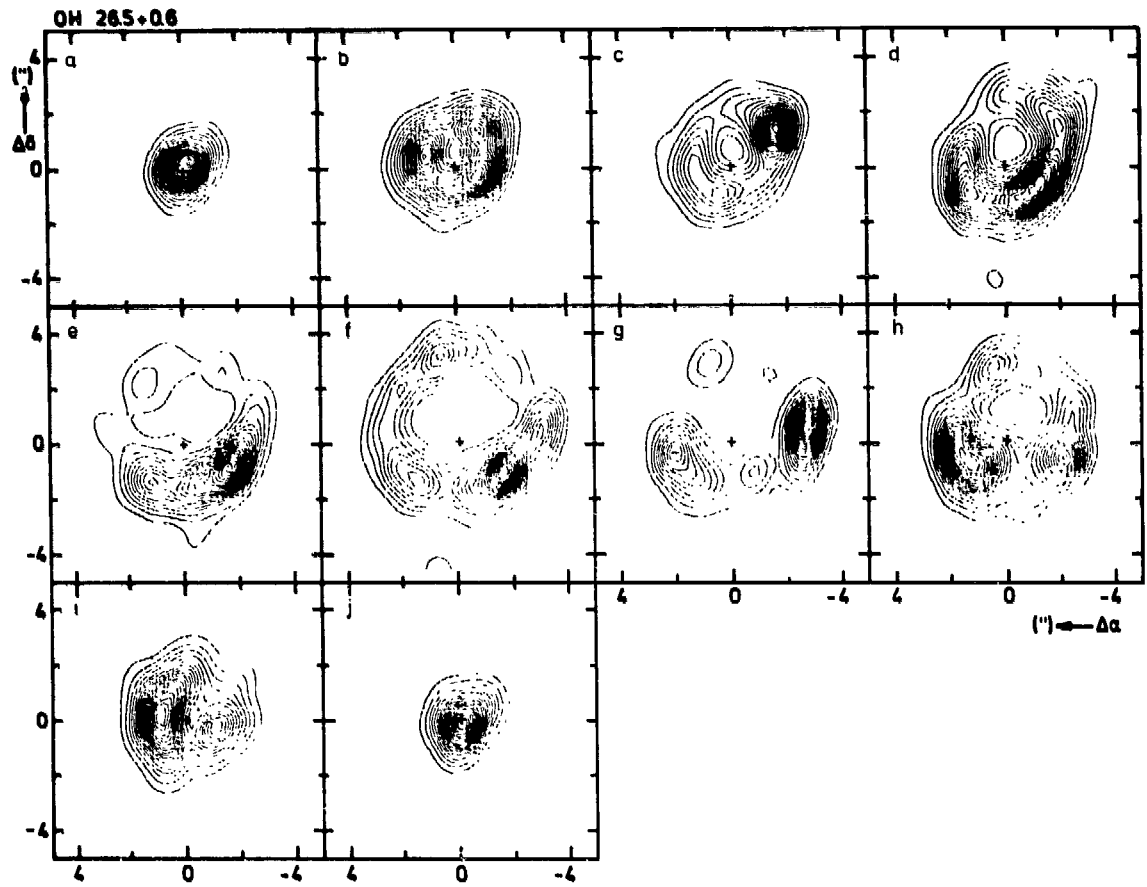


Figure 6. OH 285-0.0  $v_{\text{LSR}} = +107.64 \text{ km s}^{-1}$   $v_e = 13.12 \text{ km s}^{-1}$  Total 26 maps

map	velocity ( $\text{km s}^{-1}$ )	strongest peak (Jy)
a	13.09	11.1
b	9.64	2.1
c*	1.03	0.10
d	-8.73	1.9
e	-12.74	7.2

\*c is the mean over  $11.5 \text{ km s}^{-1}$

← Figure 5. OH 26.5+0.6  $v_{LSR}=+26.86 \text{ km s}^{-1}$   $v_e=14.07 \text{ km s}^{-1}$  Total 58 maps

map	velocity ( $\text{km s}^{-1}$ )	strongest peak (Jy)
a	14.52	263
b	12.23	15.4
c	9.93	14.3
d	7.63	2.9
e*	3.33	1.37
f*	-2.41	1.01
g	-7.29	6.2
h	-9.59	5.6
i	-11.88	13.4
j	-14.18	104

\*e and f are the mean over  $5.2 \text{ km s}^{-1}$  (only for display purposes)

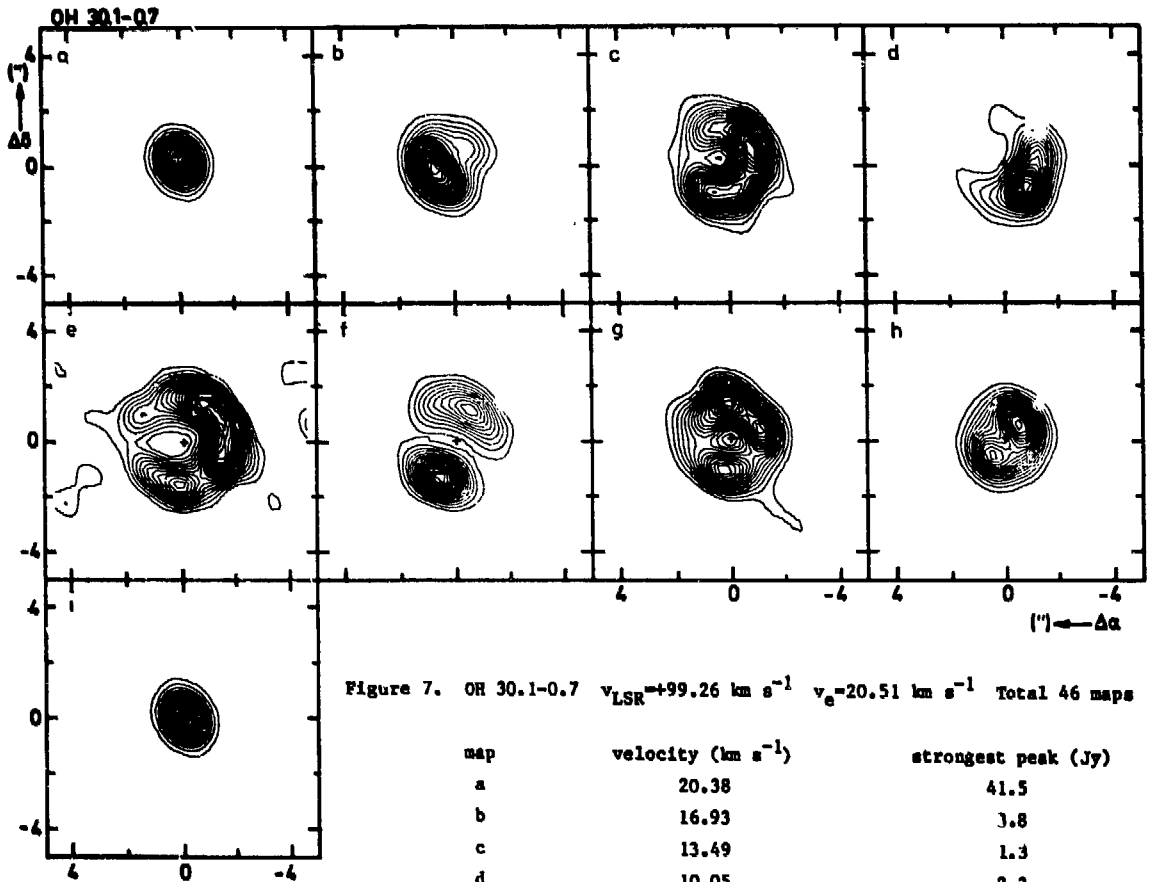
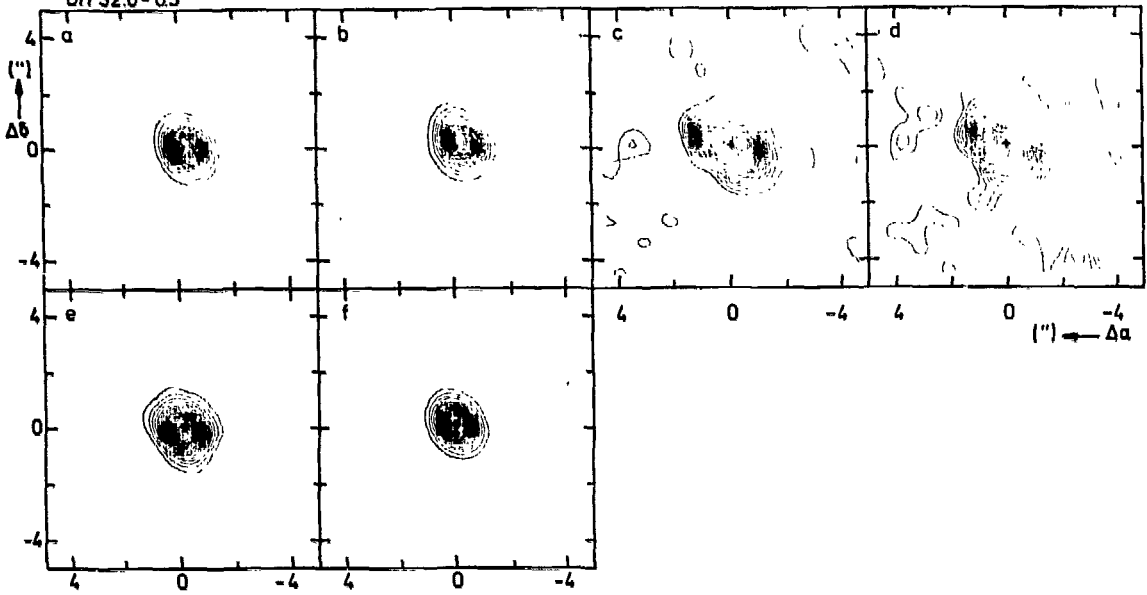


Figure 7. OH 30.1-0.7  $v_{LSR}=+99.26 \text{ km s}^{-1}$   $v_e=20.51 \text{ km s}^{-1}$  Total 46 maps

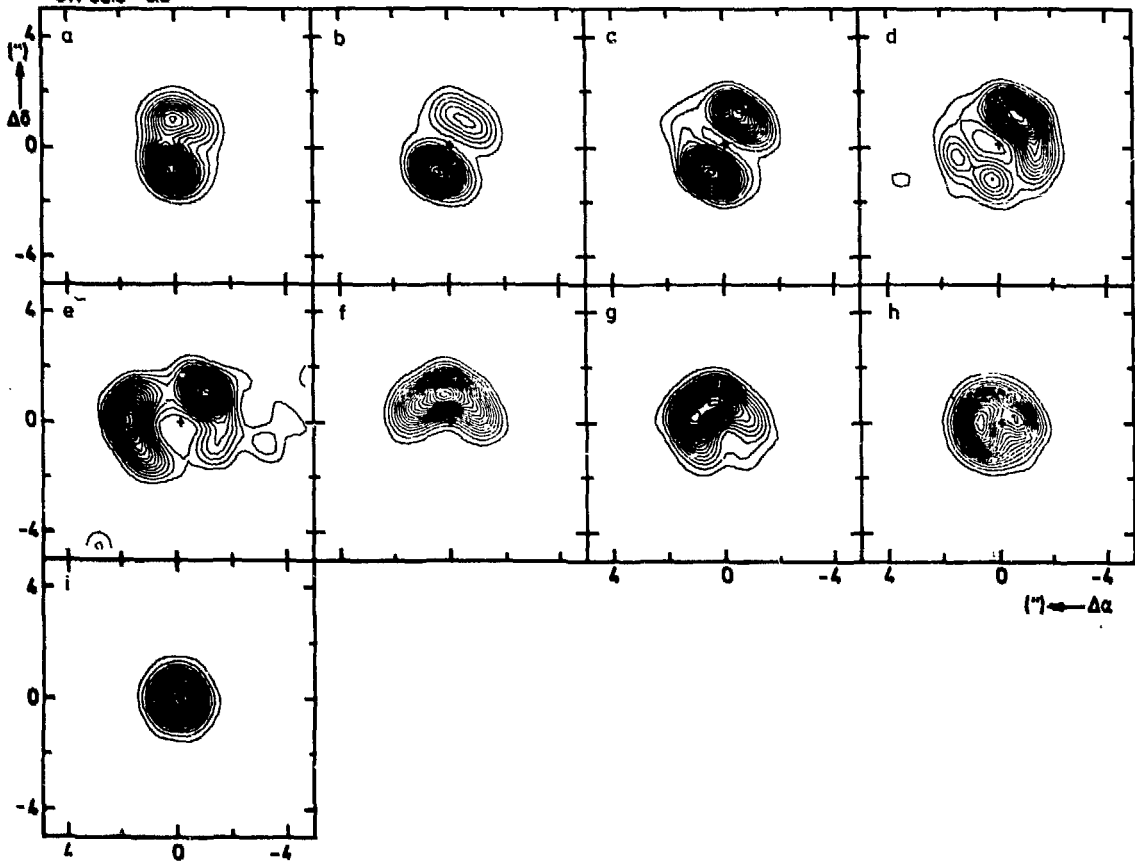
map	velocity ( $\text{km s}^{-1}$ )	strongest peak (Jy)
a	20.38	41.5
b	16.93	3.8
c	13.49	1.3
d	10.05	2.3
e*	0.57	0.20
f	-10.62	1.1
g	-13.49	1.8
h	-16.93	4.3
i	-20.95	40.7

\*e is the mean over  $12.1 \text{ km s}^{-1}$

OH 32.0-05



OH 32.8-03



← Figure 9. OH 32.0-0.5  $v_{LSR} = +76.04 \text{ km s}^{-1}$   $v_e = 20.58 \text{ km s}^{-1}$  Total 28 maps

map	velocity ( $\text{km s}^{-1}$ )	strongest peak (Jy)
a	20.09	6.8
b	18.37	2.8
c*	7.46	0.12
d*	-5.45	0.12
e	-15.50	1.8
f	-20.66	9.6

\*c is the mean over  $16.1 \text{ km s}^{-1}$   
 d is the mean over  $8.6 \text{ km s}^{-1}$

↙ Figure 10. OH 32.8-0.3  $v_{LSR} = +60.75 \text{ km s}^{-1}$   $v_e = 16.38 \text{ km s}^{-1}$  Total 32 maps

map	velocity ( $\text{km s}^{-1}$ )	strongest peak (Jy)
a	15.15	5.7
b	14.01	4.7
c	12.86	1.8
d	11.71	1.5
e*	0.80	0.22
f	-9.53	2.1
g	-11.82	2.3
h	-13.55	3.9
i	-15.27	14.0

\*e is the mean over  $17.2 \text{ km s}^{-1}$

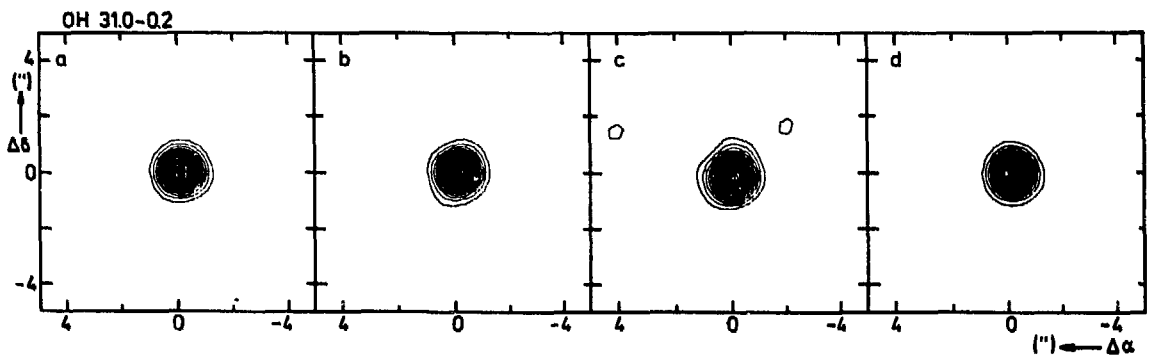


Figure 8. OH 31.0-0.2  $v_{LSR} = +125.98 \text{ km s}^{-1}$   $v_e = 14.27 \text{ km s}^{-1}$  Total 22 maps

map	velocity ( $\text{km s}^{-1}$ )	strongest peak (Jy)
a	14.35	5.9
b	11.48	2.8
c	-11.48	1.2
d	-14.35	4.1

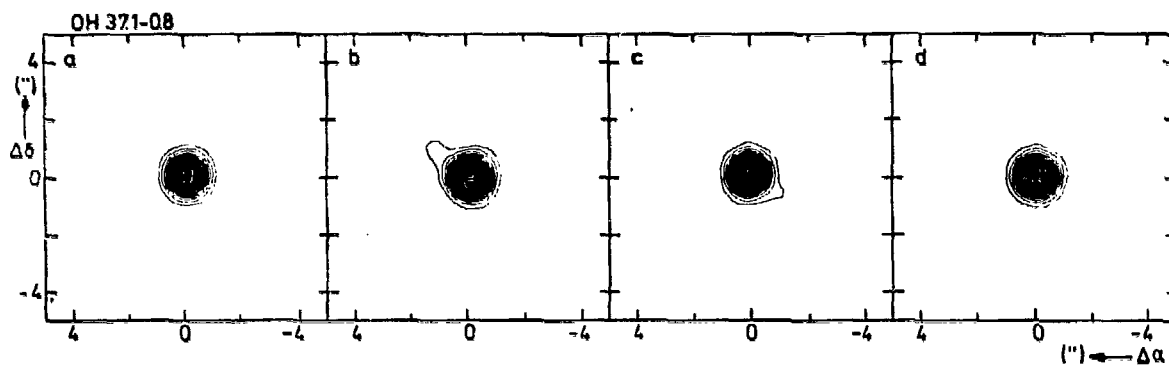


Figure 11. OH 37.1-0.8  $v_{\text{LSR}} = +88.48 \text{ km s}^{-1}$   $v_e = 13.59 \text{ km s}^{-1}$  Total 22 maps

map	velocity ( $\text{km s}^{-1}$ )	strongest peak (Jy)
a	13.26	13.6
b	9.24	1.5
c*	-8.27	1.3
d	-12.00	10.2

\*c is the mean over  $1.1 \text{ km s}^{-1}$

the theoretical synthesized beam profile (from the U-V coverage) but broadened by  $\sim 10\%$ . There are several reasons to assume that this broadening is not due to resolution of the peaks. In the first place we noted an increasing broadening with increasing galactic longitude, i.e. an increasing distance to our calibrator 1741-038 (the only calibrator usable in this region of the sky). This effect disappeared for the other peak when we used a self calibration procedure, forcing the phase of one strong feature to zero. For our final maps we employed self calibration only for sources with  $\lambda > 30^\circ$ . In the second place we were troubled by some phase instabilities at dawn. We rejected a number of measurements around that time, but the remaining, lesser phase jumps might well explain the slight broadening with respect to the theoretical beam still present. In our further analysis we shall assume that

the emission from the 'front' and 'back' sides of each star, having almost exactly the same width, are unresolved and use these as a measure of the synthesized beam for deconvolution.

b. Shell sizes

For an estimate of the overall dimension of the envelopes only, it is sufficient to measure the extent at  $v = 0$ , the stellar velocity (see figure 12). We will, however, also analyse maps at other velocities to obtain a more accurate determination of the geometry of the shells.

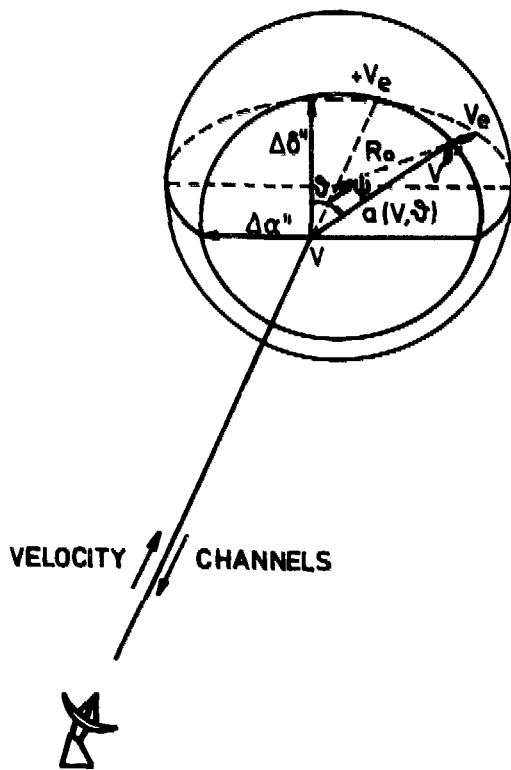


Figure 12. Model for the geometry of a thin OH shell. The small circle represents the locus of a channel map at a velocity between the expansion velocity ( $v_e$ ) and the stellar velocity ( $v_*$ ,  $v=0$ ).

For example, this allows us to find the deviations from spherical symmetry: such deviations are important to know because we want to determine distances by combining the phase lag radii (depth information) and the diameters in the plane of the sky, thus needing some knowledge about the degree of symmetry. Finally, we shall be able to discuss usefully the thickness of and the densities in the OH shells.

Assuming a simple geometry (figure 12) we may write

$$v(\psi) = -v_e \cos \psi \quad (1)$$

where  $v(\psi)$  is the velocity with respect to the stellar velocity,  $v_*$  (note that  $v(\psi) < 0$  for  $-\frac{\pi}{2} < \psi < \frac{\pi}{2}$ ), and  $v_e$  is the expansion velocity (see chapter II, tables 2 and 4). Denoting the extent of the shell perpendicular to the line of sight by  $a(v, \theta)$  for the different channels ( $=v$ ) and position angles ( $=\theta$ ) we find (figures 12 and 13)

$$a(v, \theta) = R_g(\theta) \left\{ 1 - \left( \frac{v(\psi)}{v_e} \right)^2 \right\}^{\frac{1}{2}} \quad (2)$$

with  $R_g(\theta)$  the radius of the shell (in arcsec), which is independent of  $\theta$  in the case of spherical symmetry.

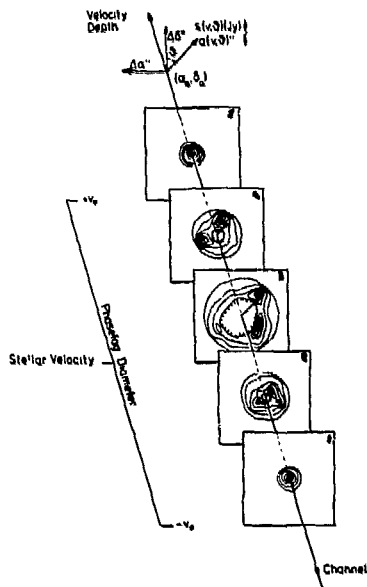


Figure 13. Schematic representation for a thin shell of the location and the morphology for channel maps at various velocities, or depths, along the line of sight.

We measured  $a(v, \theta)$  (in arcsec) by determining the position of maximum emission with respect to the stellar position

$(\alpha_0, \delta_0)$ ; see table 1) for crosscuts in the direction  $\theta - \pi \rightarrow \theta$  through each of our channel maps (figure 13). We did so for  $\theta = \pm k 20^\circ$  ( $k = 0, 1, \dots, 8$ ). For  $v(\psi) = 0$  we see a ring structure, decreasing to a point as

$v(\psi) \rightarrow \pm v_e$  (figure 14). For velocities close to the expansion velocity the two maxima in the crosscut are blended due to beam smearing (e.g. OH 26.5+0.6 for  $v_e = 2.5 \text{ km s}^{-1} < v(\psi) < v_e = 14.1 \text{ km s}^{-1}$ ; I.e. figure 5 between a and b, and between i and j, or in figure 14 between 1 and 2). At these velocities we used for  $a(v, \theta)$  half of the full width at half maximum, deconvolved with the measured synthesized beam. If  $a(v, |\theta|) < 0.125$  we assumed  $a(v, \theta) = a(v, \theta - \pi)$ , and otherwise we deleted  $a(v, \theta - \pi)$ . Putting in  $v(\psi)$ ,  $v_*$ , and  $v_e$ , that are known from the single-dish line profiles (chapter II), we solved equation (2) for  $R_g(\theta)$  using the method of least squares (figure 15). We could do this for the 6 sources in our sample that are resolved (figure 16). Note that they all

have a fairly high degree of symmetry.

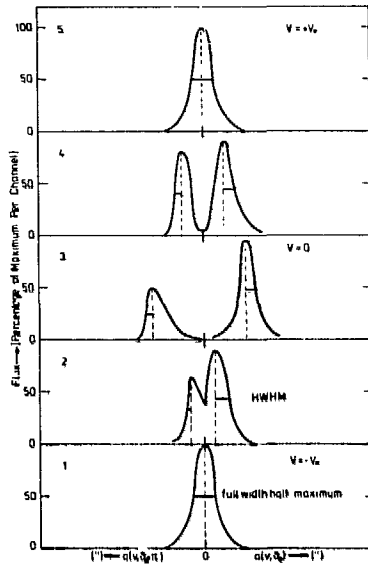


Figure 14. Example of the measured crosscuts for an arbitrarily chosen direction  $\theta$ . The numbers refer to the maps shown in figure 13.

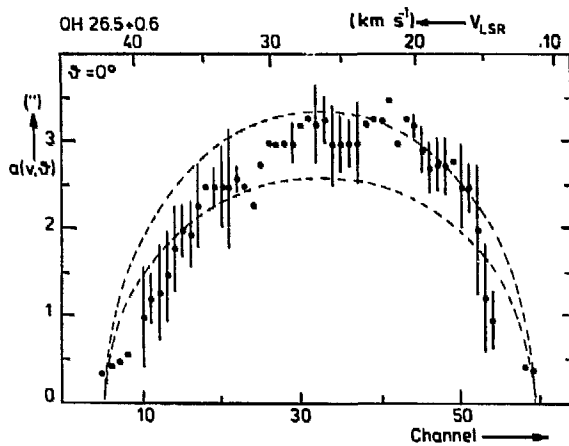


Figure 15. Example of  $a(v, \theta)$  as function of velocity for one cross direction  $\theta$ . The error bars are the full width at half maximum, deconvolved with the measured synthesized beam. They give an impression of the thickness of the shell. The dashed lines are curves of constant radius,  $R_g$ . They have been drawn at  $R_g(\theta) \pm$  m.e., the least squares solution to equation (2)  $\pm$  the standard deviation.

The five remaining objects (OH 18.5+1.4, OH 25.1-0.3, OH 28.5-0.0, OH 31.0-0.2, and OH 37.1-0.8) are virtually unresolved, i.e. they have an angular extent, only slightly broadened with respect to the theoretical beam, that is nearly the same at all velocities. However the position of the single maximum shifts somewhat with respect to  $\alpha_0, \delta_0$  (the stellar position) around  $v(\psi) = 0$ , where we expect the extent to be greatest (figure 17). Probably the density distribution in these shells is asymmetric, much more so than for the resolved sources (where we also see places in the envelopes with enhanced emission). To have at least an estimate of the shell diameter for

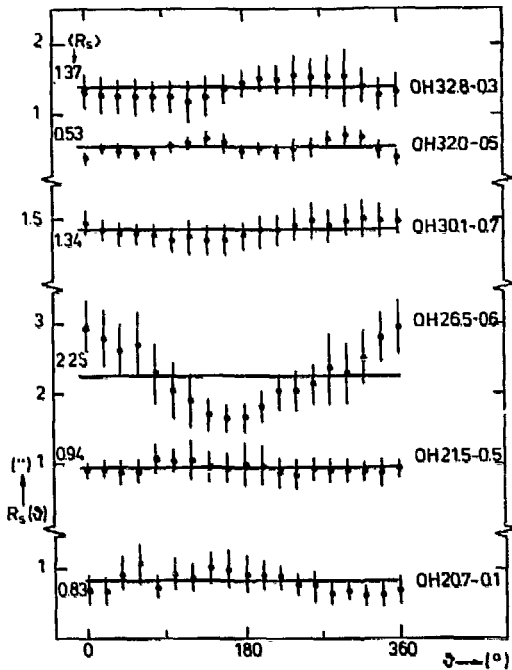


Figure 16. Radius of the OH shell as function of cross direction  $\theta$  for the resolved sources. The drawn lines are the mean radii. The error bars are the standard deviations (for individual measurements) of the measured  $a(v, \theta)$  with respect to  $R_s(\theta) [1 - (\frac{v}{v_s})^2]^{\frac{1}{2}}$ . They show the applicability of the model and are a measure for the thickness of the shells.

these unresolved stars, we measured the distance of maximum to the stellar position,  $b(v)$  (in arcsec), in each channel map. The position angle of the maximum changes abruptly from channel to channel, suggesting that sometimes we see one part, then another part of the shell. We determined a radius by a least squares fit to

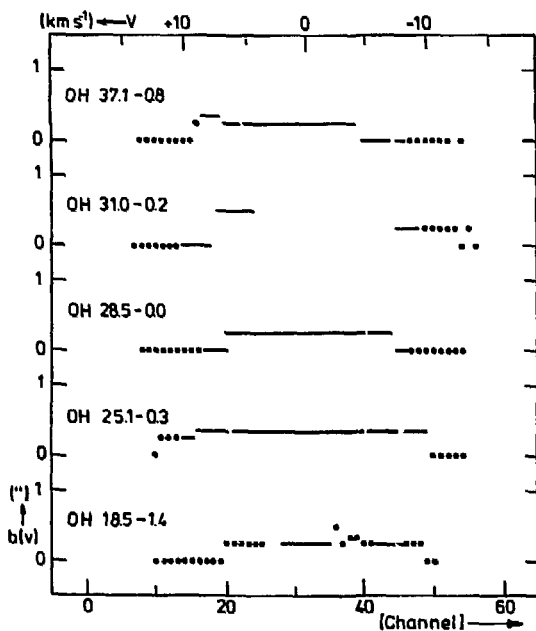


Figure 17. Displacement of the maximum in the brightness distribution as function of velocity (channel) for the unresolved sources. Drawn lines indicate that we took the average over a number of channels.

$$b(v) = \frac{R}{S} \left\{ 1 - \left( \frac{v(\psi)}{v_e} \right)^2 \right\}^{\frac{1}{2}} \quad (3)$$

We should bear in mind that the radii found in this way are presumably an underestimate of the true dimensions, because we only see the densest parts of the envelopes. A more detailed discussion will be given in the next section. It is clear, however, that quantities derived invoking equation (3) should be taken *cum grano salis*.

### c. Asymmetry and thickness of the OH shells

It is clear from inspection of the individual channel maps (figures 1-11), that the brightness distribution is not uniform and the angular extent not perfectly symmetric.\* We define

$$\Delta S(\theta) \equiv \log \left[ \sum_{\nu} S(\nu, \theta) \left\{ 1 - \left( \frac{\nu}{v_e} \right)^2 \right\} \left( \frac{v_e}{v_d} \right) \right] - \log \bar{S} \quad (4)$$

a parameter that describes the average deviation, at position angle  $\theta$ , from the brightness in a subshell. The measured peak fluxes  $\{S(\nu, \theta)\}$  in the crosscuts are corrected for the projection on the line of sight (appendix A). The summation is taken over those velocity maps only that contained a well defined ring structure (e.g. for OH 26.5+0.6 over a velocity range of 25  $\text{kms}^{-1}$ , deleting 2.5  $\text{kms}^{-1}$  on either side). The Doppler width,  $v_d$  is 0.58  $\text{kms}^{-1}$  for all sources (chapter II; equation 28), and

$$\bar{S} = \frac{1}{18} \sum_{k=1}^{18} \sum_{\nu} \left[ S(\nu, k, 20^\circ) \left\{ 1 - \left( \frac{\nu}{v_e} \right)^2 \right\} \left( \frac{v_e}{v_d} \right) \right] \quad (5)$$

By the integration over velocity the irregularities along the line of sight have been smoothed out. Similar to  $\Delta S(\theta)$  we define another parameter describing the deviations from the mean radius ( $\bar{R}_s$ )

$$\Delta R_s(\theta) \equiv \log \left[ \frac{R_s(\theta)}{\bar{R}_s} \right] \quad (6)$$

\*For OH 26.5+0.6, OH 30.1-0.7, and maybe OH 32.8-0.3 we might restore symmetry by changing the stellar position (figure 16). But for OH 26.5+0.6 this change should be 0".65, very unlikely to be the case in view of the coincidence of the 'front' and 'back' peaks.

where  $\bar{R}_s$  is the mean of  $R_s(\theta)$  (equation 2) over  $\theta$ . Plotting  $\Delta S(\theta)$  as function of  $\Delta R_s(\theta)$  we find (figure 18)

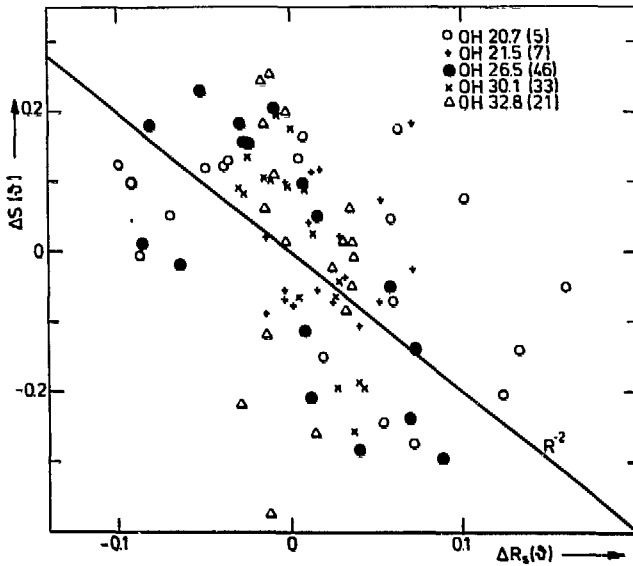


Figure 18. Deviation of the flux, corrected for projection effects, as function of the deviation in radius from their mean values, as measured for each cross direction  $\theta$ . Between parentheses are the number of channel maps that could be used for each star.

$$\Delta S(\theta) \propto \Delta R_s(\theta)^{-2} \quad (7)$$

This result is based primarily on the measurements of OH 26.5+0.6, because these show the largest deviations,  $\Delta S(\theta)$  and  $\Delta R_s$ . Equation (7) implies that the stronger, or excess emission, lies systematically closer to the star. We expect (see appendix A, equation 17) that for a given star

$$S_\nu(\nu) \sim f(\nu) n_{\text{OH}} R_{\text{pump}} \quad (8)$$

where  $n_{\text{OH}}$  is the OH-density,  $R_{\text{pump}}$  the net population transfer into the upper masing level and  $f(\nu)$  a function that describes the velocity dependence of the maser output. So one way to get brighter than average parts in the shell is 'crowding in velocity space', i.e. a local enhancement of  $f(\nu)$  because of a better velocity coherence from a larger part of the envelope than expected from the model with uniform expansion. But from the extremely steep outer edges in all OH-spectra we can deduce that turbulent, or streaming motions that can cause such a velocity crowding, are very small ( $\lesssim 0.2 \text{ km s}^{-1}$ ; see chapter II, equation 28). On the other hand we see coherent structures over much larger ranges in velocity, e.g. for OH 26.5+0.6 ( $\theta = 45^\circ$ ) from  $\nu=12.2$  to  $7.6 \text{ km s}^{-1}$ , (figure 5b to 5d). Therefore, velocity crowding as a mechanism to enhance the brightness locally can be excluded. The pump rate will be roughly

constant throughout the shell of one star, as it depends on the number of far infrared photons reemitted by the dust. And the far infrared radiation field is determined by a much larger volume than the local changes in OH brightness. The asymmetry in angular extent, not that in brightness distribution, can be explained also by assuming that the circumstellar shell is rotating slowly ( $v_{\text{rot}} \lesssim 1 \text{ km s}^{-1}$ ; see Norris *et al.*, 1982). But rotation would show up in the single-dish spectra as a slight broadening of the outer wings, which is not seen. Furthermore, the angular momentum lost by the star to a circumstellar envelope of  $\sim 2 M_{\odot}$  (see V, tables 7 and 8) is enormous. This objection is circumvented by Norris *et al.* by assuming the presence of a companion, which is at  $10^{15} - 10^{16}$  cm from the central star and has an orbital period of  $\gtrsim 100$  yr. Apart from the fact that most planetary nebulae, the end products of most OH/IR stars, are single objects (see e.g. Terzian, 1983) a number of problems arise: i) the velocity field and the density distribution are disturbed and a typical recovery time is  $R_{\text{OH}}/v_e \gtrsim 600$  yr; ii)  $\alpha$  Ceti, a well known double star, has no OH maser (Olnon *et al.*, 1980), generally attributed to the disturbing presence of the companion, because it does have a high mass loss rate, a SiO, and H<sub>2</sub>O maser; iii) the observed correlation between brightness and angular extent is hard to understand. The conclusion is that the brightness distribution reflects the density distribution of OH (see also Baud, 1981). Thus we can write equation (7) as

$$n_{\text{OH}}(R) \propto R^{-2} \quad (9)$$

which is a not totally unexpected result, because for a constant outflow velocity the mass density should drop  $\sim R^{-2}$ .

Next we compare the asymmetries as measured along the line of sight (in velocity) and perpendicular to it (in our VLA maps). Define

$$\delta S_{\text{H}} \equiv \log S_{\text{f}} - \frac{1}{2} \log (S_{\text{f}} \cdot S_{\text{b}}) = \frac{1}{2} \log (S_{\text{f}}/S_{\text{b}}) \quad (10)$$

where  $S_{\text{f}}$  and  $S_{\text{b}}$  are the flux densities of the front and back peak and

$S_{\text{H}} = (S_{\text{f}} \cdot S_{\text{b}})^{\frac{1}{2}}$  is their harmonic mean. This parameter is easily measured in the single-dish spectra.  $\delta S_{\text{H}}$  is compared with

$$\delta R_{\text{g}} = \log \left[ 1 + \frac{\overline{m.e(R_{\text{g}})}}{R_{\text{g}}(\theta)} \right] \quad (11)$$

which is nothing else than  $\overline{\Delta R_{\text{g}}(\theta)}$ . For the resolved sources roughly the same

effect as in equations (7) and (9) is found (figure 19). For the unresolved objects, however, the asymmetries in the plane of the sky,  $\delta R_g$ , seem much larger than expected from the ratio,  $\delta S_H$ , of the strongest peaks (see table 3b).

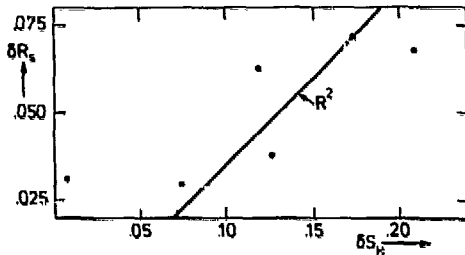


Figure 19. Plot of the parameter  $\delta R_g$ , a measure for the asymmetry in the plane of the sky, against  $\delta S_H$ , that describes the asymmetry of the single-dish line profile.

But in view of the poor determination of the shell radii for these stars, this conclusion needs to be supported by future observations using longer baselines (e.g. with MERLIN). Another way to probe the asymmetry along the line of sight is to look at  $\overline{\delta R_v}$ , the standard deviation with respect to  $R_g(\theta)$ , averaged over  $\theta$ . In other words we smoothed over the irregularities in the plane of the sky (equation 2; figure 15). Tables 3a and 3b show that  $\overline{\delta R_v}$  compares well with  $\delta R_g$  and  $\frac{1}{2}\delta S_H$ , although it is systematically larger. This is probably the case because it is a convolution of the thickness and the deviations from symmetry of the shell. Finally, the standard deviation,  $m.e(R_p)$ , in the determination of the 'phase lag' radius ( $R_p$ ; see chapter II, tables 4, and appendix C) also reflects the asymmetry along the line of sight. Define

$$\delta R_p \equiv \log \left[ 1 + \frac{m.e(R_p)}{R_p} \right] \quad (12)$$

which is for the resolved sources in very good agreement with  $\delta R_g$  (table 3a). Only for OH 30.1-0.7  $\delta R_p$  is substantially larger than all other asymmetry parameters; This is caused by one or two large phase lag deviations (see appendix C, figure 41). It is remarkable that the five unresolved sources, with only a small shift of the maximum in the brightness distribution, also have poorly defined phase lag radii. Except for OH 28.5-0.0 they have either (very) small amplitude variations, or they do not vary at all (OH 31.0-0.2 and OH 37.1-0.8 with  $\Delta m_r \lesssim 0.13$ ). And clearly the method of determining radii directly from light traveltimes stands or falls with (correlated) variations. When  $\delta R_p$  could be determined, it is in rough agreement with  $\delta R_g$  (table 3b).



OH shell after deconvolution by the (measured) synthesized beam. The values found (see table 3a:  $\overline{HWHM} \equiv \frac{1}{2} \overline{FWHM(v, \theta)}$ ), appear to increase with decreasing apparent radius. This effect is probably artificial, and hence the values of FWHM are only a uncertain indication of the shell thickness. Blending is causing this effect, although we tried to minimize its influence by measuring only the half width at the outside of the profiles and by computing the mean HWHM over the inner part of the velocity range. A second effect is that we added sometimes a number of channel maps around  $v = 0$ , thus slightly broadening the profiles, because we average over a (small) range in

$a(v, \theta)$ . Further, the values of FWHM are only marginally larger than the (measured) synthesized beam, so the deconvolution can introduce large errors. It seems that only for stars where we treated each channel separately, and with  $\overline{R_g(\theta)} > 1''$  the influences are minor. Then we find an upper limit for the thickness of the OH shells of  $\lesssim 0.2 \overline{R_g(\theta)}$ .

#### d. Distances

By combining the phase lag radius ( $R_o$ ), measured in cm, with the radius in the plane of the sky ( $R_g$ ), measured in arcsec, we can determine the distance to each individual star

$$D(\text{kpc}) = 0.6695 \frac{R_o (10^{16} \text{ cm})}{R_g (\text{arcsec})} \quad (13)$$

where  $R_g = \overline{R_g(\theta)}$ . As we have seen in the previous section, we can use the values of  $R_o$  and  $R_g$  directly, because to within our uncertainties ( $\sim 10\%$ ) the asymmetries along the line of sight and perpendicular to it are equal. The resulting distances are given in table 4, where some objects have been added with diameters known from literature (Norris *et al.*, 1982, and Baud, 1981). For our 5 unresolved sources the distances are given between parentheses, because the phase lag radii are very uncertain (two of them haven't a determination at all!) and the angular radius is probably underestimated. In the columns 2-7 some relevant quantities, as found in the Dwingeloo monitor program (chapter II; tables 2, 3 and 4), are repeated.  $S_H$  is the harmonic mean of the mean flux density from the two strongest, low- and high-velocity, peaks. For the resolved sources the tabulated shell radius ( $R_g$ ) is the mean over  $\theta$ . As a comparison to our calculated distances (D) the near and far kinematic distances are given (columns 12 and 13), based on the Schmidt mass model (Burton, 1974) and a distance to the galactic centre of  $D_o = 9.2 \text{ kpc}$

(see next section).

Table 4

Name	$v_{LSR}$ (km s <sup>-1</sup> )	$v_e$ (km s <sup>-1</sup> )	Log S <sub>H</sub> (Log Jy)	$\delta m_r$ (mag)	R <sub>16</sub> (10 <sup>16</sup> cm)	$\Delta R_{16}$ (cm)	R <sub>a</sub> (")	$\Delta R_a$ (")	D (kpc)	$\Delta D$ (kpc)	D <sub>kin</sub> (kpc)	
OH											near	far
18.5+1.4	+176.17	10.85	0.838	0.19	0.95:	3.64	0.255:	0.029 <u></u>	( 2.49:	9.54)	8.7	
20.7+0.1	+136.55	18.21	0.938	0.99	10.26	0.92	0.827	0.034	8.31	0.82	8.6	
21.5+0.5	+115.77	18.76	1.318	1.09	16.33	0.87	0.940	0.016	11.63	0.65	6.9	10.2
25.1-0.3	+142.88	12.14	0.861	0.21	0.87	0.63	0.362:	0.052 <u></u>	( 1.61	1.19)	8.3	
26.5+0.6	+ 26.86	14.07	2.440	1.13	3.29	0.26	2.245	0.098	0.98	0.09	2.1	14.4
28.5-0.0	+107.65	13.12	1.028	0.77	0.17	1.51	0.058:	0.024 <u></u>	( 1.96	1.35)	8.1	
30.1-0.7	+ 99.26	20.51	1.798	0.40	3.56	0.62	1.343	0.024	1.77	0.31	6.9	9.0
31.0-0.2	+125.98	14.27	0.811	0.13			0.259:	0.055 <u></u>			7.9	
32.0-0.5	+ 76.04	20.58	0.895	0.88	7.42	1.09	0.534	0.084	9.30	2.00	5.0	10.6
32.8-0.3	+ 60.75	16.38	1.345	1.24	16.46	0.33	1.369	0.030	8.05	0.24	4.0	11.4
37.1-0.8	+ 88.48	15.39	1.169	0.13			0.110:	0.032 <u></u>			6.9	7.8
39.7+1.5	+ 20.00	16.58	1.797	0.82	1.71	0.47	2.0 a)	0.5	0.57	0.21	1.2	12.9
104.9+2.4	- 25.62	14.91	1.634	0.66	4.37	0.42	1.44 <sup>b)</sup>	0.02	2.03	0.20	2.3	
127.9-0.0	- 54.97	10.98	1.717	1.47	12.86	0.72	1.53 <sup>b)</sup>	0.02	5.63	0.32	3.9	
IRC+10011	+ 8.96	17.91	1.521	1.15	2.81	0.05	4. c)	0.5:	0.47	0.06	0.5 <sup>d)</sup>	

a) From Diamond *et al.*, in preparation

: unresolved at all velocities

b) From Norris *et al.*, 1982

c) From Baud, 1981

d) From Hyland *et al.*, 1972

### e. Distance to the galactic centre

One of the goals of our program was a direct determination of the distance to the galactic centre. Therefore we selected sources with large radial velocities, that are expected to lie at their tangential points. But due to other restrictions (knowledge of position and time variability) some sources obey this criterion only marginally, or not at all. The velocity at the tangential point ( $v_T$ ) is

$$v_T = \sin \lambda \left[ \Theta(R) \frac{D}{R} - \Theta(D_\odot) \right] \quad (14)$$

where R is the galacto-centric distance,  $\Theta(R)$  the rotation velocity, and  $D_\odot$  the distance to the galactic centre. Denoting the uncertainty in the (geometric) distance by  $\Delta D$ , we define a weight function

$$w \propto \left( \frac{v_{LSR}}{v_T} \right)^2 \left( \frac{D}{\Delta D} \right) \quad (15)$$

where we took  $\frac{v_{LSR}}{v_T} = 1$ , when  $v_{LSR} > v_T$ ; in other words: the greater the distance ambiguity, the less we believe our sources to follow the galactic

rotation. The choice of these statistical weights is rather arbitrary, but this does not affect the result much. Taking in each case the kinematic distance that is closest to the value that we derived (taking the far distance for OH 21.5+0.5, OH 32.0-0.5, and OH 32.8-0.3), we find

$$\langle D - D_{\text{kin}} \rangle = \Sigma w^2 (D - D_{\text{kin}}) / \Sigma w^2 = 0.004 \text{ (kpc)} \quad (16)$$

$\langle D - D_{\text{kin}} \rangle$  is the (weighted) mean residual of the geometric distances,  $D$ , with respect to the kinematic distances,  $D_{\text{kin}}$  (that were calculated *assuming*  $D_{\odot} = 9.2$  kpc). And thus is found

$$D_{\odot} = 9.2 \pm 1.2 \text{ (kpc)} \quad (17)$$

This is certainly not a spectacular improvement over existing results (e.g. Oort and Plaut, 1975 who find  $D_{\odot} = 8.7 \pm 0.6$  kpc), but it shows that it is possible to determine  $D_{\odot}$  in a very direct manner. The only assumption is that a sample of OH/IR stars in the mean follows the galactic rotation. In view of the small number of stars no attempt was made to account for effects of the asymmetric drift. Notice that the uncertainty given in equation (17) is a real, straightforward error of  $D_{\odot}$ . Oort and Plaut (1975) too give an internal error, but their value of  $D_{\odot}$  is also depending on many stepping stones on the way to the absolute mean magnitudes of RR Lyrae variables.

#### III.4 Conclusions

For the six sources in our sample that were resolved ( $R_g > 0.5''$ ) we could determine distances with an accuracy to  $\sim 10\%$ . Except for OH 26.5+0.6, that lies relatively nearby, they all have large expansion velocities ( $v_e > 15 \text{ km s}^{-1}$ ). Their mean distance from the sun is 7.8 kpc. The OH shells are fairly symmetric and the thickness is less than 20% of the radius. From the inhomogeneities in the brightness distribution we could deduce that the density falls off as  $r^{-2}$ .

The five unresolved sources all have small expansion velocities ( $v_e < 15 \text{ km s}^{-1}$ ) and only one, OH 28.5-0.0, shows appreciable time variations. The angular extents not only are very small, but they seem also to be rather asymmetric. Hence no reliable distances could be found for these sources.

Acknowledgement:

The National Radio Astronomy Observatory is operated by Associated Universities, Inc., under contract with the National Science Foundation.

Literature cited in chapter III

- Baud, B.: 1981, *Astroph. J. Lett.* 250, L79
- Benson, J.M., Mutel, R.L.: 1979, *Astroph. J.* 233, 119
- Booth, R.S., Kus, A.J., Norris, R.P., Porter, N.D.: 1981, *Nature* 290, 382
- Bowers, P.F., Johnston, K.J., Spencer, J.H.: 1981, *Nature* 291, 382
- Bowers, P.F., Reid, M.J., Johnston, K.J., Spencer, J.H., Moran, J.M.: 1980, *Astroph. J.* 242, 1088
- Burton, W.B.: 1974, in *Galactic and Extra Galactic Astronomy*, ed. G.L. Verschuur, K.J. Kellerman, pp. 82-117
- Hyland, A.R., Becklin, E.E., Frogel, J.A., Neugebauer, G.: 1972, *Astron. Astroph.* 16, 204
- Norris, R.P., Diamond, P.J., Booth, R.S.: 1982, preprint
- Olnon, F.M., Winnberg, A., Matthews, H.E., Schultz, G.V.: 1980, *Astron. Astroph. Suppl.* 42, 119
- Oort, J.H., Plaut, L.: 1975, *Astron. Astroph.* 41, 71
- Reid, M.J., Muhleman, D.O., Moran, J.M., Johnston, K.J., Schwartz, P.R.: 1977, *Astroph. J.* 214, 60
- Terzian, Y.: 1983, in *Planetary Nebulae*, Ed. D.R. Flower, Reidel, pp 487-499
- Thompson, A.R., Clark, B.G., Wade, C.M., Napier, P.J.: 1980, *Astrophys. J. Suppl.* 44, 151

## IV. IR observations<sup>1)</sup>

### IV.1 Introduction

For a large number of OH/IR stars we have an extensive data base of radio observations that contains information about the variability of the stars and the sizes of the OH shells (see chapter II). For a smaller set of stars, we also possess knowledge about the brightness distribution, the structure, and the density of the OH envelope (see chapter III). By the combination of 'phase lag' radii (derived from the light travel times between the front and the back sides of the shell) with the angular extents (measured in VLA maps) we could determine in a very direct manner distances to an accuracy of  $\sim 10\%$ . Measurements of the apparent bolometric magnitudes thus yield good absolute luminosities for our limited sample of OH/IR stars.

The spectral energy distribution of OH/IR stars peaks in the near infrared, typically at wavelengths between  $2 \mu\text{m}$  and  $10 \mu\text{m}$ . A considerable fraction of the energy is radiated at longer wavelengths ( $\lambda > 10 \mu\text{m}$ ). Therefore, observations out to at least  $\lambda = 20 \mu\text{m}$  are required to obtain the luminosities of these stars. Unfortunately, longward of  $20 \mu\text{m}$  ground based observations are (almost) impossible. We used the United Kingdom Infrared Telescope (UKIRT) to obtain broad band photometry for a number of OH/IR stars in eight bands from  $\lambda=3.8 \mu\text{m}$  to  $20 \mu\text{m}$ . We had good positions for all objects, mostly from VLA measurements; a considerable advantage as serious confusion problems can arise, especially in the galactic plane around the crowded regions at  $l = 30^\circ$  (see Jones *et al.*, 1982).

### IV.2 Observations and reduction

Data were taken with the 3.8m United Kingdom Infrared Telescope on Mauna Kea, Hawaii (UKIRT) on June 25-28, 1982 to observe some 25 OH/IR stars. Another program, in which OH/IR stars at the galactic centre were measured, was interwoven with ours (involving the same observers). We did broad band photometry at the f/35 focus, using a Ge:Ga bolometer with a 7"5

<sup>1)</sup> Proposed and obtained in collaboration with I. Gatley, H.J. Habing, R. Isaacman, and A. Sargent

aperture. Sky subtraction was accomplished by chopping 30" in declination. The central wavelengths and the bandwidths of the filters are listed in table 1, together with the conversion factors to Jy ( $10^{-26} \text{ Wm}^{-2}\text{Hz}^{-1}$ ) for a  $0^m.0$  star (see Beckwith *et al.*, 1976; *cf.* Johnson, 1966, or Wamsteker, 1981).

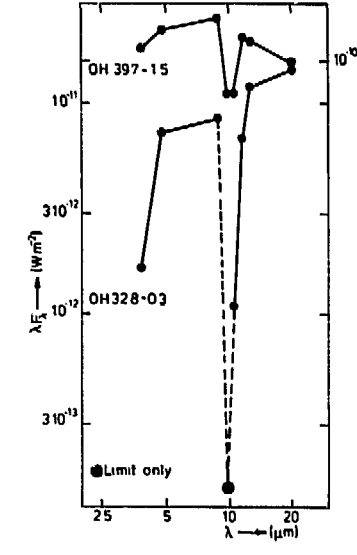
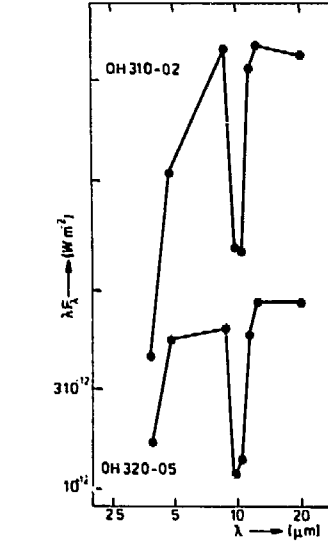
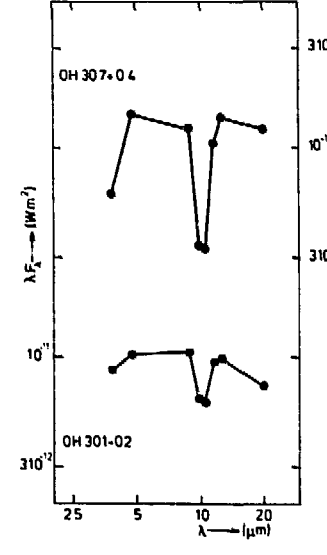
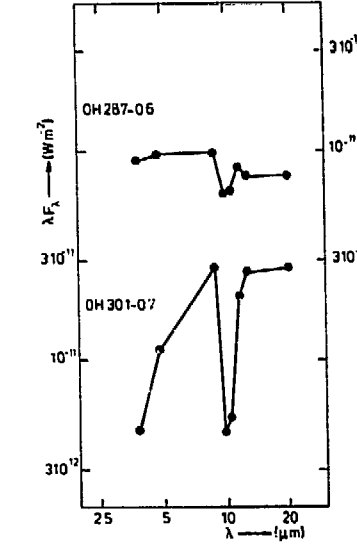
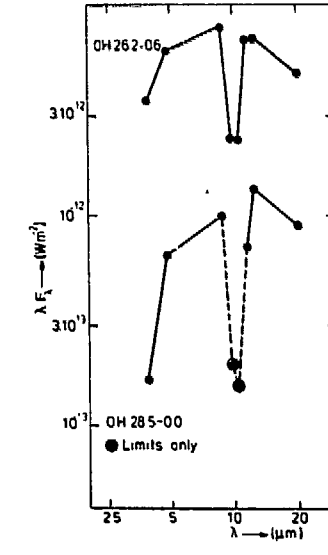
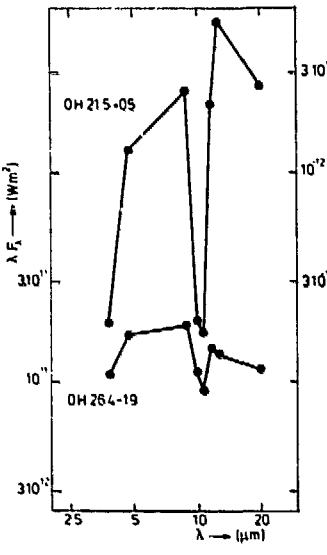
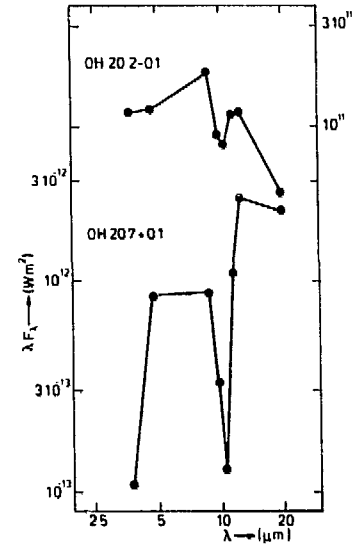
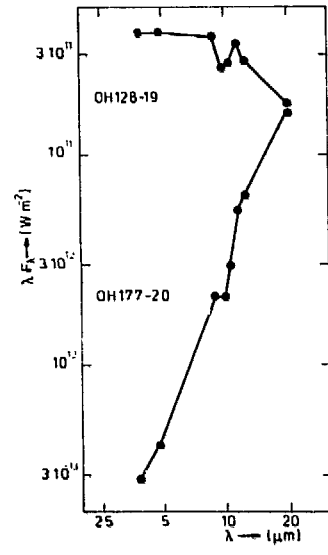
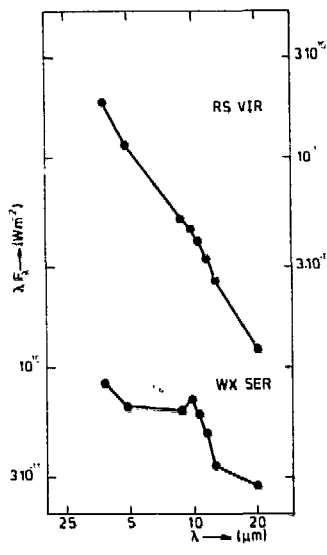
Table 1.

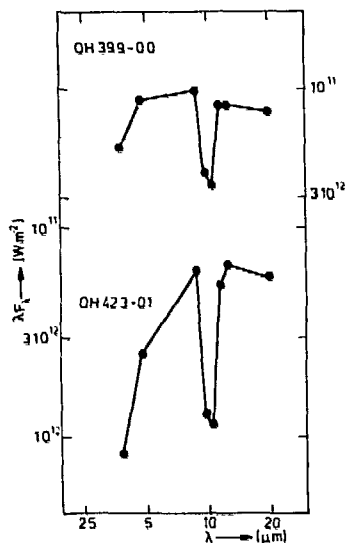
	Band	$\lambda$ ( $\mu\text{m}$ )	$\Delta\lambda$ ( $\mu\text{m}$ )	$F_{\nu}$ Jy
Bolometer	L'	3.82	0.65	238
	A	4.78	0.60	153
		8.7	1.2	50
		9.7	1.0	40
	N	10.3	1.25	34
	11.6	1.17	28	
	12.5	1.25	24	
	Q	20.0	6.0	10

The integration times for each star ranged from 24 to 160 seconds per band. For calibration standards we used  $\alpha$  Sco,  $\alpha$  Boo,  $\beta$  Peg, and occasionally some other bright stars (see appendix E).

### IV.3 Results

The energy distributions are displayed in figures 1-10, and the observed fluxes in each band are given in appendix E. Note the large difference between the two Mira variables (WX Ser and RS Vir), where we see the 9.7  $\mu\text{m}$  feature in emission, and the OH/IR stars that have, sometimes very deep, absorption at 9.7  $\mu\text{m}$ . The very unusual spectrum of OH 17.7-2.0, for which we had a very good position, was confirmed recently by a measurement of Engels at ESO (private communication). Although it is unique in our sample, preliminary IRAS data show that more similar cases of such red energy distributions exist (Habing, secret private communication). The numerical results are given in table 2, where in column 1 the names are listed. Column 2 contains information about the positions. The VLA positions (references b-d) are very accurate ( $\Delta\alpha \lesssim 1''$ ), the others less so ( $\Delta\alpha \lesssim 5''$ ). In columns 3 and 4 the radio periods and the phases (see chapter II, table 3) are given. The distances, their uncertainties, and a reference to the manner of their determination are listed in columns 5 to 7. The geometric distances (2), derived directly from the comparison of the 'phase lag' radii with the angular extents (see chapter III, table 3), are very good (10-20%). The distances marked by (3) have been found from a relation between the absolute OH luminosity and the OH radius (see chapter





Figures 1-10 Spectra of 1612 MHz OH masers observed with UKIRT. If two scales are given, the scale on the right refers to the upper spectrum.

V, section 3c). They are less certain ( $\sim 30\%$ , depending on the accuracy of the phase lag measurement). When the phase lag was poorly determined, we took the harmonic mean of the near kinematic distance and the distance derived as just described. In these cases the errors might be considerable, and no uncertainties are tabulated. For the two Mira variables we took the mean of the distances from Robertson and Feast *et al.* (1981, based on a period-luminosity relation), from Rieu *et al.* (1979, based on  $m_v$  at maximum), and from a method of our own (based on an absolute K magnitude of  $2.1^m$ ; see chapter V, section 5.a1). For RS Vir the three different methods yield quite similar distances; for WX Ser, however, there is a large discrepancy ( $\sim 1$  kpc). The luminosities were determined by integrating the energy distribution from  $3.8 \mu\text{m}$  to  $20 \mu\text{m}$ , and allowing for a 25% correction for the flux emitted at wavelengths longward of  $20 \mu\text{m}$ . This correction is in accord with the 20% used by Werner *et al.* (1980) for the flux at  $\lambda > 25 \mu\text{m}$ . The high confidence sources (geometric distances) are underlined (columns 8 and 9).  $T_c$  (column 10) is the colour temperature between  $\lambda = 3.8 \mu\text{m}$  and  $\lambda = 12.5 \mu\text{m}$ .  $W_{9.7}$  is a measure for the relative depth (emission for WX Ser and RS Vir!) of the silicate feature (column 11). It is defined as

$$W_{9.7} \equiv \Delta(f_\lambda \Delta\lambda) / S_{\text{IR}}(\text{obs}) \quad (1)$$

expressed in arbitrary units. Here  $S_{\text{IR}}(\text{obs})$  is the total flux received at

the earth, corrected for the missing part at  $\lambda > 20 \mu\text{m}$ .  $\Delta(f_{\lambda}\Delta\lambda)$  is the total flux absorbed in the  $9.7 \mu\text{m}$  feature. Simultaneously with the UKIRT observations the OH fluxes were determined with the Dwingeloo Radio Telescope. The absolute integrated flux density at  $\lambda = 18 \text{ cm}$  can be found in column 12.

Table 2.

Name	$P_r$ (days)	$\phi$	D (kpc)	$\Delta D$ (kpc)	$L_{\text{IR}}$ ( $10^{24}L_{\odot}$ )	$\Delta L$	$T_c$ (K)	$W_{9.7}$	$L_{\text{int}}^{\text{(OH)}}$ ( $10^{-22}\text{Wm}^{-2}\text{kpc}^2$ )	Remarks		
(1)	(2)	(3)	(4)	(5)	(6)	(7)	(8)	(9)	(10)	(11)	(12)	(13)
WX Ser	(a)	443	0.85	1.20	0.55	(1)	0.49	0.32	620	-7.6	7.45	Emission at $9.7 \mu\text{m}$
RS Vir	(a)	364	0.16	0.66	0.05	(1)	0.19	0.02	900	-1.2	3.29	
OH 12.8-1.9	(g)	812	0.29	1.69	0.5	(3)	0.59	0.18	580	4.8	86.4	Slightly variable
OH 17.7-2.0	(d)	890:	0.06:	7.17		(4)	0.26		280	3.0	2700	
OH 20.2-0.1	(e)	857	0.96	2.68		(4)	0.78		510	6.5	114	
OH 20.7+0.1	(b)	1130	0.10	8.31	0.82	(2)	0.55	0.08	380	10.8	2240	
OH 21.5+0.5	(b)	1975	0.61	11.63	0.65	(2)	3.42	0.27	360	13.8	4670	
OH 26.2-0.6	(e)	1181	0.50	1.48		(4)	0.088		470	12.5	36.1	
OH 26.4-1.9	(e)	652	0.75	1.54		(4)	0.23		540	6.3	48.6	
OH 28.5-0.0	(b)	559	0.32	2.45		(4)	0.033		420	>15.7	159	
OH 28.7-0.6	(e)	627	0.60	2.40		(4)	0.31		550	5.4	82.7	
OH 30.1-0.7	(b)	2060	0.91	1.77	0.31	(2)	0.39	0.10	410	17.7	551	
OH 30.1-0.2	(f)	853	0.78	1.40	0.4	(3)	0.12	0.05	510	6.6	53.9	
OH 30.7+0.4	(e)	1039	0.15	6.31		(4)	3.16		500	12.3	679	
OH 31.0-0.2	(b)			6.50		(4)	0.75		360	20.6	932	Non variable
OH 32.0-0.5	(b)	1540	0.08	9.30	2.0	(2)	3.68	1.12	450	14.6	4080	
OH 32.8-0.3	(b)	1536	0.39	8.05	0.24	(2)	3.54	0.15	440	>17.0	5690	
OH 39.7+1.5	(d)	1424	0.20	0.57	0.2i	(2)	0.25	0.13	520	10.3	61.5	
OH 39.9-0.0	(c)	823	0.98	3.07	0.8	(3)	0.49	0.20	500	9.9	226	
OH 42.3-0.1	(e)	1945	0.03	3.47		(4)	0.35		390	17.4	710	

Positions.

- (a) Kukarkin *et al.*, 1969.
- (b) VLA position. See chapter III, table 2.
- (c) VLA position. B. Baud, private communication.
- (d) VLA position. Bowers *et al.*, 1981.
- (e) IR position. Jones *et al.*, 1982.
- (f) IR position. Engels *et al.*, 1982.
- (g) Westerbork position. F. Willems, T. de Jong, private communication.

Distances.

- (1) Combination of Robertson and Feast, 1981, Rieu *et al.*, 1979 and  $K_{\text{abs}}$  ( $2.2 \mu\text{m}$ ) =  $2^{2.1}$  (at 1 kpc).
- (2) Geometric. See chapter III, table 3.
- (3)  $L_{\text{OH}}-R_0$  relation. See chapter V, section 4e.
- (4) Combination of the near kinematic distance and  $L_{\text{OH}}-R_0$  relation.

Table 3.

Name	$P_r$ (days)	$\phi$	D (kpc)	$\Delta D$	$L_{\text{int}}^{\text{(OH)}}$ ( $10^{-22}\text{Wm}^{-2}\text{kpc}^2$ )	Remarks
(1)	(2)	(3)	(4)	(5)	(7)	(12)
OH 0.3-0.2	(c)		9.2	(GC)	1470	Non variable. $[20 \mu\text{m}] = 2^{0.98}$
OH 1.5-0.0	(c)		9.2	(GC)	761	Non variable. Confusion by 'blue' object.
OH 15.7+0.8	(d)		0.3	(4)	6.0	Non variable. Undetected at [3.8], [8.7], and [12.5] within 60" around VLA position.
OH 18.5+1.4	(b)	1125:	0.02:	4.5	(4)	Slightly variable ( $\Delta m_{\text{CO}}^{0.19}$ ). Undetected at [8.7]
OH 25.1-0.3	(b)	226:	0.31:	4.7	(4)	Slightly variable ( $\Delta m_{\text{CO}}^{0.21}$ ). Undetected at [8.7]

We were unable to detect four sources, although we had good positions for all of them. OH 0.3-0.2 (together with OH 1.5-0.0 also part of the galactic centre program) was detected at  $\lambda = 20 \mu\text{m}$  only. The same quantities as in table 2 (as far as applicable) are listed for these undetected stars in table 3.

It is remarkable that three of the undetected sources appear not to be variable at radio wavelengths ( $\Delta m_r < 3\sigma$ ; see chapter II, table 3), and that the other two have very small amplitude variations. Note that two similar objects in table 2, (non-variable) OH 31.0-0.2, and (slightly variable) OH 17.7-2.0, both have very steep spectra shortward of the silicate feature. At L'(3.8  $\mu\text{m}$ ) and at M(4.8  $\mu\text{m}$ ) they are very weak. Preliminary IRAS survey results of OH 25.1-0.3 indicate also a very red spectrum (Habing, indiscrete information). This suggests that OH/IR stars with small- or zero-amplitude variations are even redder than those with large amplitude variations.

#### IV.4 Mean Luminosities

##### 4a. Variability

We can combine our luminosities with those of Evans and Beckwith (1977), and with those of Werner *et al.* (1980), using the periods and phases as found in the Dwingeloo monitor program (see figure 11). Adding their observations of OH 26.5+0.6 and OH 45.5+0.1 ('adjusted' to our distances), we find good agreement between all measurements for OH 21.5+0.5, OH 26.5+0.6, OH 32.8-0.3, and OH 45.5+0.1. The time of maximum for OH 30.1-0.7 is good, but our (radio) period seems to be somewhat too long; as we had incomplete coverage of the light curve in the Dwingeloo program (missing the maximum), and the light curve is asymmetric, this is probably the case. The luminosities for OH 30.1-0.2 show somewhat larger scatter ( $\pm 50\%$ ). This source, however, is apparently weak, and the three observers covered only the minimum ( $\phi = 0.2-0.8$ ).

Defining  $Q_R$  as the ratio of the variation in luminosity ( $A_L \equiv L_{\text{max}}/L_{\text{min}}$ ) and the 'radio' amplitude ( $A_R = 10^{0.4\Delta m_r}$ ) we find  $Q_R = 2.05$  for OH 21.5+0.5,  $Q_R = 2.07$  for OH 26.5+0.6,  $Q_R = 1.46$ : for OH 30.1-0.7,  $Q_R = 1.27$ : for OH 30.1-0.2,  $Q_R = 1.92$  for OH 32.8-0.3, and  $Q_R = 1.97$  for OH 45.5+0.1. So, quite speculatively, we derive

$$A_L = 2.0 \cdot 10^{0.4\Delta m_r} \quad (2)$$

In other words, the radio amplitude (reflecting the amplitude at  $35 \mu\text{m}$ , see section 7) is only half the amplitude of the bolometric magnitude.

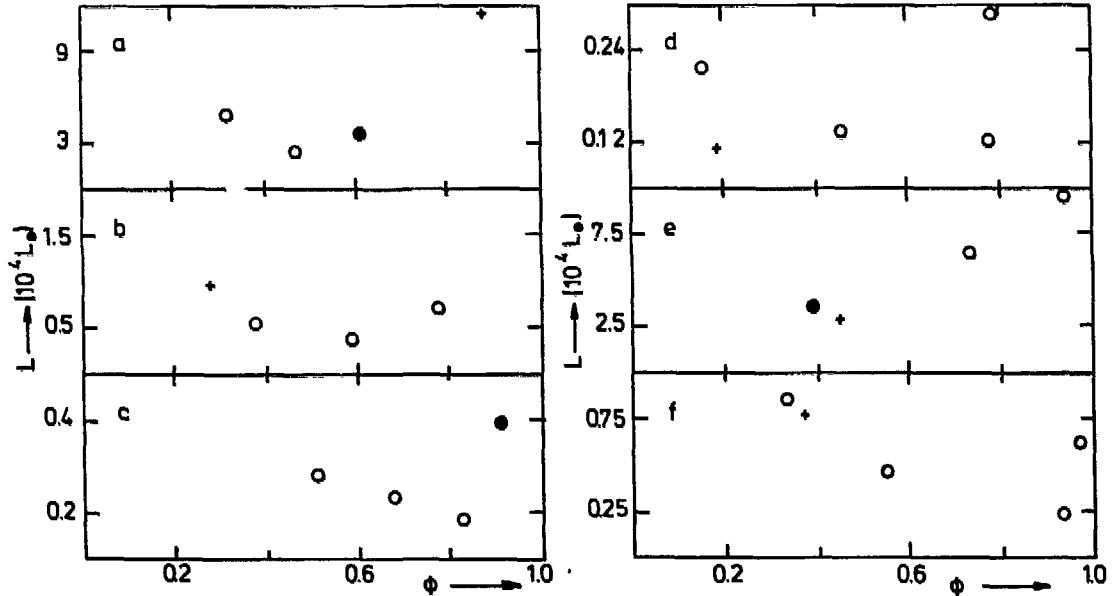


Figure 11. Variation of the luminosity. Open circles are observations of Evans and Beckwith (1977), crosses those of Werner *et al.* (1980). Dots are our own observations. a: OH 21.5+0.1, b: OH 26.5+0.6, c: OH 30.1-0.7, d: OH 30.1-0.2, e: OH 32.8-0.3, and f: OH 45.5+0.1.

We assume that equation (2) holds for all OH/IR stars. Furthermore, we assume that the luminosity varies sinusoidally. Although we know that in general the light curves are asymmetric (see chapter II, section 6e), this assumption will hardly affect our results. We then may write for the mean luminosity

$$L_M = D^2 S_{\text{IR}}(\text{obs}) [1 + \cos(2\pi\phi_{\text{obs}})] \{A_L - 1\} \{A_L + 1\}^{-1} \quad (3)$$

where  $D^2 S_{\text{IR}}(\text{obs}) = L_{\text{IR}}$ , the values listed in table 2.

#### 4b. Interstellar extinction

Although the interstellar extinction at infrared wavelengths mostly is

regarded as *quantité négligable*, we will yet correct for it, because the OH/IR stars are at low galactic latitudes and at large distances from the sun. Adopting the model advocated by de Jong (1983) we write for the extinction coefficient

$$\begin{aligned} \kappa(R, z) &= \kappa_{\odot} \left(\frac{R_{\odot}}{R}\right)^2 \exp\left(-\frac{z}{z_g}\right) && \text{for } R \geq R_m \\ &= 1.5 \kappa_{\odot} \exp\left(-\frac{z}{z_g}\right) && \text{for } R < R_m \end{aligned} \quad (4)$$

where  $\kappa_{\odot} = 1.6 \text{ mag kpc}^{-1}$  is the local extinction coefficient (Greenberg, 1968),  $R$  is the galacto centric distance,  $R_{\odot} = 9.2 \text{ kpc}$ , and  $z_g = 60 \text{ pc}$  is the scale height of the molecular gas in the galaxy (Solomon *et al.*, 1979).  $R_m = 3.7 \text{ kpc}$  is the inner radius of the molecular gas ring (Gordon and Burton, 1976). Integration along the line of sight yields the visual extinctions,  $A_V$ . Then, by using the wavelength dependence of the interstellar extinction in the infrared (Becklin *et al.*, 1978), we can calculate the corrected infrared fluxes (see for an example figure 12; *cf.* figure 9) and the corrected mean luminosities,  $L_M^C$ . The results can be found in table 4, where in column 2 the mean luminosities (from equation 3) are listed.

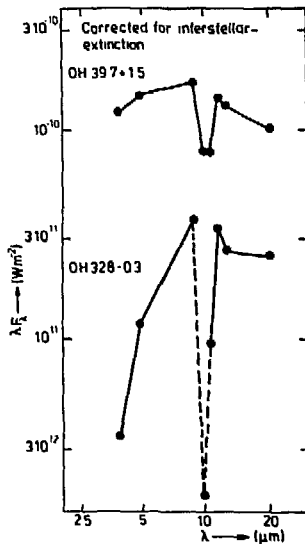


Figure 12. Example of two spectra corrected for interstellar extinction (*cf.* figure 9). OH 32.8-0.3 is far away ( $D=8.05 \text{ kpc}$ ), OH 39.7+1.5 close by ( $D=0.57 \text{ kpc}$ ).

Column 3 gives the visual extinctions,  $A_V$ , and column 4 the resulting corrected mean luminosities,  $L_M^C$ . The mean of the integrated OH flux density is listed in column 5, the radio amplitudes ( $\Delta m_r$ ) and the expansion velocities of the OH shell ( $v_e$ ) are tabulated in columns 6 and 7.

Table 4.

Name	$L_M^c$ ( $10^4 L_\odot$ )	$A_V$ (mag)	$L_M^c$ ( $10^4 L_\odot$ )	$\bar{L}_{int}$ ( $10^{-22} \text{ km}^{-2} \text{ kpc}^2$ )	$\Delta m_r$ (mag)	$v_e$ ( $\text{km s}^{-1}$ )	Remarks
(1)	(2)	(3)	(4)	(5)	(6)	(7)	(8)
WX Ser	0.37	0.02	0.37	6.69	0.58	7.59	
RS Vir	0.15	0.02	0.15	3.14	0.48	4.29	
OH 12.8-1.9	0.69	2.02	0.73	124	0.56	22.61	
OH 17.7-2.0	0.19	2.87	0.31	2460	0.16	12.89	Slightly variable.
OH 20.2-0.1	0.50	5.54	0.59	117	0.67	16.45	
OH 20.7+0.1	0.36	29.47	0.92	1680	0.99	18.21	
OH 21.5+0.5	7.32	20.66	14.05	7670	1.09	18.76	$L_M^c$ based also on observations of EB and W.
OH 26.2-0.6	0.27	2.35	0.29	89.2	1.05	22.11	
OH 26.4-1.9	0.23	1.79	0.25	55.6	0.44	12.09	
OH 26.5+0.6	0.94	1.53	1.00	615	1.13	14.07	$L_M^c$ based on EB and W. $P = 1560^d$ ; $D = 0.98$ kpc
OH 28.5-0.0	0.044	5.01	0.049	158	0.77	13.12	
OH 28.7-0.6	0.63	3.10	0.69	129	0.83	17.38	
OH 30.1-0.7	0.32	2.74	0.35	621	0.40	20.51	$L_M^c$ based also on EB and W.
OH 30.1-0.2	0.19	2.44	0.20	75.0	0.81	17.60	$L_M^c$ based also on EB and W.
OH 30.7+0.4	1.20	13.31	1.82	459	0.57	17.24	
OH 31.0-0.2	0.76	17.30	1.31	946	<0.13	14.26	Non variable.
OH 32.0-0.5	2.36	18.47	4.22	2820	0.88	20.58	
OH 32.8-0.3	7.34	20.46	14.02	6590	1.24	16.38	
OH 39.7+1.5	0.21	0.80	0.22	54.4	0.82	16.58	
OH 39.9-0.0	0.30	6.47	0.37	183	0.80	14.71	
OH 42.3-0.1	0.24	7.03	0.30	597	0.36	16.37	
OH 45.5+0.1	0.85	7.34	1.08	191	0.92	17.13	$L_M^c$ based on EB and W. $P = 761^d$ ; $D = 3.65$ kpc.

EB: Evans and Beckwith, 1977.  
W: Werner *et al.*, 1980.

Note that there are only six stars in table 4 with mean luminosities larger than  $10^4 L_\odot$ . The others lie in the luminosity range of the normal Mira variables (*cf.* Eggen, 1975). This is in good agreement with the statistical results of Jones *et al.* (1982). We also find that the sources with large expansion velocities ( $v_e > 15 \text{ km s}^{-1}$ ), that are thought to be

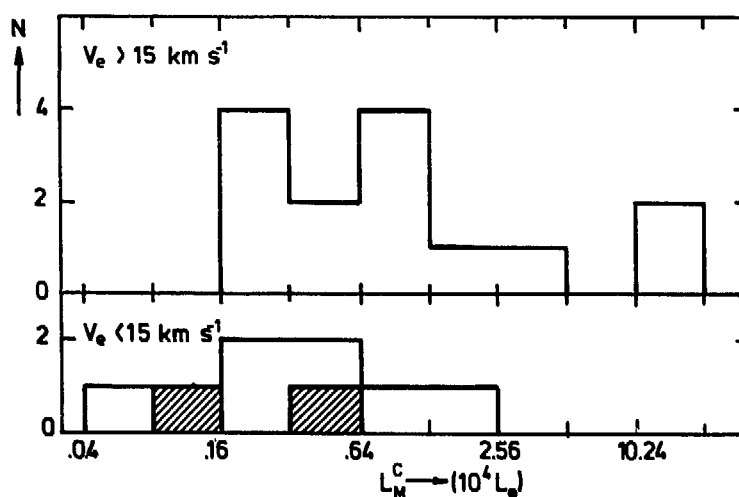


Figure 13. Distribution of the mean corrected luminosities (for our heterogeneous sample), divided into objects with small expansion velocities ( $v_e < 15 \text{ km s}^{-1}$ ) of the circumstellar envelope and objects with large ones ( $v_e > 15 \text{ km s}^{-1}$ ). The two Mira variables are shaded.

the younger and more massive stars (see Baud *et al.*, 1981), are more luminous ( $\langle L_M^C \rangle = 2.82 \cdot 10^4 L_\odot$ ) than the OH/IR stars with small expansion velocities ( $\langle L_M^C \rangle = 0.53 \cdot 10^4 L_\odot$ , see figure 13). Two of our objects, OH 21.5+0.5 and OH 32.8-0.3, have luminosities in excess of the asymptotic giant branch limit ( $\sim 5 \cdot 10^4 L_\odot$ ; see Iben, 1981). Therefore, they should be identified with supergiants. Notice, however, their large radio amplitudes, quite contrary to the small amplitudes of the optically identified supergiants (see chapter II, tables 2).

#### IV.5 The 9.7 $\mu\text{m}$ feature

The absorption or emission feature at 9.7 $\mu\text{m}$  seen in oxygen-rich stars is normally attributed to the stretching and bending vibrations in silicate materials (see Merrill, 1977). A considerable fraction of this feature is formed in the circumstellar dust shell, and certainly not solely by intervening material somewhere else along the line of sight. Evans and Beckwith (1977) give a number of arguments for this, the strongest ones being the total lack of correlation between the distance and the depth of the absorption feature (also apparent from table 2), and the positive correlation they found (for six stars only) between the colour temperature,  $T_c$ , and the relative depth of the absorption feature,  $A_{9.7}$  (see figure 14), where

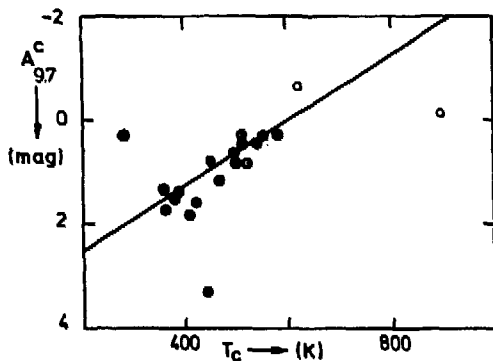


Figure 14. Depth of the silicate feature,  $A_{9.7}^C$  (corrected for interstellar extinction), as function of the colour temperature,  $T_c$ . The drawn line is the expected slope from  $\tau_{\text{sil}} \sim T_c^{-1}$  (Kwan and Scoville, 1976).

$$A_{9.7}^C \equiv -2.5 \log (I_{\text{cont}}^C / I_{9.7}^C) \quad (5)$$

corrected for interstellar extinction. The slope that we find is in agreement with the suggested correlation of  $\tau_{\text{sil}} (\sim A_{9.7})$  and  $T_c^{-1}$  (Kwan and

Scoville, 1976), based on a simple model of radiative transport. Note that the two Mira variables, where the silicate feature is seen in emission, have the highest colour temperatures. Only two OH/IR stars deviate substantially from the mean relation: the extremely cool shell of OH 17.7-2.0 hardly shows absorption at  $9.7\mu\text{m}$ , suggesting that the temperature gradient in this (very thick) envelope is small, and OH 32.8-0.3 which has a very deep absorption feature (see also table 5). As this star is far away (its geometric distance is 8.05 kpc), large deviations from the simple, uniform extinction model may account for this. Also it was found (Forrest *et al.*, 1978) that in OH 26.5+0.6 the silicate absorption feature is deeper when the star is fainter; and we observed OH 32.8-0.3 near minimum light ( $\phi=0.39$ ).

Table 5

Name	$A_{9.7}$ (mag)	$A_{9.7}^C$ (mag)	Name	$A_{9.7}$ (mag)	$A_{9.7}^C$ (mag)
(1)	(2)	(3)	(1)	(2)	(3)
WX Ser	-0.65	-0.65	OH 28.7-0.6	0.44	0.30
RS Vir	-0.10	-0.10	OH 30.1-0.7	2.02	1.81
OH 12.8-1.9	0.35	0.32	OH 30.1-0.2	0.57	0.44
OH 17.7-2.0	0.35	0.30	OH 30.7+0.4	1.54	0.81
OH 20.2-0.1	0.68	0.30	OH 31.0-0.2	2.38	1.33
OH 20.7+0.1	5.65	1.51	OH 32.0-0.5	2.01	0.82
OH 21.5+0.5	3.15	1.75	OH 32.8-0.3	>4.62	>3.31
OH 26.2-0.6	1.30	1.17	OH 39.7+1.5	0.94	0.88
OH 26.4-1.9	0.47	0.44	OH 39.9-0.0	0.96	0.63
OH 28.5-0.0	>1.90	>1.59	OH 42.3-0.1	1.81	1.37

ad. (2), (3): positive values indicate absorption at  $9.7 \mu\text{m}$ .  
ad. (3): corrected for interstellar extinction.

The depth of the silicate feature, which is primarily a measure of the amount of cold material in the envelope, is correlated with the fraction of the total luminosity that is converted, via the far infrared pump cycle, into OH luminosity at 18 cm (see figure 15). As  $A_{9.7}$  increases (i.e. the colour temperature decreases) more pump photons

are produced, and the (relative) OH strength increases.

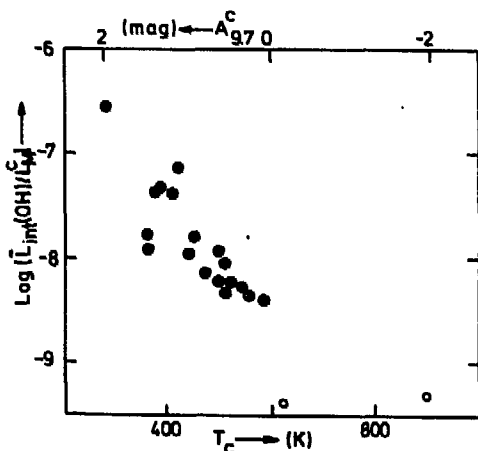


Figure 15. Fraction of the total luminosity that is converted into OH luminosity at 1612 MHz as function of colour temperature, or depth of the silicate feature.

This confirms that the OH masers are pumped by far infrared photons (Elitzur *et al.*, 1976; see also section 7). Furthermore, because we know that the OH luminosity also depends on the velocity field, and on the fraction of  $H_2O$  molecules that are photodissociated into OH (see appendix A), the relatively small scatter in figure 15 tells us that for this sample (apart from the Mira variables, a selection of only *strong* OH emitters) these quantities are roughly the same.

#### IV.6 The colour temperatures

We saw in the previous section that the colour temperature,  $T_c$  (between  $\lambda=3.8\mu m$  and  $\lambda=12.5\mu m$ ) is proportional to the inverse of the depth

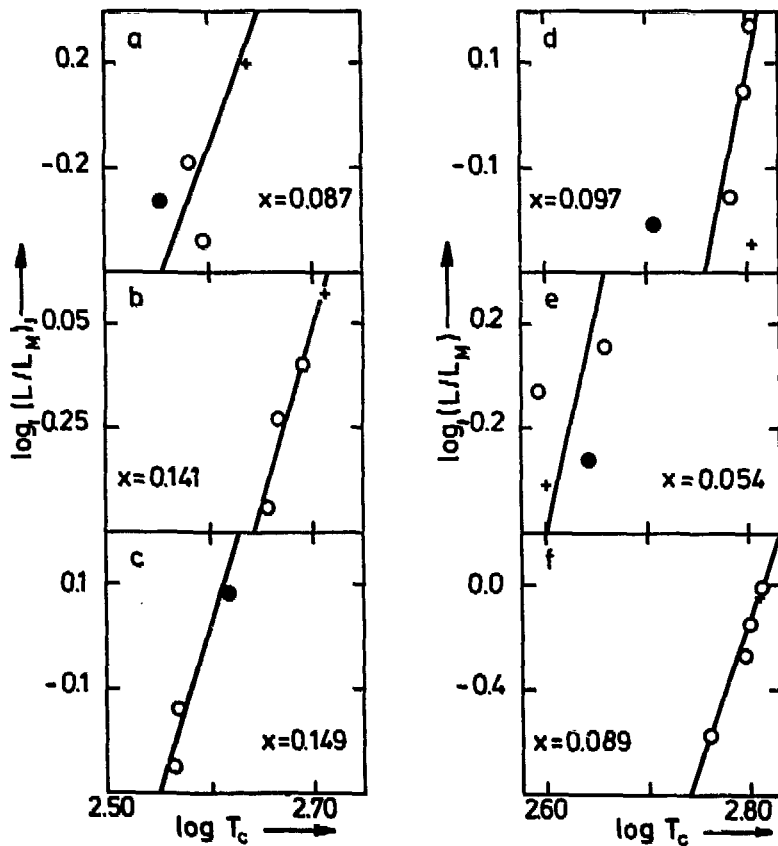


Figure 16. Variation of the colour temperature,  $T_c$ . Open circles are observations of Evans and Beckwith (1977), crosses those of Werner *et al.* (1980). Dots are our own observations. a: OH 21.5+0.5, b: OH 26.5+0.6, c: OH 30.1-0.7, d: OH 30.1-0.2, e: OH 32.8-0.3, and f: OH 45.5+0.1.

in the silicate feature (figure 14), in agreement with theoretical predictions (Kwan and Scoville, 1976). The same authors suggest that  $T_c \sim L^x$ , where  $x=0.25-0.20$  for an emissivity law of the dust  $\sim \lambda^0$  and  $\sim \lambda^{-1}$  respectively. The combination of our observations with those of Evans and Beckwith (1977), and with those of Werner *et al.*, (1980) gives us a time base for these slowly varying stars which is long enough to enable an analysis of the changes in  $T_c$  (see figure 16). Based on the six stars for which more than one observation is known (see section 4) we find  $\langle x \rangle = 0.103 \pm 0.015$ , significantly less than the theoretical prediction. Two remarks should be made: in the first place the analysis of Kwan and Scoville was for (two) pre main-sequence objects, where the density distribution of the dust seems to be proportional to  $r^{-1}$ , whereas we found (see chapter III, section 3c) a density fall off of  $r^{-2}$  (or even steeper) for the evolved stars; in the second place the variation in the temperature of dust, and hence the variation in  $T_c$ , might lag the changes in luminosity. Due to the sparse phase coverage we cannot account for such an effect. Although the uncertainties still are very large, it seems that the value of  $x$  is definitely smaller than the theoretical value of 0.2 (see also Elitzur *et al.*, 1976). This could be explained by a steeper decline of the dust emissivity with wavelength ( $\sim \lambda^{-2}$ , apart from the features at  $10\mu\text{m}$  and  $20\mu\text{m}$ ).

#### IV.7 Maser pump

The OH masers are pumped radiatively by infrared photons (see Harvey *et al.*, 1974). At first a pumping scheme was proposed involving excitation of the OH molecules to the first vibrational level at  $2.8\mu\text{m}$  (Litvak, 1969). In view of the very low fluxes of OH/IR stars at  $\lambda=2.8\mu\text{m}$  this scheme might only work for the Mira variables (see figure 17; see also Evans and Beckwith, 1977). Later (Elitzur *et al.*, 1976; Bujarrabal *et al.*, 1980) a pumping scheme was developed involving rotational excitation at  $35\mu\text{m}$  (and to a lesser extent at  $53\mu\text{m}$ ) with a predicted efficiency of  $\sim 25\%$ . Werner *et al.* (1980) have shown that for the OH/IR stars the observations are in agreement with this prediction. The efficiency is defined simply as the fraction of  $35\mu\text{m}$  photons that are converted into OH photons. And Evans and Beckwith (1977) have shown that, to first approximation, we may write for the efficiency

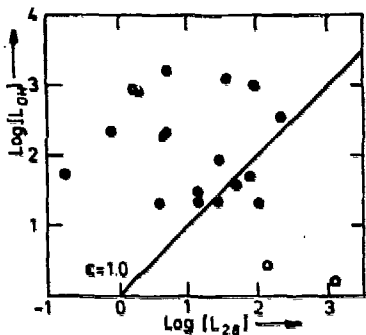


Figure 17. OH power density ( $\text{Jy kpc}^2$ ) at 1612 MHz as function of the power density ( $\text{Jy kpc}^2$ ) at  $2.8\mu\text{m}$  (same phase). Open circles represent the Mira variables, filled circles the OH/IR stars. The area to the left of the drawn line is 'forbidden' if the  $2.8\mu\text{m}$  pumping scheme is to work.

$$\epsilon \equiv \frac{S_V(\text{OH})}{S_V(35\mu\text{m})} = \frac{L(\text{OH})}{L(35\mu\text{m})} \quad (6)$$

where  $S_V(\text{OH})$  and  $S_V(35\mu\text{m})$  are the simultaneously measured fluxes (in Jy). We used  $L(\text{OH}) = D^2 \{S_L \cdot S_H\}^{\frac{1}{2}}$ , the harmonic mean of the two strongest (low- and high-velocity) peaks in the OH line profile. We determined the flux at  $35\mu\text{m}$  from an extrapolation of the spectra (corrected for interstellar extinction) between  $\lambda=12.5\mu\text{m}$  and  $\lambda=20\mu\text{m}$ , a very uncertain method (errors of a factor 3!). But we included also the much more accurate measurements of Forrest *et al.* (1979), and those of Werner *et al.* (1980), combined with the OH fluxes at the appropriate phase (see figure 18). Despite the uncertainties only one object (OH 28.5-0.0) falls in the 'forbidden' region with  $\epsilon > 1$ , and the OH/IR stars lie reasonably close to the predicted value  $\epsilon = 0.25$ . Note that the pump efficiency is roughly constant for measurements at different phases, as expected in saturated masers. We find for the OH/IR stars a mean pump efficiency  $\langle\epsilon\rangle = 0.30 \pm 0.06$ , meaning that three to four  $35\mu\text{m}$  photons are needed to produce one maser photon. The standard deviation is  $\text{me}=0.31$  (factor 2). For the (two) supergiants we find  $\langle\epsilon\rangle = 0.030 \pm 0.004$ , and for the (three) Mira variables  $\langle\epsilon\rangle = 0.030 \pm 0.004$ , an order of magnitude less than for the OH/IR stars. Rieu *et al.* (1979; see also Bujarrabal *et al.*, 1980) worked out a more detailed model in which they account for velocity gradients in the envelopes and far infrared line overlap. That does not make much difference for the OH/IR stars with their very thick dust shells, but for the OH Mira's they deduce an upper limit for the  $35\mu\text{m}$  pump efficiency of  $\epsilon < 0.1$ . The same might be true for the supergiants, that also have rather thin envelopes. It is interesting that VLBI measurements of some supergiants (Benson and Mutel, 1979) were not compatible with the simple geometry of an expanding shell, suggesting that in these objects larger velocity gradients might be present.

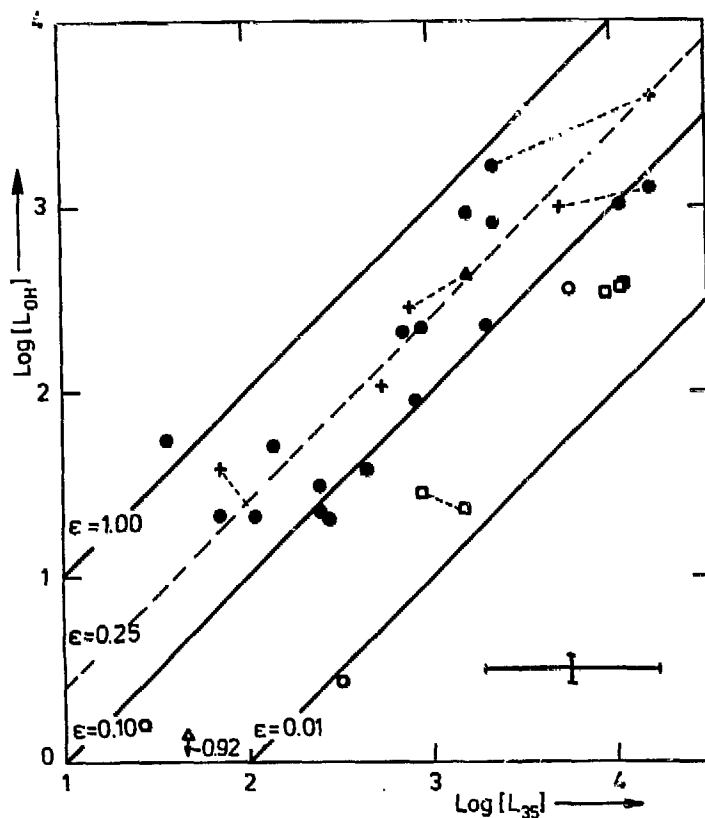


Figure 18. OH power density ( $\text{Jy kpc}^2$ ) at 1612 MHz as function of the power density ( $\text{Jy kpc}^2$ ) at  $35\mu\text{m}$  (same phase). Open symbols represent optically identified masers (triangle and squares are IR observations by Forrest *et al.*, 1979), filled symbols the OH/IR stars (crosses: Werner *et al.*, 1980; triangle: Forrest *et al.*, 1979). Measurements of the same object at different epochs are connected by dotted lines. The dashed line is the predicted pump efficiency,  $\epsilon = 0.25$  (Elitzur *et al.*, 1976).

#### IV.8 Conclusions

The IR photometry with UKIRT provided us with good absolute luminosities, and a fair estimate of the mean luminosities for a number of OH/IR stars. Only a small fraction of them have large luminosities, in excess of  $10^4 L_{\odot}$ ; most are only somewhat more luminous than the classical Mira variables. The (near infrared) colour temperatures, the depths of the silicate feature, and the fraction of the luminosity that is converted into OH luminosity, are correlated. Detailed confirmation of the far infrared

pumping scheme for 1612 MHz OH masers awaits direct measurements of the 35 $\mu$ m flux.

We were unable to detect some sources although we had very good (radio) positions for them. Together with two stars that were only marginally detectable at the shorter infrared wavelengths, these objects seem to be of a different mold than the other OH/IR stars; either they do not vary at all, or if they do, they have very small amplitudes. It is interesting that these stars appear to have small angular sizes; they were unresolved when observed with the VLA (see chapter III). Hence they are either very far away ( $D \gtrsim 8$  kpc), or much closer by ( $D \lesssim 2$  kpc) and consequently low mass stars with extraordinary large mass loss rates (see also chapter V, section 7).

Literature cited in chapter IV

- Baud, B., Habing, H.J., Winnberg, A., Mathews, H.E.: 1981, *Astron. Astroph. 95*, 156
- Becklin, E.E., Matthews, K., Neugebauer, G., Willner, S.P.: 1978, *Astroph. J. 220*, 831
- Beckwith, S., Evans II, N.J., Becklin, E.E., Neugebauer, G.: 1976, *Astroph. J. 208*, 390
- Benson, J.M., Mutel, R.L.: 1979, *Astroph. J. 233*, 119
- Bowers, P.F., Johnston, K.J., Spencer, J.H.: 1981, *Nature 291*, 382
- Tujarrabal, V., Destombes, J.L., Guibert, J., Marliere-Demuynck, C., Rieu, Nguyen-Q., Omont, A.: 1980, *Astron. Astroph. 81*, 1
- Eggen, O.J.: 1975, *Astroph. J. 195*, 661
- Engels, D.: 1982, *Zur Natur von OH/IR-Objekten. Ph.D. thesis. Veröff. Astron. Inst. Bonn 95*
- Elitzur, M.: 1981, in *Physical Processes in Red Giants*, eds. I. Iben and A. Renzini (Reidel), pp 363-382
- Elitzur, M., Goldreich, P., Scoville, N.: 1976, *Astroph. J. 205*, 384
- Evans, N.J., Beckwith, S.: 1977, *Astroph. J. 217*, 729
- Forrest, W.J., Gillett, F.C., Houck, J.R., McCarthy, J.F., Merrill, K.M., Pipher, J.L., Puetter, R.C., Russell, R.W., Soifer, B.T., Willner, S.P.: 1978, *Astroph. J. 219*, 114
- Forrest, W.J., McCarthy, J.F., Houck, J.R.: 1979, *Astroph. J. 233*, 611
- Gordon, M.A., Burton, W.B.: 1976, *Astroph. J. 208*, 346
- Greenberg, J.M.: 1968, in *Stars and Stellar Systems*, eds. B.M. Middlehurst and L.H. Aller, VII, p. 221
- Harvey, P.M., Bechis, K.B., Wilson, W.J., Ball, J.A.: 1974, *Astroph. J. Suppl. 27*, 331
- Hyland, A.R., Becklin, E.E., Frogel, J.A., Neugebauer, G.: 1972, *Astron. Astroph. 16*, 204
- Iben, I.: 1981, in *Physical Processes in Red Giants*, eds. I. Iben and A. Renzini (Reidel), pp 3-24
- Johnson, H.L.: 1966, in *Annual Review Astron. Astroph. 4*, pp 193-206
- Jong, T. de: 1983, *Astroph. J.*, submitted.
- Jones, T.J., Ashley, M., Hyland, A.R., Ruelas-Mayorga, A.: 1981, *I M.N.R.A.S. 197*, 413

- Jones, T.J., Hyland, A.R., Caswell, J.L., Gatley, I.: 1982, *II Astroph. J.* 253, 208
- Jones, T.J., Hyland, A.R., Wood, P.R., Gatley, I.: 1982, *IV*
- Kukarkin, B.V., Kholopov, P.N., Efremov, Yu.N., Kukarkina, N.P., Kurochkin, N.E., Medvedeva, G.I., Perova, N.B., Fedorovich, V.P., Frolov, M.S.: 1969, *General Catalogue of Variable Stars, Moscow (+ Suppl.)*
- Litvak, M.M.: 1969, *Astroph. J.* 156, 471
- Kwan, J., Scoville, N.: 1976, *Astroph. J.* 209, 102
- Merrill, K.M.: 1977, in *The Interaction of Variable Stars with their Environment*, eds. R. Kippenhahn, J. Rahe, and W. Strohmeier (Veröff. Remis Sternwarte, Bamberg), Bd XI, nr. 121, p. 446
- Rieu, Nguyen-Q., Laury-Micolaut, C., Winnberg, A., Schultz, G.K.: 1979, *Astron. Astroph.* 75, 351
- Robertson, B.S.C., Feast, M.W.: 1981, *M.N.R.A.S.* 196, 111
- Solomon, P.M., Sanders, D.B., Scoville, H.Z.: 1979, *IAU Symp.* 84, ed. W.B. Burton, p. 35
- Wamsteker, W.: 1981, *Astron. Astroph.* 97, 329
- Werner, M.W., Beckwith, S., Gatley, I., Sellgreen, K., Berriman, G., Whiting, D.L.: 1980, *Astroph. J.* 239, 540

## V. Properties of OH/IR stars

### V.1 Introduction

In this chapter a synthesis will be given of all observations presented in this thesis and their implications for the intrinsic properties of OH masers, as well as of the central stars, as of the extended dust shells surrounding them. We will treat all 1612 MHz OH masers as one family of evolved stars, ranging from the OH Mira variables, with optically thin envelopes and weak masers, via the IRC Mira's to the strong masers in OH/IR stars, that often are shrouded in a dust shell with as much as  $100^m$  of visual extinction. After presenting ample evidence in favour of a simple shell model of a saturated maser (described in appendix A), a method for the determination of distances, based on the apparent OH luminosity and the phase lag radius, is developed.

Then at first the masers in the solar neighbourhood are considered; the probability that a star shows maser emission, their space distribution, and the luminosity function. Although the emphasis lies with the 1612 MHz OH masers (type IIb, satellite line), other masers that occur in late-type stars (main line OH, H<sub>2</sub>O and SiO) are discussed also. The results are compared with and extended to the OH/IR stars as a galactic population in the next section. Finally, we will derive a complete set of stellar and envelope parameters in section 7.

### V.2 Shell geometry

The observed OH line profiles are easily explained if the emission originates in an expanding circumstellar shell (see e.g. Olmon, 1977; Reid *et al.*, 1977). Throughout this thesis the geometry of a spherically symmetric envelope, that expands with an uniform and constant velocity, has been used and now we will summarize briefly the observational support for this picture.

In the first place we found (see chapter II, section 6f) definite phase lags between emission peaks at various velocities in the line profile, *in the right sense*. From the model we expect (see appendix A) that

$$\Delta\phi_v \propto \left(1 + \frac{v}{v_e}\right) \quad (1)$$

where  $v$  is the velocity of a peak with respect to the stellar velocity,  $v_e$  is the expansion velocity of the shell, and  $\Delta\phi_v$  the corresponding phase lag. Such a correlation was found indeed (see appendix C), except for those stars that showed no variation, or had very small amplitudes. In the second place the radius,  $a(v)$ , of the angular brightness distribution in maps at various velocities is predicted to be (see chapter III, section 3b)

$$a(v) = R_s \left\{ 1 - \left( \frac{v}{v_e} \right)^2 \right\}^{\frac{1}{2}} \quad (2)$$

with  $R_s$  the radius of the shell. This relation proved to be a very good description for the sources that we resolved with the VLA. The deviations from these relations for the phase lags and for the angular radii were found to be quite small ( $\lesssim 20\%$ ) for most stars, implying a rather high degree of spherical symmetry. In the third place the two strongest peaks in the line profile, the low velocity (front) and the high velocity (back) peaks, are on the average equally strong (see figure 1).

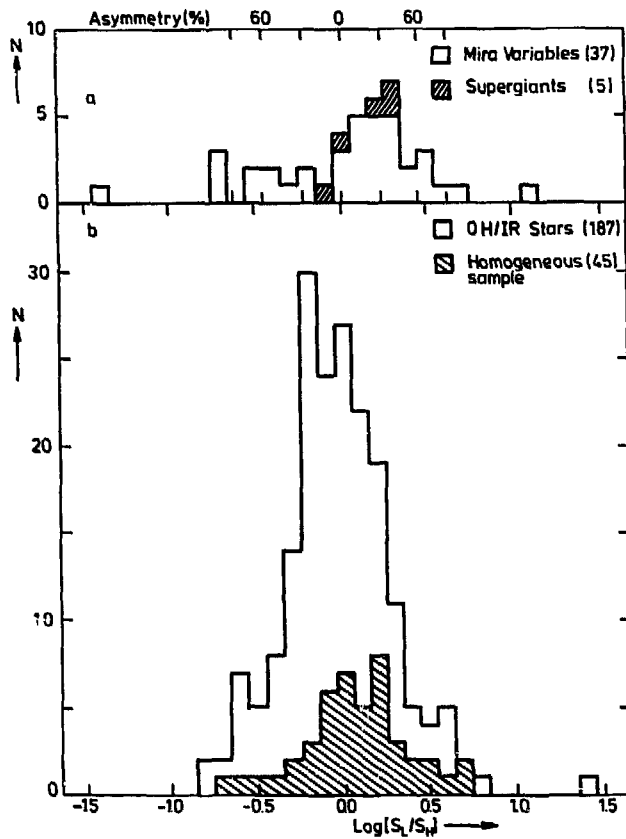


Figure 1. Distribution of the ratio,  $S_L/S_H$ , of the 'front' and 'back' peak flux density for a) Mira variables and M-type supergiants and b) for the OH/IR stars in Baud's catalogue (Baud *et al.*, 1979). Our homogeneous sample is indicated. The flux ratio is a measure of the deviations from spherical symmetry in the shell. A rough scale is given along the topmost axis.

The ratio of the 'front' and 'back' peak fluxes gives, as we found in chapter III (section 3c), the degree of asymmetry in the shells. For the type IIB OH/IR stars we then deduce a median value for the deviations from spherical symmetry of  $\sim 25\%$ , where for the 1612 MHz OH Mira variables this median value is  $\sim 40\%$ . Note that this is in good agreement with the deviations from the theoretical relations for phase lag and angular extent, and also with the upper limit ( $\lesssim 0.2 R_g$ ) found for the thickness of the OH shells (chapter III, section 3c). In the fourth place the central velocity of the OH line profile (halfway between the outer peaks) should be the velocity of the star. This is most strongly confirmed by observations of thermal SiO lines in the ground vibrational state (see Buhl *et al.*, 1975; Reid and Dickinson, 1976). In the past (Wallerstein, 1975) the velocity of the optical absorption lines, A, was thought to be correlated with the high velocity OH peak, and the emission line velocities, E, with the low velocity OH peak. Figure 2 shows there is no such correlation.

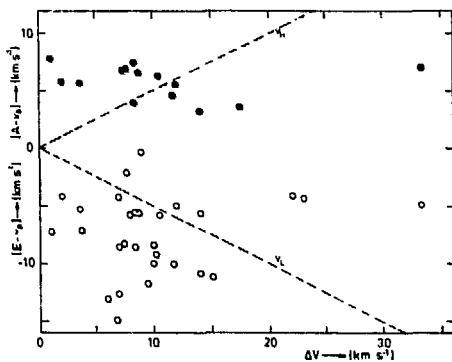


Figure 2. Velocity of the optical emission (E) and absorption (A) lines with respect to the stellar velocity (i.e. the central velocity of the OH line profile) plotted as function of  $\Delta v$ , that is twice the expansion velocity of the shell. If E, or A were correlated with the low-, or high-velocity OH peak, the points should lie on the dashed lines marked  $v_L$  and  $v_H$ .

Furthermore, the stellar velocity does not coincide with the velocities of the optical absorption lines. If only optical data are available, the best value for the stellar velocity is

$$v_* = \frac{1}{2} (A+E) + 0.77 \text{ kms}^{-1} \quad (3)$$

### V.3 Saturation and radiative pumping

All type IIB OH masers are saturated (see chapter II, section 6a; see also Harvey *et al.*, 1974) with a possible exception for some features in

the line profiles of the supergiants. The infrared and radio fluxes vary in close harmony, as we found in chapter IV (section 4), where we combined our observations with those of Evans and Beckwith (1977), and with those of Werner *et al.* (1980). The same is also apparent when we compare our radio light curves with the IR light curves as measured by Engels (1982), or by Feast (private communication, see appendix B). The far infrared flux (at 35 $\mu$ m) of all these sources is sufficient to pump the OH masers, but only the forthcoming observations of the IRAS will give a definite answer whether or not other IR transitions (e.g. 53  $\mu$ m, see Elitzur *et al.*, 1976; and Bujarrabal *et al.*, 1980) may play a role in the pumping schemes. The efficiency of the 35  $\mu$ m pump was found to be  $\sim 0.3$  for the OH/IR stars (i.e. 3 to 4 IR photons are needed to produce 1 maser photon), and  $\sim 0.03$  for the Mira variables and the supergiants (see chapter IV, section 7). As expected for saturated masers the efficiencies do not vary in time. Finally, it should be noted that the line profiles of the OH masers now known over the longest period of time ( $\sim 11$  yr) generally remained exactly the same all those years (*cf.* Wilson and Barrett, 1972).

#### V.4 Distance determinations

Table 1

Name	D (kpc)	$\Delta D$	$ z $ (pc)	Log $L_{int}$	Log $L'_{int}$	$\Delta$ Log L	Log $R_0$	$\Delta$ Log $R_0$	Weight
mean Mira <sup>1)</sup>	0.54		200	0.400	-0.462	0.120	-0.471	0.060	0.5
IRC + 10011	0.47	0.06	361	0.969	0.019	0.104	0.473	0.008	0.5
OH 25.1-0.3	1.6 <sub>1</sub>		10	1.530	0.624	0.481	-0.060	0.237	0.2
OH 39.7+1.5	0.5 <sub>2</sub>	0.21	15	1.735	0.831	0.272	0.233	0.105	0.4
OH 28.5-0.0	1.9 <sub>0</sub>		1	2.004	1.109	0.455	-0.770	0.995	0.2
OH 18.5+1.4	2.49		61	2.125	1.265	1.368	-0.022	0.684	0.1
OH104.9+2.4	2.03	0.20	86	2.717	1.827	0.082	0.640	0.040	1.0
OH 26.5+0.6	0.98	0.09	10	2.788	1.885	0.076	0.517	0.033	1.0
OH 30.1-0.7	1.7 <sub>2</sub>	0.31	21	2.793	1.890	0.140	0.551 <sub>1)</sub>	0.070	0.7
OH 31.0-0.2	7.9		29	3.145	2.270	0.602	0.542 <sub>2)</sub>	0.301	0.2
OH 20.7+0.1	8.31 <sub>2)</sub>	0.82	11	3.225	2.319	0.082	1.011 <sub>3)</sub>	0.037	1.0
OH 37.1-0.8	6.9 <sub>2)</sub>		101	3.258	2.368	0.602	0.054 <sub>3)</sub>	0.301	0.2
OH 32.0-0.5	9.30	2.00	75	3.450	2.562	0.169	0.870	0.060	0.5
OH127.9-0.0	5.63	0.32	1	3.594	2.710	0.048	1.109	0.024	1.0
OH 32.8-0.3	8.05	0.24	44	3.819	2.949	0.026	1.216	0.009	2.0
OH 21.5+0.5	11.63	0.65	101	3.884	2.975	0.047	1.213	0.023	1.0

<sup>1)</sup> Mean of the values for R Aql, RR Aql, SY Aql, Z Cyg, IK Tau, and RS Vir. Distances were taken to be the mean of those from Robertson and Feast (1981), and from Riau *et al.* (1979), and from an own method based on  $K_{abs}$  (2.2  $\mu$ m)=2<sup>m</sup> (at 1 kpc).

<sup>2)</sup> Kinematic distance.

<sup>3)</sup> Radius based on kinematic distance + angular extent.

For a limited number of stars we could derive accurate (~ 10%) distances in a very direct manner (see chapter III, section 3d). For most objects, however, we do know their phase lag radii but not the angular extents. For those we will derive distances through a relation found for the stars with known distances (see table 1).

#### 4.a OH luminosity as function of the radius of the OH shell

We know that (see appendix A)

$$S_{\nu}(v, R_o) D^2 \propto f(v) R_o^3 n_{OH}(R_o) R_{pump} \quad (4)$$

where  $S_{\nu}$  is the time averaged OH flux density (Jy),  $D$  the distance,  $R_o$  the radius of the OH shell ( $10^{16}$  cm),  $n_{OH}(R_o)$  the OH number density ( $\text{cm}^{-3}$ ) at  $R_o$ , and  $R_{pump}$  the net population transfer into the upper masing level ( $\text{s}^{-1}$ ).

$$f(v) = \frac{(v_d/v_e)}{1-(v/v_e)^2} \quad \text{for } v < v_p < v_e \quad (5)$$

with  $v_d$  the Doppler width ( $\approx 0.58 \text{ kms}^{-1}$  for all OH masers. See chapter II, section 6h). For the strongest (front and back) peaks in the line profile  $f(v_p) \approx 2v_d/\delta$ , where  $\delta \equiv v_p - v_e$ . For the OH/IR stars  $\delta$  typically has values of 0.01-0.1  $\text{kms}^{-1}$  (see chapter II, figure 13), and so  $\delta^{-1}$  can differ by an order of magnitude from star to star. Therefore we integrate equation (4) over the total velocity range of emission ( $-v_e \rightarrow +v_e$ ) to find

$$S_{int}(R_o) D^2 \propto \left\{ 1 + \ln\left(\frac{2v_e}{\delta} - 1\right) \right\} R_o^3 n_{OH}(r_o) R_{pump} \quad (6)$$

which depends only lightly on the (difficult to determine) value of  $\delta$ . Now let us define

$$L'_{int} \equiv S_{int}(R_o) D^2 \left\{ 1 + \ln\left(\frac{2v_e}{\delta} - 1\right) \right\}^{-1} \quad (7)$$

where  $L'_{int}$  and  $L_{int} \equiv S_{int} D^2$  are the time averaged values over the radio light curve (see table 1). Then we find from a least squares fit to the observations (see figure 3)

$$\log L'_{\text{int}} = (1.84 \pm 0.12) \log R_o + (0.68 \pm 0.12) \quad (8)$$

with a (weighted) standard deviation  $me=0.31$ .

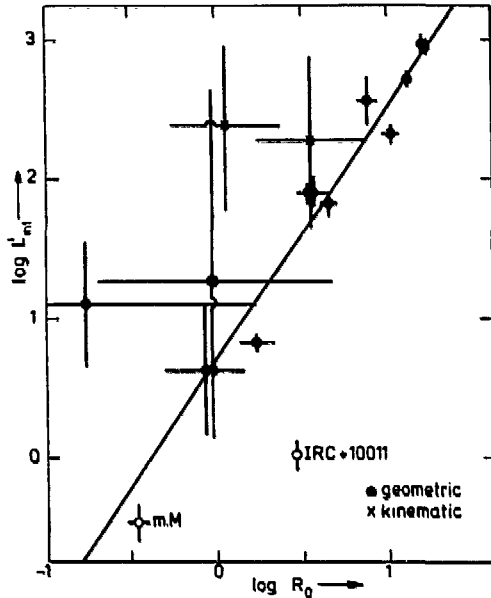


Figure 3.  $L'_{\text{int}}$  (see text) as function of  $R_o$ , the radius of the OH shell. m.M. stands for mean Mira. The drawn line is the least squares fit (equation 8).

This implies a constant surface brightness for OH masers ( $L \sim R_o^2$ ), whereas equation (3) seems to predict a constant volume emissivity ( $L \sim R_o^3$ ). But for a saturated OH maser a *minimum* column density ( $N_{\text{OH}} \gtrsim 10^{17} \text{ cm}^{-2}$ ; see Elitzur *et al.*, 1976) is needed

$$N_{\text{OH}} \approx \int_{R_o}^{\infty} n_{\text{OH}}(R) R^2 dR = n_{\text{OH}}(R_o) R_o \quad (9)$$

will be roughly constant from star to star, because the interstellar UV radiation permeates in the envelopes to about the same optical depth  $\tau_{\text{UV}} \sim N_{\text{OH}}$ . Further, the 1612 MHz inversion is quenched by collisions for number densities  $n_{\text{OH}}(R) \sim N_{\text{OH}}/R_o$  much higher than the mean value (about  $20 N_{\text{OH}}^{\text{min}}$ ). Note that this leaves open at most a very weak dependence of the net pump rate on  $R_o$ , as argued already in chapter III (section 3c), and as seen in chapter IV (section 7), where we found the pump efficiency for OH/IR stars to be constant, as well in time, as from source to source.

#### 4.b Influence of the interstellar UV field on the size of the OH shells

Equation (8) seems obeyed satisfactorily by all OH/IR stars, but the

OH Mira WX Psc (IRC+10011) is more than a magnitude off, although its radius and distance are quite well determined. Also the 'mean Mira' has a flux that is too small as compared to its radius. A major difference between the Mira variables and the OH/IR stars is the distance to the galactic plane ( $z$ ). Whereas the OH/IR stars have  $|z| < 100$  pc, IRC+10011 is at  $|z| = 361$  pc and the mean Mira at  $|z| = 200$  pc. The residuals in equation (8) seem to be correlated with  $|z|$  (see figure 4).

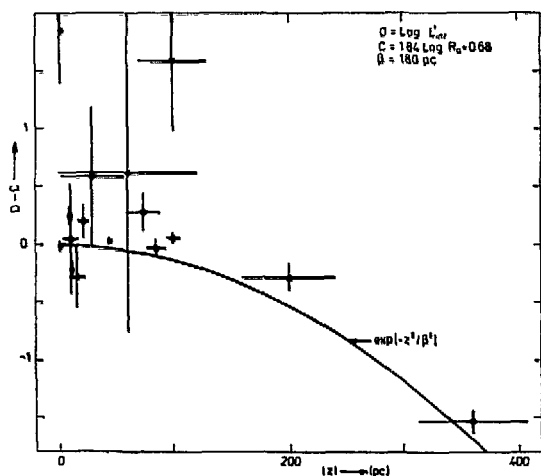


Figure 4. Residuals of  $\text{Log } L'_{\text{int}}$  with respect to the least squares fit (equation 8) as function of the distance to the galactic plane,  $z$ .

The distance to the galactic plane is physically significant, if OH molecules are produced in the envelope by the interstellar UV radiation field through photodissociation of  $\text{H}_2\text{O}$  ( $\lambda \lesssim 1650 \text{ \AA}$  photons; see Goldreich and Scoville, 1976). Assume

$$n_{\text{OH}}(R_0) \propto \exp[-z^2/\beta^2] \quad (10)$$

and we find

$$\text{Log } L'_{\text{int}} = (1.84 \pm 0.07) \text{Log } R_0 - (13.0 \pm 8.0) z^2 + (0.68 \pm 0.07) \quad (11)$$

where  $z$  is in kpc. The (weighted) standard deviation decreases to  $m\sigma = 0.19$ . We find a scaleheight  $\beta = (180 \pm 90) \text{ pc}$ , in reasonable agreement with the scaleheight  $\beta = 120 \text{ pc}$ , as found by Habing (1968). Although the result is satisfying, caution is needed because we compare stars in the solar neighbourhood ( $D < 1 \text{ kpc}$ ) with OH/IR stars at large ( $D \lesssim 12 \text{ kpc}$ ) distances, and the new result is based effectively, on three points only.

Nevertheless, the use of equation (11) also leads to reasonable distances for the individual OH Mira's, whereas equation (8) which ignores the z-dependence yields far too large distances (see section 4c). Observations of a larger sample of OH/IR stars, especially of those that lie relatively nearby and have the larger distances to the plane, should confirm this relation.

#### 4.c Resulting distances

Rewrite, with D in kpc, equation (11) as follows

$$g(D) = \text{Log } D^2 + 13 D^2 \sin^2 b \quad (12)$$

and on the other hand, with  $R_0$  in  $10^{16}$  cm, and  $S_{\text{int}}$  in  $10^{-22} \text{ Wm}^{-2}$

$$g(D) = 1.84 \text{ Log } R_0 + 0.68 - \text{Log } S_{\text{int}} + \text{Log} \left\{ 1 + \ln \left( \frac{2v}{\delta} e - 1 \right) \right\} \quad (13)$$

which is completely known for all stars with a determined phase lag radius. Thus we can solve equation (13) to find the distance. The uncertainties are  $\leq 25\%$  (based on the standard deviation in equation 11), without taking into account the errors in the phase lag determinations. For the Mira variables and M-type supergiants the computed distances,  $D_c$ , can be found in table 2a.

Table 2a

Mira variables and M supergiants

Name	$D_c$ (kpc)	D (kpc)	$\Delta D$	Remarks
R Aql	0.70	0.29	0.01	
RR Aql	0.44	0.60	0.09	
SY Aql	0.65	1.10	0.12	
Z Cyg	0.77	0.86	0.02	
U Ori	1.25:	0.27	0.02	Phase lag radius dubious.
WX Psc	0.45	0.47	0.06	IRC+10011. D geometric.
WX Sgr	0.27:	1.20	0.55	Phase lag radius dubious.
IK Tau	0.28	0.24	0.03	NML Tau.
RS Vir	0.35	0.66	0.05	
UY Ori	0.50	1.50	?	Distance from Herbig (1969). Hyland's D = 0.40 kpc. <sup>1)</sup>
PZ Cas	5.30	2.70	?	Distance from Engels (1979).
NML Cyg	0.55	0.50	0.05	OH 80.8-1.9, table 2c.

<sup>1)</sup> Hyland et al., 1972.

They may be compared with values taken from the literature. We find for the Mira's  $\langle D_c \rangle = 0.57$  kpc, in good agreement with  $\langle D \rangle = 0.63$  kpc. Due to the uncertain determination of the (small) phase lag radii the errors in individual cases can be considerable.

In table 2b the results are given for the OH/IR stars with large radio amplitudes ( $\Delta m_r > 0^m.60$ ). In this group the phase lag radius, and hence the computed distance, is determined very well, except for OH 20.2-0.1 and OH 26.2-0.6 (see chapter II, table 4b). The computed distances are compared to the geometric distances (from the combination of the angular sizes and the phase lag radii), and the near kinematic distances (adopting  $R_0 = 9.2$  kpc, see chapter III, section 3e). In the last column the adopted distances,  $D_{ad}$ , are listed. They are the geometric distances, when these are known, or else a weighted mean of  $D_c$  and  $D_{kin}$ , where the weight depends on the uncertainty in  $R_0$ . Because most stars in table 2b have a well defined phase lag,  $D_{ad}$  is almost completely determined by  $D_c$ . We find  $\langle D_c \rangle = 3.74$  kpc, compared to  $\langle D_{kin} \rangle = 4.43$  kpc.

Table 2b

OH/IR stars with large amplitudes ( $\Delta m_r > 0^m.60$ )

OH	$D_c$ (kpc)	$D_g$ (kpc)	$D_{kin}$ (kpc)	$D_{ad}$ (kpc)	Remarks
20.2-0.1	3.35		2.4	2.68	
20.7+0.1	10.75	8.31	8.6	8.31	Tangential point source
21.5+0.5	9.75	11.63	10.2f	11.63	$D_{kin}$ (near) = 6.9 kpc
26.2-0.6	0.14		4.8	1.48	
26.5+0.6	0.73	0.98	2.1	0.98	
28.5-0.0	0.23	1.96	8.0	2.45	
28.7-0.6	1.35		3.2	2.40	
30.1-0.2	0.90		3.7	1.40	
32.0-0.5	6.40	9.30	5.0	9.30	$D_{kin}$ (far) = 10.6 kpc
32.8-0.3	7.55	8.05	4.0	8.05	$D_{kin}$ (far) = 11.4 kpc
35.6-0.3	3.80		5.2	4.22	
39.7+1.5	0.75	0.57	1.3	0.57	Angular radius from Diamond <sup>1)</sup>
39.9-0.0	2.05		6.9	3.07	
44.8-2.3	4.00		2.8	3.72	
45.3+0.1	4.10		2.3	3.65	
75.3-1.8	7.70		5.1	7.09	
83.4-0.9	1.70		4.0	2.11	
104.9+2.4	2.00	2.03	2.3	2.03	Angular radius from Norris et al. (1982)
127.9-0.0	5.70	5.63	3.9	5.63	Angular radius from Norris et al. (1982)
138.0+7.2	1.92		2.8	2.18	

<sup>1)</sup> Private communication.

The OH/IR stars with intermediate radio amplitudes ( $0^m.30 < \Delta m_r < 0^m.60$ ) are listed in table 2c. A few stars have no phase lag

determination. In those cases we used the mean radius of this group. Now  $D_c$  and  $D_{kin}$  have about the same weight in the determination of the adopted distances,  $D_{ad}$ . Here we find  $\langle D_c \rangle = 2.55$  kpc, and  $\langle D_{kin} \rangle = 3.19$  kpc.

Table 2c

OH/IR stars with intermediate amplitudes ( $0.30 < \Delta m_r < 0.60$ )

OH	$D_c$ (kpc)	$D_g$ (kpc)	$D_{kin}$ (kpc)	$D_{ad}$ (kpc)	Remarks
12.3-0.1	5.30:		4.2	4.54	$R_0 = 3.75 \cdot 10^{16}$ cm adopted
12.8-1.9	1.80		1.5	1.69	
12.8+0.9	4.25:		3.2	3.52	$R_0 = 3.75 \cdot 10^{16}$ cm adopted
13.1+5.0	3.15		-	3.15	
16.1-0.3	1.10		2.3	1.41	
17.4-0.3	0.60		2.0	1.30	
26.4-1.9	<0.92		2.0	1.54	
27.3+0.2	<0.16		3.5	1.25	
30.1-0.7	1.42	1.77	6.9	1.77	
30.7+0.4	9.05		4.4	6.31	
36.9+1.3	0.80		-	0.80	Harmonic mean flux less than 4 Jy
42.3-0.3	2.90:		3.8	3.47	$R_0 = 3.75 \cdot 10^{16}$ cm adopted
80.8-1.9	0.55:	<1.67	0.5	0.52	Angular radius ( $\sim 1''$ ) from VLBI maps (e.g. Benson and Mutel, 1979)

The results for the stars with only slight variation in the radio ( $\Delta m_r < 0.30$ ) and for the non variable OH/IR stars are given in tables 2d and 2e. The adopted distances are determined primarily by the kinematic distance, because the phase lag radii are very uncertain, or not known at all. For the non-variables we adopted a radius  $R_0 = 3.75 \cdot 10^{16}$  cm. Taking the stars from tables 2d and 2e together, but omitting the galactic centre sources that are no part of our homogeneous sample, we find  $\langle D_c \rangle = 3.2$  kpc, and  $\langle D_{kin} \rangle = 4.8$  kpc.

Table 2d

OH/IR stars with small amplitudes ( $\Delta m_r < 0.30$ )

OH	$D_c$ (kpc)	$D_g$ (kpc)	$D_{kin}$ (kpc)	$D_{ad}$ (kpc)	Remarks
11.5+0.1	0.32		4.8	1.95	
17.7-2.0	1.27:	2.01	5.0	3.17	Angular radius from Diamond <sup>1)</sup>
18.3+0.4	12.20		13.44	12.79	
18.5+1.4	1.20	2.49	8.7	4.50	Phase lag and angular radius poorly determined
18.8+0.3	0.35		1.1	0.75	
25.1-0.3	1.50	1.61	8.3	4.69	Angular radius poorly determined
31.0+0.0	1.45		2.3	1.97	

<sup>1)</sup> private communication

Table 2e

OH/IR stars without recognizable variation

OH	$D_c$ (kpc)	$D_g$ (kpc)	$D_{kin}$ (kpc)	$D_{ad}$ (kpc)	Remarks
359.4-1.3	4.15:		9.2	7.06	Galactic centre source
0.3-0.2	5.00:		9.2	7.51	Galactic centre source
1.5-0.0	7.00:		9.2	8.40	Galactic centre source
15.7+0.8	2.40:		0.1	0.29	
31.0-0.2	4.40:	<9.69	7.9	6.50	Angular radius poorly determined
37.1-0.8	3.30:	<22.8	6.9	5.40	Angular radius poorly determined
51.8-0.2	5.05:		0.2	0.59	
53.6-0.2	3.70:		0.8	1.33	
77.9+0.2	5.10:		3.5	3.97	

$\langle D_c \rangle$  is systematically smaller than  $\langle D_{kin} \rangle$ . This is caused by the selection of strong sources from Baud's catalogue (Baud *et al.*, 1981) only, thus limiting ourselves to relatively nearby objects.

#### V.5 Masers in the solar neighbourhood

We define the solar neighbourhood as  $r < 1$  kpc,  $|z| < 1$  kpc, where  $r = D \cos b$  the distance projected onto the galactic plane. There are only a few OH/IR stars in the solar neighbourhood (in our sample 8: see table 2). Two of them, OH 26.5+0.6 (AFGL 2205) and OH 39.7+1.5 (AFGL 2290), have well established (geometric) distances. Table 3 shows, however, that in all these stars the usually weak main line maser (at 1667 MHz) could be detected, which is otherwise rarely the case.

Table 3

Name	D (kpc)	$V_{LSR}$ ( $\text{km s}^{-1}$ )	$\text{Log } S_H$ 1612 MHz	$\text{Log } S_H$ 1667 MHz	$\text{Log } S$ 22.2 GHz	$\text{Log } S$ 43.1 GHz	Remarks
OH 15.7+0.8	0.29	- 0.62	1.494	0.239			
OH 18.8+0.6	0.75	+12.75	1.458	0.278	n.d		OH 1821-12
OH 26.5+0.6	0.98	+26.86	2.440	0.841		n.d	AFGL 2205. Geometric distance
OH 36.9+1.3	0.80	-12.22	0.642				Not observed at other frequencies
OH 39.7+1.5	0.57	+20.00	1.797	-0.222			AFGL 2290. Geometric distance
OH 51.8-0.2	0.59	+ 2.01	0.750	0.000			
OH 80.8-1.9	0.50	- 1.97	2.417	1.176	1.903	2.000	AFGL 2650. IRC+40448. NML Cyg. 1.398 (86.2 GHz)

Furthermore, the velocities of these eight stars with respect to the local standard of rest are small. Of the OH/IR stars in Baud *et al.* (1979), that were not included in our monitor program, only 11 also have low

velocities; assuming that their luminosity has the mean value of the OH Mira's (an underestimate), not more than two of them will have distances (just) below 1 kpc.

All other masers, SiO at 43.1 GHz and 86.2 GHz, H<sub>2</sub>O at 22.2 GHz, and OH at 1612 MHz, at 1667 MHz, and occasionally at 1665 MHz, are associated with Mira variables and IRC sources. We will first look in some more detail at these objects.

### 5.a1 Distances

For the Mira variables we can find the distance (i) from a period-luminosity relation (see e.g. Robertson and Feast, 1981; Glass and Lloyd Evans, 1981), or (ii) from the visual magnitude at maximum (see Rieu *et al.*, 1979). Also the K (2.2 $\mu$ m) magnitude is (iii) a reasonable distance indicator (see figure 5; see also Dyck *et al.*, 1974). Because 2.2  $\mu$ m is about midway between the maximum of the stellar energy distribution and that of the dust shell (see Forrest *et al.*, 1979), the flux there is more or less the same for all stars. For the IRC Mira's we used the last method, and for the classical Mira variables the mean of the three methods; generally they yield quite similar distances.

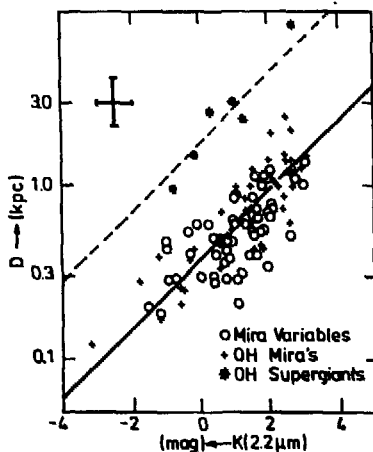


Figure 5. Distance as function of the apparent K magnitude.  $K_{abs}$  (1 kpc) = 2.1<sup>m</sup> may serve as a reasonable distance indicator for those sources where other distance determinations are impossible or controversial.

### 5.a2 Probability of maser emission in classical Mira's

To find the percentage of classical Mira variables that has maser emission we will use the sample of Feast (1963), which has the same distribution over the periods as the complete sample of Mira's (see Wood

and Cahn, 1977). and is homogeneous in distance to  $\sim 1$  kpc (see figure 6).

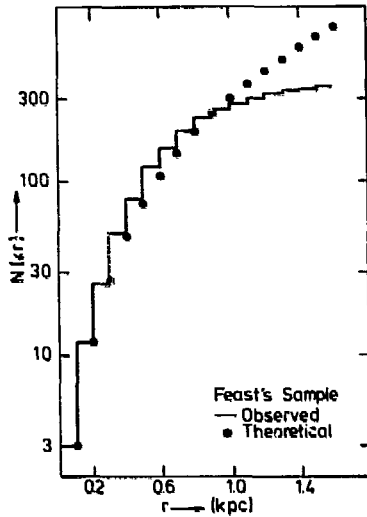


Figure 6. Number distribution of Mira variables in Feast's (1963) sample within projected distance,  $r$ . The dots are the expected values for a cylindrical space distribution.

Feast's sample was searched for various kinds of maser emission by numerous observers, always incompletely and each with a different sensitivity and/or velocity resolution. Therefore we used the integrated flux densities and included a positive detection only if it was stronger than the highest lower limit (e.g.  $0.4 \cdot 10^{-22} \text{ Wm}^{-2}$  for the OH masers). The distribution of the observed objects (including the negative detections) over the periods

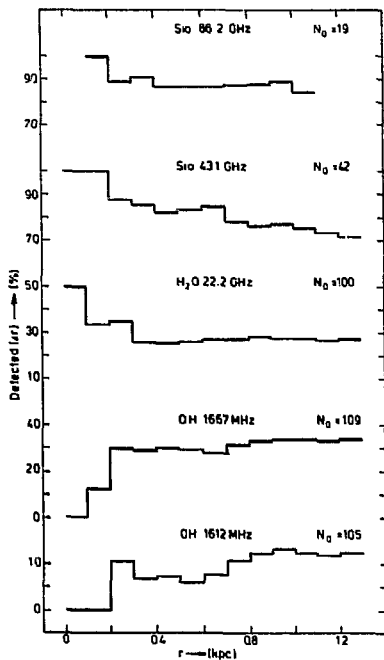


Figure 7. Percentage of Mira variables that were detected (above a certain completeness limit,  $L_c$ ) at various maser transitions within projected distance,  $r$ .

and over the distances was checked against Feast's sample to guard against selection effects. The percentage of positive detections (see Engels, 1979 and references cited there) for the classical Mira's is displayed as a function of the (projected) distance in figure 7. Clearly, the poor sensitivity at the higher frequencies puts the 'completeness' horizon for the SiO and H<sub>2</sub>O masers close to the sun ( $r \lesssim 200$  pc), whereas the OH masers have a fairly constant detection percentage out to 1.2 kpc. Probably all M-type Mira's exhibit SiO maser emission, both at 43.1 GHz and at 86.2 GHz, and a high percentage ( $\gtrsim 30\%$ ) has an H<sub>2</sub>O maser. 1667 MHz OH masering is seen in 34% of the stars (cf. Kieu *et al.*, 1979) and 1612 MHz OH in 12.5% of the cases. All 1612 MHz emitters also have (in a few cases stronger) emission at 1667 MHz. As was noted before (see Bowers and Kerr, 1974; Olnon, 1977) the probability on OH maser emission increases with increasing periods, corresponding to stars with a steeper rise to maximum (i.e. smaller  $f$ -values) and higher colour indices (i.e. redder, and so thicker dust shells). Therefore, a higher success rate is expected for the IRC Mira's, and indeed Wilson and Barrett (1972) detected 5 out of 35 (14.3%) 1612 MHz masers in the solar neighbourhood (IRC sources with  $K < 2^m$ ).

#### 5.b1 Z-distribution for OH masers

For the determination of the  $z$ -distribution of 1612 MHz OH masers in the solar neighbourhood (Mira's, IRC- and OH/IR stars) we used all sources to  $r=1.2$  kpc that are stronger than  $0.4 \cdot 10^{-22} \text{ W m}^{-2} \text{ kpc}^2$ . The results are given in table 4; the masers have been divided into four groups according to the velocity separation,  $\Delta v$ , of the two strongest peaks in the OH line profile.

Table 4

$\Delta v$ ( $\text{kms}^{-1}$ )	$n$	$v_e$ ( $\text{kms}^{-1}$ )	$\langle  z  \rangle$ (pc)	$\sigma_z$ ( $\text{kms}^{-1}$ )	$\langle P \rangle$ (days)	$\langle I-K \rangle$ (mag)
0 - 10	8	3.60	408	45.3	343	3.96 (5)
10 - 20	6	6.93	525	58.2	362 (5)	5.25 (4)
20 - 30	14	13.25	198	22.0	761 (7)	5.98(11)
> 30	8	18.76	113	12.5	850 (7)	6.76 (6)
Total	36	11.28	280.3	31.1	586.4	5.659

$v_e (\equiv \frac{1}{2} \Delta v)$  is the expansion velocity of the shell. The velocity dispersion,  $\sigma_z$ , is related to the average  $z$ -distance (in pc) by (see also section 6a)

$$\sigma_z (\text{kms}^{-1}) = \sqrt{\frac{\pi}{2}} \alpha^{-1} \langle |z| \rangle \quad (14)$$

where, denoting the galactocentric distance by  $R$  (in kpc),

$$\alpha = 4.289 \{3.930 R^{-1} - 0.02489 R\}^{-1} \quad (15)$$

(see Schmidt, 1965). The tabulated velocity dispersions can be compared with  $\sigma_z = 45 \pm 11 \text{ kms}^{-1}$  for Long Period Variables (with  $P > 300$  days), and  $\sigma_z = 27 \text{ kms}^{-1}$  for planetary nebulae (Oort, 1965). The mean  $z$ -distances are in good agreement with the values from Ikaunieks (1963), who gives  $\langle |z| \rangle = 638 \pm 193 \text{ pc}$  for LPV with  $P \lesssim 250$  days decreasing to  $\langle |z| \rangle = 165 \pm 22 \text{ pc}$  for those with  $P \gtrsim 410$  days. We derive for the OH masers in the solar neighbourhood (see figure 8)

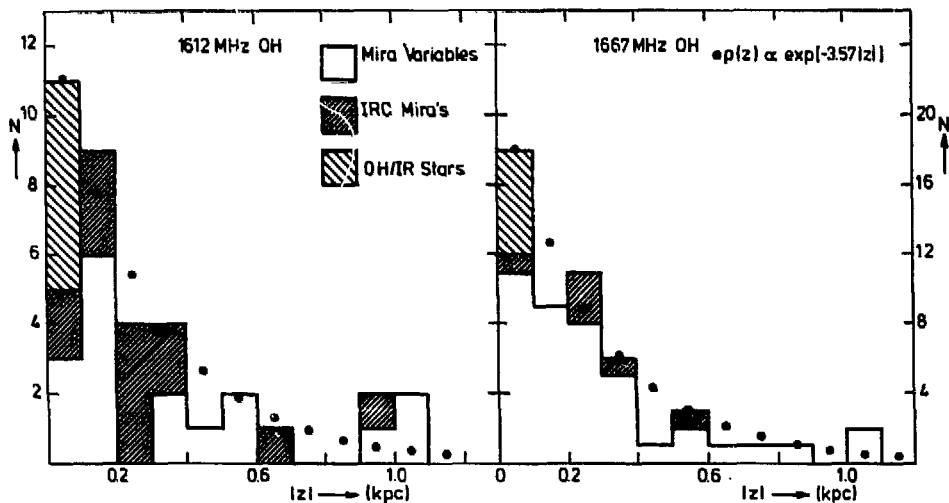


Figure 8.  $z$ -distribution of OH masers in the solar neighbourhood.

$$p(z) \propto \exp[-3.57|z|] \quad (16)$$

Here  $z$  is expressed in kpc, implying a scaleheight of 280 pc. This is somewhat smaller than the 314 pc for the classical Mira variables (see Wood and Cahn, 1977), that are on the average somewhat older, and have shorter periods ( $\langle P \rangle = 375$  days) than the OH Mira's.

#### 5.b2 Space density of 1612 MHz OH masers

There are four groups of objects that make up the space density of

1612 MHz OH masers in the solar neighbourhood:

- i) classical Mira variables
- ii) IRC Mira's, without visual counterparts
- iii) OH/IR stars, at most identified with AFGL sources
- iv) one M-type supergiant

We will consider the number density in each group, and its completeness separately.

i) Wood and Cahn (WC, 1977) give the space density of Mira variables as

$$\rho(z) = 245 \exp[-3.18|z|] \quad (\text{kpc}^{-3}) \quad (17)$$

leading to 464 Mira's within  $r < 1$  kpc,  $|z| < 1$  kpc, over all periods. Using the detection percentage for OH maser emission (section 5.a2) we conclude there are 58 OH masers (1612 MHz) in this group stronger than the chosen lower limit ( $S_{\text{int}} > 0.4 \cdot 10^{-22} \text{ Wm}^{-2}$ ). WC claim that their sample is complete out to  $r=1.7$  kpc and we will accept that in our calculations, although we feel some reservation: stars could have been missed because observers often work in limited areas, or because the variability has not been recognized.

ii) There are 35 IRC Mira's with distances  $D < 1$  kpc (i.e.  $K < 2.1$ ) with a colour index  $I-K > 6.0$ . All were observed for 1612 MHz maser emission (Wilson and Barrett, 1972) and 5 (14.3%) were detected at our completeness limit ( $S_{\text{int}} > 0.4 \cdot 10^{-22} \text{ Wm}^{-2}$ ; 6 others were detected at lower levels). In the range  $5.5 < I-K < 6.0$  there are 18 IRC Mira's with  $D < 1$  kpc, none of which was observed at 1612 MHz. But WC have also 18 (classical) Mira variables in this (I-K) range of which *two* show maser emission. Thus we conclude that among the unobserved IRC sources there will be 2 masers. For  $I-K < 5.5$  all IRC sources (of interest to us!) are optically identified and included in WC's sample.

The IRC catalogue covers 77.2% of the sky ( $\delta > -33^\circ$ ). Furthermore, in selecting the IRC sample we used spherical coordinates instead of cylindrical. Finally, we conclude that in the local neighbourhood

$$(5+2) \frac{1.5}{0.772} = 13.6 \text{ IRC masers exist, of which 5 are known at present.}$$

iii) Already we found in the solar neighbourhood only six OH/IR stars in Baud's survey (Baud *et al.*, 1979), two of them identified with AFGL sources. Baud's radio survey covered reasonably completely the area  $\ell = 0^\circ -$

180°,  $b = -4^\circ$  to  $+4^\circ$ . When we assume  $\langle |z| \rangle = 80$  pc (the mean period of the OH/IR stars is  $\sim 1000$  days) the completeness at  $r=1$  kpc is 61.3%. So we conclude that  $6 \frac{2}{0.613} = 19.6$  OH/IR stars exist, of which 6 are known at present.

iv) There is one supergiant in the solar neighbourhood: NML Cyg (see table 3). Its distance is rather controversial but our result seems to support the most commonly adopted value of 500 pc (e.g. Hyland *et al.*, 1972), but recently Morris and Jura (1983) argued that 2 kpc is more likely. NML Cyg probably is a singular object and of no significance for the statistics; the detection rate for OH emission from supergiants is very low (see e.g. Bowers, 1975).

A total of 92.2 1612 MHz OH masers with  $S_{\text{int}} > 0.4 \cdot 10^{-22} \text{ Wm}^{-2}$  is found ( $r < 1$  kpc,  $|z| < 1$  kpc), or

$$\rho_{1612}(z) = 53.9 \exp[-3.57|z|] \quad (\text{kpc}^{-3}) \quad (18)$$

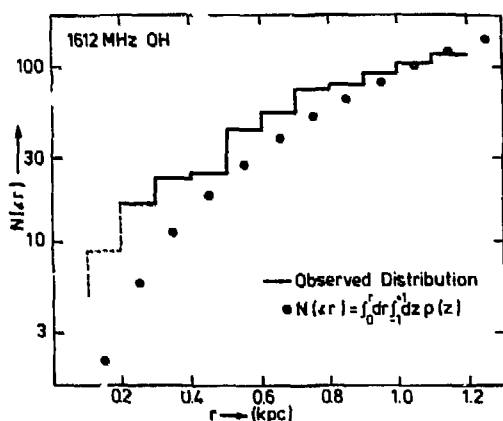


Figure 9. Number distribution of 1612 MHz OH masers within projected distance,  $r$ .

This may be compared with the observed distribution (corrected for incompleteness) in figure 9. The number of stars in each bin is small

( $< 6$ ), but it seems that the correction factor for the Mira variables is somewhat too large for  $r \lesssim 0.5$  kpc, and somewhat too small for  $r \gtrsim 0.5$  kpc. We suggest that this is the case, because observers have looked preferentially at the optically brighter, more nearby stars, although the detection probability remains virtually constant out to  $r = 1.2$  kpc. For the IRC Mira's, more homogeneously selected (see Wilson and Barrett, 1972), such an effect is not present. It may prove worthwhile to search for 1612 MHz OH emission from weak Mira variables ( $m_v < 9.5$  at max.) within 1.2 kpc.

### 5.c1 Luminosity function of OH masers (1612 MHz)

The distribution of all OH masers observed in the solar neighbourhood (corrected for incompleteness) over the absolute ( $D=1$  kpc) integrated flux densities ( $L_{\text{int}}$ , expressed in  $10^{-10} L_{\odot}$ ) is shown in figure 10. To minimize the influence of variability (for most sources unknown), and of statistical errors the data were Hanning smoothed. The slope at the high luminosity end is known from radio surveys. We will adopt  $N(L) \propto L_{\text{int}}^{-2}$  as suggested by Olsson (private communication), where  $N(L)$  denotes the number of sources in an interval of  $\pm 0.15$  around  $\text{Log } L_{\text{int}}$ . This relation has a somewhat steeper slope than that of  $-1.65$  used by Baud *et al.* (1981). Adjusting the curve at the low luminosity end, we write (at  $z=0$ )

$$\text{Log } N = -0.477 \text{Log}^2 L_{\text{int}} + 0.706 \text{Log } L_{\text{int}} + 0.784 \text{ for } \text{Log } L_{\text{int}} < 2.834 \quad (19a)$$

$$\text{Log } N = -2 \text{Log } L_{\text{int}} + 4.619$$

$$\text{for } \text{Log } L_{\text{int}} > 2.834 \quad (19b)$$

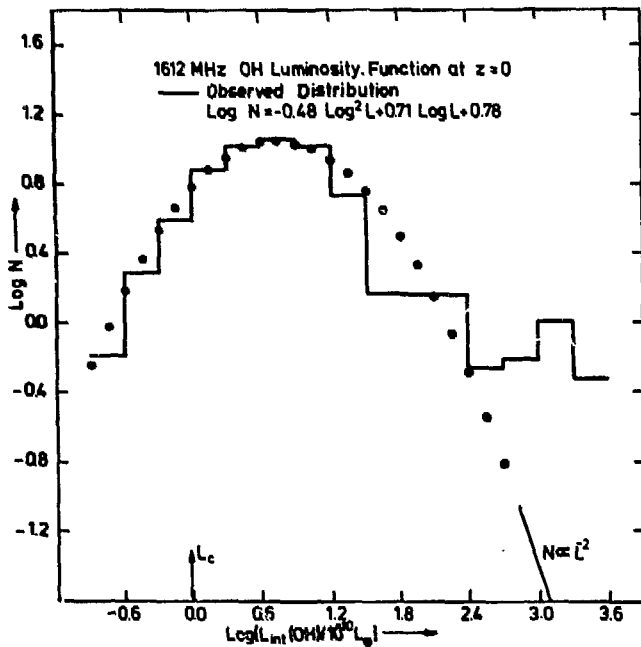


Figure 10. Luminosity function for 1612 MHz OH masers in the solar neighbourhood.  $L_c$  is the completeness limit.

Note that the completeness limit,  $L_c = 0.95 \cdot 10^{-10} L_\odot$ , falls well below the maximum in the luminosity function at  $L_{int} = 5.5 \cdot 10^{-10} L_\odot$ . The decline at the low luminosity end certainly is real, because about 30 Mira variables with  $D < 0.4$  kpc have been observed without detection (i.e.  $\text{Log } L_{int} < -0.818$ ), whereas the few sources at small distances that were detected have fluxes well above the completeness limit. For a number of stars an even more stringent upper limit was set for the (1612 MHz) maser emission in programs with much better sensitivity (see e.g. Olnon *et al.*, 1980). The two stars with low fluxes (RU Hya and U Ori, which was much stronger a few years ago; see Jewell *et al.*, 1979, and chapter II, figure 9) therefore have been included in the analysis.

From the luminosity function we predict 0.7 masers stronger than  $\text{Log } L_{int} = 2.4$  in the solar neighbourhood, and, apart from the singular object NML Cyg, one (OH 26.5+0.6) is known. Out to  $r=2$  kpc a total of 46.9 strong ( $\text{Log } L_{int} \geq 1.6$ ) OH emitters is expected. As none of the IRC Mira's is that strong, there are only 18 objects (all OH/IR stars; see table 2) known, that satisfy these conditions. However, they correspond to a total number of 47.2 after correcting for the incomplete sky coverage ( $0^\circ < \ell < 180^\circ$ ;  $|b| \lesssim 4^\circ$ ). Furthermore, of the IRC Mira's with  $2.0^m < K < 3.5^m$  (or  $0.96 < D < 1.91$  Kpc) 9.6% should be detectable above  $\text{Log } L_{int} = 0.6$ . Wilson and Barrett (1972) found 9 OH emitters out of 113 candidates (or 8%, see their figure 25), in good agreement with the prediction ( $\sim 11$  sources),

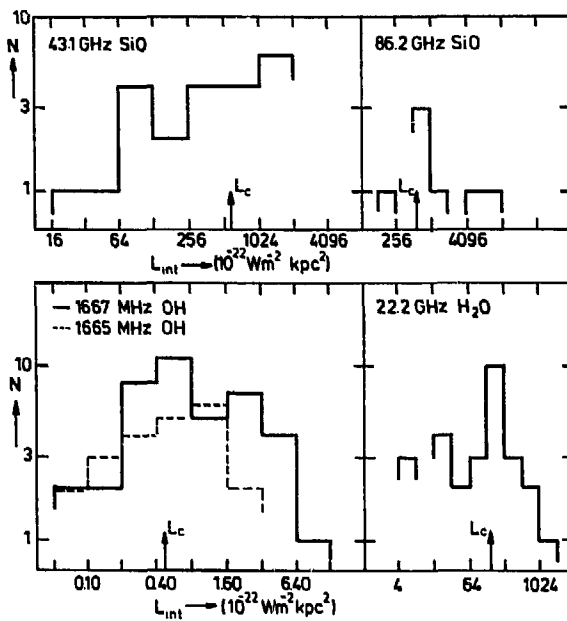


Figure 11. Luminosity distribution of other masers in the solar neighbourhood.  $L_c$  is the completeness limit.

especially in view of the small numbers involved and the fact that Wilson and Barrett may have missed a few sources because they were at their minimum.

### 5.c2 Other masers

The luminosity distributions of the other masers in the solar neighbourhood, the main lines of OH at 1665 MHz, and at 1667 MHz, the  $6_{16} \rightarrow 5_{23}$  transition of H<sub>2</sub>O at 22.2 GHz, and the two transitions of SiO in the first vibrational state ( $v=1$ )  $J=1 \rightarrow 0$  (43.1 GHz) and  $J=2 \rightarrow 1$  (86.2 GHz), all have a maximum at their completeness limit (see figure 11). Clearly, a lot more low luminosity objects still might be detected, and an extension of more sensitive searches (e.g. Olmon *et al.*, 1980) to a larger and more homogeneous data base is called for.

### V.6 OH/IR stars as a galactic population

OH/IR stars can be seen (at 1612 MHz) out to very large distances: a strong source such as OH 26.5+0.6 is detectable ( $> L_c = 0.95 \cdot 10^{-10} L_\odot$ ) out to  $D=50$  kpc. Furthermore, the distances to individual objects can be determined very accurately when good radio light curves and maps of the brightness distribution both are available, and reasonably well when the variability only is known. Radial velocities we get directly from the radio spectra. Therefore, OH/IR stars give valuable information on the structure and on the kinematics of a stellar population throughout the Galaxy. Because in our program we have limited ourselves to the apparently stronger sources ( $S_{OH} > 4$  Jy), probably somewhat more nearby objects were selected.

### 6.a Z-distribution for 1612 MHz OH masers.

In the solar neighbourhood we found (see table 4, and figure 13) a dependence of the scaleheight on the expansion velocity, which can be written as

$$\text{Log } \langle |z| \rangle = -0.044 v_e + 2.889 \quad (20)$$

where  $\langle |z| \rangle$  is in pc when  $v_e$  is given in  $\text{kms}^{-1}$ . To analyse the  $z$ -distribution at larger distances from the sun we delete objects with  $D < 2$  kpc, because Baud's survey (Baud *et al.*, 1979) is for  $|b| \lesssim 4^\circ$ . The sample was divided into three bins, according to galacto centric distance  $R$ . We may write for the density as function of  $z$

$$\rho(z) = \rho_0 \exp\left[-\frac{1}{\sigma_z^2} \int_0^z K_z dz\right] \quad (21)$$

where  $K_z$  is the force in the  $z$ -direction, and  $\sigma_z$  the velocity dispersion (see Oort, 1965). Taking

$$\frac{dK_z}{dz} = -4\pi G m_\odot(R) \quad (22)$$

with  $m_\odot(R)$  the mass density ( $M_\odot \text{pc}^{-3}$ ) in the plane, we find

$$\rho(R, z) = \rho_0(R) \exp[-\alpha^2 z^2] \quad (23)$$

with

$$\alpha(R) = \sigma_z^{-1} \{2\pi G m_\odot(R)\}^{\frac{1}{2}} \quad (24)$$

The mass density,  $m_\odot(R)$  is given as function of  $R$  (in kpc) by

$$m_\odot(R) = 3.930 R^{-1} - 0.02489R \quad (25)$$

(Schmidt, 1965:  $R_\odot = 10$  kpc). So, finally, we find a predicted value for the mean  $z$ -distance

$$\langle |z| \rangle_p = \sqrt{\frac{2}{\pi}} 4.289 \sigma_z m_\odot(R)^{-\frac{1}{2}} \quad (26)$$

For the moment we take  $R_\odot = 10$  kpc. Baud *et al.* (1981) found that the values of  $\sigma_\pi$  and  $\sigma_\theta$ , the velocity dispersions in the plane, are roughly the same (or only slightly higher) for the OH/IR stars at  $R=5$  kpc as for the same population in the solar neighbourhood. Martinet and Mayer (1975) showed that for various galactic mass models the ratio  $\sigma_z/\sigma_\pi$  is constant between  $R=5$  kpc and 15 kpc. So, we will assume that  $\sigma_z$  is a constant for a given population throughout the Galaxy, bearing in mind that it is likely to increase slightly

towards the inner parts of our Galaxy. Then, a decrease of  $\langle |z| \rangle$  is expected towards smaller values of  $R$ . For  $v_e = 15 \text{ km s}^{-1}$  we found  $\sigma_z = 18.75 \text{ km s}^{-1}$ , or  $\langle |z| \rangle = 169 \text{ pc}$  (equations 20 and 26) in the solar neighbourhood. Adjusting the measured values of  $\langle |z| \rangle$  (see table 5) at slightly differing  $\langle v_e \rangle$  to  $v_e = 15 \text{ km s}^{-1}$ , the mean expansion velocity for all OH/IR stars, the expected decrease of the mean  $z$ -distance is found indeed (see figure 12).

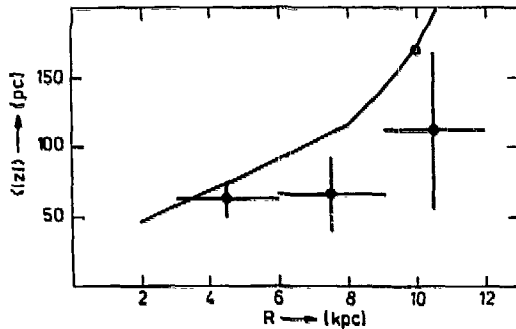


Figure 12. Scale height,  $\langle |z| \rangle$ , of 1612 MHz OH masers as function of  $R$ , the galactocentric distance. The drawn line is the expected dependence of  $\langle |z| \rangle$  on  $R$  from a Schmidt mass model and a constant velocity dispersion,  $\sigma_z$ .

The measured  $\langle |z| \rangle$  values lie somewhat lower than expected from equation (26). There are two reasons for this: in the first place even at a distance  $D=3 \text{ kpc}$  (where  $b=4^\circ$  corresponds to  $z=210 \text{ pc}$ ) still 10% of the total number of OH/IR stars are, if the scaleheights inferred from equation (26) are right, outside the observed area. And only one star at  $z=300 \text{ pc}$  would increase the mean in the second bin to  $\langle |z| \rangle = 90 \text{ pc}$ . In the second place at larger distances, i.e. at on the average smaller  $R$ , we see the intrinsically stronger sources. If the interstellar UV field indeed plays a role in determining the strength of a maser, we might consequently underestimate the scaleheight. On the other hand it seems likely that the strength (and height) of the UV field increases with decreasing  $R$ , thus balancing this effect. The *measured* decrease for the scaleheight of a factor 3, and the constancy of the velocity dispersions, *deduced* from fitting the observed  $\lambda$ - $v$  distribution (see Baud *et al.*, 1981), certainly is real. It seems in contradiction with the assumption made by van de Kruit and Searle (1981), that  $\langle |z| \rangle$  is a constant for an entire galaxy (implying that  $\sigma_z$  increases by a factor 10 over 5 scalelengths inward). However, van de Kruit and Searle model the total light distribution of a galaxy, that is made up by different populations in differing regions of a galaxy. As was the case in the solar neighbourhood, the OH/IR stars with smaller expansion velocities,  $v_e$ , have a larger  $\langle |z| \rangle$ , i.e. a higher velocity dispersion (see table 5).

Table 5

$n$	$\langle v_e \rangle$ ( $\text{kms}^{-1}$ )	$\langle  z  \rangle$ (pc)	$\langle  z  \rangle$ (pc)	$v_e$ ( $\text{kms}^{-1}$ )	$n$	$\langle v_e \rangle$ ( $\text{kms}^{-1}$ )	$\langle  z  \rangle$ (kpc)	$\langle  z  \rangle$ (pc)	$\langle v_e \rangle$ ( $\text{kms}^{-1}$ )
3 - 6	10	15.73	58.5	13.1	> 17	7	18.20	6.43	47.5
6 - 9	12	14.81	67.2	25.8	14-17	9	15.52	7.12	82.8
9 -12	5	13.09	136.5	56.4	< 14	12	12.03	8.18	82.9

Again equation (26) is used to compare the scaleheights of the OH/IR stars, measured at  $\langle R \rangle = 7$  kpc, with the values for the OH masers in the solar neighbourhood. There is good agreement (see figure 13), although  $\langle |z| \rangle_{\text{meas.}}$  is systematically somewhat smaller, especially for the group with  $v_e < 14 \text{ kms}^{-1}$ .

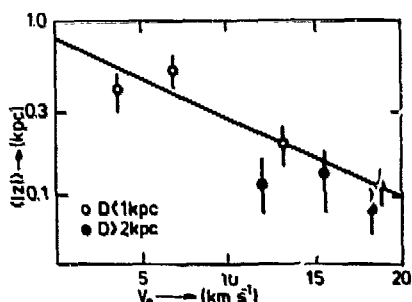


Figure 13. Scale height,  $\langle |z| \rangle$ , of 1612 MHz OH masers as function of the shell expansion velocity  $v_e$ . Open circles are masers in the solar neighbourhood, dots are OH/IR stars at large distances. The drawn line is a least squares fit for the local sources (equation 20).

As the galacto centric distance is largest for this group, the incompleteness of Baud's survey may account for this. If we include the OH/IR stars in the determination of the  $\log \langle |z| \rangle - v_e$  relation, which was based on the small sample of masers in the solar neighbourhood, equation (20) may be rewritten as

$$\text{Log } \langle |z| \rangle = -0.060 v_e + 3.009 \quad (20')$$

#### 6.b Space density of OH masers as function of galacto centric distance

The radial dependence of the density can be determined by fitting the observed longitude distribution (see Baud *et al.*, 1981). Baud *et al.* used a power law ( $\rho \sim R^{-4}$ ) but, although there is not much difference in the quality of the fit, we will assume an exponential decrease of the density with  $R$ . This is in better accord with current galaxy models (see Bahcall and Soneira, 1980), and it yields better agreement between the number densities measured at  $R = 5$  kpc and in the solar neighbourhood. Using Baud's programs that correct for incompleteness and for differing sensitivities in different parts of the

survey, the density distribution may be written as (see figure 14)

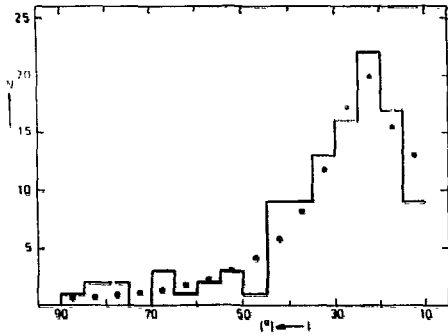


Figure 14. Distribution of the OH/IR stars in Baud's survey (Baud *et al.*, 1979) over the galactic longitude. Dots are our fit (equations 27a and 27b).

$$\rho(R) = \rho_0 \exp[-0.815 R] \quad \text{for } R > R_M = 3.9 \text{ kpc} \quad (27a)$$

$$= \rho_1 R^{+7} \quad \text{for } R < R_M \quad (27b)$$

Here we adopt  $R_0 = 9.2$  kpc, the radial dependence of the z-distribution as described by equation (26) (for  $v_e = 15 \text{ km s}^{-1}$ ; the mean value for all OH/IR stars), and the luminosity function as given by equations (19a) and (19b). The shape of the steep decline at low galactic longitudes (equation 27b) is taken to be that of Baud *et al.* (1981). Note that the maximum of the distribution,  $R_M = 3.9$  kpc, coincides with that of the molecular ring (see Gordon and Burton, 1976). Continuity at  $R=R_M$  requires that the coefficients  $\rho_0$  and  $\rho_1$  are related by  $\rho_1 = 2.96 \cdot 10^{-6} \rho_0 \text{ (kpc}^{-3}\text{)}$ .

### 6.c Synthesis

We may combine the results from sections 5b, 5c, 6a, and 6b. Expressing densities in  $\text{kpc}^{-3}$ , all length scales in kpc, luminosities in  $10^{-10} L_\odot$ , and velocities in  $\text{km s}^{-1}$ , the density distribution of 1612 MHz OH masers can be written as

$$\rho(R,z,L) = 10^5 \Phi(L) \exp[-0.815 R] \exp[-\alpha |z|] \quad \text{for } R > 3.9 \text{ kpc} \quad (28a)$$

$$= 0.30 \Phi(L) R^7 \exp[-\alpha |z|] \quad \text{for } R < 3.9 \text{ kpc} \quad (28b)$$

The distribution over the integrated OH luminosity is given by

$$\Phi(L) = -0.207 \ln^2 L + 0.706 \ln L - 2.183 \quad \text{for } \ln L < 6.526 \quad (29a)$$

$$= -2 \ln L + 6.648 \quad \text{for } \ln L > 6.526 \quad (29b)$$

normalized in such a way that

$$\int_{L_c}^{\infty} \Phi(L) dL = 1 \quad (30)$$

where the completeness limit  $L_c = 0.95 \cdot 10^{-10} L_{\odot}$ , corresponding to  $L_{int} \approx 0.4 \cdot 10^{-10} W_m^{-2} \text{kpc}^2$ . Further

$$\alpha(R, v_e) = \langle |z_{\odot}(v_e)| \rangle m_{\odot}(R)^{\frac{1}{2}} \quad (31)$$

where the scaleheight is given by (equations 20' and 31)

$$\langle |z_{\odot}(v_e)| \rangle = 0.387 \cdot 10^{-0.060 v_e} \quad (32)$$

and the mass distribution (in  $M_{\odot} \text{pc}^{-3}$ , following Schmidt, 1965)

$$m_{\odot}(R) = 3.616 R^{-1} - 0.02705 R \quad \text{for } R < 9.2 \text{ kpc} \quad (33a)$$

$$= 1038.2 R^{-4} \quad \text{for } R > 9.2 \text{ kpc} \quad (33b)$$

A total number of 59400 1612 MHz masers stronger than  $L_c$  is deduced for our Galaxy ( $1.5 \text{ kpc} < R < 14 \text{ kpc}$ ).

#### V.7 Properties of OH/IR stars

Up till here we have discussed almost solely the phenomenological aspect of OH masers. But the measured quantities, such as luminosity, period, expansion velocity of the shell etc., contain unique information on the properties of the central star, and of the surrounding dust envelope. In this section we will limit ourselves to those stars for which IR observations are available (see chapter IV, table 4). It should be borne in mind that, where the OH/IR stars in the Dwingeloo monitor program form a complete sample for (harmonic mean) fluxes stronger than 4 Jy, the objects included in the UKIRT program were selected rather arbitrarily. Throughout this section it will be

assumed that the OH/IR stars are pulsating in the *fundamental* mode, and that their composition is solar:  $(X,Z) = (0.68, 0.02)$ . All results are summarized in tables 7 and 8 at the end of this section.

### 7.a Effective temperatures

Knowledge of the effective temperature,  $T_{\text{eff}}$ , is essential for the determination of several stellar parameters (radius, mass, pulsation mode). Even for the classical Mira variables  $T_{\text{eff}}$  is very difficult to determine (see e.g. Ridgeway *et al.*, 1980; or Feast, 1981), let alone for the OH/IR stars where the central object is completely obscured, sometimes by as much as  $100^m$  of visual absorption. We will use the *mean* luminosities (see chapter IV) and assume that on the average the OH/IR stars lie on the asymptotic giant branch (AGB). The locus of the AGB in the HR diagram is given by (Fox and Wood, 1982)

$$M_{\text{bol}} = 38 \text{ Log } T_{\text{eff}} - 138.5 \quad (34)$$

It is derived by using the observed relation between  $M_{\text{bol}}$  and the colour index  $[R-I]$  for old disk giant branch stars (Eggen, 1975); this relation can be converted to a  $L_*$ ,  $T_{\text{eff}}$  relation by adoption of the  $[R-I]$ ,  $\text{Log } T_{\text{eff}}$  conversion given by Bessel (1979), that is based on the effective temperature scale from Ridgeway *et al.* (1980). For the two Mira variables in our sample (WX Ser and RS Vir) the assumption of fundamental mode pulsation might be in error (*cf.* Robertson and Feast, 1981; Glass and Feast, 1981). Furthermore note that, if the temperature scale of Johnson (1966) and Lee (1970) is used, a different definition of the AGB is found.

With the temperatures found from equation (34) the stellar radii can be calculated using the standard definition

$$L_* = 4\pi R_*^2 T_{\text{eff}}^4 \quad (35)$$

Typical values are  $T_{\text{eff}} \approx 3100$  K, and  $R_* \approx 500 R_\odot$  (see table 7). Later (section 7.g), we shall see that the effective temperatures derived in this way probably are  $\sim 10\%$  too high, and hence the radii  $\sim 20\%$  too small.

## 7.b Pulsation masses

The pulsation 'constant',  $Q$ , is defined as

$$Q \equiv P/\rho = P M_{\text{pul}}^{1/2} R_{\star}^{-3/2} \quad (36)$$

Fox and Wood (1982) have calculated pulsation 'constants', that vary slowly with period, for various pulsation modes, and abundances. They find for stars pulsating in the fundamental mode (solar abundance)

$$\text{Log} \frac{M_{\text{pul}}}{M_{\odot}} = 2.5 \text{Log} \frac{R_{\star}}{R_{\odot}} - 1.25 \text{Log} P - 2.769 \quad \text{for} \frac{M}{M_{\odot}} \lesssim 2 \quad (37a)$$

$$\text{Log} \frac{M_{\text{pul}}}{M_{\odot}} = 2.651 \text{Log} \frac{R_{\star}}{R_{\odot}} - 1.205 \text{Log} P - 3.246 \quad \text{for} \frac{M}{M_{\odot}} > 2 \quad (37b)$$

As we know the periods ( $P$ ) from the Dwingeloo monitor program (chapter II, table 2), and the radii ( $R_{\star}$ ) the pulsation masses,  $M_{\text{pul}}$ , can be determined.  $M_{\text{pul}}$  is the *present* mass of the star and it should be less (in view of the large mass loss rates) than the initial main-sequence mass. Although the use of equations (37a) and (37b) is an uncontrolled extrapolation (pulsation constants have only been determined for stars with  $P \lesssim 1000$  days), it is reassuring that generally the pulsation mass is found to be smaller than the main-sequence mass, and larger than the core mass. Note that an uncertainty of  $\sim 10\%$  in the effective temperature leads to errors up to 60% in  $M_{\text{pul}}$ .

## 7.c Main-sequence masses

Although these stars left the zero age main-sequence (ZAMS)  $\sim 10^6$  yr ago and lost a considerable fraction of their mass in the subsequent evolution, still their initial masses can be reasonably estimated. There are three different ways to do so; one is based on the initial core mass (Iben and Truran, 1978), the other two methods use the observed expansion velocity of the shell (Olson, 1981; Baud and Habing, 1983).

### 7.c1 Iben and Truran

Theory predicts (Iben and Truran, 1978) that the ZAMS mass of a star determines the initial core mass,  $M_{\text{co}}$  at the moment when hydrogen is reignited

$$M_{\text{CO}} = 0.95 + 0.075 \left( \frac{M_{\text{ZAMS}}}{M_{\odot}} - 7 \right) \quad (38)$$

where  $M_{\text{CO}}$  is in  $M_{\odot}$ . Using the Paczynski relation between core mass and luminosity (see section 7.d) we derive  $M_{\text{ct}}$ , the core mass after some time  $t$  on the AGB. Because the core mass is slowly growing (Iben, 1981; section 7.d) ZAMS masses found by using  $M_{\text{ct}}$  are slightly overestimated.

### 7.c2 Olton

At large distances from the star the expansion velocity of the circumstellar envelope is constant. The driving force of the flow, radiation pressure on the dust grains, is balanced by the gravitational and the drag forces. Olton (1981) writes for the expansion velocity

$$v_e^2 = C_1 \left( \frac{M}{M_{\odot}} \right) \left( \frac{L}{10^4 L_{\odot}} \right)^{-1} \left\{ C_2 \left( \frac{M}{M_{\odot}} \right)^{-1} \left( \frac{L}{10^4 L_{\odot}} \right) - 1 \right\} \quad (39)$$

where  $C_1$  and  $C_2$  are constants, whose values depend on the properties of the dust grains. For grains composed of dirty silicates (Jones and Merrill, 1976; Bedijn, 1977) the best values become  $C_1 = 150$  and  $C_2 = 4$ , giving  $v_e$  in  $\text{km s}^{-1}$ . This leads to

$$M_{\text{dyn}} = 4L_{\star} - v_e^2 L_{\star}^{\frac{1}{2}} / 150 \quad (40)$$

where  $M_{\text{dyn}}$  is in  $M_{\odot}$ , when  $L_{\star}$  is in  $10^4 L_{\odot}$  and  $v_e$  in  $\text{km s}^{-1}$ . Although here  $v_e$  is the expansion velocity of the dust grains, we use for  $v_e$  the expansion velocities of the gas, as measured from the single-dish radio spectra (see chapter II, table 2). Because the drift velocity of the grains through the gas can be very large (see Kwok, 1975) the dynamical mass found is overestimated. On the other hand in Olton's simple model the velocity the grains initially have at their condensation point is neglected, and furthermore the dynamical mass, i.e. the total mass within the radius where the outflow velocity becomes constant, is a lower limit to the ZAMS mass.

### 7.c3 Baud and Habing

In sections 5.b1 and 6.a it was found that the expansion velocity of

the OH shell,  $v_e$ , is correlated with the scaleheight above the galactic plane, i.e. with population age (cf. Baud *et al.*, 1981). The stars with larger  $v_e$  have a smaller mean z-distance, and consequently are increasingly more massive and younger. Baud and Habing (1983) interpreted the decrease of the number of sources with large expansion velocities ( $v_e > 15 \text{ km s}^{-1}$ ) as the reflection of the initial mass function (see Miller and Scalo, 1979). They find

$$\text{Log} \left( \frac{M_{ve}}{M_{\odot}} \right) = (v_e - 8)/16 \quad (41)$$

where  $v_e$  is in  $\text{km s}^{-1}$ . For several reasons (their effective temperatures are lower, their minimum OH luminosity and mass loss rates are higher than assumed here) this yields an *underestimate* of the ZAMS mass for low-mass, and an *overestimate* for high-mass stars.

In the further calculations we will assume that the initial main sequence mass is given by

$$M_{*i} = \frac{1}{3} (M_{\text{ZAMS}} + M_{\text{dyn}} + M_{v_e}) \quad (42)$$

the mean of the three different methods. The mean value,  $M_{*i}$ , may be used to derive a better form of the Baud and Habing relation (41). Then we find

$$\text{Log} \left( \frac{M_{*i}}{M_{\odot}} \right) = (v_e - 8.8)/12.3 \quad (41')$$

In table 6 the  $M_{*i}$ , derived for three groups of OH/IR stars, and the scaleheights (equation 20') are compared with the values as they are known for main-sequence stars in the solar neighbourhood.

Table 6

Objects	Mass <sup>1)</sup> ( $M_{\odot}$ )	$\langle  z  \rangle^2$ (pc)	OH/IR stars group	$\langle v_e \rangle$ ( $\text{km s}^{-1}$ )	$M_{*i}$ ( $M_{\odot}$ )	$\langle  z  \rangle$ (pc)	
O - B5	40-7	50	I	$v_e > 18$	21	8	56
B8 - A5	4-2	70	II	$12 < v_e < 18$	17	5	97
F	1.5	130	III	$v_e < 15$	12	1.6	194
dG	1.0	180					
dK	0.7	270					
dM	0.3	270					

1) Allen, 1976

2) Blaauw, 1965

The comparison of the scaleheights provides us with an independent check on the determination of the main-sequence masses. The progenitors of most OH/IR stars (the  $v_e$  distribution peaks sharply at  $15 \text{ km s}^{-1}$ ) are B5-F stars. A good example is OH 26.5+0.6 with  $M_{*i} = 2.8 M_{\odot}$ . Most OH Mira variables, with  $v_e < 10 \text{ km s}^{-1}$  in general, are the end products of F and dG stars. Very few massive stars ( $M_{*i} > 10 M_{\odot}$ ) are found. OH 21.5+0.5, for which  $M_{*i} = 33 M_{\odot}$ , is one and the supergiant NML Cygni (not included in the UKIRT program) is another. It is probably as massive as  $50 M_{\odot}$  (see Morris and Jura, 1983).

#### 7.d Mass of the stellar cores

##### 7.d1 Present core mass

The core mass of the stars at their present stage in evolution may be derived from the luminosity, using the theoretical Paczynski relation (Paczynski, 1970) for double-shell burning AGB stars

$$\left(\frac{L_{*}}{10^4 L_{\odot}}\right) = 5.925 \left\{ \left(\frac{M_{ct}}{M_{\odot}}\right) - 0.495 \right\} \quad (43)$$

where we use the mean luminosities, as found in chapter IV (table 4). Only two stars in our sample (OH 21.5+0.5 and OH 32.8-0.3) have core masses well above the Chandrasekhar limit ( $M_c = 1.4 M_{\odot}$ ), all the others have  $M_c \lesssim 1 M_{\odot}$ . The mean value is  $\langle M_{ct} \rangle = 0.623 M_{\odot}$  with a standard deviation of  $0.16 M_{\odot}$ .

##### 7.d2 Initial core mass

When we take the average value of the ZAMS mass from the three different methods described above, we may use equation (38) to derive the initial core mass,  $M_{co}$ . In all cases we find that  $M_{co} < M_{ct}$  by an amount of  $\lesssim 0.06 M_{\odot}$ . The rate of growth for the core mass during the thermal pulse phase is given by (Iben, 1981)

$$\dot{M}_c = \frac{6 \cdot 10^{-7}}{X} \left\{ \left(\frac{M_{co}}{M_{\odot}}\right) - 0.5 \right\} \quad (44)$$

where  $X = 0.68$  as before. This enables us to estimate the time spent until now on the AGB:  $t_{AGB}$ . The duration of the thermal pulse phase is found to be  $\sim 6 \cdot 10^5 \text{ yr}$  for the low mass stars (small  $v_e$ ) down to  $\sim 2 \cdot 10^5 \text{ yr}$  for the

more massive objects. Theoretical calculations by Becker and Iben (1979) indicate that the time from the start of the AGB phase until the onset of pulsation is roughly of the same order (their abundances are different, but for the most similar values  $(X,Z)=(0.71,0.01)$  they find  $\sim 6.7 \cdot 10^5$  yr for  $M_{*i}=5 M_{\odot}$ , and  $1.8 \cdot 10^5$  yr for  $M_{*i}=7 M_{\odot}$ ). Then  $t_{AGB}$  becomes  $\sim 1.2 \cdot 10^6$  yr for  $M_{*i} \approx 1.6 M_{\odot}$ , down to  $\sim 5 \cdot 10^5$  yr for  $M_{*i} \approx 8 M_{\odot}$ . Despite the large uncertainties in this calculation, this provides strong support for the hypothesis of Renzini and Voli (1981) that  $t_{AGB}$  is of the order of one million years, irrespective of the initial mass (for  $\sim 1 < M_{*i} < \sim 8$ ). Furthermore, our values of the AGB life time are long enough for the third dredge-up process to occur, that the theoreticians need to explain the envelope composition of planetary nebulae and the number of carbon stars (see Iben and Truran, 1978; Iben, 1981). Note that  $t_{AGB}$  is *not* the total life time on the AGB yet. Especially for the more massive stars  $M_{pul} \gg M_{ct}$ , and although the present mass loss rates are extremely high (see section 7.e), they can stay on the AGB for another  $\lesssim 10^5$  yr.

## 7.e Mass loss rates

### 7.e1 $\dot{M}$ based on infrared observations

For a mass outflow driven by radiation pressure on the dust grains we may write (see Elitzur, 1981; Knapp *et al.*, 1982)

$$\dot{M} = -2.67 \cdot 10^{-5} \left(\frac{\tau_d}{2}\right) \left(\frac{L_{*}}{10^4 L_{\odot}}\right) \left(\frac{v_e}{15 \text{ kms}^{-1}}\right)^{-1} M_{\odot} \text{ yr}^{-1} \quad (45)$$

where  $\tau_d$  is the optical depth corresponding to the dust response to radiation pressure. Following Werner *et al.* (1980) we choose  $\tau_d = 2$ , probably a slight *underestimate* for the OH/IR stars with the thickest envelopes.

### 7.e2 $\dot{M}$ based on radio observations

In section 4.a we found that the OH masers have a nearly constant surface brightness ( $L_{OH} \sim R_{OH}^2$ ). Baud and Habing (1983) use this result, and assuming a constant mass outflow they derive

$$\begin{aligned} \dot{M} &= -1.77 \cdot 10^{-7} v_e \frac{1}{2} L_{OH}^{\frac{1}{2}} = & (46) \\ &= -2.65 \cdot 10^{-5} \left( \frac{v_e}{15 \text{ kms}^{-1}} \right) \left( \frac{L_{OH}}{100 \text{ Jy kpc}^2} \right)^{\frac{1}{2}} M_{\odot} \text{ yr}^{-1} \end{aligned}$$

The constant is determined by assuming a *minimum* OH column density needed for a saturated maser to operate (see Elitzur *et al.*, 1976), consequently *overestimating* the mass loss rate (see figure 15). When we consider  $\dot{M} t_{AGB}$  we find that, if the mass loss rate had been constant during the time spent on the AGB, more than  $10 M_{\odot}$  would have been ejected, i.e. more than  $M_{*i}$ ! Thus it is clear that the high mass loss rates can occur only during a small fraction of  $t_{AGB}$ .

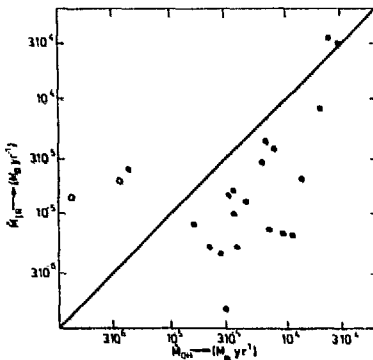


Figure 15. Comparison of the mass loss rates as determined from the stellar luminosity,  $\dot{M}_{IR}$ , and from the OH luminosity,  $\dot{M}_{OH}$ . Open circles are Mira variables, dots OH/IR stars.

### 7.e3 Reimers formula

The Reimers formula (Reimers, 1975; Kudritzki and Reimers, 1978), that is valid for ordinary red giants, gives us an impression of the mass loss rate at the beginning of the evolution along the AGB.

$$\dot{M}_R = -4 \cdot 10^{-9} \eta \left( \frac{L_*}{10^4 L_{\odot}} \right) \left( \frac{R_*}{R_{\odot}} \right) \left( \frac{M_*}{M_{\odot}} \right)^{-1} M_{\odot} \text{ yr}^{-1} \quad (47)$$

where the correct value of  $\eta$  (one usually assumes  $1/3 < \eta < 1$ ) is still subject of discussions (see Renzini, 1981a). Choosing  $\eta=1$  we calculate

$\dot{M}_R$  with the mean ZAMS mass, and the luminosity and radius at the start of the AGB ascent (inferred from the initial core mass), yielding values of  $10^{-7}$  to  $10^{-6} M_{\odot} \text{ yr}^{-1}$ . It should be noted that, even when we take into account a possible enhancement of  $\dot{M}_R$  by a factor 2.8 due to helium flashes

(duration  $\sim 600$  yr and 0.15 increase of  $\text{Log } L_*$ : Wood, 1981; recurrent over  $\sim 3000$  yr for  $M_c = 0.9 M_\odot$ : Iben, 1981),  $\dot{M}_R t_{\text{AGB}} \lesssim 0.3 M_\odot$ , also in contradiction with our findings (total mass lost is  $M_{*i} - M_{\text{pul}}$ ). So, either the mass loss rate increased steadily during the evolution, or else it changed almost instantaneously by a factor 100 to its present value.

#### 7.f Envelope mass and time scales

Under the assumption that prior to the AGB phase hardly any mass is lost, we found already (section 7.d2) the time a star has spent so far on the AGB:  $t_{\text{AGB}}$ . Now first consider the case where the mass loss rate increases steadily during the evolution. Write

$$\dot{M}(t) = \dot{M}_R \exp[\alpha t] \quad (48)$$

such that at  $t=0$  the mass loss rate is given by the Reimers formula, and at  $t=t_{\text{AGB}}$  by the present, observed values. This defines a time scale  $\alpha^{-1}$  in which  $\dot{M}$  increases by a factor  $e$ . Typically  $\alpha^{-1}$  is  $0.2-0.25 t_{\text{AGB}}$ , corresponding to an increase of  $\dot{M}$  with a factor 100. Then we find (at  $t=t_{\text{AGB}}$ )

$$M_{\text{lost}} = \int_{t=0}^{t_{\text{AGB}}} \dot{M}(t) dt = -\alpha^{-1} \dot{M}_R \{ \exp[\alpha t_{\text{AGB}}] - 1 \} \quad (49)$$

This mass might be compared with the 'observed' envelope mass; the initial minus the present stellar mass

$$M_{\text{env}} \equiv M_{*i} - M_{\text{pul}} \quad (50)$$

With this procedure we find  $M_{\text{lost}} \approx 2 M_{\text{env}}$ ! Therefore, it seems better to assume that the mass loss rate remains nearly constant ( $\dot{M}_R$ ) during the first part of the AGB evolution and starts growing, according to equation (47), at the onset of the thermal pulses. The new time scale  $\alpha_n^{-1} = \frac{1}{2} \alpha^{-1}$ , because the length of the phases before and after the start of pulsations was taken to be the same. For our total sample the mean values, using equation (49) with  $\alpha_n$  and  $t_0 = \frac{1}{2} t_{\text{AGB}}$ , and adding the (small) amount of mass lost before  $t_0$ , become  $M_{\text{lost}} = 2.89 M_\odot$ , and  $M_{\text{env}} = 2.79 M_\odot$ . The residual mass ( $M_{\text{pul}} - M_{\text{ct}}$ ), combined with equation (48), gives an impression how

long it will take before the star comes down to its bare core, the remnant that is the central object of a planetary nebula (cf. the mass distribution for PN nuclei from Schönberner and Weidemann, 1981 and 1983). This time is found to be  $\lesssim 2 \cdot 10^4$  yr, implying that these stars are seen in the very last stage of their AGB life ( $\lesssim 10\%$ ). Because the transition time from the tip of the AGB to a visible PN is of the same order (see section 7.g), a reasonable fraction of objects, especially the ones with the highest mass loss rates, might be expected to be in a transition state between AGB and PN. However, a search for 6 cm continuum emission from a small, ionized region around these stars was unsuccessful (see appendix D). Further we may estimate, using equations (48) and (46) for a minimum OH luminosity of  $0.4 \text{ Jy kpc}^2$ , what fraction of its AGB life a star is active as an OH maser. Limiting ourselves to the stars with small expansion velocities ( $v_e < 15 \text{ kms}^{-1}$ ) we find this fraction to be  $\sim 28\%$ , or  $\sim 55\%$  of the phase in which the star is pulsating ( $t_{\text{pul}} \equiv \frac{1}{2} t_{\text{AGB}}$ ). The average ZAMS mass of this sample ( $M_{*i} = 1.6 M_{\odot}$ ) probably is higher than the initial mass of a classical Mira ( $\gtrsim 1 M_{\odot}$ ). Even when we correct for this difference, we still find at least an active phase of  $\sim 0.25 t_{\text{pul}}$ , a discrepancy of a factor 2 with the observed percentage of OH Mira's ( $\sim 12.5\%$ , see section 5.a2). The fact that only one object (VY 2-2, see appendix D) is known that appears to be in the transition state between AGB and PN, and that the actual detection probability for Mira variables is at least a factor 2 lower than the prediction, present two severe drawbacks to the hypothesis that the mass loss rate is steadily growing during the thermal pulse rate.

The other possibility is that the mass loss rate remains virtually constant during the largest fraction of the time on the AGB, but increases in a very short time interval by a factor of 100. Wood *et al.* (1983) suggest this might be caused by a switch in pulsation mode. The Reimers equation (47), combined with the observed present mass loss rate and the envelope mass (equation 50), then gives the length of the OH phase (i.e. the 'superwind' phase of Renzini, 1981b).

$$\Delta t_{\text{OH}} = \{M_{\text{env}} + \dot{M}_R t_{\text{AGB}}\} \{\dot{M}_R - \dot{M}\}^{-1} \quad (51)$$

(Remember that  $\dot{M}$  and  $\dot{M}_R < 0$ ).  $\Delta t_{\text{OH}}$  is found to be  $\sim 5 \cdot 10^4$  yr, almost the same for all stars in our sample (a selection effect, because the OH completeness limit shifts to higher values for larger expansion

velocities). Thus we find a duration of the OH phase ranging from  $\Delta t_{\text{OH}} \approx 0.1 t_{\text{pul}}$  for the smallest  $v_e$  to  $\Delta t_{\text{OH}} \approx 0.3 t_{\text{pul}}$  for the objects with the largest expansion velocities, in good agreement with the derived detection probabilities ( $\sim 12.5\%$  for the classical Mira's, section 5.a2:  $\sim 15\%$  for the IRC Mira's, section 5.c1). A problem here is that over 70% of the pulsation phase the more massive stars should be optically visible (low mass loss rate, first overtone pulsation). But there is no galactic counterpart to the so-called Shapley-Nail variables, as seen in the Small Magellanic Cloud. These are massive ( $\sim 5 M_{\odot}$ ) and luminous ( $-7^{\text{m}} < M_{\text{bol}} < -6^{\text{m}}$ ) long period variables with large amplitudes (see Feast, 1981), a complete equivalent of the more massive OH/IR stars, except that the Shapley-Nail variables have low mass loss rates and periods (500-800 days) about half as long as the periods of OH/IR stars (1000-2000 days), just as expected if they pulsate in the first overtone and OH/IR stars in the fundamental mode. If our theory is correct, there should be about 30 of these objects in the solar neighbourhood. A possible solution is that in our Galaxy the Shapley-Nail variables show up as irregulars or semi-regulars with small amplitudes. It has been suggested (Feast, 1981), because they are not found in the Large Magellanic Cloud either, that the temperature at which large amplitude instability sets in is a function of chemical composition in this mass range.

The observed expansion velocity,  $v_e$ , and the OH radius,  $R_{\text{OH}}$ , define a dynamical time scale

$$t_{\text{dyn}} = 211 \left( \frac{R_{\text{OH}}}{10^{16} \text{ cm}} \right) \left( \frac{v_e}{15 \text{ kms}^{-1}} \right)^{-1} \text{ yr} \quad (52)$$

that is quite small. Notice that when the central star becomes hot enough to ionize its surroundings, yielding a typical size of the planetary nebula of  $\sim 0.1 \text{ pc}$ , the amount of material within this ionization radius (based on the present mass loss rate) is  $0.1\text{-}0.2 M_{\odot}$  (cf. Pottasch, 1981). This implies that the transition time from AGB to PN must be short ( $\lesssim 5 \cdot 10^3 \text{ yr}$ ). The ionized mass of a PN represents only  $\lesssim 10\%$  of the mass that is lost during the total AGB life time. For NGC 7027 the estimated mass of the molecular envelope is  $\sim 5 M_{\odot}$ , compared to  $0.5 M_{\odot}$  for the ionized mass (see Terzian, 1983). When the expansion velocity remained roughly constant during the evolution, as it should be because the luminosity does not change too much, around the planetaries with the more massive nuclei ( $0.7\text{-}1$

$M_{\odot}$ ) there is a huge (out to  $\sim 10^{19}$  cm) envelope of neutral material. The density is  $\sim 7 \cdot 10^{-22} \text{ g cm}^{-2}$  at the ionization front, falling off to  $\sim 6 \cdot 10^{-25} \text{ g cm}^{-3}$  at the outer edge. In a number of cases (Terzian, 1980) this envelope is visible as a faint halo, or second shell, probably due to ram pressure of the interstellar medium, confining the envelope to  $\sim 1$  pc. Giant halo's around PN should be common, and recent results seem to indicate this is indeed the case (see Terzian, 1983). Near infrared observations of molecular hydrogen in the most massive (nearby) PN,  $\lambda=21$  cm absorption measurements (Rodriguez and Moran, 1982 detected a HI envelope around NGC 6302), or extinction measurements over an extent  $\sim 10$  times the nebula 'radius' should be rewarding.

## 7.g Results and discussion

Although we calculated the stellar parameters for each individual object, here we present only average values, "a dangerous concept, because the AGB and post-AGB phases of intermediate mass stars may *qualitatively* be alike, they actually are *quantitatively* extremely different" (Renzini, 1981b). However, for only a few stars really accurate distances are known (see table 2), for most the uncertainties are  $\sim 30\%$ . Three typical, individual cases (a Mira variable, a nominal OH/IR star, and a 'supergiant' OH/IR star), for which we have reliable distances and information on the variability of the luminosity, will be considered in section 7.h. A discussion of more individual cases will be postponed until more 'geometric' distances have been measured. The stars are divided into three groups according to their expansion velocity, i.e. population age.

In lines 1 to 7 observed quantities can be found.  $v_e$  is the expansion velocity of the OH shell and  $L_{\text{OH}}$  is the harmonic mean of the two strongest peaks in the OH line profile. The periods are from the radio light curves. The luminosity,  $L_{\star}$ , is the mean over a period and corrected for interstellar extinction. In each group there is a considerable spread around the mean values: see for the distribution of  $P_R$ ,  $L_{\text{OH}}$ , and  $R_{\text{OH}}$  chapter II (figures 12 and 19, table 3), and for the distribution over  $L_{\star}$  chapter IV (figure 13). The two Mira variables in the sample (WX Ser and RS Vir) are in the first group, as are the two OH/IR stars that show no, or hardly any, variation (OH 17.7-2.0 and OH 31.0-0.2). Thus the idea is strengthened that these non-variable OH/IR stars are (relatively) low mass,

low luminosity stars, undergoing however, enormous mass loss as judged from their OH luminosity and their colour temperature (energy maximum for  $\lambda \gtrsim 20 \mu\text{m}$ ). OH 17.7-2.0 and OH 31.0-0.2 probably are the most evolved objects in group I.

Table 7

		I $v_e < 15$	II $15 < v_e < 18$	III $v_e > 18$	Remarks
1	Number	8	8	6	
2	$v_e$ $\text{km s}^{-1}$	11.63	16.89	20.46	Chapter II, table 2. Expansion velocity.
3	$L_{\text{OH}}$ $\text{Jy kpc}^2$	203	268	724	Id. Harmonic mean OH flux.
4	$L_{\text{int}}$ $10^{-3} L_{\odot}$	239	244	515	Id. Integrated OH flux.
5	$R_{\text{OH}}$ $10^{16} \text{cm}$	$\lesssim 1.06$	4.53	6.65	Id., table 4. Radius of OH shell.
6	$P_r$ days	757	1130	1450	Id. Radio period.
7	$L_{\text{H}}$ $10^4 L_{\odot}$	0.46	2.36	3.43	Chapter IV, table 4. Luminosity.
8	$T_{\text{eff}}$ K	3367	3023	2950	This chapter, section 7.a.
9	$T_{\text{eff}}(\text{it})$ K	2934	2850	2776	Revised value. See text.
10	$R_{\text{H}}$ $R_{\odot}$	205	577	731	
11	$R_{\text{H}}(\text{it})$ $R_{\odot}$	270	649	826	Revised value. See text.
12	$M_{\text{CO}}$ $M_{\odot}$	0.548	0.834	1.005	Section 7.d2. Core mass at onset of pulsation.
13	$M_{\text{ct}}$ $M_{\odot}$	0.573	0.893	1.074	Section 7.d1. Present core mass.
14	$M_{\text{pul}}$ $M_{\odot}$	0.26	2.48	3.44	Section 7.b. Present stellar mass.
15	$M_{\text{pul}}(\text{it})$ $M_{\odot}$	0.52	3.33	4.66	Revised value. See text.
16	$M_{\text{dyn}}$ $M_{\odot}$	1.23	6.52	8.55	Section 7.c2.
17	$M_{\text{ZAMS}}$ $M_{\odot}$	1.97	6.24	8.65	Section 7.c1.
18	$M_{\text{ve}}$ $M_{\odot}$	1.69	3.59	6.01	Section 7.c3.
19	$M_{\text{si}}$ $M_{\odot}$	1.63	5.45	7.74	Mean ZAMS mass (16, 17 and 18).
20	$\dot{M}_{\text{IR}}$ $10^{-5} M_{\odot} \text{yr}^{-1}$	-1.58	-5.59	-6.71	Section 7.e1. Based on IR data.
21	$\dot{M}_{\text{OH}}$ $10^{-5} M_{\odot} \text{yr}^{-1}$	-2.93	-4.89	-9.73	Section 7.e2. Based on radio data.
22	$\dot{M}_{\text{R}}$ $10^{-7} M_{\odot} \text{yr}^{-1}$	-1.21	-7.69	-10.5	Section 7.e3. Reimers wind.
23	$M_{\text{env}}$ $M_{\odot}$	$\lesssim 1.12$	2.12	3.08	$M_{\text{si}} - M_{\text{pul}}(\text{it})$ .
24	$t_{\text{AGB}}$ $10^3 \text{yr}$	12.9	4.12	3.18	Section 7.d2. Pulse phase $\equiv \frac{1}{2} t_{\text{AGB}}$
25	$\alpha^{-1}$ $10^3 \text{yr}$	1.23	0.49	0.37	Section 7.f. Time scale if $\dot{M}$ increases steadily.
26	$\Delta t_{\text{OH}}$ $10^4 \text{yr}$	4.30	3.49	3.38	Section 7.f. Length of OH (superwind) phase if $\dot{M}$ changes ad hoc.
27	$\Delta t_{\text{cat}}$ $10^4 \text{yr}$	-	3.03	2.88	
28	$t_{\text{dyn}}$ $10^3 \text{yr}$	0.29	0.85	1.03	Section 7.f. $R_{\text{OH}}/v_e$ .

In group II and III there are two stars (OH 21.5+0.5 and OH 32.8-0.3) with luminosities well above the AGB limit:  $L_* > 5.4 \cdot 10^4 L_{\odot}$  corresponding to the Chandrasekhar limit  $M_C > 1.4 M_{\odot}$  (see e.g. Renzini, 1981b). For these stars carbon is ignited in the C-O core, and a supernova explosion probably terminates their evolution. Putting in the total number of OH masers, and the mean length of the pulsation phase ( $\frac{1}{2} t_{\text{AGB}}$ ) we predict one supernova explosion in 125 yr. Usually, one assumes a SN rate of  $25 \text{ yr}^{-1}$  (uncertain by a factor 2; see for a review Tammann, 1974) in our Galaxy, a factor 5 larger. The actual difference will still be larger, because in our UKIRT sample there is a selection effect towards stronger OH emitters (better positions). This is compatible with the fact that only a small fraction of the supergiants has an OH maser (see Bowers, 1975). Most likely, these

stars dredged up so much carbon that  $C/O > 1$  by the time their envelopes are thick enough to produce a maser, and they appear as carbon stars such as IRC+10216. They seem, therefore, the best candidates to look for maser emission from carbon molecules, e.g. from CS.

All parameters listed in lines 8 to 27 have been derived directly, or indirectly from the measured quantities. The effective temperatures as found in section 7.a (line 8) are probably too high for the following reason. Becker and Iben (1979) find for intermediate mass stars

( $3 \lesssim M_{*i} \lesssim 7 M_{\odot}$ ) that the asymptotic giant branches do not coincide, but lie parallel in the  $\text{Log } L_*$ ,  $\text{Log } T_{\text{eff}}$  plane for stars with different initial mass. They derive (their equation 1)  $\text{Log } T_{\text{eff}} \propto 0.120 \text{ Log } (M_*/7)$ , in other words stars with a lower mass, but with the same luminosity and chemical composition, will have a lower effective temperature. Because of the enormous mass loss rate (not included in their models), a star will deviate from its original Hayashi track (say that of a  $5 M_{\odot}$  star) towards the red (e.g. the track of a  $3 M_{\odot}$  star. See de Jong, 1983; Renzini 1983). We may use Becker and Iben's equation (1), with our abundances and slightly adjusted to our temperature scale, to derive a new value of  $T_{\text{eff}}$  by putting in the *present* stellar mass ( $M_{\text{pul}}$ , line 14), instead of  $M_{*i}$ . Then a better value for the radius (section 7a) and for the pulsation mass,  $M_{\text{pul}}$  (section 7.b) is found. This process may be repeated, and the values of  $T_{\text{eff}}$ ,  $R_*$ , and  $M_{\text{pul}}$  are found to converge very rapidly. The revised values are listed in lines 9, 11, and 15. The effect is largest for group I, because here already  $\sim 75\%$  of the initial mass has been ejected, compared to  $\sim 40\%$  in the other groups. This is no surprise, because the stars in group I are seen as OH maser only during the last 10% of the thermal pulse phase. Important to note from table 7 is that  $M_{\text{ct}} < M_{\text{pul}} (\text{it}) < M_{*i}$ , except for the pulsation mass of group I, that is  $0.05 M_{\odot}$  smaller than  $M_{\text{ct}}$ . As the two Mira variables are in this group (maybe a different pulsation mode is applicable for them), this presents strong support for a) fundamental mode pulsation and b) for the occurrence of extremely large mass losses during (part of) the AGB evolution. Up to 75% of the initial main-sequence mass has been ejected already when we observe them as OH/IR stars.

It might be asked if all these stars will eventually show up as planetary nebulae. The necessary condition to get an observable PN is that the transition time,  $t_{\text{TR}}$  (the time needed for the remnant central star to become hot enough to illuminate the envelope), is smaller than the

expansion time of the nebula, that is typically  $5 \cdot 10^3$  yr (cf.  $t_{\text{dyn}}$ , line 27). Iben and Renzini (1982) give the following expression for  $t_{\text{TR}}$

$$t_{\text{TR}} = 1.6 \cdot 10^6 \{M_{\text{RES}} - M_{\text{RES,N}}\} \{M_{\text{CN}} - 0.44\}^{-1} \text{ yr} \quad (53)$$

where  $M_{\text{RES}}$  is the residual stellar envelope mass at the moment that the superwind ceases and the star starts evolving to the blue leaving the AGB.  $M_{\text{RES,N}}$  is the envelope mass when the star reaches  $T_{\text{eff}} = 30\,000$  K, and  $M_{\text{CN}}$  the core mass at that moment. As the superwind stops, probably the Reimers wind takes over once more. Then equation (53), neglecting  $M_{\text{RES,N}}$ , can be approximated by (see Renzini, 1981b)

$$t_{\text{TR}} = - \frac{M_{\text{RES}}}{\dot{M}_{\text{R}}} \text{ yr} \quad (54)$$

We may speculate that if the superwind is started by the onset of fundamental mode pulsation, it will stop again when the pulsation ceases, or the period becomes too long. Assuming that the cut-off occurs at the longest periods observed for these stars in the Dwingeloo monitor program ( $P_{\text{max}} = 2000$  days), the core masses (from  $M_{\text{env}}/\dot{M}$  and equation 44), the pulsation masses (equations 43, 34, 35, and 37a), and hence the residual envelope masses can be calculated. We find  $M_{\text{RES}} < 0.02 M_{\odot}$  for group I,  $\sim 0.1 M_{\odot}$  for group II, and  $\sim 0.8 M_{\odot}$  for group III. These values are at least a factor 10 higher than expected by theory (Renzini, 1983), but an increase of only 10% in the cut-off period yields differences of a factor 2 (group II) to 10 (group I) in  $M_{\text{RES}}$ ! Combined with the Reimers formula at that moment the transition times are found to be  $\ll 1.9 \cdot 10^4$  yr for group I,  $< 1.2 \cdot 10^4$  for group II, and  $\sim 9.7 \cdot 10^4$  yr for group III. We may conclude, although the uncertainties are large, that virtually all stars in group I, a reasonable fraction ( $\sim 50\%$ ) of the stars in group II, and almost none of group III, will be visible as a planetary nebula. This means that PN have progenitors with main sequence masses predominantly in the range  $2-5 M_{\odot}$ . The observed narrow mass distribution for the central stars of PN, and the much wider distribution for white dwarfs (see Schönberner and Weidemann, 1983) is in good agreement with this. We predict a birth rate of PN of  $\sim \frac{12}{22} 59400/4 \cdot 10^4 = 0.8 \text{ yr}^{-1}$ . With a canonical nebular lifetime of  $\sim 3 \cdot 10^4$  yr this leads to 24000 planetaries in our Galaxy (cf. the review of Terzian, 1983, who quotes  $\sim 1 \text{ yr}^{-1}$  and a total of 28000). A considerable

fraction of PN has once been active as an OH maser, thus having an oxygen rich envelope. Maybe the last dredge up causes the final change of  $C/O < 1$  to  $C/O > 1$  in the envelopes. If that is the case a gradient of the  $C/O$  ratio should be observable through the envelope. Anyhow, abundances are difficult to determine in themselves, and it is therefore reassuring that a large fraction of PN still has a  $C/O < 1$  (see Kaler, 1983). For Sw St 1, possibly a very young PN, Cohen *et al.* (1983) found  $C/O = 0.5$ .

Finally, the space distribution and kinematics of OH/IR stars with small expansion velocities ( $v_e < 15 \text{ kms}^{-1}$ ) are consistent with that of planetary nebulae (see Baud *et al.*, 1981: also sections 5.b1 and 6.a). The only major difference is the maximum in the space density of OH/IR stars at  $R=3.9 \text{ kpc}$  (see section 6.b), not present in the distribution of PN. This is naturally explained when one assumes that the same type of objects is normally present within the radius of the molecular ring, but due to the lack of UV photons, necessary for the photodissociation of  $\text{H}_2\text{O}$  into OH, do not show up as Oh/IR stars.

#### 7.h Individual cases

In this section results are presented for three individual stars: WX Ser, a classical Mira variable, OH 26.5+0.6, a nominal OH/IR star identified with the infrared source AFGL 2205, and OH 21.5+0.5, a supergiant OH/IR star. For the two OH/IR stars geometric distances ( $\lesssim 10\%$ ) are available. In table 8 almost the same quantities as in table 7 are listed, but here an estimate of the accuracy for each of them is given also. The listed uncertainties are the formal errors; actually, the true values might deviate more than this. For instance, the period of OH 21.5+0.5 is, due to its extreme length ( $> 5 \text{ yr}$ ), not well established yet, because we did not cover a full cycle in the Dwingeloo monitor program (see appendix B, figure 30). This implies a larger uncertainty in the mean OH luminosity (line 3), as well as in the mean stellar luminosity (line 6). The variation of  $L_*$  still is very poorly known (three or four measurements only; see chapter IV) and the mean bolometric magnitude therefore is based primarily on the known variations in the radio. Furthermore, we had to apply a considerable correction ( $\sim 25\%$ ) for the unobserved part of the energy distribution ( $\lambda > 20 \mu\text{m}$ ). Finally, OH 21.5+0.5 is far away and the interstellar extinction consequently large, leading to a correction

of  $\sim 0.75^m$  in the bolometric magnitude. Errors in the mean luminosity have consequences for almost all derived quantities. The listed  $T_{\text{eff}}$ ,  $R_*$ , and  $M_{\text{pul}}$  are the iterated values, corrected for mass loss during the thermal pulse phase, as described in the previous section.

Table 8

		WK Serpentis	OH 26.5+0.6	OH 21.5+0.5	
1.	D	kpc	$1.20 \pm 0.55$	$0.98 \pm 0.09$	$11.63 \pm 0.65$
2.	$v_e$	$\text{kms}^{-1}$	$7.59 \pm 0.005$	$14.07 \pm 0.005$	$18.76 \pm 0.005$
3.	$L_{\text{OH}}$	$\text{Jy kpc}^2$	$3.35 \pm 3$	$264 \pm 51$	$2813 \pm 300$
4.	$R_{\text{OH}}^2$	$10^{16} \text{cm}^2$	$< 0.17$	$3.29 \pm 0.26$	$16.33 \pm 0.87$
5.	$P_{\text{r}}$	days	$443 \pm 10$	$1566 \pm 30$	$1975 \pm 200$
6.	$L_m$	$10^3 L_{\odot}$	$0.37 \pm 0.3$	$1.00 \pm 0.19$	$14.05 \pm 1.6$
7.	$T_{\text{eff}}(\text{it})$	K	$2922 \pm 150$	$2505 \pm 125$	$2644 \pm 132$
8.	$R_*(\text{it})$	$R_{\odot}$	$245 \pm 25$	$549 \pm 56$	$1841 \pm 189$
9.	$M_{\text{co}}$	$M_{\odot}$	$0.524 \pm 0.026$	$0.632 \pm 0.032$	$2.542 \pm 0.127$
10.	$M_{\text{ct}}$	$M_{\odot}$	$0.557 \pm 0.028$	$0.664 \pm 0.033$	$2.866 \pm 0.143$
11.	$M_{\text{pul}}(\text{it})$	$M_{\odot}$	$0.79 \pm 0.22$	$1.22 \pm 0.34$	$27.5 \pm 8.2$
12.	$M_{\text{dyn}}$	$M_{\odot}$	1.25	2.68	47.4
13.	$M_{\text{ZAMS}}$	$M_{\odot}$	1.76	3.19	32.6
14.	$M_{\text{ve}}$	$M_{\odot}$	0.94	2.40	4.7:
15.	$M_{*i}$	$M_{\odot}$	$1.32 \pm 0.24$	$2.76 \pm 0.23$	$33 \pm 8$
16.	$\dot{M}_{\text{IR}}$	$10^{-3} M_{\odot} \text{yr}^{-1}$	$-1.95 \pm 1.5$	$-2.84 \pm 0.56$	$-30.0 \pm 3.4$
17.	$\dot{M}_{\text{OH}}$	$10^{-3} M_{\odot} \text{yr}^{-1}$	$-0.35 \pm 0.16$	$-6.17 \pm 0.57$	$-29.0 \pm 1.6$
18.	$\dot{M}_{\text{z}}$	$10^{-7} M_{\odot} \text{yr}^{-1}$	$-1.5 \pm 0.49$	$-3.46 \pm 0.80$	$-46.7 \pm 13.4$
19.	$M_{\text{env}}$	$M_{\odot}$	$0.54 \pm 0.18$	$1.54 \pm 0.45$	$5.5 \pm 2.1$
20.	$\tau_{\text{AGB}}$	$10^5 \text{yr}$	$31.2 \pm 2.2$	$5.49 \pm 0.39$	$3.60 \pm 0.25$
21.	$\alpha^{-1}$	$10^5 \text{yr}$	$2.3 \pm 0.21$	$0.56 \pm 0.04$	$0.43 \pm 0.03$
22.	$\Delta t_{\text{OH}}$	$10^4 \text{yr}$	$3.15 \pm 3.0$	$3.02 \pm 1.27$	$1.30 \pm 0.54$
23.	$\Delta t_{\text{cat}}$	$10^4 \text{yr}$	$1.98 \pm 1.19$	$1.23 \pm 0.40$	$8.33 \pm 3.26$
24.	$\tau_{\text{dyn}}$	$10^3 \text{yr}$	$< 0.07$	$0.74 \pm 0.06$	$2.76 \pm 0.15$

Note that  $M_{\text{ct}} < M_{\text{pul}} < M_{*i}$  for all three stars. The measured expansion velocity of OH 21.5+0.5 is much lower than that for optically identified supergiants ( $25\text{--}35 \text{ kms}^{-1}$ ) probably meaning that in this star the drift velocity of the dust grains through the gas is large. Consequently, the value of  $M_{\text{dyn}}$  (see section 7.c2) is too large, and of  $M_{\text{ve}}$  (see section 7.c3) much too small. In this case we adopted for  $M_{*i}$  the Iben and Truran value (see section 7.c1). The huge envelope mass ( $> 5 M_{\odot}$ ) around OH 21.5+0.5, lost in only  $\sim 2 \cdot 10^5 \text{ yr}$ , is compatible with the fact that optically identified OH supergiants (such as NML Cyg and VY CMa) are embedded in a 'molecular cloud' (see e.g. Herbig, 1969; Morris and Jura, 1983), sometimes even leading to the speculation that these objects are still in *statu nascendi*. The masses within  $R_{\text{OH}}$ , i.e.  $M_{\text{dyn}}$ , are much smaller than  $M_{\text{env}}$ , the total mass lost. Determination of the sizes of the dust shells for the more nearby objects (lunar occultation, speckle interferometry, IR scanning) at various infrared wavelengths

(preferentially at  $\lambda > 20 \mu\text{m}$ !) may confirm the presence of an extended halo ( $\sim 1 \text{ pc}$ ) around them. Lunar occultation experiments for IRC+10011 (Zappala *et al.*, 1974), and IR scanning for OH 26.5+0.6 (Baud, private communication) revealed diameters in the *near* infrared already comparable with the OH diameters. In line 23 the time is given that each star still has to spend on the AGB, provided the mass loss rate remains constant

$(\Delta t_{\text{cat}} = \{M_{\text{pul}} - M_{\text{ct}}\} / \dot{M})$ ,  $\Delta t_{\text{OH}} + \Delta t_{\text{cat}}$  then is the total time the stars are active as OH masers; it is also the length of the superwind phase. For WX Ser this is only a small fraction ( $\sim 3\%$ ) of the length of the thermal pulse phase, and for OH 26.5+0.6 a somewhat larger part ( $\sim 15\%$ ). The time scales for OH 21.5+0.5 are highly uncertain; probably it will explode as a supernova (long) before its steady superwind has blown away the residual stellar mass ( $M_{\text{pul}} - M_{\text{ct}}$ ).

#### V.8 Conclusion and suggestions for future work

OH/IR stars are found to have intermediate main-sequence masses ( $1M_{\odot} < M_{*i} < 10 M_{\odot}$ ), with the majority in the range  $2-5 M_{\odot}$ . A small percentage has very massive progenitors ( $> 10 M_{\odot}$ ), finally producing supernovae. The number of OH/IR stars with low masses ( $M_{*i} < 2M_{\odot}$ ) is also relatively small, not because stars in this mass range are rare but because the duration of their superwind is short. They are seen as strong OH emitters during the last 5% of their AGB lives only. The kinematics and galactic distribution of OH/IR stars are in good agreement with that of their progenitors, as well as with that of their end products: planetary nebulae. About 55% of them will eventually show up as a planetary nebulae, the others produce so-called lazy PN; their envelopes will be dissipated before the central star becomes hot enough to illuminate the shell. Up to 75% of their initial mass can be lost during the superwind phase, thus producing giant 'halos' around the final PN. A total number of  $59400$   $1612 \text{ MHz}$  OH masers stronger than  $0.95 \cdot 10^{-10} L_{\odot}$  is predicted to exist in our Galaxy.

By the combination of time variability, radio data, and infrared observations many basic stellar parameters could be derived, as well as properties of the circumstellar shells. Very accurate, geometric distances ( $\sim 10\%$ ) are available for a few stars only; for them we obtained a complete and consistent description of their intrinsic properties. Observations of the angular extents of the envelopes (e.g. with the VLA, or

with MERLIN) should increase the number of stars with accurately known distances, and enable an analysis of each individual object. For a better estimate of the mean luminosities these sources must be observed regularly in the infrared. Furthermore, to remove the uncertain correction for the energy emitted at long wavelengths ( $\lambda \gtrsim 20 \mu\text{m}$ ), observations, that will be provided by IRAS, are essential. Finally, for a number of OH/IR stars a better coverage of the radio light curves, that are still very incomplete for the longest periods (see appendix B), is needed to improve the periods, amplitudes, and above all the phase lag radii. The increase of the number of sources with well known geometric distances, and eventually an extension of the program to lower OH luminosities, including more distant stars, gives an unique possibility to study the stellar density distribution of our Galaxy, and to establish a very accurate distance scale. In the near future this may yield even distances to nearby galaxies: for M31 a monitor with a  $1\sigma$  of  $\sim 1 \text{ mJy}$  and VLBI experiments with a resolution of  $\sim 0''.01$  and the same sensitivity are needed.

Literature cited in chapter V

- Allen C.W.: 1973, *Astrophysical Quantities*, 3<sup>rd</sup> ed., Univ. of London, Athlone
- Bahcall, J.N., Soneira, R.M.: 1980, *Astroph. J. Suppl.* 44, 73
- Baud, B., Habing, H.J., Winnberg, A., Matthews, H.E.: 1979, *Astron. Astroph. Suppl.* 35, 179
- \_\_\_\_\_: 1979, *Astron. Astroph. Suppl.* 36, 193
- \_\_\_\_\_: 1981, *Astron. Astroph.* 95, 156
- Baud, B., Habing, H.J.: 1983, *Astron. Astroph.* (in press)
- Becker, S.A., Iben, I.: 1979, *Astroph. J.* 232, 831
- Nedijn, P.: 1977, *Dust shells around stars*, Ph. D. thesis, Leiden
- Benson, J.M., Mutel, R.L.: 1979, *Astroph. J.* 233, 119
- Bessel, M.S.: 1979, *P.A.S.P.* 91, 584
- Blaauw, A.: 1965, in *SSS V, Galactic Structure*, Eds. A. Blaauw and M. Schmidt, Chicago, pp. 435-452
- Bowers, P.F.: 1975, *Astron. Astroph.* 39, 473
- Bowers, P.F., Kerr, F.J.: 1974, *Astron. Astroph.* 36, 225
- Buhl, D., Snijder, L.E., Lovas, F.J., Johnson, D.R.: 1975, *Astroph. J. Lett.* 201, L29
- Bujarrabal, V., Destombes, J.L., Guibert, J., Marliere-Demuynck, C., Rieu, Nguyen-Q., Omont, A.: 1980, *Astron. Astroph.* 81, 1
- Cohen, M., Flower, D.R., Goharji, A.: 1983, in *Planetary Nebulae*, Ed. D.R. Flower, Reidel, p. 520
- Dijck, H.M., Lockwood, G.W., Capps, R.W.: 1974, *Astroph. J.* 189, 89
- Eggen, O.J.: 1975, *Astroph. J.* 195, 661
- Elitzur, M.: 1981, in *Physical Processes in Red Giants*, Eds. I. Iben and A. Renzini, Reidel, pp 363-382
- Elitzur, M., Goldreich, P., Scoville, N.: 1976, *Astroph. J.* 205, 384
- Engels, D.: 1979, *Astron. Astroph. Suppl.* 36, 337
- Engels, D.: 1982, *Zur Natur von OH/IR-Objekten*. Ph.D. thesis. Veröff. der Astron. Inst. Bonn 95
- Feast, M.W.: 1963, *M.N.R.A.S.* 125, 367
- Feast, M.W.: 1981, in *Physical Processes in Red Giants*, Eds. I. Iben and A. Renzini, Reidel, pp 193-204
- Forrest, W.J., McCarthy, J.F., Houck, J.R.: 1979, *Astroph. J.* 233, 611
- Fox, M.W., Wood, P.R.: 1982, *Astroph. J.* 259, 198

- Glass, I.S., Feast, M.W.: 1982, *M.N.R.A.S.* **199**, 245
- Glass, I.S., Lloyd Evans, T.: 1981, *Nature* **291**, 303
- Gordon, M.A., Burton, W.B.: 1976, *Astroph. J.* **208**, 346
- Goldreich, P. Scoville, N.: 1976, *Astroph. J.* **205**, 144
- Habing, H.J.: 1968, *Bull. Astron. Inst. of the Netherlands*, **19**, No. 6, pp 421-431
- Harvey, P.M., Bechis, K.P., Wilson, W.J., Ball, J.A.: 1974, *Astroph. J. Suppl.* **27**, 331
- Herbig, G.H.: 1969, *Mém. Soc. Roy. Sci. Liège* **19**, 13
- Hyland, A.R., Becklin, E.E., Neugebauer, G., Wallerstein, G.: 1972, *Astron. Astroph.* **16**, 204
- Iben, I.: 1981, in *Physical Processes in Red Giants*, Eds. I. Iben and A. Renzini, Reidel, pp 3-24
- Iben, I., Renzini, A.: 1982, *Illinois Astroph. Preprint IAP 82-2*
- Iben, I., Truran, J.W.: 1978, *Astroph. J.* **220**, 980
- Ikaunieks, J.J.: 1963, *Tran. Astroph. Lab. Acad. Sci. Latvian, SSR* **11**, 58
- Jewell, P.R., Elitzur, M., Webberm J.C., Snijder, L.E.: 1979, *Astroph. J. Suppl.* **41**, 191
- Johnson, H.L.: 1966, *Ann. Rev. Astron. Astroph.* **4**, 193
- Jones, T.W., Merrill, K.M.: 1976, *Astroph. J.* **109**, 509
- Jong, T. de.: 1983, *Astroph. J.* (submitted)
- Kaler, J.B.: 1983, in *Planetary Nebulae*, Ed. D.R. Flower, Reidel, pp 245-257
- Knapp, G.R., Phillips, T.G., Leighton, R.B., Lo, K.Y., Wannier, P.G., Wootten, H.A., Huggins, P.J.: 1982, *Astroph. J.* **252**, 616
- Kruit, P.C. van de, Searle, L.: 1981, *Astron. Astroph.* **95**, 105
- Kudritzki, R.P., Reimers, D.: 1978, *Astron. Astroph.* **70**, 227
- Kwok, S.: 1975, *Astroph. J.* **198**, 583
- Lee, T.A.: 1970, *Astroph. J.* **162**, 217
- Martinet, L., Mayer, F.: 1975, *Astron. Astroph.* **44**, 45
- Miller, G.E., Scalo, J.M.: 1979, *Astroph. J. Suppl.* **41**, 513
- Morris, M., Jura, M.: 1983, *Astroph. J.* **264**, 546
- Norris, R.P., Diamond, P.J., Booth, R.S.: 1982, preprint
- Olson, F.M.: 1979. *Shells, around stars*, Ph. D. thesis, Leiden
- Olson, F.M.: 1981, in *Physical Processes in Red Giants*. Eds. I. Iben and A. Renzini, Reidel, pp 237-240

- Olnon, F.M., Winnberg, A., Matthews, H.E., Schultz, G.V.: 1980, *Astron. Astroph. Suppl.* **42**, 119
- Oort, J.H.: 1965, in *SSS V, Galactic Structure*, Eds. A. Blaauw and M. Schmidt, Chicago, pp 455-509
- Paczynski, B.: 1970, *Acta Astron.* **20**, 47
- Pottasch, S.R.: 1983, in *Planetary Nebulae*, Ed. D.R. Flower, Reidel, pp 391-409
- Reid, M.J., Dickinson, D.F.: 1976, *Astroph. J.* **209**, 505
- Reid, M.J., Muhlemann, D.O., Moran, J.M., Johnston, K.J., Schwartz, P.R.: 1977, *Astroph. J.* **214**, 60
- Reimers, D.: 1975, *Mém. Soc. Roy. Sci. Liège*, 6<sup>e</sup> Ser., **8**, 369
- Renzini, A.: 1981a, in *Effects of Mass Loss on Stellar Evolution*, Eds., C. Chiosi, R. Scalo, Reidel, p 319
- Renzini, A.: 1981b, in *Physical Processes in Red Giants*, Eds. I. Iben and A. Renzini, Reidel, pp 431-446
- Renzini, A.: 1983, in *Planetary Nebulae*, Ed. D.R. Flower, Reidel, pp 267-280
- Renzini, A., Voli, M.: 1981, *Astron. Astroph.* **94**, 175
- Ridgeway, S.T., Joyce, R.R., White, N.M., Wing, R.F.: 1980, *Astroph. J.* **235**, 126
- Rieu, Nguyen-O., Laury-Micolaut, C., Winnberg, A., Schultz, G.V.: 1979, *Astron. Astroph.* **75**, 351
- Robertson, B.S.C., Feast, M.W.: 1981, *M.N.R.A.S.* **196**, 111
- Rodriguez, L.F., Moran, J.M.: 1982, *Nature*, **299**, 323
- Schmidt, M.: in *SSS V, Galactic Structure*, Eds. A. Blaauw and M. Schmidt, Chicago, pp 513-529
- Schönberner, D., Weidemann, V.: 1981, in *Physical Processes in Red Giants*, Eds. I. Iben and A. Renzini, Reidel, pp 463-468
- \_\_\_\_\_: 1983, in *Planetary Nebulae*, Ed. D.R. Flower, Reidel, pp 359-371
- Tamman, G.R.: 1974, in *Supernovae and Supernova Remnants*, Ed. C.B. Cosmovici, Reidel, pp 155-185
- Terzian, Y.: 1980, *Quart. I.R.A.S.*, **21**, 81
- Terzian, Y.: 1983, in *Planetary Nebulae*, Ed. D.R. Flower, Reidel, pp 487-499
- Wallerstein, G.: 1975, *Astroph. J. Suppl.* **29**, 375
- Werner, M.W., Beckwith, S., Gatley, I., Sellgren, K., Berriman, G.: 1980, *Astroph. J.* **239**, 540

- Wilson, W.J., Barrett, A.H.: 1972, *Astron. Astroph.* *17*, 385
- Wood, P.R.: 1981, in *Physical Processes in Red Giants*, Eds. I. Iben and A. Renzini, pp 135-139, and pp 205-223
- Wood, P.R., Cahn, J.H.: 1977, *Astroph. J.* *211*, 499
- Wood, P.R., Bessel, M.S., Fox, M.W.: 1983, preprint
- Zappala, R.R., Becklin, E.E., Matthews, K., Neugebauer, G.: 1974, *Astroph. J.* *192*, 109

## Appendix A

### Simplified model for maser emission from a circumstellar shell

Assumptions	Justifications
i) $\Delta R \ll R_0$ , or $\Delta\psi \ll 1$ . Thin OH shell	See chapter III, section 3c, where we found that $\Delta R < 0.2 R_0$
ii) The shell expands uniformly with a constant velocity $v_e$	See chapter III, section 3b. See also chapter V, section 2
iii) The radial velocity differential across $\Delta$ is equal to the Doppler width	Velocity coherence is required (see Cook, 1968)
iv) The masers are saturated and radiatively coupled to the central star	See chapter II, section 6a
v) The central stars vary sinusoidally	See chapter II, sections 6a and 6c
vi) The densities in the shell are proportional to $R^{-2}$	See chapter III, sections 3c and 5

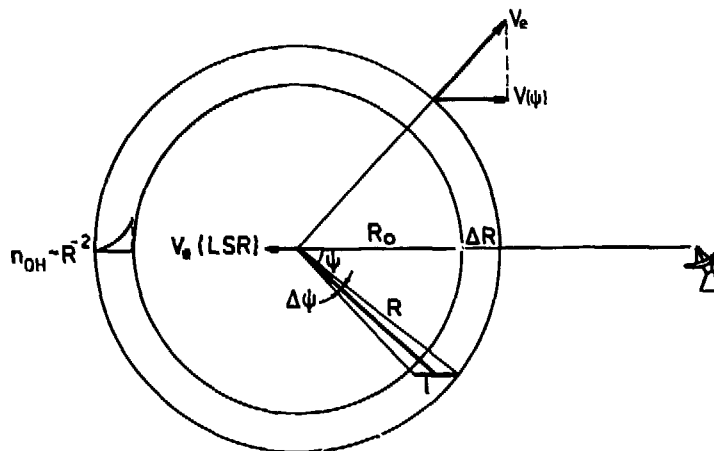


Figure 1. Geometry of a thin OH shell. It has spherical symmetry and expands with a constant velocity,  $v_e$ .

We may write

$$v(\psi) \equiv v_r(\psi) - v_* \text{ (LSR)} \tag{1}$$

and

$$v(\psi) = -v_e \cos \psi \tag{2}$$

where we choose  $v(\psi) < 0$  for  $-\frac{\pi}{2} < \psi < \frac{\pi}{2}$ . Following Reid *et al.* (1977) we write for the pathlength along the line of sight

$$l(R, \psi) = \frac{R \Delta\psi}{\sin \psi} \quad (3)$$

In the direction of the star ( $\psi=0$ ,  $\psi=\pi$ ) we assume that  $l=\Delta R$ ; for other directions  $l$  is limited by  $\Delta\psi$ . The Doppler width is given by (iii)

$$v_d = \left| \frac{\partial v}{\partial \psi} \right| \Delta\psi = v_e \Delta\psi \sin \psi \quad (4)$$

Combining equations (2), (3), and (4) yields

$$l(R, v) = \frac{R(v_d/v_e)}{1-(v(\psi)/v_e)^2} \quad (5)$$

valid for  $|v(\psi)| < v_e - \delta$ , where  $\delta \ll v_e$  (typically  $\delta = 0.01 - 0.1 \text{ kms}^{-1}$  for OH masers. See chapter II, figure 14), but  $\delta \neq 0$ . The equation of line transfer is

$$\frac{dI_v}{d\ell} = \frac{h\nu}{4\pi} \phi_v \{ (n_2 - n_1) B I_v + N_2 A \} \quad (6)$$

where  $A$  and  $B$  are the Einstein coefficients (as defined by Mihalas, 1978), and  $n_2$  and  $n_1$  are the number densities of OH molecules in the upper and lower state of the maser transition. The (normalized) profile function is assumed to be the same for emission and absorption

$$\phi_v = \frac{1}{\Delta v} \exp \left[ - \frac{4 l n_2 (v - v_0)^2}{\Delta v^2} \right] \quad (7)$$

For saturated OH masers, where the effects of line narrowing are negligible

$$\phi_v = \frac{1}{\Delta v_d} \quad (8)$$

with  $\Delta v_d$  the thermal line width. Assuming that collisions are unimportant and that spontaneous emission is negligible, we find in the steady state approximation ( $dn_1/dt = dn_2/dt = 0$ ) for a *saturated* maser (see ter Haar and Pelling, 1974; Goldreich and Keeley, 1972)

$$dI = \alpha I_s d\ell \quad (9)$$

where  $\alpha(\text{cm}^{-1})$  is defined as

$$\alpha \equiv \frac{h\nu}{4\pi\Delta\nu} B n_{\text{OH}} \quad (10)$$

Here  $n_{\text{OH}}$  is the number density in the masing states ( $n_1+n_2$ ), which is approximately the total OH density. Defining  $R_{\text{pump}}$  ( $\text{s}^{-1}$ ) as the net population transfer from the lower into the upper masing level

$$I_s \equiv \frac{R_{\text{pump}}}{(1 + g_2/g_1)\beta} \quad (11)$$

with  $g_1$  and  $g_2$  the statistical weights ( $g_1=5$ ,  $g_2=3$  for the 1612 MHz transition) and

$$\beta = \frac{B\Omega_s}{4\pi} \quad (12)$$

where  $\Omega_s$  is the solid angle into which the stimulated radiation is emitted. The population inversion ( $\Delta n \equiv n_2 - n_1$ ) for a saturated maser is given by

$$\Delta n = n_{\text{OH}} \frac{(g_2/g_1) - 1}{(g_2/g_1) + 1} \quad (13)$$

The total OH peak flux density, measured at a distance  $D$  from the star, is denoted by the symbol  $S_\nu$  as is common in radio astronomy.  $S_\nu$  is made up by contributions from a ring in the shell at constant (projected) velocity

$$D^2 S_\nu(R_o, \nu) = \int_{R_o}^{R_o + \Delta R} dR \int_{\psi}^{\psi + \Delta\psi} R d\psi \int_0^{2\pi} R \sin\psi d\theta \left[ \frac{h\nu}{4\pi\Delta\nu} B n_{\text{OH}}(R) \frac{R_{\text{pump}}}{8/3 \beta} \right] \quad (14)$$

Assuming that none of these quantities depends on  $\psi$ , or  $\theta$  (spherical symmetry) and writing

$$n_{\text{OH}}(R) = n_{\text{OH}}(R_o) \left(\frac{R}{R_o}\right)^2 \quad \text{for } R > R_o \quad (15)$$

$$= 0 \quad \text{for } R < R_o$$

we find

$$D^2 S_\nu(R_o, \nu) = \frac{3}{16} \frac{h\nu}{\Delta\nu} \frac{BR_{\text{pump}}}{\beta} n_{\text{OH}}(R_o) R_o^2 \frac{1}{2} \int_{\ell} d\ell \int_0^{2\pi} d\theta \quad (16)$$

or

$$S_v(R_o, v) = n_{OH}(R_o) R_o^3 R_{pump} f(v) \gamma D^{-2} \quad (17)$$

with

$$f(v) = \frac{(v_d/v_e)}{1 - (v(\psi)/v_e)^2} \quad \text{for } |v(\psi)| < v_e - \delta \quad (18)$$

and

$$\gamma = \frac{3\pi \hbar v}{16 \Delta v} \frac{B}{\beta} \quad (19)$$

Equation (10) is a time independent model spectrum, valid for velocities approaching, but never equal to, the expansion velocity. The shape of the spectrum is rather well obeyed by the type IIb OH masers (see figure 2).

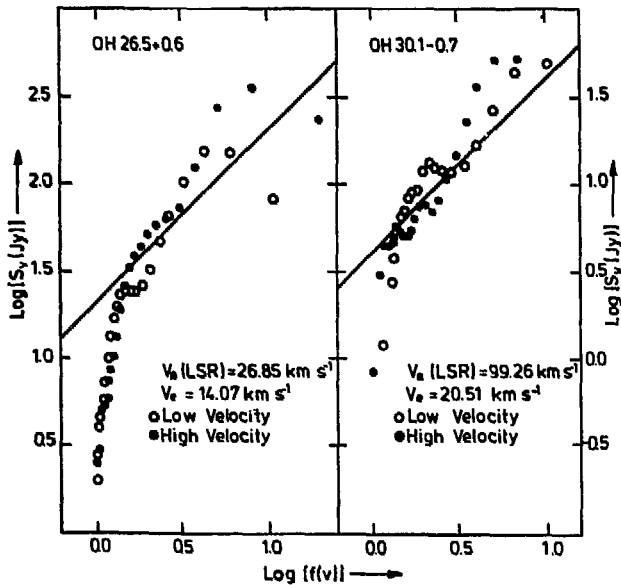


Figure 2. Peak flux density,  $S_v$ , as measured with the VLA (chapter III), as function of  $f(v)$  for two strong OH masers (where each individual channel in the spectrum could be measured). The drawn line indicates the slope expected from the simple model. Substantial deviations from it occur only in the weaker, inner part of the spectrum where part of the flux is missed with the VLA;

$$f(v) \lesssim 1.3, \text{ or } v \lesssim 0.5 v_e.$$

We will assume that  $S_v(R_o, v)$  remains constant for  $v_e - \delta < v(\psi) < v_e$ , and then drops to zero. Then write

$$S(R_o, v, t) = [S^{(0)} + S^{(1)} \cos \{2\pi(\omega t - \Delta\phi)\}] \left\{1 - \left(\frac{v}{v_e}\right)^2\right\}^{-1} \quad (20)$$

where  $\omega$  is the pulsation frequency of the star, or  $\omega \equiv P^{-1}$  with  $P$  the period.

$$\Delta\phi = \frac{\omega R_0}{c} \{1 - \cos \phi\} = \frac{\omega R_0}{c} \left\{1 + \frac{v(\phi)}{v_e}\right\} \quad (21a)$$

the phase lag with respect to the zero phase (star: front), or

$$\Delta\phi_{kj} = \frac{\omega R_0}{c v_e} (v_k - v_j) \quad (21b)$$

the phase difference between peaks at velocities  $v_k$  and  $v_j$ . For a given star the mean 'flux',  $S^{(0)}$ , and the 'amplitude',  $S^{(1)}$ , are constants.  $S^{(0)}$  is given by equation (17), and  $S^{(1)} < S^{(0)}$ . Note that (of course) the largest phase lag occurs when  $v_k = v_e - \delta$  and  $v_j = -(v_e + \delta)$ , i.e. between the back and the front sides of the shell, giving

$$\Delta\phi_{\max} = \frac{2\omega R_0}{c} \left(1 - \frac{\delta}{v_e}\right) = \frac{2\omega R_0}{c} \quad (22)$$

We integrate equation (20) over velocity to find the integrated flux densities

$$S_{LV}(R_0, t) = \int_{-v_e}^0 S_v(R_0, v, t) dv \quad (23a)$$

and

$$S_{HV}(R_0, t) = \int_0^{v_e} S_v(R_0, v, t) dv \quad (23b)$$

Denoting the velocities of the two strongest (front and back) peaks in the spectrum by  $v_{\pm p} (\equiv \pm v_e \mp \delta_{\pm})$  we may write

$$1 - \left(\frac{v_p}{v_e}\right)^2 \approx \frac{2\delta}{v_e} \quad (24)$$

Further we note that  $\omega R_0/c \ll 1$ , because even for extreme (and unlikely) values as  $P(\approx \omega^{-1}) = 200$  days and  $R_0 = 10^{17}$  cm we find  $\omega R_0/c = 0.19 < 1$ , so that we may write

$$\cos\left[2\pi\omega\left\{t - \frac{R_0}{c}\left(1 + \frac{v}{v_e}\right)\right\}\right] \approx \cos[2\pi\omega t] + \frac{2\pi\omega R_0}{c} \left(1 + \frac{v}{v_e}\right) \sin[2\pi\omega t] \quad (25)$$

Using these two approximations we find for the Low Velocity integrated flux density

$$S_{LV}(R_o, t) = \frac{1}{2} v_e \left\{ S^{(0)} + S^{(1)} \cos[2\pi\omega t] \right\} \left\{ 1 + \ln\left(\frac{2v_e}{\delta_-} - 1\right) \right\} + \frac{2\pi\omega R_o}{c} S^{(1)} \sin[2\pi\omega t] \left\{ \frac{\delta_-}{2} + v_e \ln\left(2 - \frac{\delta_-}{v_e}\right) \right\} \quad (26a)$$

and for the High Velocity integrated flux density

$$S_{HV}(R_o, t) = \frac{1}{2} v_e \left\{ S^{(0)} + S^{(1)} \cos[2\pi\omega t] \right\} \left\{ 1 + \ln\left(\frac{2v_e}{\delta_+} - 1\right) \right\} + \frac{2\pi\omega R_o}{c} S^{(1)} \sin[2\pi\omega t] \left\{ v_e - \frac{\delta_+}{2} + v_e \ln\left(\frac{v_e}{\delta_+}\right) \right\} \quad (26b)$$

If the profile is symmetric, i.e.  $\delta_+ = \delta_-$ , we find for the total integrated flux density

$$S_I(R_o, t) = v_e \left\{ S^{(0)} + S^{(1)} \left( \cos[2\pi\omega t] + \frac{2\omega R_o}{c} \sin[2\pi\omega t] \right) \right\} \left\{ 1 + \ln\left(\frac{2v_e}{\delta} - 1\right) \right\} \quad (27)$$

The time of maximum is found from  $\frac{\partial}{\partial t} S(R_o, t) = 0$ . For  $S_{LV}(R_o, t)$

$$\tan[2\pi\omega t] = \frac{4\pi\omega R_o}{cv_e} \left\{ \frac{\delta_-}{2} + v_e \ln\left(2 - \frac{\delta_-}{v_e}\right) \right\} \left\{ 1 + \ln\left(\frac{2v_e}{\delta_-} - 1\right) \right\}^{-1} \quad (28)$$

yielding

$$\phi_M(LV) = \frac{2\omega R_o}{cv_e} \left\{ \frac{\delta_-}{2} + v_e \ln\left(2 - \frac{\delta_-}{v_e}\right) \right\} \left\{ 1 + \ln\left(\frac{2v_e}{\delta_-} - 1\right) \right\}^{-1} \quad (29)$$

The determination of  $\phi_M(HV)$  is completely analogue. The measurable phase difference between the high- and low-velocity integrated flux densities, again assuming  $\delta_+ = \delta_-$ , then becomes

$$\Delta\phi(HV-LV) = \frac{2\omega R_o}{c} f_c \quad (30)$$

with

$$f_c = \left\{ 1 - \frac{\delta}{v_e} + \ln\left(\frac{v_e}{2\delta}\right) \right\} \left\{ 1 + \ln\left(\frac{2v_e}{\delta} - 1\right) \right\}^{-1} \quad (31)$$

Typical values for OH/IR stars of  $v_e = 15 \text{ kms}^{-1}$ , and  $\delta = 0.1 \text{ kms}^{-1}$  yield

$$\Delta\phi(\text{HV-LV}) = 0.8 \frac{2\omega R_o}{c} = 0.8 \Delta\phi_{\text{max}} \quad (32)$$

circa 80% of the phase lag between the 'front' and 'back' peaks. For observed values of the phase lags see chapter II, table 3: for the inferred radii, and the values of  $f_c$ , chapter II, tables 4a-4e.

For the time average of the strongest peaks, at  $\pm v_p$ , we find

$$\bar{S}(R_o, v_p) = S^{(0)} \left\{ 1 - \left( \frac{v_p}{v_e} \right)^2 \right\}^{-1} = \frac{v_e}{2\delta} S^{(0)} \quad (33)$$

And for the integrated flux density

$$\bar{S}_{\text{LV}}(R_o) = S^{(0)} \frac{v_e}{2} \left\{ 1 + \ln \left( \frac{2v_e}{\delta} - 1 \right) \right\} \quad (34)$$

and thus for the ratio of the mean integrated- and peak-flux densities

$$\bar{S}_{\text{LV}} / \bar{S} = \delta \left\{ 1 + \ln \left( \frac{2v_e}{\delta} - 1 \right) \right\} \quad (35)$$

For the canonical values  $v_e = 15 \text{ kms}^{-1}$  and  $\delta = 0.1 \text{ kms}^{-1}$  we find a ratio of 3.6 KHz. As expected from equation (35) this 'equivalent width' is rather the same for all OH/IR stars, that have a limited range of  $\delta$  and  $v_e$  values (see chapter II, figure 14).

#### Literature cited in Appendix A

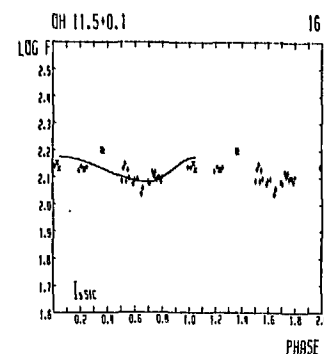
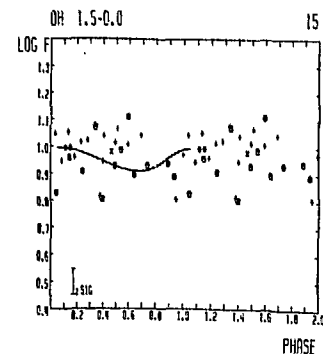
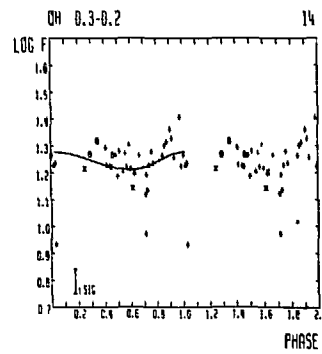
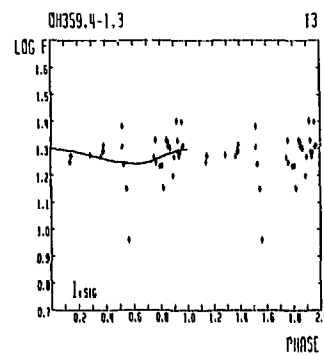
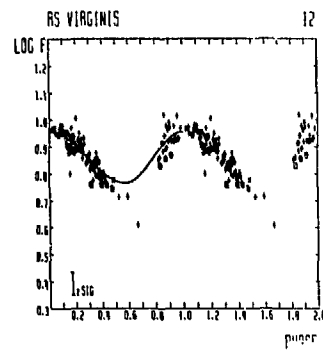
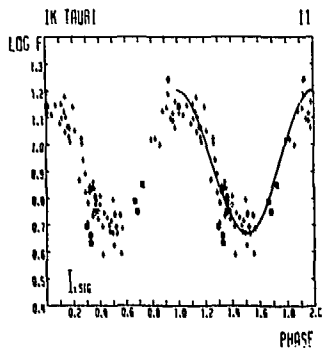
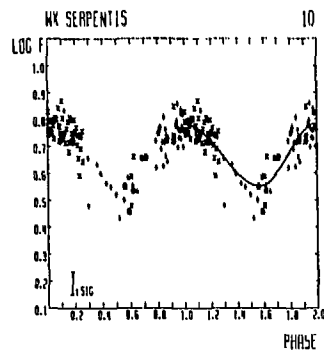
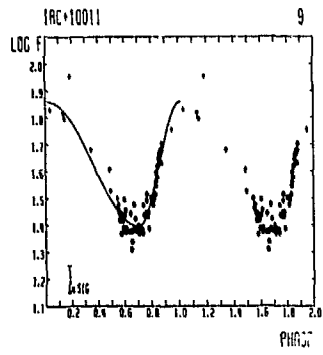
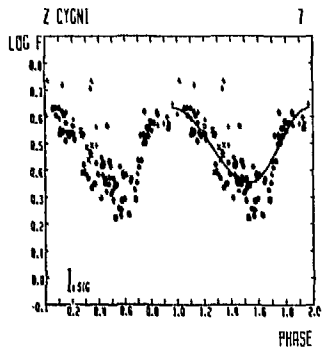
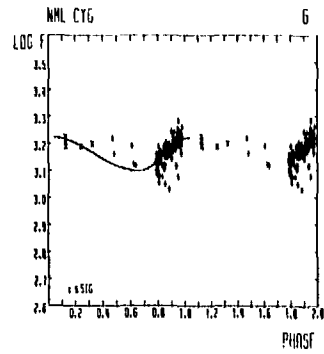
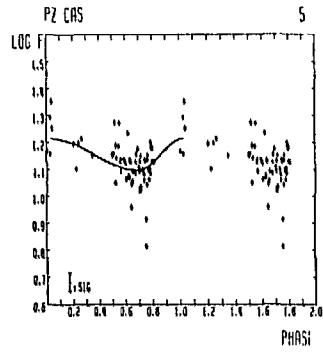
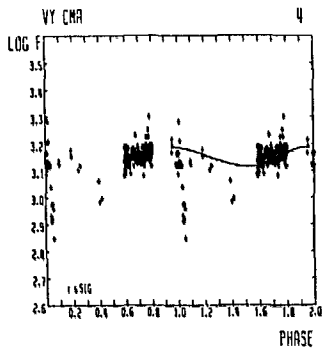
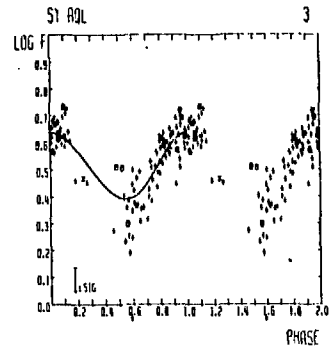
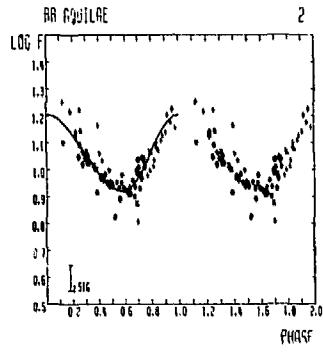
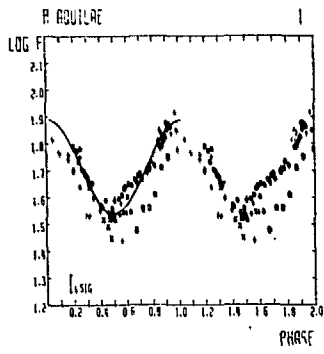
- Cook, A.H.: 1968, *M.N.R.A.S.* 140, 299  
 Goldreich, P., Keeley, D.A.: 1972, *Astroph. J.*, 174, 517  
 Haar, D. ter. Pelling, M.A.: 1974, *Reports on Progress in Physics*, 37, 481  
 Mihalas, D.: 1978, *Stellar Atmospheres*, 2<sup>nd</sup> ed by W.H. Freeman and Co, San Francisco  
 Reid, M.J., Muhlemann, D.O., Moran, J.M., Johnston, K.J., Schwartz, P.R.: 1977, *Astroph. J.* 214, 60

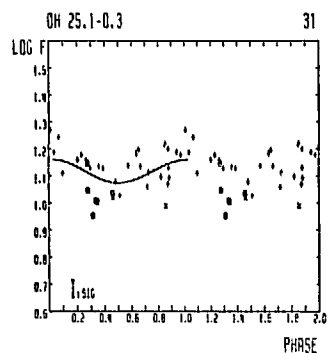
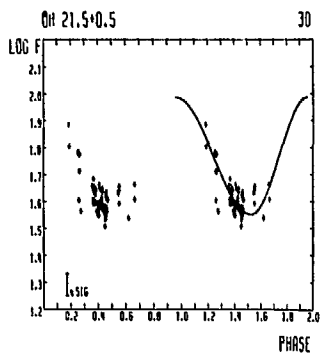
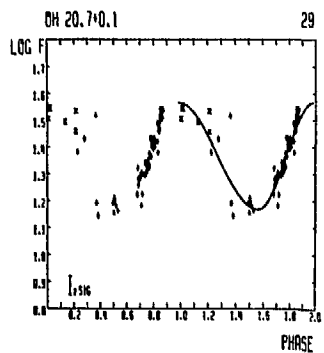
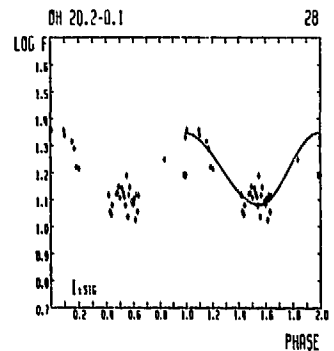
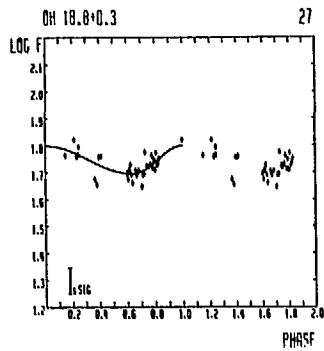
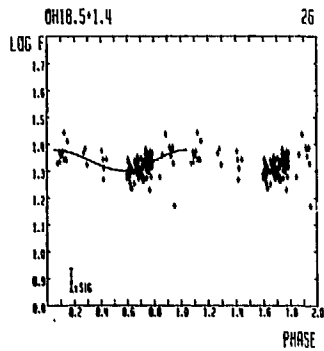
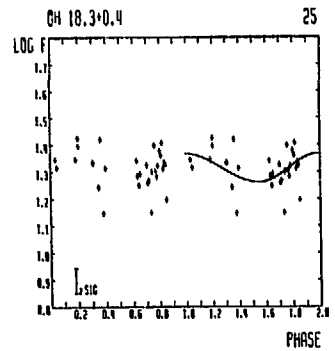
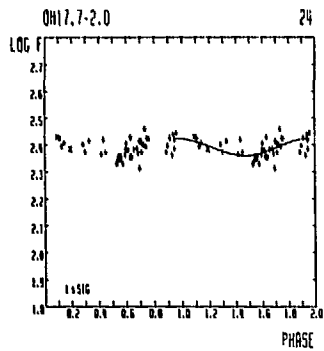
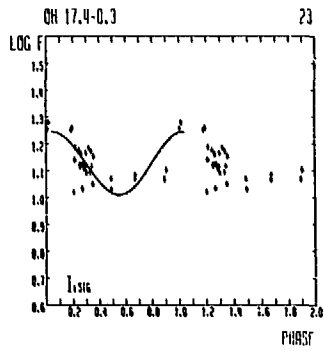
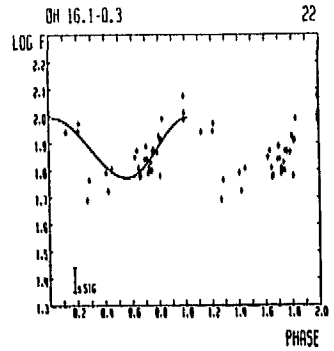
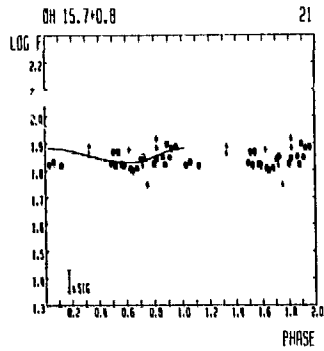
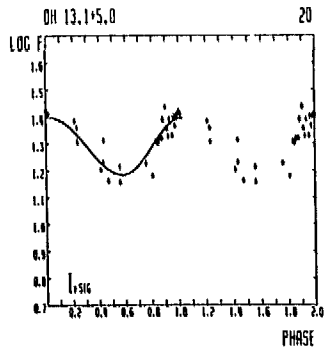
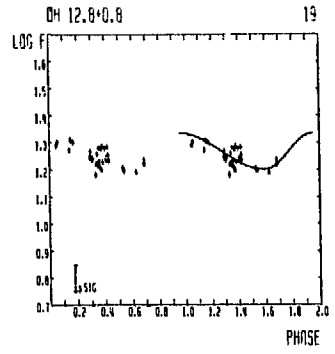
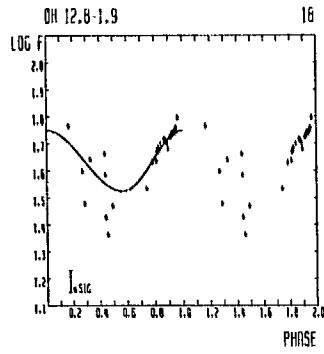
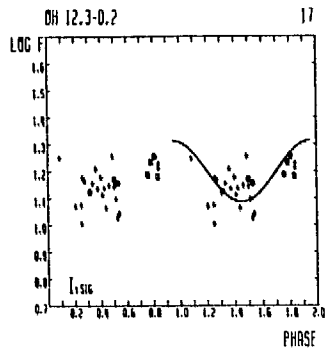
## Appendix B

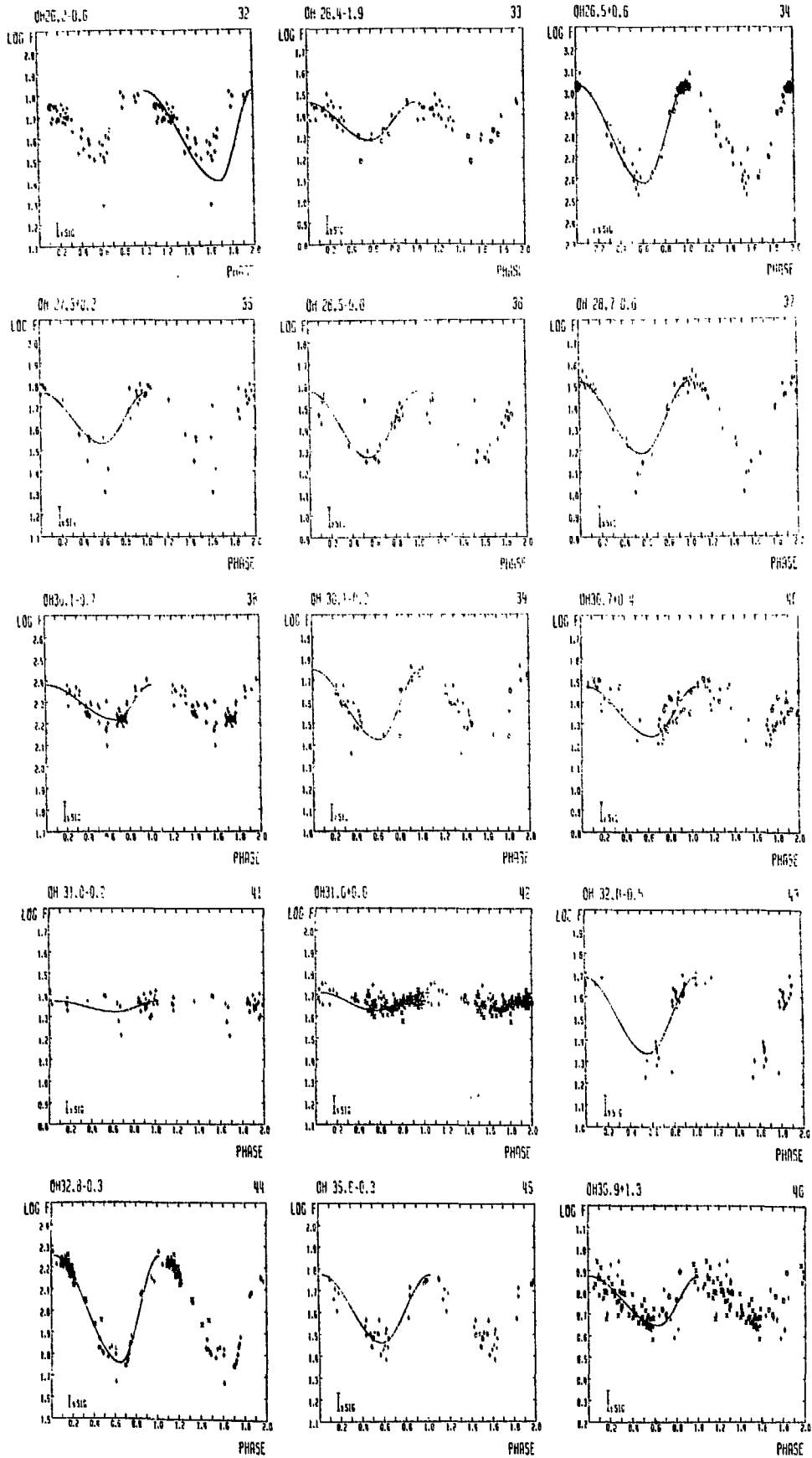
### a. Radio light curves of OH masers

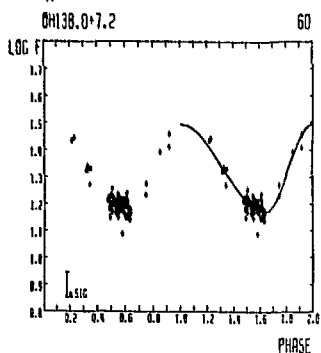
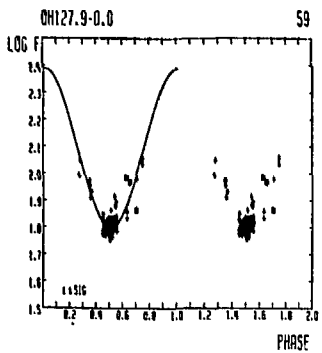
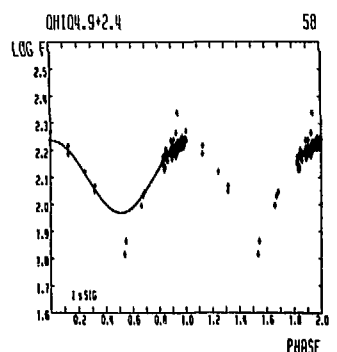
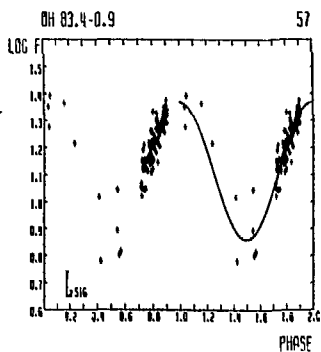
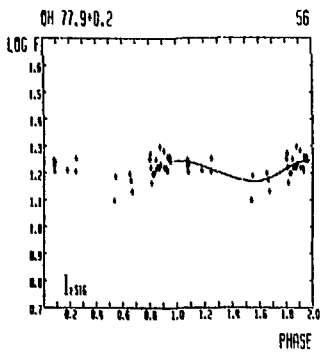
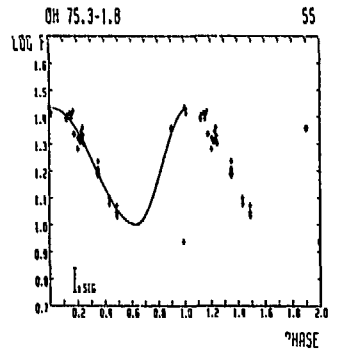
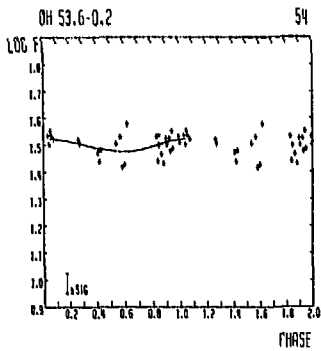
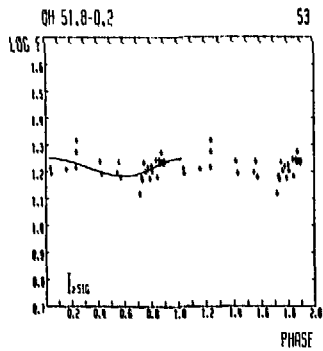
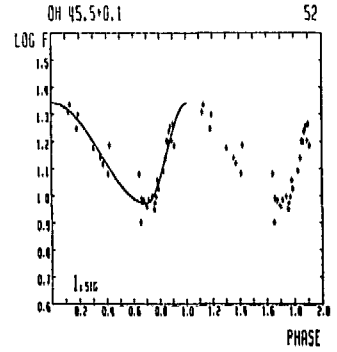
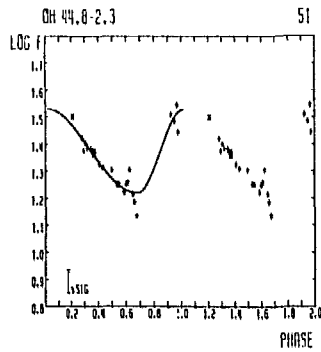
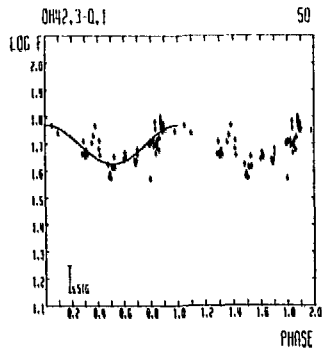
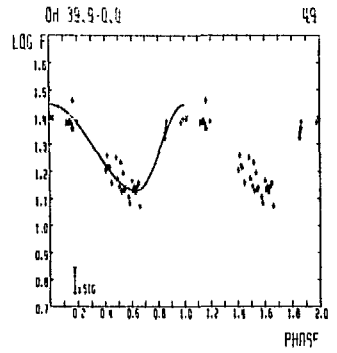
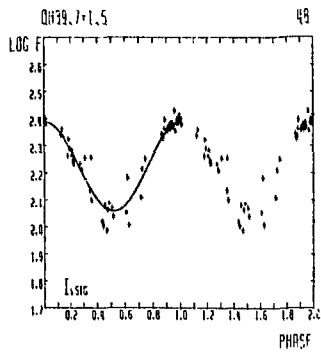
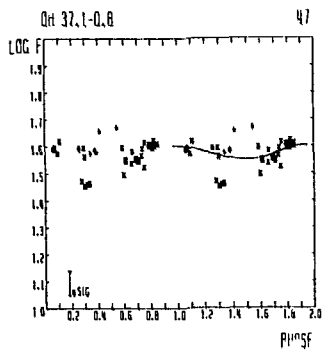
For all stars included in the Dwingeloo monitor program the variation of the total integrated flux density, here denoted by  $F(10^{-22} \text{Wm}^{-2})$  is shown. The labeling of the figures refers to the numbers used in chapter II (tables 2 and 3). The light curve of U Ori (no. 8) can be found in chapter II (figure 9). Phases were calculated with the periods and phase zero points as listed in table 3 (chapter II). Different symbols represent different cycles (squares:  $n=-6$ ; circles;  $n=-5$ ; triangles;  $n=-4$ ; plusses:  $n=-3$ ; crosses:  $n=-2$ ; diamonds:  $n=-1$ ; arrows:  $n=0$ ). For display purposes all curves are repeated; thus every observed point is shown *twice*.

The curve drawn is *not* the best fit to the observed integrated fluxes, but is based on the curves of the peak flux densities also. For the parameters describing the mean values, the amplitudes, and the shapes of the curves see chapter II, table 3. In the lower left corner an error bar indicates the  $1-5 \sigma$  (depending on its magnitude) uncertainty for an *individual* measurement (average value).









b. IR light curves of OH Mira variables

Feast (private communication) observed for us a number of OH Mira's in the near infrared (J,H,K, and L) at the South African Astronomical Observatory from May, 1975 until December, 1981. The light curves at  $3.45 \mu\text{m}$  (L band) with the best phase coverage are shown in figures 60-67. Phases were calculated with the periods and phase zero points from the radio curves (see chapter II, table 3). Different symbols represent different cycles.

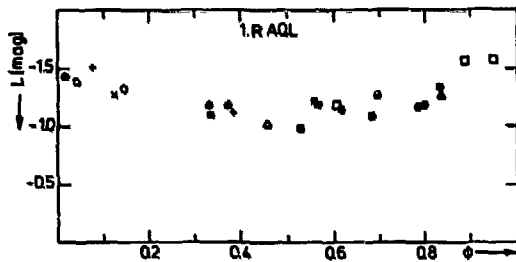


Figure 60 R Aquilae (no. 1)

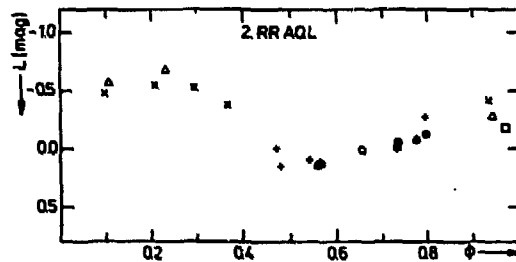


Figure 61 RR Aquilae (no. 2)

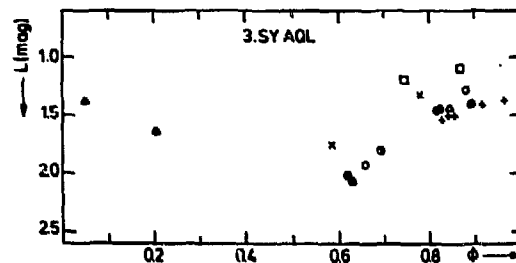


Figure 62 SY Aquilae (no. 3)

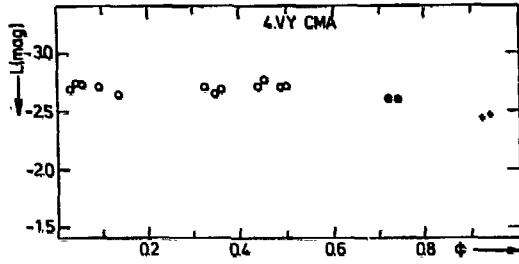


Figure 63 VY Canis Majoris  
(no. 4)

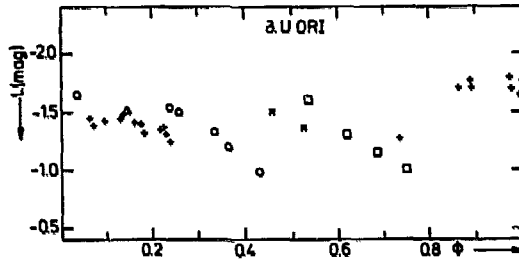


Figure 64 U Orionis (no. 8)

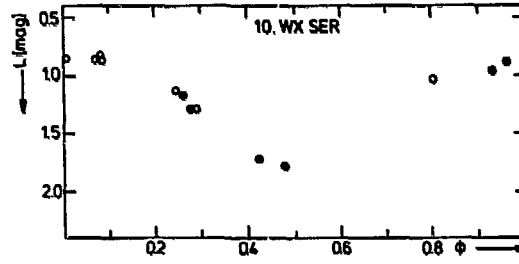


Figure 65 WX Serpentis  
(no. 10)

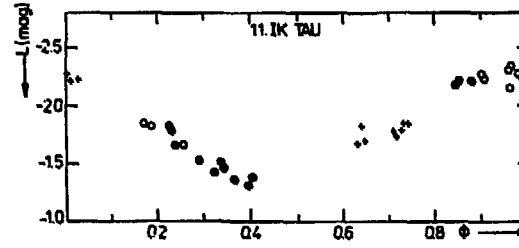


Figure 66 IK Tauri (no. 11)

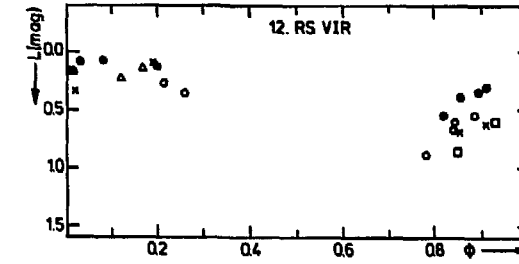


Figure 67 RS Virginis (no. 12)

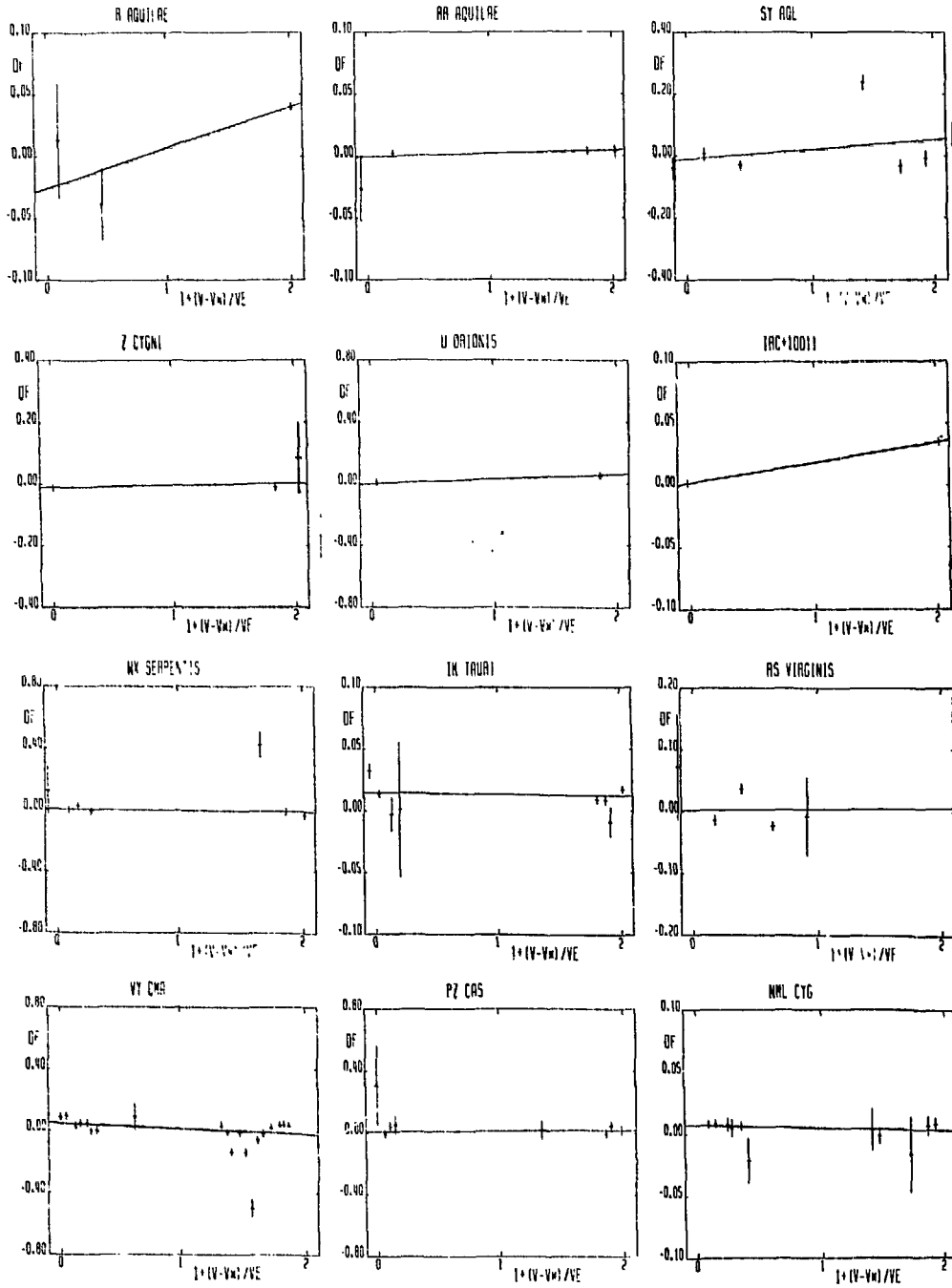
## Appendix C

### Phase lag as function of velocity

In the geometry of an uniformly expanding shell the phase lag,  $\Delta\phi_{k_0}$ , for various peaks in the spectrum is expected to be correlated with their velocities (with respect to the stellar velocity). We choose the phase of the low velocity integrated flux as zero point and plotted the phase difference, here denoted by DF, for every peak of a given star as function of  $1 + \frac{v(\psi)}{v_e}$ , where  $v(\psi) \equiv v_{\text{rad}}(\text{peak}) - v_{\text{rad}}(\text{star})$ . The drawn lines are the least squares fits, weighted with the uncertainties in the phase lags (indicated by the error bars; see chapter II, table 3 for the values), but also with the mean signal-to-noise ratio of the peaks. The slope of the line is  $R_0/c$ , where  $R_0$  is the radius of the shell. So in this simple model a negative value for the slope is 'forbidden'.

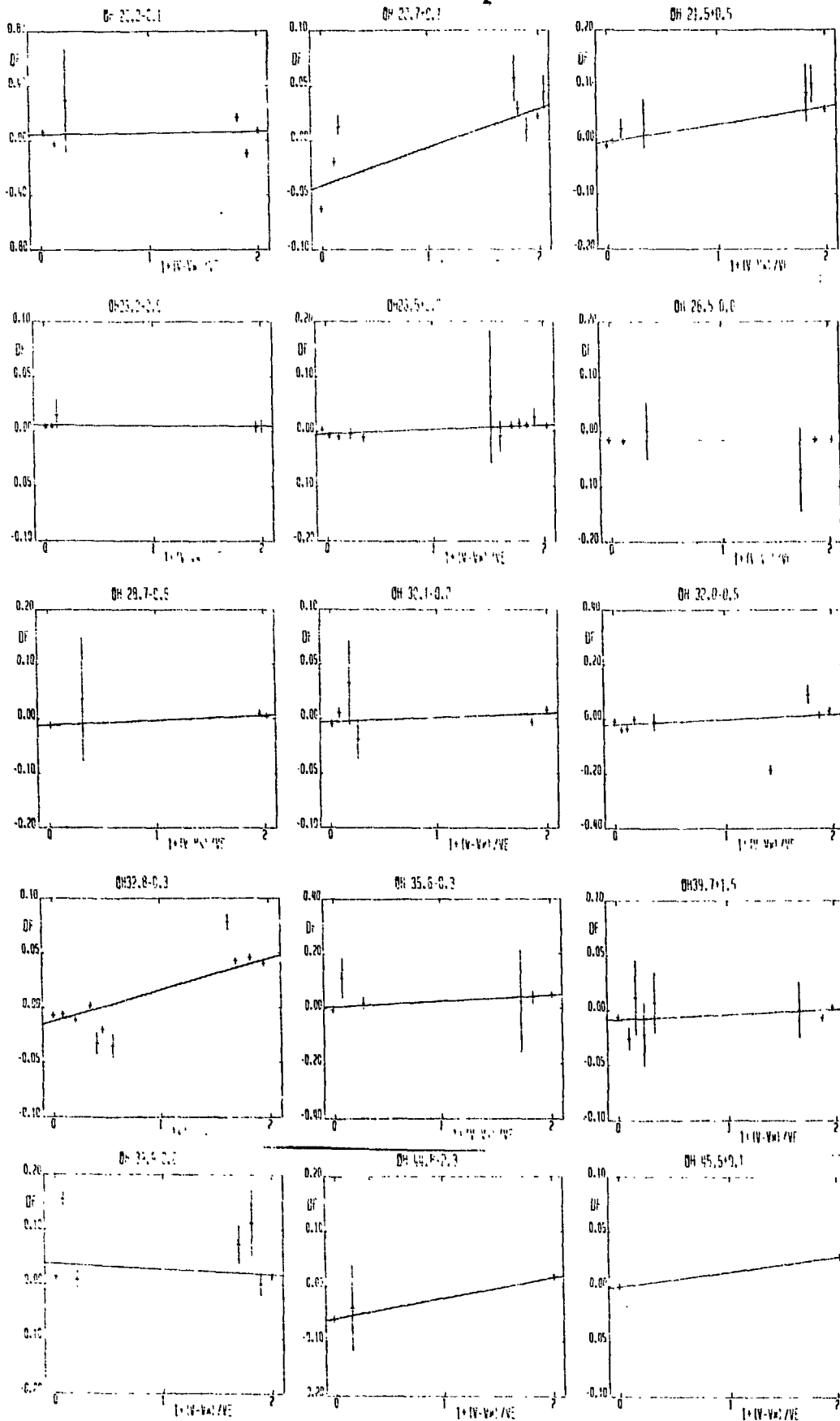
a. Mira variables and M-type supergiants

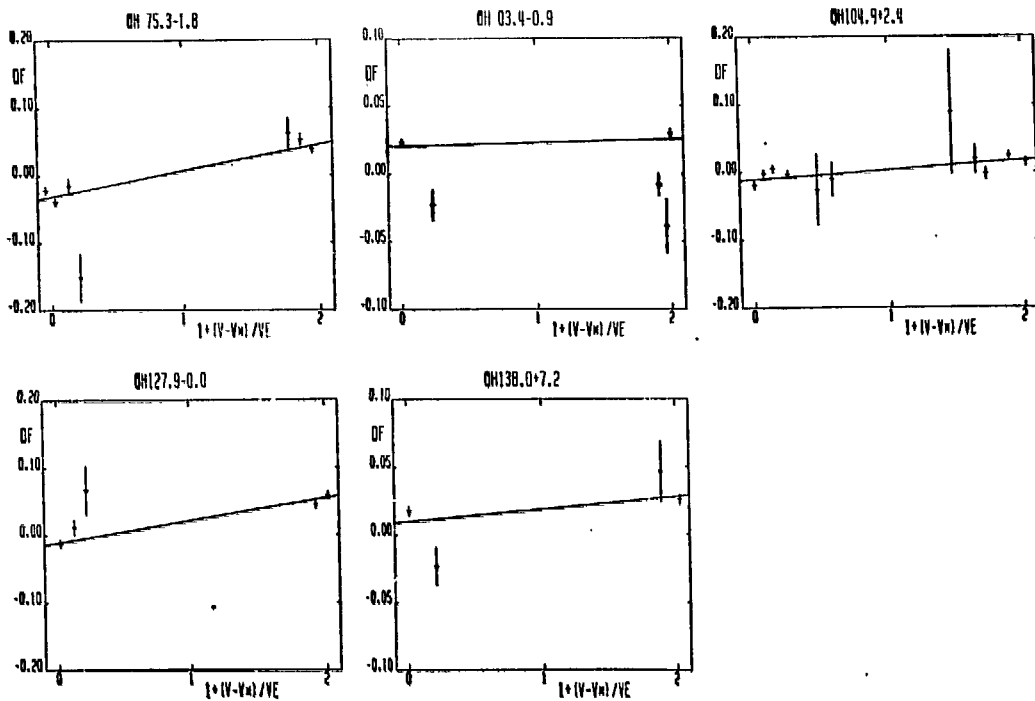
Figures 1-12



b. OH/IR stars with large amplitudes ( $\Delta m_r > 0.60$ )

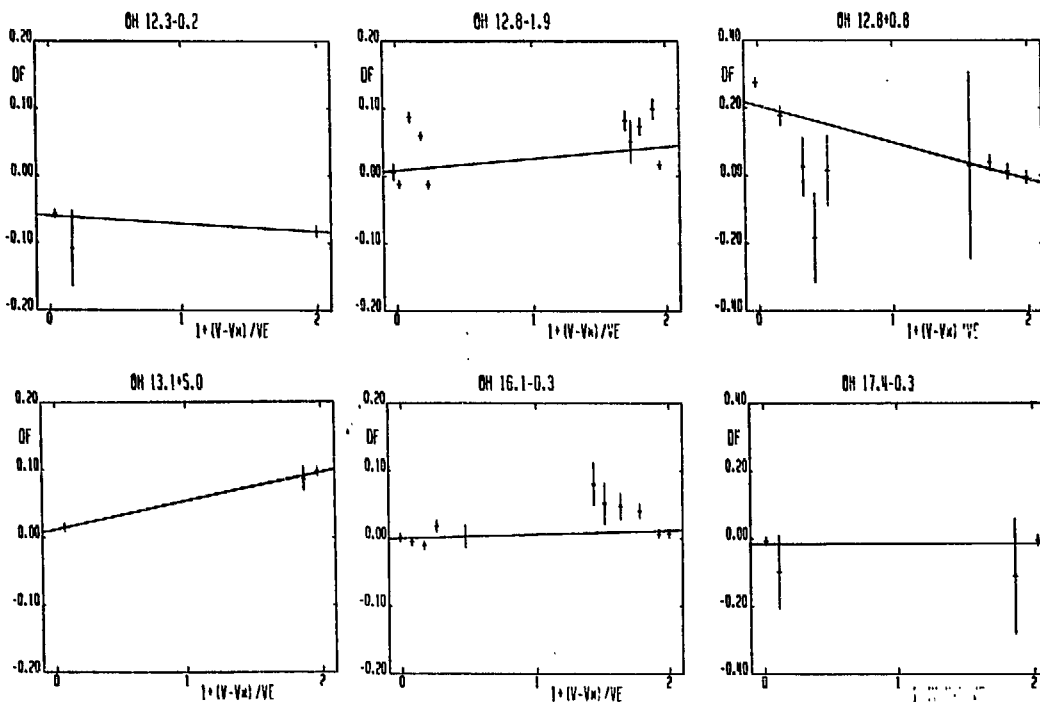
Figures 13-32

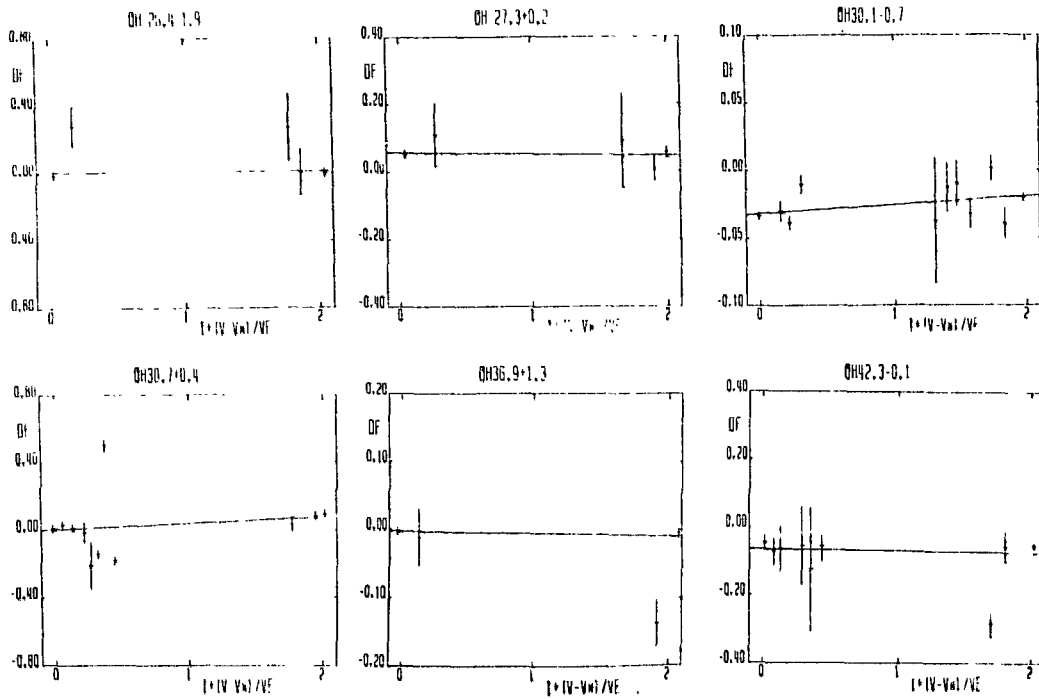




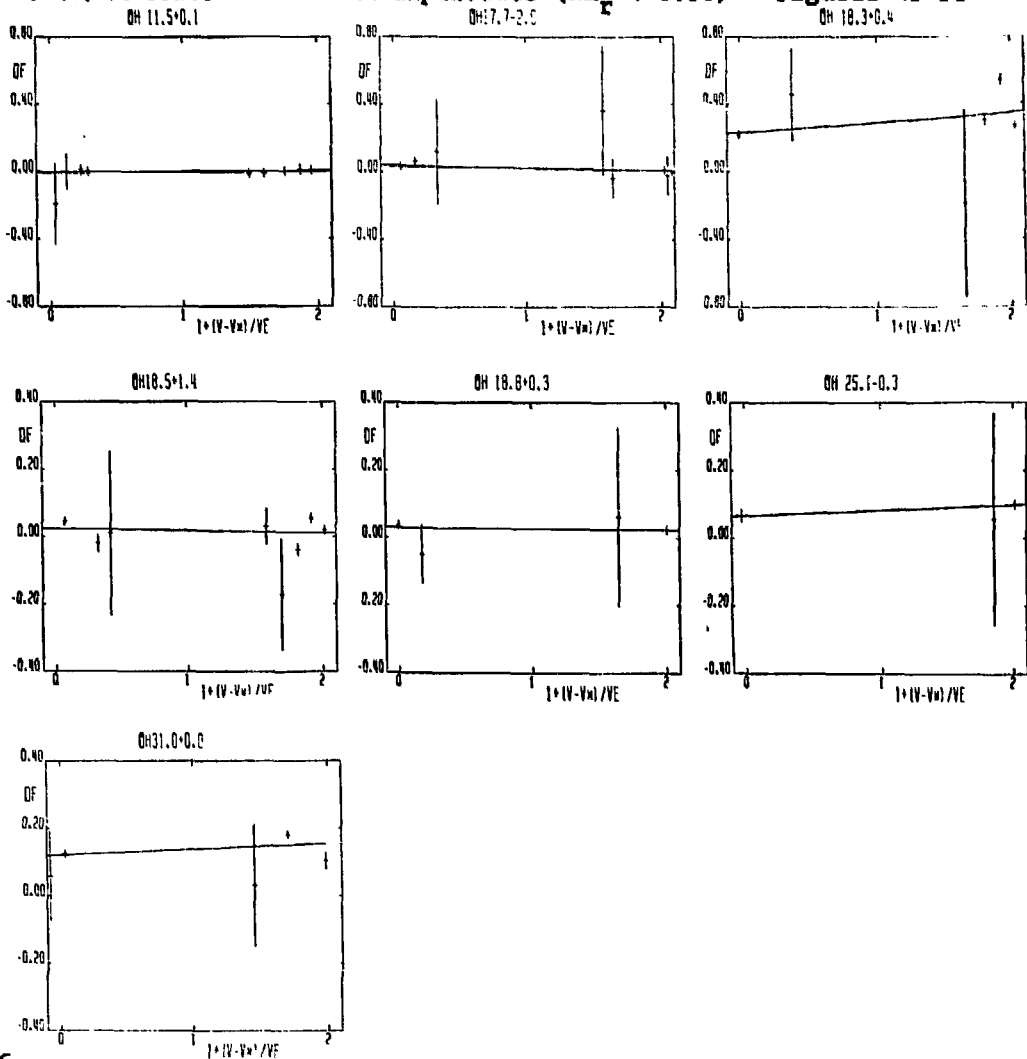
c. OH/IR stars with intermediate amplitudes ( $0.30 < \Delta m_r < 0.60$ )

Figures 33-44





**d. OH/IR stars with small amplitudes ( $\Delta m_r < 0.30$ ) Figures 45-51**



Appendix D  
VLA continuum observations at 6 cm<sup>1)</sup>

a. Introduction

OH/IR stars are evolved M-type (super)giants with masses from 1  $M_{\odot}$  to  $\gtrsim 10 M_{\odot}$ . They all are losing mass at a very high rate ( $10^{-6}$  to  $10^{-4} M_{\odot} \text{ yr}^{-1}$ ) and consequently are in a short lived, but dramatic phase in their evolution. Probably in  $10^3 - 10^4$  yr the star sheds its entire envelope and hence it might be in the process of forming a planetary nebula. If the OH/IR stars indeed are the precursors of population I planetary nebulae, then some of them might be in an intermediate stage, where still the maser emission from the outer parts of the shell is visible, but also radio continuum emission from a hot, ionized region close to the star. Especially those objects with the highest expansion velocities of the shell, that are thought to be the youngest ( $10^7$  yr), the most massive ( $\gtrsim 5 M_{\odot}$ ), and the most luminous ( $\gtrsim 5 \cdot 10^4 L_{\odot}$ ) stars, could have a stellar wind energetic enough create a small HII region. Such a scenario has been proposed (Kwok, 1981) for the OH emitting planetary nebula Vy 2-2 (see Davis *et al.*, 1979). Recent VLA observations (Lindsay, private communication) have confirmed the positional coincidence between the OH maser and the radio continuum source associated with Vy 2-2.

Winnberg, Goss, and Habing have used the VLA in 1980 to search for 21 cm continuum emission from VY CMa, an optically identified OH/IR supergiant. No emission was found to a limit of 0.1 mJy (Goss, private communication). However, judged from its optical visibility, the mass loss rate of this object might not be high enough to create an HII region. Furthermore, such a dense ionized region probably is optically thick and should therefore be searched for at shorter wavelengths.

b. Observations

We have used the VLA to search for 6 cm continuum emission from a sample of 12 OH/IR stars. The observations were made by R. Perley in the 'remote observing mode' on July 16, 1982 when the VLA was in a hybrid

1) Proposed and obtained by B. Baud, H.J. Habing, and J. Herman.

configuration between A and B array (see for a general description of the VLA: Thompson *et. al.*, 1980). All 27 telescopes were used at  $\lambda = 6$  cm with a bandwidth of 50 MHz. We selected 12 OH/IR stars, for which we had VLA positions available, that covered a range in  $v_e$  values (i.e. expansion velocities) and in mass loss rates (see chapter V, section 7). All sources were observed in three shortcuts of 10 minutes each, yielding a  $1\sigma$  sensitivity of  $60 \mu\text{Jy}$ . Calibrations were done every 20 minutes on the continuum source 1741-038, and on 3C286 at the beginning and the end of the run. The reduction was completed in Leiden, where the Charlottesville package is operating.

### c. Results

None of the OH/IR stars was detected at  $\lambda = 6$  cm stronger than the  $1\sigma$  level. In table 1 we list the names of the objects, and the phase at which they were observed (see for the periods, and phase zero points: chapter II, table 3). The distances were taken from chapter V (table 2), or when the star was not included in the monitor program, the (near) kinematic distance was used. The expansion velocities,  $v_e$ , and the absolute (at  $D = 1\text{kpc}$ ) OH peak flux density,  $L_{\text{OH}}$ , are tabulated. When the star was included in the monitor program,  $L_{\text{OH}}$  is the averaged value over the light curve.

Table 1

Name OH ———	$\phi$	D (kpc)	$v_e$ ( $\text{km s}^{-1}$ )	$\langle L_{\text{OH}} \rangle$ ( $\text{Jy kpc}^2$ )	$f$ ( $10^{-3} M_{\odot} \text{ yr}^{-1}$ )	$F_{6\text{cm}}$ ( $\mu\text{Jy}$ )	Remarks
18.5+1.4	.037	4.50 (1)	10.85	139.5	2.27	95	Slightly variable
20.7+0.1	.122	6.31 (1)	18.21	598.7	7.88	90	
21.3+0.5	.616	11.63 (1)	18.76	2813	17.59	91	
25.1-0.3	.405	4.69 (1)	12.14	159.7	2.71	114	Slightly variable
27.0-0.4		6.76 (2)	14.50	138.9	3.02	90	Not in monitor program
27.5-0.9		7.35 (2)	13.50	170.1	3.11	82	Not in monitor program
28.5-0.0	.353	2.45 (1)	13.12	63.95	1.86	195	
29.4-0.8		8.02 (2)	11.75	240.7	3.22	95	Not in monitor program
30.1-0.7	.921	1.77 (1)	20.51	196.8	5.09	94	
31.0-0.2	.276	6.50 (1)	14.27	273.4	4.17	213	Non variable
32.0-0.5	.090	9.30 (1)	20.58	678.4	9.48	80	
39.9-0.0	.009	3.07 (1)	14.71	63.14	2.07	110	

(1): see chapter V, table 2.

(2): kinematic distance;  $R_0 = 9.2$  kpc

The mass loss rates were inferred from  $v_e$  and  $L_{OH}$  (see chapter V, section 7.e2). In the last column the rms-values as measured in the cleaned maps (10"x10") are given. At the, accurately known, stellar positions even more stringent upper limits can be set to the continuum flux received.

#### d. Conclusion

Although we searched for radio continuum emission from OH/IR stars in some of the most likely candidates, we were unsuccessful. This means that either OH/IR stars do not evolve to planetary nebulae, or if they do (in chapter V, section 7.g this is shown to be the case) that the phase, in which both the maser and the continuum emission are visible, is very short ( $< 10^3$  yr).

#### Acknowledgements

We are indebted to R. Perley for carrying out the observations and calibrations, and to A. Slootmaker for doing part of the reduction. The National Radio Astronomy Observatory is operated by Associated Universities, Inc., under contract with the National Science Foundation.

#### Literature cited in Appendix D

- Davis, L.E., Seaquist, E.R., Purton, C.R.: 1979, *Astroph. J.* **230**, 434  
Kwok, S.: 1981, in *Physical Processes in Red Giants*, eds. I. Iben and A. Renzini, Reidel, pp 421-426  
Thompson, A.R., Clark, B.G., Wade, C.M., Napier, P.J.: 1980, *Astroph. J. Suppl.* **44**, 151

## Appendix E

### Results of the infrared observations at UKIRT

Table 1 gives the magnitudes in each band for all stars in our program that were detected. The precise wavelengths and widths of the bands, and the conversion factors of magnitudes to Jansky's can be found in chapter IV (table 1). The uncertainties in the tabulated magnitudes are typically 0.05<sup>m</sup>. For each source the largest error, and the band in which that occurs, are listed.

Table 1

Band Name	L' $\lambda(\mu\text{m})$	M 3.8	N <sub>1</sub> 4.8	N <sub>2</sub> 8.7	N <sub>3</sub> 9.7	N <sub>4</sub> 10.5	N <sub>5</sub> 11.5	N <sub>6</sub> 12.5	Q 20	Largest error	Band
MX Ser	0.88	0.40	-1.40	-1.90	-1.98	-2.06	-1.94	-3.15	0.05	N <sub>1</sub>	
RS Vir	0.03	-0.21	-1.18	-1.45	-1.55	-1.64	-1.65	-2.28	0.07	N <sub>1</sub>	
OH 12.8-1.9	1.73	0.99	-0.85	-0.80	-1.14	-1.67	-1.72	-2.67	0.07	N <sub>5</sub>	
OH 17.7-2.0	7.06	5.90	2.17	1.85	1.30	0.32	-0.14	-2.58	0.08	M	
OH 20.2-0.1	3.00	2.24	-0.08	0.31	0.17	-0.49	-0.77	-1.28	0.06	N <sub>3</sub>	
OH 20.7+0.1	8.12	5.13	3.24	3.97	4.70	2.06	1.07	-0.36	0.15	N <sub>3</sub>	
OH 21.5+0.5	7.48	4.69	2.11	4.50	4.40	1.34	0.10	-0.61	0.14	N <sub>2</sub>	
OH 26.2-0.6	4.30	2.99	0.85	1.80	1.55	0.06	-0.22	-1.25	0.08	Q	
OH 26.4-1.9	3.09	1.90	-0.08	0.11	0.07	-0.74	-0.94	-2.23	0.04	N <sub>5</sub>	
OH 28.5-0.0	7.64	5.41	3.09	>4.5	>4.5	2.53	1.56	0.56	0.11	Q	
OH 28.7-0.6	3.30	2.50	0.62	0.73	0.45	-0.14	-0.29	-1.78	0.06	N <sub>1</sub>	
OH 30.1-0.7	4.03	8.33	-0.50	1.09	0.66	-1.11	-1.65	-3.17	0.12	N <sub>2</sub>	
OH 30.1-0.2	3.34	2.42	0.54	0.72	0.49	-0.30	-0.58	-1.74	0.03	N <sub>4</sub>	
OH 30.7+0.4	3.73	2.06	0.34	1.46	1.21	-0.41	-0.96	-2.31	0.06	N <sub>2</sub>	
OH 31.0-0.2	7.77	4.86	1.56	3.53	3.29	1.17	0.30	-1.06	0.09	N <sub>3</sub>	
OH 32.0-0.5	4.96	3.01	1.01	2.40	1.95	0.15	-0.49	-1.95	0.06	N <sub>2</sub>	
OH 32.8-0.3	5.14	2.82	0.77	>4.8	2.37	0.08	-0.81	-2.45	0.07	N <sub>3</sub>	
OH 39.7+1.5	0.52	-0.42	-2.42	-1.89	-2.16	-3.15	-3.36	-4.56	0.05	N <sub>2</sub>	
OH 39.9-0.0	3.90	2.60	0.62	1.23	1.11	-0.12	-0.37	-1.79	0.05	N <sub>2</sub>	
OH 42.3-0.1	5.87	3.97	1.08	2.47	2.33	0.35	-0.16	-1.47	0.11	N <sub>2</sub>	

Before, and after an observation of a program star standard stars have been observed, allowing a good air mass correction and flux calibration. In table 2 these standards are listed with the magnitudes adopted for each band.

Table 2

Standard	Band $\lambda(\mu\text{m})$	L' 3.8	M 4.8	N <sub>1</sub> 8.7	N <sub>2</sub> 9.7	N <sub>3</sub> 10.5	N <sub>4</sub> 11.5	N <sub>5</sub> 12.5	Q 20	
$\alpha$ Sco			-3.84	-4.55	-4.60	-4.64	-4.77	-4.76	-4.70	BS 6134
$\alpha$ Boo			-2.95	-3.17	-3.22	-3.15	-3.23	-3.33	-3.30	
B Peg	-2.34	-2.21	-2.45	-2.56	-2.55	-2.59	-2.70	-2.90		BS 8775
BS 6406		-3.44	-3.84	-3.89	-3.87	-4.05	-4.16	-4.30		

Some other bright stars (BS, or HR catalogue) were used for the L'band. They were (with their magnitude at  $L' = 3.8\mu\text{m}$  between brackets): BS 4689 ( $3^{\text{m}}.76$ ), BS 5200 ( $0^{\text{m}}.20$ ), BS 5447 ( $3^{\text{m}}.44$ ), BS 6746 ( $0^{\text{m}}.65$ ), BS 7120 ( $1^{\text{m}}.90$ ), and BS 8167 ( $2^{\text{m}}.13$ ).

## Nederlandse samenvatting

In dit proefschrift worden de eigenschappen en karakteristieken van OH/IR sterren, een geëvolueerde populatie, bestudeerd. Zoals reeds blijkt uit naam en titel, gaat het hier om geëvolueerde sterren, voornamelijk opvallend door hun infrarood (IR) emissie en anomale straling van het OH molecuul in het radio golflengte gebied. Laat ik beginnen met iets te zeggen over het infrarood. Tegen het einde van hun leven, als hun kernbrandstof vrijwel uitgeput is, zwellen de sterren enorm op; sommigen zijn zo groot dat zij de gehele aardbaan zouden vullen. De temperatuur aan het steroppervlak wordt steeds lager, en de ster steeds roder om te zien. Nu blijken deze sterren grote hoeveelheden materie uit te stoten, die een uitgestrekte schil van gas en stof rondom hen vormt. Op een gegeven moment wordt de ster geheel aan het zicht onttrokken: alle sterstraling wordt door het stof geabsorbeerd en weer uitgezonden op de langere infrarode golflengten. Zodoende heeft de energieverdeling haar maximum in het infrarood (ter vergelijking: voor de zon valt dit maximum midden in het visuele golflengtegebied, voor hete sterren meer naar het blauw en voor koele sterren meer naar het rood).

De sterren zelf zijn al bijzonder groot (1 astronomische eenheid: per definitie de afstand aarde-zon), maar de circumstellaire stofschillen strekken zich uit over zo'n 1000 astronomische eenheden, ongeveer 30 maal de afstand van Pluto tot de zon! De totale massa in de schillen is vrij groot (1 à 2 zonsmassa's) en astronomen spreken van deze gevallen als sterren met dikke stofschillen. Maar het aantal deeltjes per kubieke centimeter is, zeker in de buitenste lagen van de schil, klein, soms minder dan wat wij op aarde onder vacuüm verstaan! Onder zulke omstandigheden kan door invloeden van buitenaf, straling van nabij gelegen hete sterren, het stabiele molecuul  $H_2O$  (water) gedissocieerd worden tot het, in aardse laboratoria nauwelijks in stand te houden, OH radicaal. Zoals ieder molecuul heeft OH een (groot) aantal karakteristieke spectraallijnen: in het visueel en nabij infrarood van de zogenaamde vibratie-overgangen, in het ver infrarood van de rotatie-overgangen en in het radio golflengtegebied van overgangen tussen zgn. hyperfijn niveaus. De vier overgangen tussen de vier hyperfijn niveaus in de grond (rust) toestand liggen bij een golflengte van 18cm. Deze lijnen werden aan het eind van de zestiger en het begin van de zeventiger jaren voor het eerst in sterrenkundige objecten waargenomen. Allereerst ontdekte men ze in de richting van gebieden met stervorming, maar later ook in de richting van geëvolueerde

sterren. Te zelfder tijd vond men in beide categorieën objecten (jong en oud) ook radio emissielijnen van enkele andere moleculen, zoals SiO en H<sub>2</sub>O. De emissie was behoorlijk sterk en ook bleken de verhoudingen tussen de lijnen totaal anders te zijn dan men op theoretische gronden verwachtte. Nadere onderzoeken, met name VLBI (very long baseline interferometry) experimenten, waarbij ver uitelkaar staande telescopen tegelijk worden gebruikt, maakten duidelijk dat wij te maken hadden met 'masers' (microwave amplification by stimulated emission of radiation), een natuurlijke tegenhanger van de op aarde zeer bekende lasers.

Een maser of laser is het best te vergelijken met een lawine, of zo men wil met de parabel van de graankorrels op het schaakbord. Begin met één foton (in het geval van OH één met een golflengte van 18cm) dat een (OH) molecuul in aangeslagen toestand tegenkomt. Mits de golflengte 'past', kan nu een foton geïnduceerd worden. Het molecuul valt terug naar een lager energieniveau en er komt een foton vrij met dezelfde golflengte en richting als het eerste foton. Op hun beurt kunnen de twee weer twee nieuwe makkers induceren, en zo kan een groot aantal gelijk gerichte, monochromatische (d.w.z. met één golflengte, één bepaalde energie) fotonen vrijkomen. Er zijn wel twee voorwaarden om dit proces te laten werken. In de eerste plaats moet de golflengte passen: d.w.z. de moleculen moeten allemaal dezelfde snelheid hebben, anders 'zien' zij de fotonen niet vanwege het welbekende Doppler effect. In de tweede plaats moet er energie in het systeem gepompt worden (niets voor niets) om te zorgen dat er steeds voldoende moleculen in de (juiste) aangeslagen toestand zijn. Bovendien is het duidelijk dat hoe langer de weg is die de fotonenbundel aflegt door de verzameling moleculen, hoe groter de uiteindelijke lawine zal zijn. Bij de aardse laser is dit alles niet zo moeilijk: men heeft een buis met (stilstaande) gasmoleculen en door de steeds sterker wordende bundel tussen twee spiegels heen en weer te laten kaatsen (de zgn. trillingsholte) kan men een willekeurig grote weglengte verkrijgen. Ook de energietoevoer is (afgezien van futiele technische details) niet moeilijk: overal zijn stop-contacten. Laat ik mij bij de bespreking van de situatie in de natuur beperken tot de OH masers, die in de periferie van de dikke stofschillen rond pas gevormde en op sterven na dode sterren voorkomen. In beide gevallen wordt het licht van de zeer lichtsterke centrale ster (zo'n 10 000 maal de zonslichtkracht) geabsorbeerd door de circumstellaire schil en heruitgezonden in het infrarood. Door het opvangen van infrarode straling worden de OH moleculen geëxciteerd (in de reeds genoemde rotatie niveaus) en cascaderen vervolgens

terug naar de grondtoestand onder uitzending van lichtquanta. Door allerlei, tamelijk ingewikkelde, oorzaken echter komen zij niet in het laagste, maar in een van de hogere hyperfijn niveaus van de grondtoestand terecht. Op die manier pompen de infrarood fotonen energie in de moleculen en zorgen ervoor dat er steeds in de aangeslagen hyperfijn toestand zijn, die 'past' bij de 18cm fotonen. Zoals reeds opgemerkt is de dichtheid in de schillen laag; naast velerlei andere deeltjes ongeveer 10 OH moleculen per cc. Maar door de gigantische afmetingen (1000 astronomische eenheden is ongeveer 10 miljoen miljard cm) komt de fotonenbundel toch voldoende moleculen tegen. Vooral rond de geëvolueerde sterren, die de stofschild rustig naar buiten blazen, hebben alle stof en gasdeeltjes dezelfde, van de ster afgerichte, snelheid. Zo kan een lawine fotonen ontstaan, allen met dezelfde golflengte, die tot op zeer grote afstand waarnaar is. Aardig is hierbij op te merken dat dergelijke masers per seconde op één golflengte net zoveel fotonen uitzenden als de zon op alle golflengten tezamen, maar dat de totale energie van zo'n bundel nog geen miljardste deel is van de totale zonsenergie.

Er blijkt een duidelijk verschil te bestaan tussen de OH maseremissie in extreem jonge en in oude sterren: beide hebben hun eigen 'radio'handtekening. Zoekacties naar OH masers met het signatuur van geëvolueerde objecten brachten enkele honderden van deze, meestal type IIb genoemde, OH masers aan het licht. Hun radio emissie ziet er hetzelfde uit als voor de bekende, dichterbij gelegen, oude sterren, maar is in het algemeen veel sterker. In het visueel en het infrarood waren de nieuw ontdekte bronnen nog totaal onbekend. In dit proefschrift probeer ik iets meer te weten te komen over deze sterren en de hun omringende schillen.

In de nabijheid van de zon zijn een aantal, wat zwakkere, OH masers bekend, die (ik beperk mij nu uitsluitend tot de masers in geëvolueerde sterren), op een doodenkele uitzondering na, allen geassocieerd blijken te zijn met lang periodiek variabelen (LPV), pulserende reuzesterren, die ook wel Mira veranderlijken worden genoemd naar het prototype Mira Ceti (de wonderlijke ster in de walvis; zie de historische inleiding in hoofdstuk I). Deze sterren variëren met een periode van ongeveer een jaar, en in hun maximum kunnen zij 100 tot 10 000 maal helderder zijn dan in hun minimum. Infrarood waarnemingen tonen meer emissie dan verwacht op grond van een eenvoudige stralingswet: een aanwijzing voor een circumstellaire schil van stof en gas. Nader onderzoek van de visuele variaties van deze LPV en de veranderingen in hun OH maseremissie bracht aan het licht dat deze gekoppeld zijn: beide

variaties hebben dezelfde vorm en periode. Het eerste deel van het in dit proefschrift beschreven onderzoek bestond dan ook uit het bestuderen van het gedrag in de tijd van OH masers, waarvan geen optische tegenhangers bekend zijn (zie hoofdstuk II). Deze waarnemingen zijn gedaan met de Dwingeloo Radio Telescoop en er bleek uit dat wij inderdaad van doen hadden met (zeer) lang periodiek variabele sterren. De vorm van de lichtkrommen lijkt zeer op die van de klassieke Mira veranderlijken, maar de perioden zijn veel langer, wel 3 tot 5 jaar. Door een eenvoudig geometrisch model aan te nemen voor de circumstellaire stofschild konden wij uit de tijdvariaties de lineaire afmetingen van de schild bepalen: een belangrijk en uniek resultaat, want in de sterrenkunde is de derde dimensie (diepte, afstand) vaak de moeilijkst te bepalen grootte.

In het derde hoofdstuk worden de waarnemingen beschreven die gedaan zijn met de VLA (very large array: New Mexico, USA) voor een klein aantal van onze OH masers. Met dit instrument, zoals Westerbork een zogenaamde radio synthese telescoop waar de informatie van een aantal afzonderlijke telescopen wordt samengevoegd, kunnen op radio golflengten plaatjes worden gemaakt van een gebiedje aan de hemel, analoog aan de bekende fotografische plaat. Hiermee werden de circumstellaire schillen in kaart gebracht om hun structuur, helderheids- en dichtheidsverloop, en hoekafmeting te bestuderen. Door combinatie met de Dwingeloo waarnemingen waren wij in staat om nauwkeurig de afstand tot ieder object te bepalen (belangrijk zie boven). Uit onze gegevens konden wij zelfs een onafhankelijke bepaling van de afstand van de zon tot het centrum van ons melkwegstelsel halen ( $9.2 \text{ kpc} = 30\,000 \text{ lichtjaar}$ ), een afstand waar alle schalen in ons stelsel vanaf hangen.

In hoofdstuk IV kijken wij eindelijk verder dan onze radioneus lang is, nl. naar het infrarood. Wanneer eenmaal door nauwkeurige metingen, zoals met de VLA, goede posities bekend zijn, is het mogelijk om deze verweg staande, en dus schijnbaar zwakke, sterren in het infrarood terug te vinden. Deze waarnemingen werden gedaan met de United Kingdom Infrared Telescope (UKIRT) op Mauna Kea, Hawaii. Veel van onze OH masers blijken zeer lichtsterke ( $10\,000$  zonslichtkrachten) centrale sterren te hebben met nog veel dichtere circumstellaire stofschillen dan gevonden rond de reeds genoemde Mira veranderlijken. Alle OH/IR sterren vertonen een diepe absorptie in het nabij infrarood (op  $10\mu\text{m}$ ), een bewijs voor grote hoeveelheden koel materiaal rond de ster. Er blijkt een duidelijk verband te bestaan tussen de lange periode, de grotere lichtkracht en de grotere massa van de schild met de sterkte van de OH maser.

Alle waarnemingen, zoals beschreven in de hoofdstukken II t/m IV, en reeds bekende gegevens, zoals de galactische verdeling van de bronnen en intrinsieke eigenschappen van masers, vormen de hoeksteen voor de interpretatie in hoofdstuk V. Daar bekijken wij wat voor eigenschappen van de centrale sterren en de omhullende schillen nu kunnen worden afgeleid. Voor het eerst is het mogelijk om een goede bepaling te geven van allerlei basis parameters: de lichtkracht en de massa van de sterren op dit moment, maar ook wat dit oorspronkelijk (gedurende het grootste deel van hun leven) op de hoofdreeks geweest is. Wij kunnen zeggen hoeveel massa de ster verloren heeft, en nog zal uitstoten; hoe lang deze objecten zichtbaar zijn als OH maser, hoeveel er van dit soort zijn in ons melkwegstelsel en wat er uiteindelijk van hen overblijft. Het blijkt dat de meeste sterren, die nu nog sterke OH masers zijn binnen 10 000 jaar planetaire nevels zullen vormen: zeer hete, kleine steroverblijfselen met een, door de intense sterstraling zichtbare, omringende nevel van stof en gas. Een aantal produceert zgn. witte dwergen, hete mini sterren. In beide gevallen blijft slechts de kern van de oorspronkelijke ster over, nadat alle hogere sterlagen afgestoten zijn. Een enkele van de meest zware OH/IR sterren evolueert zo snel, dat de normale processen van massa afstoting het niet kunnen bijbenen. Deze sterren zullen spoedig (1000 jaar) ontploffen als supernovae: gigantische gebeurtenissen waarbij in één ster voor korte tijd een hoeveelheid energie vrijkomt, die wij normaal van een geheel melkwegstelsel ontvangen.

## Curriculum vitae

In 1972 behaalde ik het eindexamen gymnasium  $\beta$  aan het Stedelijk Gymnasium te Haarlem en besloot sterrenkunde te gaan studeren in Leiden. Na aanvankelijk alles behalve studeren gedaan te hebben, her begon ik in 1973 met frisse moed en ernstige vermaningen van de studiebegeleider (R.S. Le Poole). In februari 1976 behaalde ik het kandidaats - en in juni 1979 het doctoraal examen. In de doctoraal fase volgde ik een (tegenwoordig door de strakke programmering helaas niet meer haalbaar) aantal colleges: Infrarood sterrenkunde (H.C. van de Hulst), Astronomische waarneemtechnieken (R.S. Le Poole), Stralingsprocessen (H.J. Habing), Melkwegstructuur (A. Blaauw en P. Woodward), Hoge energie astrofysica (H. van der Laan en C. Norman), Interstellaire materie (J.M. Greenberg), Variabele sterren (Th. Walraven), Cosmologie (R.J. Takens, V. Icke en H. van der Laan), Quantummechanica II (C.D. Hartogh), Mathematische fysica (J. van de Linde), Numerieke Wiskunde B en C (F. Bakker e.a.), en Numerieke oplossingen van partiële differentiaalvergelijkingen 1 en 2 (M. Spijker en B. van Leer). In sommige vakken deed ik daadwerkelijk tentamen. Mijn klein onderzoek bij K.K. Kwee betrof de eclipsveranderlijke V548 Cygni, mijn groot onderzoek bij H.J. Habing tijdsvariaties van OH masers. Een aantal maanden verrichtte ik correctiewerk t.b.v. J. Lub, twee jaar lang was ik student-assistent en gedurende een jaar had ik zitting in de universiteitsraad.

Van september 1979 tot maart 1983 was ik als wetenschappelijk assistent in dienst van ZWO (stichting voor zuiver wetenschappelijk onderzoek) en kon het onderzoek aan OH masers voortzetten en uitbreiden. In die tijd bezocht ik tweemaal de YERAC (young european radio astronomers conference): in 1980 te Bologna (Italië) en in 1983 te Göteborg (Zweden). Voorts nam ik deel aan de workshop 'Physical Processes in Red Giants' te Erice (Italië) in 1980, en aan IAU symposium 103 'Planetary Nebulae' te Londen (UK) in 1982. Op iedere conferentie werd een eigen bijdrage geleverd (in Londen in de vorm van een poster). Ik bracht werkbezoeken aan de VLA (very large array; New Mexico, USA), aan Jodrell Bank (UK) en talloze malen aan Dwingeloo (nabij Lhee). Colloquia over mijn werk werden gegeven in Amsterdam en Groningen.

## Dankbetuiging

Een ieder die aan de totstandkoming van dit proefschrift heeft bijgedragen, en dat waren er zeer vele, dank ik daarvoor hartelijk.

Tekeningen: Jaques Ober

Foto's : Wim Brokaar

Typewerk : Wanda van Grieken-Rückert, Lenore Hakkaart-de Leeuw, Marja van Haastert en Lena Cijntje.

This research was supported by a grant from ASTRON, the Netherlands Foundation for Astronomical Research. The Dwingeloo Radio Telescope is operated by SRZM, the Netherlands Foundation for Radio Astronomy. Both ASTRON and SRZM receive their funds from ZWO, the Netherlands Organization for the Advancement of Pure Research. The VLA is run by NRAO, the National Radio Astronomy Observatory (USA), which is operated by Associated Universities, Inc., under contract with the National Science Foundation. The UKIRT facility is run on behalf of the United Kingdom Science Research Council from the Royal Observatory, Edinburgh.

Stellingen  
behorende bij het proefschrift  
'The nature of OH/IR stars'

1. De verklaring van asymmetrieën in de helderheidsverdeling van OH maseremissie door rotatie van de circumstellaire schil is onjuist.

Norris, R.P., Diamond, P.J., Booth, R.S.: 1982, preprint  
.Dit werk, hoofdstuk III

2. Maser hotspots, zoals waargenomen in VLBI experimenten, kunnen in combinatie met het bestuderen van variaties op zeer korte tijdschalen inzicht verschaffen in de meest fundamentele eigenschappen van masers en hun directe omgeving.

Dit werk, hoofdstuk II

3. OH masers geven ons niet alleen nauwkeurige afstanden tot individuele objecten, en de mogelijkheid tot een goede bepaling van de schaallengte van ons melkwegstelsel, maar zij kunnen tevens, wanneer een monitorprogramma met het VLBI netwerk binnen de grenzen van het mogelijke komt, directe afstandsbepalingen tot de meer nabijgelegen extragalactische stelsels opleveren.

Dit werk, hoofdstuk V

4. Meer dan 60% van de zichtbare planetaire nevels is ooit OH maser geweest. Het verdient daarom aanbeveling, ondanks het gebrek aan succes tot op heden, te zoeken naar meer objecten die, zoals Vy 2-2, in het overgangsstadium zijn.

Kwok, S.: 1981, in 'Physical Processes in Red Giants', p. 421  
Dit werk, hoofdstuk V en appendix D

5. Floor van Leeuwen's zesde stelling "Het onderzoek naar variabele sterren dient gestimuleerd te worden" is juist, mits aangevuld met de voorwaarde dat de subsidieduur voor zulk een onderzoek de variatietijdschaal van dergelijke sterren overtreft.

Floor van Leeuwen: 1983, 'The Pleiades', proefschrift RUL

6. Bij evolutie berekeningen voor sterren op de asymptotische reuzentak dient het zeer hoge massaverlies in de 'superwind' fase in rekening te worden gebracht.

7. Fred Hoyle's opvatting over het ontstaan van superhelder inzicht en van Kunst door het opvangen van signalen van een cosmische, alles omvattende intelligentie is in tegenspraak met de gebrekkige kennis van en inzichten in fysische en astronomische waarheden bij onze voorvaderen, terwijl daarentegen in literair en filosofisch opzicht de klassieken op een zeer hoog niveau staan.

Fred Hoyle: 1982, Ann. Rev. Astron. Astroph. 20, 1

8. Het is aan te bevelen dat zowel de referee als de auteur(s) van artikelen anoniem blijven.

9. Het eerstejaarsprogramma sterrenkunde zou topografie van de hemelbol moeten bevatten.

10. Instellingen als de VU en de Vaticaansterrewacht hebben geen bestaansrecht. Geloof en wetenschap zijn elkaars tegenpolen.

11. Hedendaagse politiek bedrijven met een boek van 2000 jaar oud in de hand, is als sterrenkunde doen gebaseerd op de Almagest.

12. Religie en marxisme zijn beide vormen van snarxisme.

Vrij naar Lewis Carroll: 1876. 'The hunting of the snark'

13. Instellingen als de krijgsraad en het medisch tuchtcollege zijn in strijd met de leer van de trias politica en vormen als zodanig een bedreiging voor de democratie.

14. Emancipatie, evenals het bieden van gelijke kansen zonder onderscheid naar ras, huidskleur, sociaal aanzien of geloof, is het accepteren en niet het egaliseren van verschillen.

15. Het is tekenend voor de minachting van onze voorvaderen en van de wortels van onze cultuur dat de theorieën van Charles de Grave, Theophile Cailleux en Ernst Gideon over de Ilias en Odyssee, als erfstuk van de Kelten, door classici niet aux serieux worden genomen.

Ernst Gideon: 1973, 'Homerus, zanger der Kelten'

16. De Dow-Jones index voor industriële aandelen lijkt in meer dan getalsmatig opzicht op een barometer.

17. De sticker met de tekst 'atoomenergie, nee bedankt' rond de afbeelding van een lachende zon getuigt van weinig inzicht in (astro) fysica.

Leiden, 8 september 1983.



84.05.16